

Investigation of Effervescent Atomization Using Laser-Based Measurement Techniques

“Science is the belief in the ignorance of experts”

Richard P. Feynman, 1981

University of Alberta

Investigation of Effervescent Atomization Using Laser-Based Measurement
Techniques

by

Sina Ghaemi

A thesis submitted to the Faculty of Graduate Studies and Research
in partial fulfillment of the requirements for the degree of

Master of Science

Department of Mechanical Engineering

©Sina Ghaemi
Fall 2009
Edmonton, Alberta

Permission is hereby granted to the University of Alberta Libraries to reproduce single copies of this thesis and to lend or sell such copies for private, scholarly or scientific research purposes only. Where the thesis is converted to, or otherwise made available in digital form, the University of Alberta will advise potential users of the thesis of these terms.

The author reserves all other publication and other rights in association with the copyright in the thesis and, except as herein before provided, neither the thesis nor any substantial portion thereof may be printed or otherwise reproduced in any material form whatsoever without the author's prior written permission.

Examining Committee

Payam Rahimi (Supervisor), Mechanical Engineering

David S. Nobes (Supervisor), Mechanical Engineering

Alidad Amirfazli, Mechanical Engineering

Sean Sanders, Chemical Engineering

This dissertation is dedicated to my father and mother for their endless support.

Abstract

Effervescent atomization has been a topic of considerable investigation in the literature due to its important advantages over other atomization mechanisms. This work contributes to the development of both effervescent atomizers and also laser-based techniques for spray investigation

In order to develop non-intrusive measurement techniques for spray applications, a procedure is suggested to characterize the shape of droplets using image-based droplet analyzers. Image discretization which is a major source of error in droplet shape measurement is evaluated using a simulation. The accuracy of StereoPIV system in conducting droplet velocity measurement in a spray field is also investigated.

To assist in the design of effervescent atomizers, bubble formation during gas injection from a micro-tube into liquid cross-flow is investigated using a Shadow-PIV/PTV system. The generated spray fields of two effervescent atomizers which operate using a porous and a typical multi-hole air injector are compared using qualitative images and Shadow-PTV measurement.

Acknowledgement

I would like to express my appreciation to my advisors Dr. Payam Rahimi and Dr. David Nobes for their guidance throughout my graduate studies. I would like to thank Dr. Rahimi for advising me on proper presentation of the results and conducting independent research. I also would like to deeply thank Dr. David Nobes and confess that without him an MSc program in this university was a waste of time and resources. He spent long hours on teaching me how to analyze a phenomenon, conduct a reliable experiment, and write a scientific article. His office door has always been open to me and I greatly enjoyed our numerous discussions.

Contents

1. Introduction	1
1.1. Motivation	1
1.2. Thesis Outline.....	2
2. Experimental Setup	5
2.1. Liquid and Air Supply	5
2.2. Micro-Bubble Generator.....	9
2.3. Effervescent Atomizers.....	11
2.3.1. <i>Atomizer Mark I</i>	12
2.3.2. <i>Atomizer Mark II</i>	13
3. Measurement Setup	16
3.1. Shadow-PTV	16
3.1.1. <i>Working Principle of the Shadow-PTV Technique</i>	16
3.1.2. <i>Image Acquisition</i>	17
3.1.3. <i>Shadow-PTV Image Processing</i>	19
3.2. Stereo-PIV	22
3.2.1. <i>Overview of the Stereo-PIV Technique</i>	22
3.2.2. <i>Image Acquisition</i>	22
3.2.3. <i>Image Processing</i>	24
3.3. Shadow-PIV/PTV	26
3.3.1. <i>Overview of the Shadow-PIV/PTV Technique</i>	26
3.3.2. <i>Image Acquisition</i>	26
3.3.3. <i>Image Processing</i>	27
4. Assessment of Parameters for Distinguishing Droplet Shape in a Spray Field Using Image-Based Techniques	31
4.1. Introduction	31
4.2. The Experiment	35
4.3. Droplet Shape in a Spray Field	36
4.4. An Overview of Shape Quantifying Parameters.....	40
4.5. Assessment of Shape Parameters.....	46
4.6. Conclusion	53

5. Evaluation of Digital Image Discretization Error in Droplet Shape Measurement	
Using Simulation	54
5.1. Introduction	54
5.2. Digital Image Discretization	57
5.3. Simulation of Digital Images	59
5.4. Effect of Image Discretization on Area and Perimeter	61
5.5. Effect of Image Discretization on the Performance of Shape Parameter	64
5.6. Conclusion	75
6. Evaluation of StereoPIV Measurement of Droplet Velocity in an Effervescent	
Spray	76
6.1. Introduction	76
6.2. The Experiment	79
6.3. Comparison of StereoPIV and Shadow-PTV Velocity Measurement	81
6.4. Effect of Droplet Number Density	84
6.5. Effect of Droplet Axial Velocity Radial Distribution	87
6.6. Effect of Droplet Size Distribution	89
6.7. Conclusion	96
7. The Effect of Gas-Injector Location on Bubble Formation in Liquid Cross-Flow	98
7.1. Introduction	98
7.2. The Experiment	102
7.3. Bubble Size	103
7.4. Bubble Shape	107
7.5. Bubble Location	110
7.6. Bubble Velocity	112
7.7. Liquid Velocity Field	118
7.8. Discussion	125
7.9. Conclusion	127
8. The Effect of Internal Flow Structure on the Performance of Effervescent	
Atomization	128
8.1. Introduction	128
8.2. The Experiment	131
8.3. Qualitative Investigation of Internal Flow and the Produced Spray	132
8.4. Quantitative Investigation of the Generated Spray Field	141
8.4.1. Droplet Number Frequency	141
8.4.2. Droplet SMD	148
8.4.3. Ligaments and Large Droplets	154
8.5. Conclusion	156

9. Conclusion.....	157
9.1. Summary of Results.....	157
9.2. Future work.....	160
10. References.....	161
11. Appendix A: CVI Code.....	175
Appendix A1: The CVI panel:.....	176
Appendix A2: The CVI code:.....	177
Appendix B: Drawings.....	197
Appendix B1: Atomizer Mark I.....	198
<i>Atomizer Body:</i>	198
<i>Multi-Hole Air Injector</i>	199
Appendix B2: Atomizer Mark II.....	200
<i>Atomizer Body:</i>	200
<i>Porous Air Injector</i>	201
<i>Multi-Hole Air Injector</i>	202
Appendix B3: Air and Liquid Supply.....	203
Appendix B3: Bubble Generator Setup.....	204
<i>The Assembly:</i>	204
<i>Middle Plane:</i>	205
<i>Front Window:</i>	206
<i>Back Window:</i>	207
Appendix C: Processes using Davis Software.....	208
Appendix C1: Shadow-PTV Process.....	209
Appendix C2: StereoPIV Process.....	211
Appendix C3: The PTV Process of the Shadow-PIV/PTV Experiment.....	213
Appendix C4: The PIV process of the Shadow-PIV/PTV Experiment.....	215
Appendix D: Simulation Codes.....	217
Appendix D1: The Main Script.....	218
Appendix D2: The Preprocessing Function.....	221
Appendix D3: Basic Geometric Features.....	222
Appendix D4: Parameter 1.....	225
Appendix D5: Parameter 2.....	225
Appendix D6: Parameter 3.....	225
Appendix D7: Parameter 4.....	225
Appendix D8: Parameter 5.....	226
Appendix D9: Parameter 6.....	226
Appendix D10: Parameter 7.....	226

Appendix D11: Parameter 8.....	226
Appendix D12: Parameter 9.....	226
Appendix D13: Parameter 10.....	227
Appendix D14: Parameter 14.....	227
Appendix D15: Circular and Elliptical Discs.....	227
Appendix E: Contributions:	229
Publications:.....	229
Refereed Conference Proceedings:	229
Presentations:.....	230

List of Tables

Table 2-1. List of the flow controllers and flow meters used in different experiments.....	7
Table 2-2. Specification of the variable-area flow meter.	7
Table 2-3. Specifications of the mass and volumetric flow controllers.....	8
Table 3-1. Specifications of the Nd:YAG laser.....	18
Table 3-2. Specifications of LaVision Image Intense Camera.	19
Table 3-3. Configuration of the zoom lens system and the corresponding specifications used to spray droplets experiment.....	19
Table 3-4. Configuration of the applied zoom lens system and the corresponding specifications used micro-bubble experiment.....	27
Table 4-1. An overview of shape quantifying parameters.....	44

List of Figures

Figure 2-1. Schematic diagram of the flow supply and control setup used to deliver pressurized air and water.	6
Figure 2-2. Schematic of the micro-bubble generator. (1) water inlet, (2) water exit, (3) water channel, (4) water reservoir, (5) washer, (6) screw, (7) micro-tube.	9
Figure 2-3. Image of the bubble generator setup.....	10
Figure 2-4. The atomizer and the spray collecting system installed on a frame.....	12
Figure 2-5. Schematic of the effervescent atomizer mark I, air injector, and water and air inlets.	13
Figure 2-6. An image of the effervescent atomizer mark I made from cast acrylic.	13
Figure 2-7. Schematic of the effervescent atomizer mark II consisting of (1) mixing chamber, (2) liquid inlet, (3) air injector.....	14
Figure 2-8. An image of the body of the atomizer mark II manufactured from cast acrylic.	15
Figure 2-9. An image of the two air injectors used in the second effervescent atomizer.	15
Figure 3-1. Shadow-PTV images of droplets in a spray field. (a) $t = t_0$. (b) $t = t_0 + 0.6$ μ s.	17
Figure 3-2. The Shadow-PTV configuration.....	18
Figure 3-3. An image of the Shadow-PTV system.....	18
Figure 3-4. The Shadow-PTV process using Davis software (a) calculated reference image (b) preprocessed image (c) global segmentation (d) the detected droplets and their measured area equivalent diameter (μ m) and velocity (m/s).....	20
Figure 3-5. StereoPIV system configuration.....	23
Figure 3-6. An image of the StereoPIV system configuration.....	23
Figure 3-7. StereoPIV image (a) at the nozzle vicinity, $z/d= 20$ (b) at the far field, $z/d=140$ (c) after the preprocessing step (d) the computed vector field averaged over 500 images.....	25

Figure 3-8. StereoPIV image (a) at the nozzle vicinity, $z/d= 20$ (b) at the far field, $z/d=140$ (c) after the preprocessing step (d) the computed vector field averaged over 500 images.....	25
Figure 3-9. The shadow-PIV/PTV configuration.....	27
Figure 3-10. Double-frame Shadow-PIV/PTV image. (a) $t = t_0$. (b) $t = t_0 + 0.6 \mu\text{s}$	29
Figure 3-11. The PTV process applied to the Shadow-PTV/PIV images (a) the micro-tube has been manually masked out (b) the bubbles area has been detected using the PTV algorithm.....	29
Figure 3-12. The PIV process applied to the Shadow-PTV/PIV images (a) the bubbles and the micro-tube are masked out (b) preprocessing algorithm has been applied to the images (c) the calculated vectors over the complete image field (d) calculated vector field around the micro-tube.....	30
Figure 4-1. Liquid jet disintegration at the nozzle location.....	36
Figure 4-2. Disintegration of ligaments and droplets at $z/d=10$	36
Figure 4-3. Two images of an example of droplet breakup into two droplets through the vibrational mechanism at (a) $t = t_0$. (b) $t = t_0 + 0.6 \mu\text{s}$	37
Figure 4-4. Two images of an example of droplet breakup into fragments through the vibrational mechanism at (a) $t = t_0$. (b) $t = t_0 + 0.6 \mu\text{s}$	37
Figure 4-5. Two images of the breakup of a droplet into many fragments through the bag breakup mechanism at (a) $t = t_0$. (b) $t = t_0 + 0.6 \mu\text{s}$	37
Figure 4-6. Two images of the breakup of a droplet into many fragments through the bag breakup mechanism at (a) $t = t_0$. (b) $t = t_0 + 0.6 \mu\text{s}$	37
Figure 4-7. Collision of droplets that leads to droplet coalescence; (a) $t = t_0$. (b) $t = t_0 + 0.6\mu\text{s}$	37
Figure 4-8. Collision of droplets that leads to droplet breakup into fragments (a) $t = t_0$. (b) $t = t_0 + 0.6\mu\text{s}$	37
Figure 4-9. Droplet shapes at a spray field. (a)-(b) spherical droplets, (c)-(f) elliptical droplets, and (g)-(t) ligaments.	39
Figure 4-10. Assessment of shape identification using <i>Parameter 1</i>	49
Figure 4-11. Assessment of shape identification using <i>Parameter 2</i> , method (IV).....	49
Figure 4-12. Assessment of shape identification using <i>Parameter 2</i> , method (VI).....	50
Figure 4-13. Assessment of shape identification using <i>Parameter 3</i>	50
Figure 4-14. Assessment of shape identification using <i>Parameter 4</i>	51
Figure 4-15. Assessment of shape identification using <i>Parameter 8</i>	51
Figure 4-16. Assessment of shape identification using <i>Parameter 9</i>	52
Figure 4-17. Assessment of shape identification using <i>Parameter 10</i>	52

Figure 5-1. Formation of discretized images on the CCD grid. (a) Center of the assumed circle is at the centroid of the central pixel. Boundary pixels are 4-connected to the background. (b) Center of the assumed circle is shifted 1/6 pixel to right. Boundary pixels are 8-connected to the background. Center of the assumed circle is shifted (c) 1/2 pixel to right (d) 1/6 pixel downward (e) 1/6 pixel to right and 1/6 pixel downward (f) 1/2 pixel to right and 1/6 pixel downward (g) 1/2 pixel downward (h) 1/2 pixel to right and 1/2 pixel downward. (i) The diameter of the assumed circle is twice that of other images.	58
Figure 5-2. Two-dimensional discretized images of used in the simulation. (a) simulated circular disc, (b) simulated elliptical disc with $b/a = 0.7$, and (c) simulated elliptical disc with $b/a = 0.4$	60
Figure 5-3. Image discretization effect on area measurement.	63
Figure 5-4. Image discretization effect on perimeter measurement.	63
Figure 5-5. Effect of image discretization on shape quantification using Parameter 1.	67
Figure 5-6. Effect of image discretization on shape quantification using Parameter 2.	68
Figure 5-7. Effect of image discretization on shape quantification using Parameter 3.	68
Figure 5-8. Effect of image discretization on shape quantification using Parameter 4.	69
Figure 5-9. Effect of image discretization on shape quantification using <i>Parameter 8</i>	69
Figure 5-10. Effect of image discretization on shape quantification using <i>Parameter 9</i>	70
Figure 5-11. Definition of the terms used in the “clearance factor”.....	72
Figure 5-12. The clearance factor expressing the capability of shape parameters to distinguish circular discs and 0.7 elliptical discs.	73
Figure 5-13. The clearance factor expressing the capability of shape parameters to distinguish 0.7 and 0.4 elliptical discs.	74
Figure 6-1. Droplet axial velocity decay along the spray centerline measured by the StereoPIV and Shadow-PTV systems at (a) GLR=0.198 (b) GLR=0.085 (c) GLR=0.054.....	82
Figure 6-2. StereoPIV image (a) at the nozzle vicinity, $z/d = 20$ (b) at the far field, $z/d=140$. The images have the same level of gray-scale.	84
Figure 6-3. PDF of pixels in the StereoPIV images with intensity higher than 2.4 percent of the maximum count along the spray centerline.....	85
Figure 6-4. Droplet velocity profile at two axial locations for GLR of 0.085. Half of the laser sheet thickness is also shown in this plot.	88
Figure 6-5. StereoPIV and size-classified Shadow-PTV measurement of axial velocity of spray droplets at (a) GLR=0.198 (b) GLR=0.085 (c) GLR=0.054.....	89

Figure 6-6. N_f , and $N_f \times A$ at different GLRs and locations along the spray centerline. The cross sign (\times) shows the mean diameter based on the $N_f \times A$ plot and the circular sign (\circ) shows the mean diameter based on N_f .	94
Figure 7-1. Bubble size versus y distance for four different location of the air injector tip of (a) $x/w = 0$, (b) $x/w = 1/6$, (c) $x/w = 1/3$, and (d) $x/w = 1/2$. The average of the size of all the bubbles, the preliminary bubbles and the secondary bubbles in the axial range of $y/w = [0.1 \ 1.1]$ are shown by ‘—’, ‘- -’, and ‘- -’, respectively.	104
Figure 7-2. Bubble centricity versus diameter for two different location of the air injector tip of (a) $x/w = 0$ and (b) $x/w = 1/2$.	108
Figure 7-3. Samples of low centricity large bubble observed in the secondary group of bubbles.	109
Figure 7-4. The location of high centricity (>0.6) and low centricity (<0.6) bubbles. The tip of the air injector tube is located at $x/w = 1/2$ and $y/w = 0$.	111
Figure 7-5. Axial velocity of the bubbles versus axial distance. The air injector is located at (a) $x/w = 0$ (b) $x/w = 1/2$.	113
Figure 7-6. The double-frame image corresponding to data point 3 in Figure 7-5(a).	114
Figure 7-7. The double-frame image corresponding to data point 2 in Figure 7-5(a).	114
Figure 7-8. The double-frame image corresponding to data point 3 in Figure 7-5(a).	115
Figure 7-9. The double-frame image corresponding to data point 4 in Figure 7-5(a).	115
Figure 7-10. The double-frame image corresponding to data point 1 in Figure 7-5(b).	117
Figure 7-11. The double-frame image corresponding to data point 2 in Figure 7-5(b).	117
Figure 7-12. Contours of liquid axial velocity field in the channel. The tip of the air injector is located at (a) $x/w = 0$ (b) $x/w = 1/2$.	121
Figure 7-13. Profiles of water axial velocity at different locations in the channel.	122
Figure 7-14. RMS of axial velocity field in the channel. The tip of the air injector is located at (a) $x/w = 0$ (b) $x/w = 1/2$.	123
Figure 7-15. Vorticity field in the channel. The tip of the air injector is located at (a) $x/w = 0$ (b) $x/w = 1/2$.	124
Figure 8-1. The generated bubbles in the mixing chamber by (a) the porous media air injector and (b) the multi-hole air injector. The liquid flow is downward.	134
Figure 8-2. The air-water mixture near the discharge orifice produced by the (a) porous media air injector and (b) the multi-hole air injector.	135
Figure 8-3. Shadowgraphy images of the spray produced by the effervescent atomizer applying the porous air injector.	136
Figure 8-4. Shadowgraphy images of the spray produced by the effervescent atomizer applying the multi-hole air injector.	137

Figure 8-5. Number frequency of droplets at GLR=0.0148 for (a) $z/d = 37.5$, (b) 50, (c) 62.5, (d) 75, and (e) 87.5 locations along the spray centerline.....	143
Figure 8-6. Number frequency of droplets at GLR=0.0181 for (a) $z/d = 37.5$, (b) 50, (c) 62.5, (d) 75, and (e) 87.5 locations along the spray centerline.....	144
Figure 8-7. Number frequency of droplets at GLR=0.0208 for (a) $z/d = 37.5$, (b) 50, (c) 62.5, (d) 75, and (e) 87.5 locations along the spray centerline.....	145
Figure 8-8. Number frequency of droplets at GLR=0.0237 for (a) $z/d = 37.5$, (b) 50, (c) 62.5, (d) 75, and (e) 87.5 locations along the spray centerline.....	146
Figure 8-9. Number frequency of droplets at GLR=0.0267 for (a) $z/d = 37.5$, (b) 50, (c) 62.5, (d) 75, and (e) 87.5 locations along the spray centerline.....	147
Figure 8-10. SMD of droplets generated versus axial distance generated at (a) GLR = 0.0148, (b) 0.0181, (c) 0.0208, (d) 0.0237, (e) 0.0267. All the droplets have been considered in the SMD calculations.	150
Figure 8-11. SMD of droplets generated versus axial distance generated at (a) 0.0148 (b) 0.0181 (c) 0.0208 (d) 0.0237 (e) 0.0267. Droplets larger than 200 μm have not been considered in the SMD calculation.....	151
Figure 8-12. SMD of droplets generated versus axial distance generated at (a) 0.0148 (b) 0.0181 (c) 0.0208 (d) 0.0237 (e) 0.0267. Droplets larger than 100 μm have not been considered in the SMD calculation.....	152
Figure 8-13. SMD of droplets generated versus axial distance generated at (a) 0.0148 (b) 0.0181 (c) 0.0208 (d) 0.0237 (e) 0.0267. Droplets larger than 50 μm have not been considered in the SMD calculation.....	153
Figure 8-14. Number of droplets larger than 200 μm generated at (a) GLR = 0.0148, (b) 0.0181, (c) 0.0208, (d) 0.0237, (e) 0.0267.....	155

List of Nomenclatures

Abbreviations

ACH	area of convex hull
CCD	charge-coupled device
con	convexity parameter
GLR	gas-liquid-ration
PCH	perimeter of convex hull
PDF	probability density function
PTV	Particle tracking velocimetry
rect	rectangle
sign	the sign function
StereoPIV	stereoscopic particle image velocimetry
Shadow-PTV	shadowgraphy particle tracking velocimetry
S-PIV/PTV	shadowgraphy particle image velocimetry and particle tracking velocimetry
N_f	droplet number frequency
QE	quantum efficiency
SMD	Sauter mean diameter
We	Weber number

Symbols

a	long axis
A	area
b	short axis
d	diameter of the discharge orifice
D	droplet diameter
e	correction factor
e_r	<i>Parameter 4</i> (as defined in Table 4-1)
f	correction factor (Eq. 4-2)
(i, j)	pixel coordinate in Cartesian system
l	length of the discharge orifice
\dot{m}	mass flow rate
P	perimeter
r	radius, radial distance (as shown in Figure 3-2 and Figure 3-5)
t	time
T	image thickness
V_r	<i>Parameter 8</i> (as defined in Table 4-1 [60])
V_p	<i>Parameter 9</i> (as defined in Table 4-1 [60])
w	channel thickness
x	distance across the channel (as shown in Figure 2-2)
y	distance along the channel (as shown in Figure 2-2)
z	distance along the spray centerline (as shown in Figure 3-2 and Figure 3-5)

Subscripts

<i>A</i>	area
<i>G</i>	gas
<i>i</i>	a location on the perimeter
<i>l</i>	liquid
<i>m</i>	mean
<i>p</i>	perimeter
<i>G</i>	centroid pixel

1. Introduction

1.1. Motivation

Spray systems and the atomization process play an important role in many applications within automotive [1-3], chemical [4-6], and pharmaceutical industries [7, 8]. Design of an optimized atomizer has prompted industries and researchers to measure various characteristics of spray fields such as droplet size, droplet velocity, dispersion, cone angle, and liquid distribution [9]. Laser-based techniques have developed into a viable tool for conducting non-intrusive measurement of spray and droplets characteristics. Although substantial work has been devoted in the literature on the development of laser-based techniques, there are still numerous phenomena in the spray field which have escaped characterization [10]. The first part of this thesis contributes to the development of laser-based measurement techniques to meet the demanding challenge of investigating spray fields.

One of the most challenging atomization processes is effervescent atomization [11]. Effervescent atomization involves several complex mechanisms in both the atomizer mixing chamber and the external spray field. In this atomization mechanism, a mixture of liquid and gas is introduced into a mixing chamber located at an upstream location of the discharge orifice. The atomization performance is enhanced through the interactions between the gas and the liquid phase. The pattern of the two-phase flow formed in the mixing chamber can significantly affect the atomization performance [12, 13] and is a function of several parameters such as the gas flow rate, the liquid flow rate, the geometry of the mixing chamber, the flow direction, and pressure in the mixing chamber. The second section of this thesis describes the investigations related to the design and operation of effervescent atomization.

1.2. Thesis Outline

The thesis includes 9 chapters and 5 appendices. Chapters 2 and 3 describe the experimental setup and the applied measurement techniques, respectively. Chapters 4, 5, 6, 7, and 8 have been included with minor changes from their original publications which have been submitted to journals [14, 15, 16, and 17]. These chapters are relatively self-contained. The chapters have their own introduction and discussion on the literature and also cover the motivation and the aims of each chapter. Chapters 4, 6, and 6 contribute to the development of laser-based measurement techniques for the investigation of spray fields. Chapter 7 and 8 contribute to the design and development effervescent atomizers. A brief note on applied experimental setup and measurement technique is also provided in each chapter. The following chapters are included.

Chapter 2: The experimental setups used in the different investigation are recorded in this chapter. The facility developed to deliver pressurized water and air, the micro-bubble generator setup, and the designed effervescent atomizers are described.

Chapter 3: This chapter aims to describe the measurement techniques used in the investigations. Shadowgraphy particle tracking velocimetry (Shadow-PTV), stereoscopic particle image velocimetry (StereoPIV), and shadowgraphy particle image velocimetry/particle tracking velocimetry (Shadow-PIV/PTV) are described.

Chapter 4: This chapter is devoted to provide a standard procedure for quantification of droplet shape in a spray field using image-based droplet analyzers. Several parameters from different applications are presented in terms of their mathematical definition, calculation procedure, and characteristics. An experimental investigation using a shadowgraph droplet analyzer is also conducted to provide visual evidence of droplet shapes in a spray field. The capability of the shape parameters in distinguishing between these droplets is investigated. Finally, a modified shape parameter is suggested for droplet shape characterization.

Chapter 5: The error caused by discretization of digital images in droplet shape measurement is investigated in this chapter. The accuracy of calculating the shape parameters and their capability in revealing shape deviation is considerably affected by the discretization of the image with a charge-coupled device (CCD) sensor. A simulation of digital images is conducted to investigate the error caused by image discretization on

calculating area, perimeter, and also a selected number of shape parameters. The shape parameters have been ranked based on their sensitivity to shape deviation and image discretization.

Chapter 6: The StereoPIV measurement of droplet velocity in a spray field is evaluated in this chapter. Particle image velocimetry (PIV) is a well known technique for measuring the instantaneous velocity field of flows. But this technique may introduce considerable error in measuring the velocity field of sprays when the spray droplets are used as the seed particles. The effect of droplet number density, droplet velocity profile, and droplet size distribution of a spray produced by an effervescent atomizer on velocity measurement using a StereoPIV has been investigated. A Shadow-PTV system provided measurement of droplet size and velocity for comparison.

Chapter 7: This chapter describes an experimental investigation conducted on bubble formation during gas injection from a micro-tube into downward liquid cross-flow. This experiment has been conducted to assist in the design of the internal geometry of effervescent atomizers. Liquid flows incorporating small-size bubbles also play a vital role in many industrial applications. In this work, the tip of the air injector has been located at the wall (wall orifice) and also three other locations across the channel (nozzle injection). The size, shape, and velocity of the bubbles along with liquid velocity field are measured using a Shadow-PIV/PTV system.

Chapter 8: The performance of an effervescent atomizer which applies a porous media part to inject air into the mixing chamber is investigated in this chapter. A typical multi-hole air injector has also been used in this atomizer for comparison. The two-phase flows inside the mixing chamber and the atomization mechanism have been investigated using visual images. The droplet size distribution, droplet SMD, and the number of large droplets in the spray field have been investigated using the Shadow-PTV system.

A number of appendices are also included in this thesis to provide more detail on components, procedures, and contributions. These appendices include:

Appendix A: This appendix provides the code developed to communicate with the flow controllers and the pressure transducers.

Appendix B: This appendix provides the detailed drawings of the components.

Appendix C: The parameters used for Shadow-PTV, StereoPIV, and Shadow-PIV/PTV processes are recorded in this appendix.

Appendix D: The codes developed in MATLAB are recorded in this appendix.

Appendix E: This appendix provides a list of the journal papers, conference proceedings, and presentations resulting from this work.

2. Experimental Setup

The intent of this chapter is to describe the experimental setup and the equipments used in the investigations. The described setups have been used to generate the required flow field in the two main investigations on micro-bubble generation and effervescent atomization. The first part of the following subsections describes the facility which is developed to supply and control pressurized air and water flows in the experiments. Next, the setup developed to generate micro-bubbles in liquid cross-flow is explained. Finally, the effervescent atomizers which have been designed and manufactured for different investigations are detailed.

2.1. *Liquid and Air Supply*

A facility was developed to deliver pressurized air, water, and also a mixture of PIV seeding particle in water. A schematic diagram of the facility is illustrated in Figure 2-1. Shop air is used to deliver pressurized air of up to 95 psig. The required flow of clean water is supplied from a 36 liter capacity storage tank. The water in this storage tank was pressurized by the shop air to maintain a steady flow from an opening at the lower side of the tank. A smaller storage tank (6 liter) has been used to store a mixture of PIV seeding particles (20 μ m glass particles) in water. A dense mixture of seeding particles is manually fed by a syringe into this tank before pressurizing the fluid. A dip tube that extends downward into the bottom of the tank is used to extract the mixture of seeding particles and water. The flow rates of the clean water and the seeding mixture can be adjusted to obtain appropriate concentration of seeding particles in the final flow.

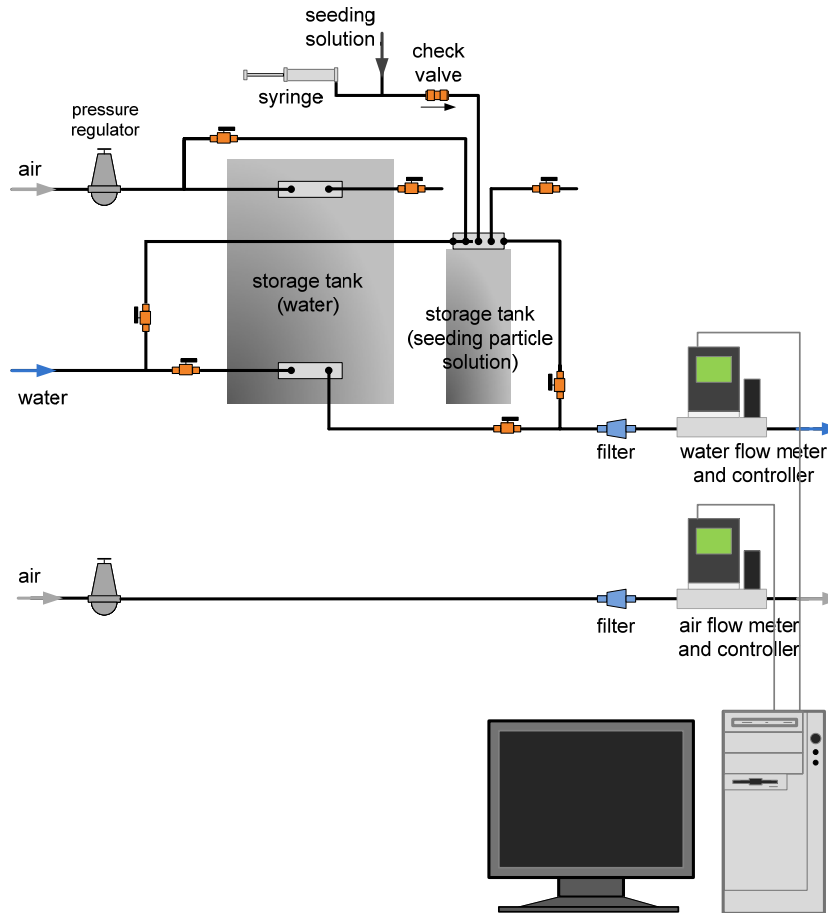


Figure 2-1. Schematic diagram of the flow supply and control setup used to deliver pressurized air and water.

The air and water flow rates are controlled and measured using different flow controllers each appropriate for a certain flow range. The flow controllers operate based on differential pressure technology and particles larger than $20\ \mu\text{m}$ should not populate the flow stream [18]. Therefore, in order to prevent any possible damage to the flow controllers, as it is shown in Figure 2-1, a $20\ \mu\text{m}$ in-line filter has been installed at an upstream location of the flow controllers. The flow controllers also measure flow temperature and line-pressure. The controllers are PC controlled for data monitoring and recording using a code developed in the LabWindows/CVI (National Instruments) software. This code provides a visual panel in order to communicate with the flow controllers and also has the capability to communicate with two pressure transducers. The main script of this code is attached in Appendix A. The experiments which require a

mixture of seeding particles are conducted using a variable-area flow meter and the in-line filter is bypassed. A list of the flow meters/controllers used in the experiments is presented in Table 2-1. Specifications of the variable-area flow meter and the flow controllers are also presented in Table 2-2 and Table 2-3, respectively.

Table 2-1. List of the flow controllers and flow meters used in different experiments.

Model	Type	Full Scale (mL/min)	Technology
EW-32907-46 (Cole-Parmer)	Water flow controller	500	Differential pressure
RK-03217-36 (Cole-Parmer)	Water flow meter	1800	Variable area
EW-32907-55 (Cole-Parmer)	Air flow controller	10	Differential pressure
EW-32907-69 (Cole-Parmer)	Air flow controller	5000	Differential pressure

Table 2-2. Specification of the variable-area flow meter.

Specifications

Accuracy	$\pm 0.2\%$ of full scale
Repeatability	$\pm 0.25\%$
Max operating temperature	121 °C
Maximum pressure	200 psig

Table 2-3. Specifications of the mass and volumetric flow controllers.

Specifications	Mass controller	Volumetric controller
Accuracy	± 0.8% of reading	± 0.2% of full scale
High accuracy option	± 0.4% of reading	± 0.2% of full scale
Repeatability	± 0.2%	± 0.2%
Operation range	1% to 100% full scale	1% to 100% full scale
Typical response time	100 ms	100 ms
Operating temperature	-10 to 50 °C	-10 to 50 °C
Maximum pressure	125 psig	125 psig

2.2. Micro-Bubble Generator

A setup has been developed to generate micro-bubbles by air injection from a micro-tube into liquid cross-flow. A schematic view of the components of the micro-bubble generator setup is shown in Figure 2-2. An image of the manufactured setup is also illustrated in Figure 2-3. The setup has a sandwich configuration consisting of three plates made from cast acrylic to facilitate visualization of the inside flow and accessible for laser-based measurements. The channel has square cross section of 6×6 mm and is machined in the middle plate. Circular reservoirs are made at the two ends of the channel. A fine steel mesh is placed at the upstream reservoir to prevent the formation of large vortices in the channel. Rubber rings are placed in grooves surrounding the channel to seal it. This setup is hanged from a holder to obtain downward water flow in the channel.

The micro-tube is inserted into a passage machined in the middle plate. The micro-tube has OD and ID of 0.02 and 0.01 inch, respectively. The passage has circular cross section of 1 mm in diameter and is sealed with a washer surrounding the micro-tube, see Figure 2-2. The micro-tube is connected to a 0.25 inch steel tube positioned on a micro-scale stage for accurate movement of its tip across the channel.

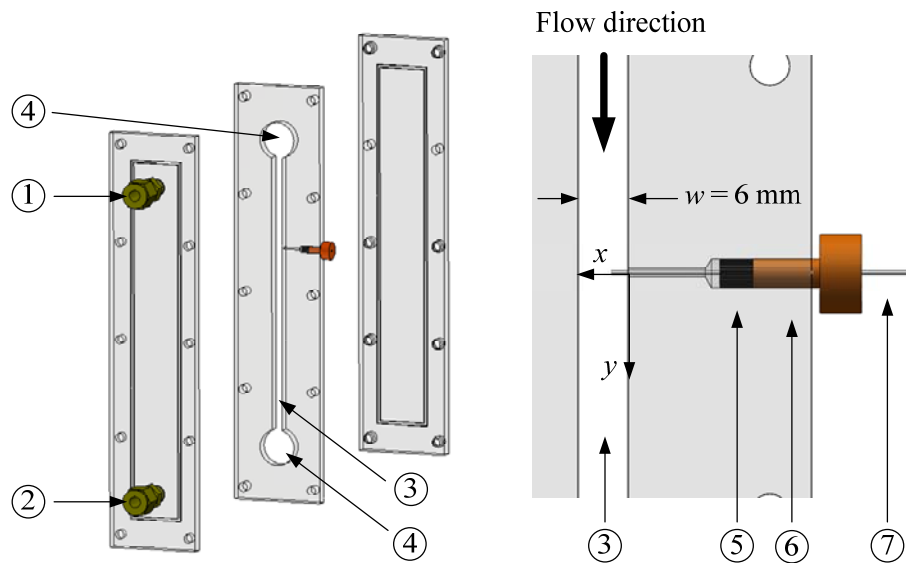


Figure 2-2. Schematic of the micro-bubble generator. (1) water inlet, (2) water exit, (3) water channel, (4) water reservoir, (5) washer, (6) screw, (7) micro-tube.

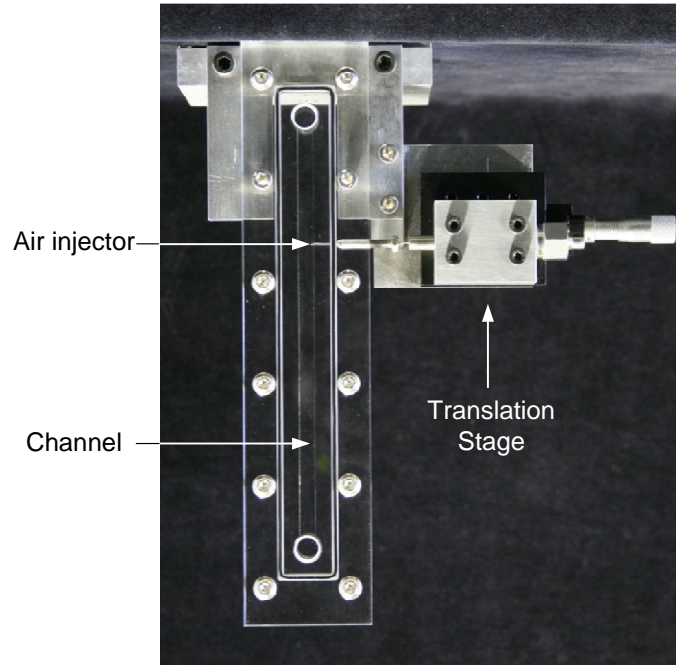


Figure 2-3. Image of the bubble generator setup.

2.3. Effervescent Atomizers

Effervescent atomization is a special type of internal-mixing twin-fluid atomizers. In effervescent atomization, air and water are introduced into the atomizer chamber through separate inlets. Air is injected into the mixing chamber from aeration holes on a tube located in the mixing chamber or from aeration holes located on the mixing chamber wall. The mixture of air and water flows in the mixing chamber and is squeezed in the narrow discharge orifice. At the exit plane of the discharge orifice, the flow is exposed to a sudden pressure drop. The expansion of the gas phase as a result of the pressure drop [19] along with the surface waves on the liquid phase and the aerodynamic forces [20] would break-up the liquid stream into ligaments and droplets to form the spray droplets.

Two different designs of effervescent atomizer have been used in this work. The atomizer mark I has been developed for the preliminary investigations on effervescent atomization [21, 22] and also to generate the required spray field for the investigation of spray droplet characteristics [14, 15, 23, 24]. The internal geometry of the atomizer mark II has been developed based on the results obtained from the previous tests of atomizer mark I and several other effervescent atomizers. The atomizer mark II is also designed to operate with two types of air injectors and facilitates their comparison.

The atomizers are connected with separate water and air supplies. The operation mode of the atomizers is characterized using the GLR parameter. This parameter is defined as

$$\text{GLR} = \frac{\dot{m}_g}{\dot{m}_l} \quad 2-1$$

where \dot{m}_g and \dot{m}_l are the gas and liquid flow rates, respectively.

The atomizers have been installed downward on a frame shown in Figure 2-4. The produced spray is collected using a funnel connected to a suction pump. This spray collection mechanism prevents the recirculation of the droplets back to the upstream flow.

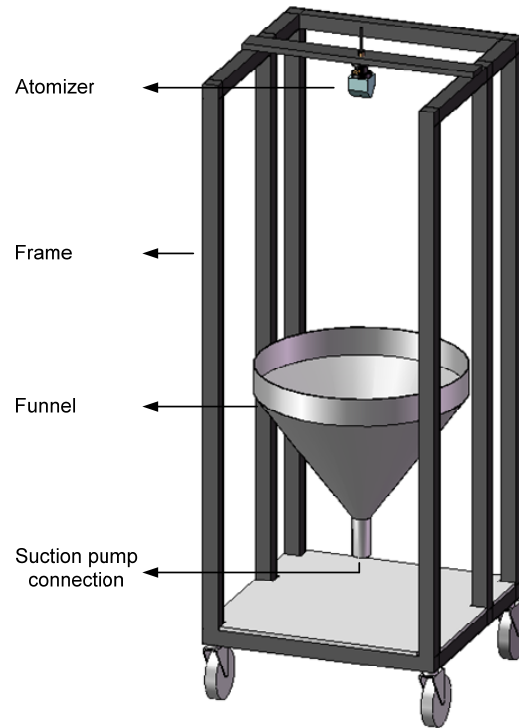


Figure 2-4. The atomizer and the spray collecting system installed on a frame.

2.3.1. Atomizer Mark I

A schematic view of the effervescent atomizer mark I used in the investigations is shown in Figure 2-5. Air and water are introduced to the atomizer through separate inlets. Similar to other inside-out effervescent atomizers [25, 26], air enters the mixing chamber through holes of the aeration tube. The aeration tube is made from stainless steel and has 9 rows of 3 holes each 0.5mm in diameter and is located at the central axis of the mixing chamber. The upstream section of the mixing chamber has a circular cross section of 20mm diameter and is followed by a smaller circular section of 8mm in diameter in the vicinity of the exit nozzle. The exit nozzle also has a circular cross section of 0.8mm in diameter and length over diameter ratio, l/d , of 6.25. The atomizer body has a rectangular outside cross-section and is made from cast acrylic, allowing visualization of the internal flow pattern. An image of the manufactured atomizer is shown in Figure 2-6. The detailed drawings of the atomizer, the air injector, and the liquid supply part are present in Appendix B.

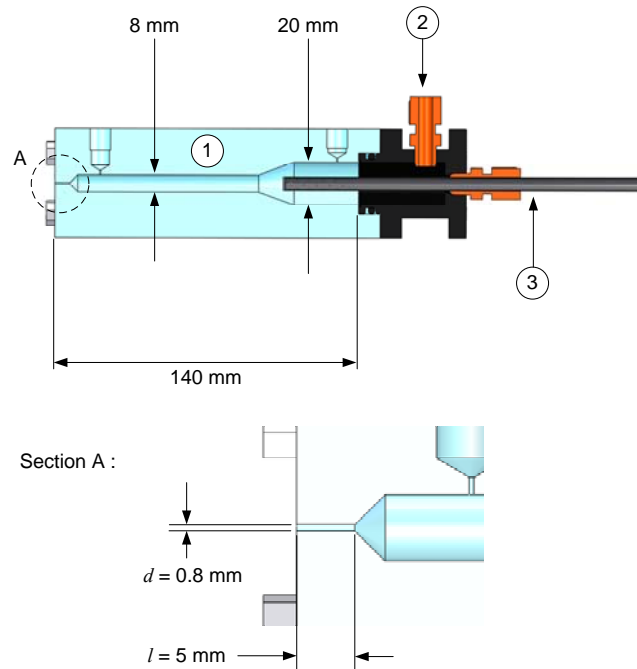


Figure 2-5. Schematic of the effervescent atomizer mark I, air injector, and water and air inlets. (1) Atomizer main body, (2) liquid supply port (3) air injector.



Figure 2-6. An image of the effervescent atomizer mark I made from cast acrylic.

2.3.2. Atomizer Mark II

A schematic view of the effervescent atomizer mark II is shown in Figure 2-7. Air enters the mixing chamber through an aeration tube. The mixing chamber has circular cross section of 8.4 mm diameter. The exit nozzle also has a circular cross section of 0.8mm in diameter and length over diameter ratio of $l/d = 2$. The atomizer body has a rectangular outside cross-section and is made from cast acrylic, allowing visualization of the internal flow pattern. An image of the manufactured atomizer is shown in Figure 2-8.

The detailed drawings of the atomizer and the liquid supply part are present in Appendix B.

The internal geometry of the atomizer mark II has been improved in several aspects in comparison to the atomizer mark I. As it is shown in Figure 2-7, atomizer mark II has smaller internal volume which prevents the presence of trapped air in the mixing chamber and allows it to be filled faster with liquid. There is also a smaller distance between the air injector surface and the adjacent mixing chamber wall which results in higher liquid velocity and shear force at this region. This feature has been applied to break the injected air into smaller bubbles. The length over diameter ratio, l/d , of the exit nozzle has also been reduced to obtain the highest discharge coefficient as suggested by Lefebvre [9].

Two different air injectors have also been considered to be used in the atomizer mark II. One of the air injectors has 9 rows of 3 holes each 0.5mm in diameter. The other air injector has a porous media section for aeration. This porous part is 25.4 and 6.4 mm in length and diameter, respectively, and has 0.5 pore grading [27]. An image of the two air injectors is shown in Figure 2-9. The detailed drawings of the air injectors are present in Appendix B.

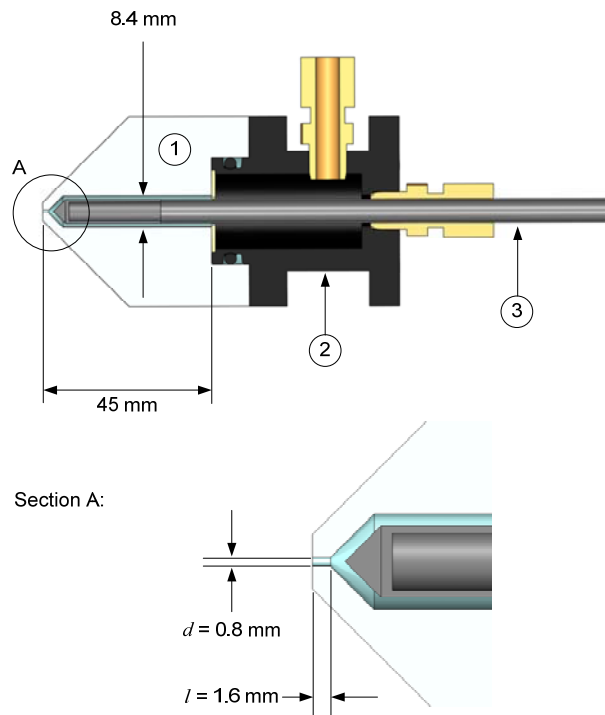


Figure 2-7. Schematic of the effervescent atomizer mark II consisting of (1) mixing chamber, (2) liquid inlet, (3) air injector.

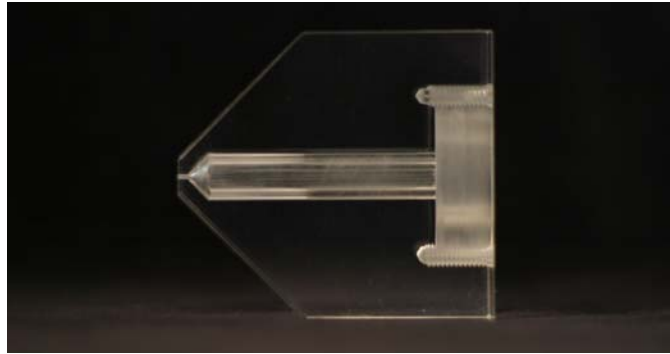


Figure 2-8. An image of the body of the atomizer mark II manufactured from cast acrylic.



Figure 2-9. An image of the two air injectors used in the second effervescent atomizer.

3. Measurement Setup

Three non-intrusive laser-based measurement techniques have been used in the investigations. These techniques consist of (1) shadowgraph particle tracking velocimetry (Shadow-PTV), (2) stereoscopic particle image velocimetry (StereoPIV), and (3) shadowgraphy particle image velocimetry / particle tracking velocimetry (Shadow-PIV/PTV). The Shadow-PTV and the StereoPIV techniques have been applied to characterize spray droplets generated by the effervescent atomizers. The Shadow-PIV/PTV technique has been used to investigate formation of micro-bubbles in liquid cross flow.

3.1. *Shadow-PTV*

3.1.1. *Working Principle of the Shadow-PTV Technique*

The Shadow-PTV is an image-based technique using pulsed backlight illumination. This system has been used to measure geometrical characteristics and the velocity of the spray droplets [12, 23, 24, 28-34]. In the Shadow-PTV technique a light source is used to provide a uniform low-intensity backlight illumination. A CCD camera is placed in front of the light source to record the shadow of the droplets located in a measurement volume. The measurement volume is defined by the field-of-view and the depth-of-field of the imaging system. A short illumination pulse may be required to freeze the motion of the droplets depending on their velocity. The images contain two-dimensional projection of droplets geometry and their geometric features can be calculated using an image processing algorithm. The velocity of the droplets can also be measured by recording double-frame or time-resolved images and applying a particle tracking algorithm. A

sample double-frame shadow-PTV image is shown in Figure 3-1 demonstrating the shadow of the droplets formed on a bright background.

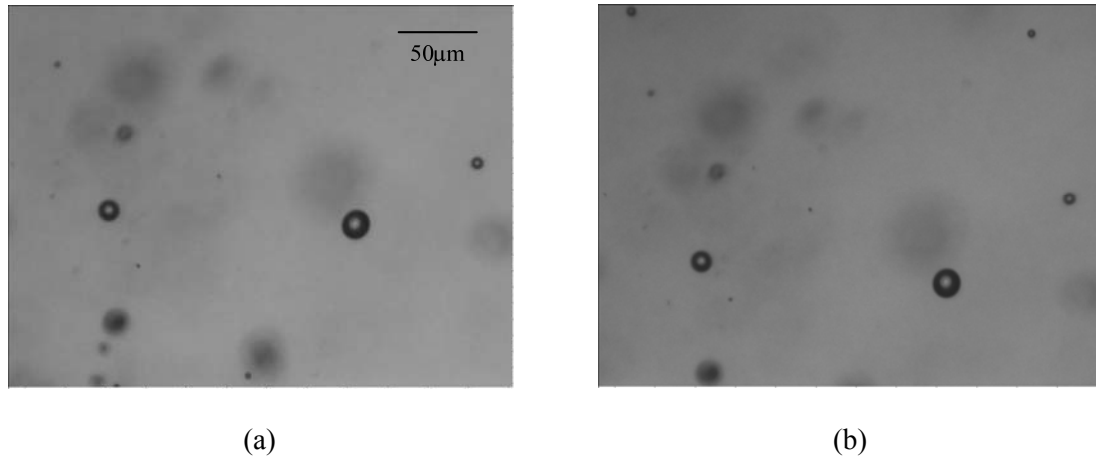


Figure 3-1. Shadow-PTV images of droplets in a spray field. (a) $t = t_0$. (b) $t = t_0 + 0.6 \mu\text{s}$.

3.1.2. Image Acquisition

The shadow-PTV system used in this work consists of three main components: an illumination source, a camera, and a zoom lens. A schematic and also an image of the Shadow-PTV setup used in the experiments are shown in Figure 3-2 and Figure 3-3, respectively. An Nd:YAG laser (Solo PIV III, New Wave Research Inc.) with 50 mJ energy per a 3-5 ns pulse width is used to illuminate the spray field and freeze the motion of the droplets. The specifications of this laser are presented in Table 3-1. The laser is equipped with a light diffuser and is located in front of a 12-bit digital camera (Image Intense, LaVision) with 1376×1040 pixels CCD sensor. The camera specifications are shown in Table 3-2. The camera was equipped with a 12X zoom lens (Navitar). Different magnifications can be achieved by using appropriate adapters and lens attachment. The lens configuration used in the investigations along with the specifications is demonstrated in Table 3-3. Image acquisition has been conducted at several locations in the spray by placing the camera and the laser on a computer controlled three-axis traverse. This enables precise movement of the Shadow-PTV system.

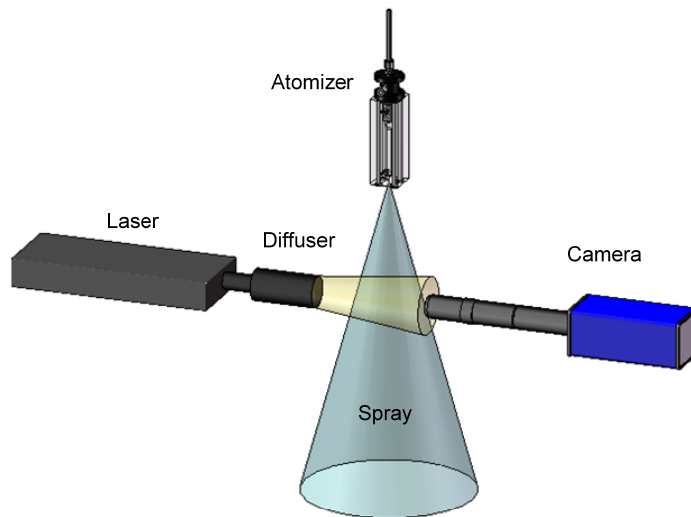


Figure 3-2. The Shadow-PTV configuration.



Figure 3-3. An image of the Shadow-PTV system.

Table 3-1. Specifications of the Nd:YAG laser.

Laser model	Main wavelength	Repetition rate	Pulse width	Beam diameter	Beam divergence
Solo III-15 New Wave	532 nm	15 Hz	3-5 ns	4 mm	<4 mrad

Table 3-2. Specifications of LaVision Image Intense Camera.

Double shutter	Exposure time	Number of pixels	Pixel size	Sensor format	Spectral range
500 ns interframing time	500 ns - 1000s	1376 × 1040	6.45 × 6.45 μm ²	2/3"	290-1100 nm
Maximum QE	CCD temperature	Dynamic range	Readout rate	Readout noise	Frame rate
65 % @ 500 nm	-12°C	12 bit	16 MHz	4-5 e- @ 16 MHz	10 frames/s

Table 3-3. Configuration of the zoom lens system and the corresponding specifications used to spray droplets experiment.

Lens configuration	Working distance (mm)	System magnification	Feature size (μm)	Depth of Field (mm)
2× lens attachment 12× zoom lens 2× lens adapter	32	2.32 - 28×	4.50 - 0.83	0.35 - 0.01

3.1.3. Shadow-PTV Image Processing

The acquired Shadow-PTV images are processed to measure a number of geometric features and the velocity of the spray droplets. The process is conducted through a commercial code (DaVis 7.2, LaVision 2007) which consists of three main steps of (1) preprocessing, (2) particle recognition, and (3) velocity calculation [35]. The algorithms and parameters used in each of these processes are detailed in Appendix C.

The preprocessing step is mainly devoted to correct the non-uniformities of the background illumination, see Figure 3-1. These non-uniformities are caused by the dense spray field and the deficiencies of the illumination source which can cause both spatial and temporal non-uniformities. In this process, a minimum intensity has been subtracted from each image. Next, a reference image is calculated using the “strict sliding maximum filter” option [35]. After subtraction of the reference image, the high intensity areas represent the droplets and the low intensity areas represent the background. The

calculated reference image and the preprocessed image for the illustrated example of Figure 3-1 are shown in Figure 3-4 (a) and (b), respectively.

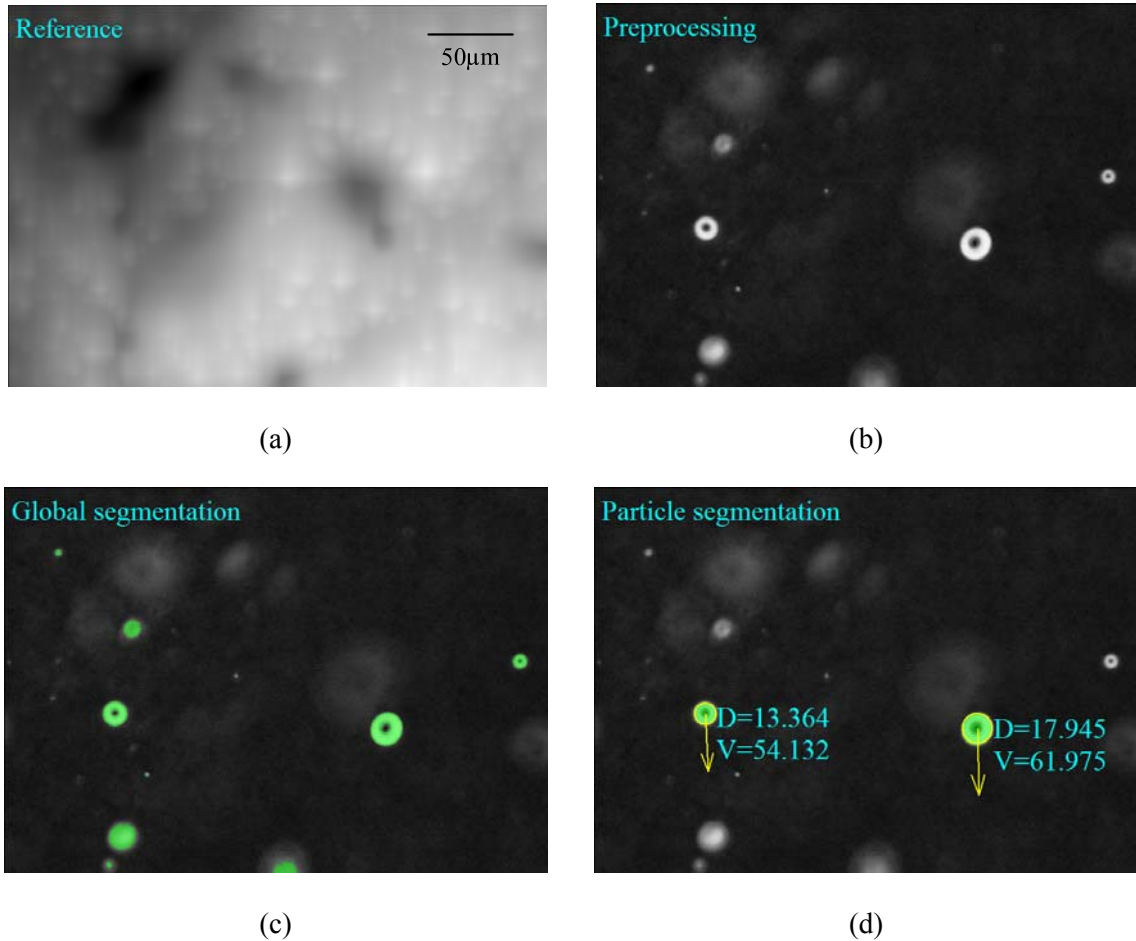


Figure 3-4. The Shadow-PTV process using Davis software (a) calculated reference image (b) preprocessed image (c) global segmentation (d) the detected droplets and their measured area equivalent diameter (μm) and velocity (m/s).

The particle recognition step is designed to find the droplets in the images and determine their boundaries. The Davis software conducts this process using a two-step segmentation algorithm. In the first segmentation algorithm, areas with an intensity higher than a selected global threshold are detected. An example of an image after this process is shown in Figure 3-4 (c). A bounding box is considered around the detected regions prior to the second segmentation process. In the second segmentation, two thresholds which are called low level and high level thresholds are used to specify the droplet region. These thresholds are expressed as the percentages of the maximum

intensity in the bounding box and specify a large and a small region as the droplet area. The Davis software finally calculates the average of the geometric features of both the large and the small regions. The geometric features include the center of the droplet region, longest and shortest diameter, and area equivalent diameter. The shortest and longest diameters are defined as the longest and shortest lines connecting the droplet image. Area equivalent diameter is defined as

$$D_a = \sqrt{\frac{4A}{\pi}}. \quad 3-1$$

where A is the area of the droplet image measured in number of pixels. A recognition filter is also applied to remove out-of-focus and spurious droplets. This filtering step is conducted using the ratio of high over low level areas and also criteria set for size, shape, and location of droplet images.

In the last step, the Shadow-PTV system measures velocity of the individual droplets. The algorithm identifies droplet pairs in the double-frame images using two criteria of allowed size and shift. The process can be conducted using a multi-pass algorithm to achieve accuracy. The droplet displacement and the time interval between the two frames are used to calculate droplet velocity. Figure 3-4 (d) shows the detected droplets and their measured area equivalent diameter and velocity.

3.2. Stereo-PIV

3.2.1. Overview of the Stereo-PIV Technique

PIV is a well known technique that can conduct instantaneous measurement of velocity vectors in a planar grid and has successfully been applied to numerous experiments [36-38]. This technique involves addition of light-reflective seeding particles which follow the flow motion. A laser sheet generated by a double-pulse laser is typically used as an illumination source. The measurement plane is simultaneously illuminated and imaged. In two-dimensional PIV, a camera images perpendicular to the measurement plane and only records two components of particles displacement. The double-frame images are processed by a cross-correlation algorithm to calculate the velocity vectors at the measurement plane. In StereoPIV, the measurement capability is extended to the three velocity components by using two cameras that image the field of view from different angles.

3.2.2. Image Acquisition

The StereoPIV system is implemented with the configuration shown in Figure 3-5 and Figure 3-6. An Nd:YAG laser (Solo PIV III, New Wave Research Inc.) is used to illuminate the field of view. Two 12-bit digital cameras (LaVision) with 1376×1040 pixel CCD sensors are equipped with 55 mm lenses (Nikkor) and Scheimpflug adaptors. The specifications of the laser and the camera are presented in Table 3-1 and Table 3-2, respectively. The cameras view perpendicular to the laser sheet in a stereo configuration with an included angle of 62° with respect to each other. The time interval between the two image frames is set to 0.6 μ s. As it is shown in Figure 3-5 and Figure 3-6, the two cameras are located in a vertical plane perpendicular to the laser sheet to receive equal illumination. The field-of-view is 50×38mm which results in 36 μ m/pixel magnification.

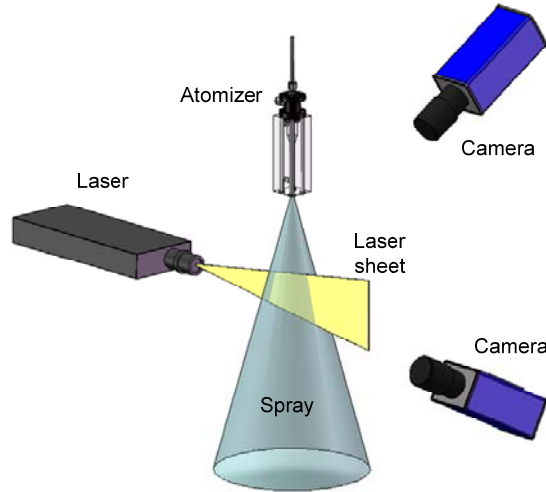


Figure 3-5. StereoPIV system configuration.

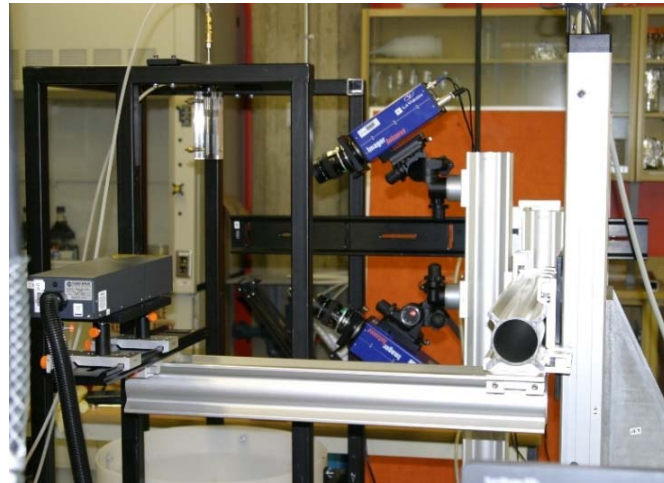


Figure 3-6. An image of the StereoPIV system configuration.

In this experiment, the laser beam is passed through a set of two spherical lenses (a telescope) to focus the beam at the center of the field-of-view and is expanded in one dimension using a cylindrical lens. Although an expanded laser beam can be converted to a thinner laser sheet by the spherical lens, the minimum feasible laser sheet thickness is limited by the quality of the initial laser beam [39]. This is characterized by the M^2 factor of the laser [39]. The minimum laser sheet thickness is also obtained only at a small region and the practical thickness is its average over the field-of-view of the PIV system. The laser utilized in this experiment has an M^2 factor of 9 which results in the minimum laser sheet thickness of 0.5mm averaged over the field-of-view [35].

The cameras and the laser are placed on a computer controlled three-axis traverse to enable precise movement and location of the system. The StereoPIV images have been obtained at 7 consecutive axial locations downstream of the nozzle exit orifice. In droplet velocity measurements using the StereoPIV technique, no seeding particle is added to the spray field and the spray droplets play the role of the seeding particles. Two sample PIV image recorded from the near-field and far-field of the spray are shown in Figure 3-7 (a) and (b), respectively.

3.2.3. Image Processing

The StereoPIV images have been processed using a commercial code (DaVis 7.2, LaVision 2007). The preprocessing step consists of subtracting a background image, subtracting an offset, and normalizing the images. The image of Figure 3-7(b) after the preprocessing step is shown in Figure 3-8(a). The vector maps are calculated by comparison of the image pairs using a multi-pass cross-correlation algorithm applied to interrogation window of 32×32 pixels. The processing algorithm and the used parameters are described in Appendix C. The computed vector field averaged over the set of 500 images is shown in Figure 3-8(b).

The StereoPIV images have also been used to obtain a measure of the droplet number density within the spray field. The probability density function (PDF) of intensity higher than 2.45 percent (100 counts) of the maximum count (4096 for the 12-bit camera) have been calculated for the image pixels over the recorded sets of 500 images. The calculations have been conducted using the PDF operation available in the *statistics* group of Davis software. The details are available in Appendix C. Next, the results have been averaged over a number of selected windows of the StereoPIV images using a code written in MATLAB. A sample of these windows which have height and width of 50 and 120 pixels, respectively, is shown in Figure 3-7(a). The height is along the z axis and the windows are located symmetrically with respect to the z axis.

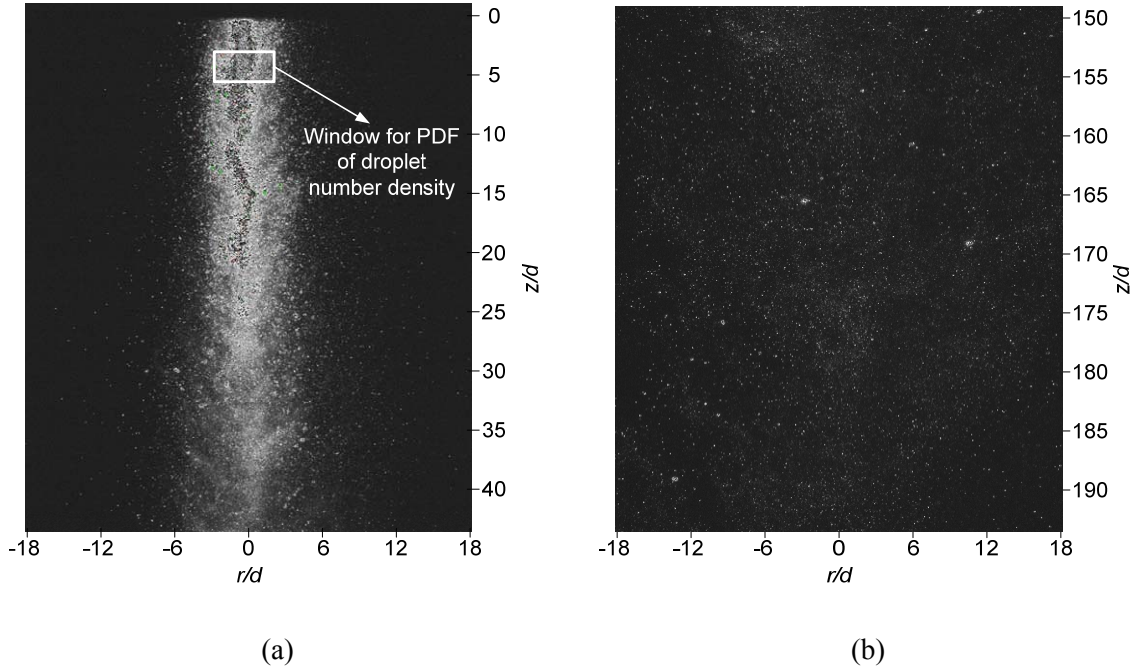


Figure 3-7. StereoPIV image (a) at the nozzle vicinity, $z/d=20$ (b) at the far field, $z/d=140$ (c) after the preprocessing step (d) the computed vector field averaged over 500 images.

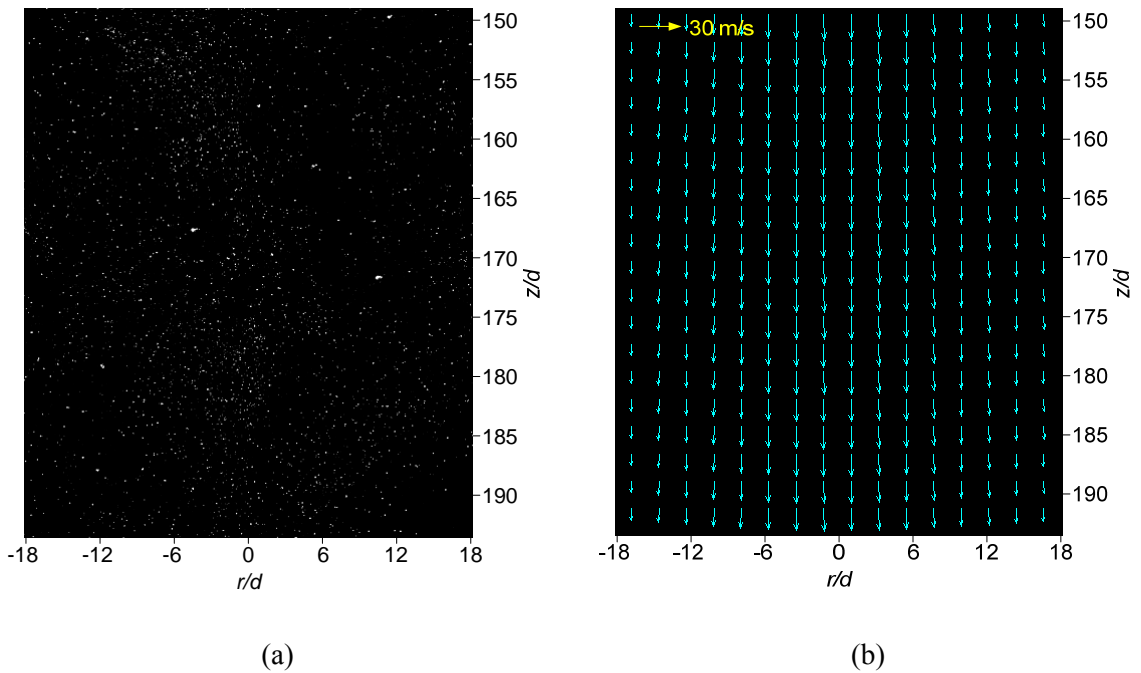


Figure 3-8. StereoPIV image (a) at the nozzle vicinity, $z/d=20$ (b) at the far field, $z/d=140$ (c) after the preprocessing step (d) the computed vector field averaged over 500 images.

3.3. Shadow-PIV/PTV

3.3.1. Overview of the Shadow-PIV/PTV Technique

The Shadow-PIV/PTV system is used in this work to investigate the mechanism of bubble formation by air injection into liquid cross-flow. This system has been first used by Bröder and Sommerfeld [40] to investigate bubbly flows and is capable of conducting simultaneous measurement of velocity and geometric features of the bubbles along with the velocity of the liquid phase. The Shadow-PIV/PTV technique is a combination of the Shadow-PTV and the two-dimensional PIV techniques. In this technique, appropriate seeding particles are added to the liquid phase for the PIV process. Similar to the Shadow-PIV system, a hardware configuration consisting of a CCD camera is located in front of a diffused light source to image the shadow of the bubbles and also the seeding particles. In this technique, the camera lens is required to have a relatively thin depth-of-field. This feature of the imaging system fades the shadow of the seeding particles which are out of the depth-of-field and limits the measurement to a desired volume. After the images are recorded, a PTV processing algorithm is applied to calculate the velocity and the geometry of the bubbles from their recorded shadow. The images are also separately processed by a typical PIV algorithm to calculate the liquid velocity field using the shadow of the seeding particles.

3.3.2. Image Acquisition

The Shadow-PIV/PTV system uses the same base equipment as the other two described systems of section 3.1 and 3.2. A schematic of the Shadow-PIV/PTV configuration imaging the flow field of the bubble generator setup is shown in Figure 3-9. The Nd:YAG laser (Solo PIV III, New Wave Research Inc.) with specifications presented in Table 3-1 is used to illuminate the flow field. The laser is equipped with a light diffuser to provide a uniform distribution of relatively low intensity illumination. A 12-bit digital camera (Image Intense, LaVision) with specifications shown in Table 3-2 is placed in front of the light source. The camera was equipped with a 12X zoom lens (Navitar). Appropriate adapters and lens attachment are used to adjust the field of view and the measurement depth-of-field. The lens configuration used in the investigation

along with its specifications is demonstrated in Table 3-4. This configuration images a field-of-view of $8.44 \times 6.29 \text{ mm}$ with an approximate depth-of-field of 1 mm and magnification of $6.1 \mu\text{m}/\text{pixel}$. Image acquisition has been conducted at a location in the vicinity of the micro-tube as it is shown in the sample double-frame image of Figure 3-10.

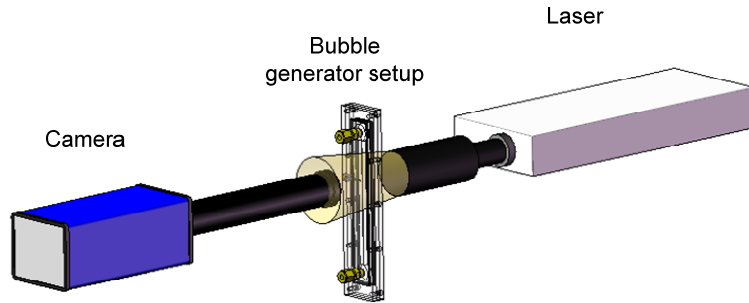


Figure 3-9. The shadow-PIV/PTV configuration.

Table 3-4. Configuration of the applied zoom lens system and the corresponding specifications used micro-bubble experiment.

Lens configuration	Working distance (mm)	System magnification	Feature size (μm)	Depth of Field (mm)
1 \times lens attachment 12 \times zoom lens 1 \times adapter	86	0.58 \times - 7 \times	9.26 - 1.67	1.39 - 0.05

3.3.3. Image Processing

The recorded images are separately used for PIV and PTV processes. The detail of the applied PIV and PTV processes are presented in Appendix C.

The PTV algorithm is applied by limiting the process to the shadow of objects larger than 900 pixels in area. As a result only the bubbles are considered for PTV process and the seeding particles are ignored in this process. In the recorded images, most of the bubbles were in sharp focus. This is because the generated bubbles continue to flow in the plane which contains the air injector. A criteria based on the intensity profile at the boundary of the bubbles image has been applied using the Davis software to remove any rare defocused bubble. An algorithm is also applied to mask out the seeding particles and

the micro-tube. The sample image after the mask out algorithm is shown in Figure 3-10(a). The location and the size of the bubbles are calculated using a procedure similar to the Shadow-PTV process of section 3.1.3. The detected bubbles along with the associated circles which have the same area as the bubbles are shown in Figure 3-11(b). The velocity of the bubbles is also calculated by dividing the displacement of the centroid of the bubbles by the time interval of the successive image frames.

In the PIV process, the shadow of the bubbles is first masked out from the images. The mask process is conducted using the lower grey level intensity of the shadow of the bubbles in comparison to the shadow of the seeding particles. The shadow of the micro-tube is manually masked out in situations that the tube was inserted into the channel. The sample image after masking out the bubbles and the air injector tube is shown in Figure 3-12(a). Next, a preprocessing step is applied which inverts the image, subtracts an offset (50 counts), and normalizes the intensity field. This preprocessing step enhances the shadow of the in-focus particles and removes the shadow of the defocused ones. A sample image after the preprocessing step is shown in Figure 3-12(b). The images are processed using a multi-pass PIV algorithm with a minimum interrogation window of 16×16 pixels. The resulted vector field and the magnified region around the air injector are shown in 3-11(c) and 3-11(d), respectively. Small vectors with non-uniform directions are observed at the upstream and downstream vicinity of the air injector tube in 3-11(c). Small vectors are also observed at the boundary formed by the side walls. The magnified vector plot of 3-11(d) illustrates change in the direction of the velocity field as it passes over the tip of the air injector and also the velocity field formed around the bubbles.

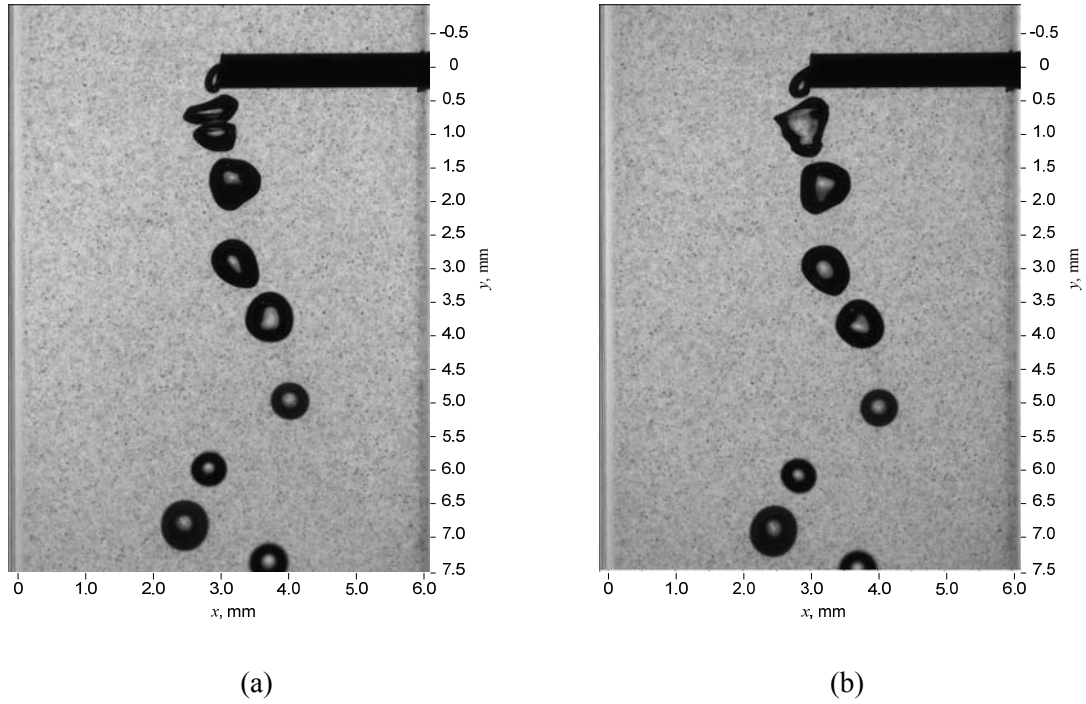


Figure 3-10. Double-frame Shadow-PIV/PTV image. (a) $t = t_0$. (b) $t = t_0 + 0.6 \mu\text{s}$.

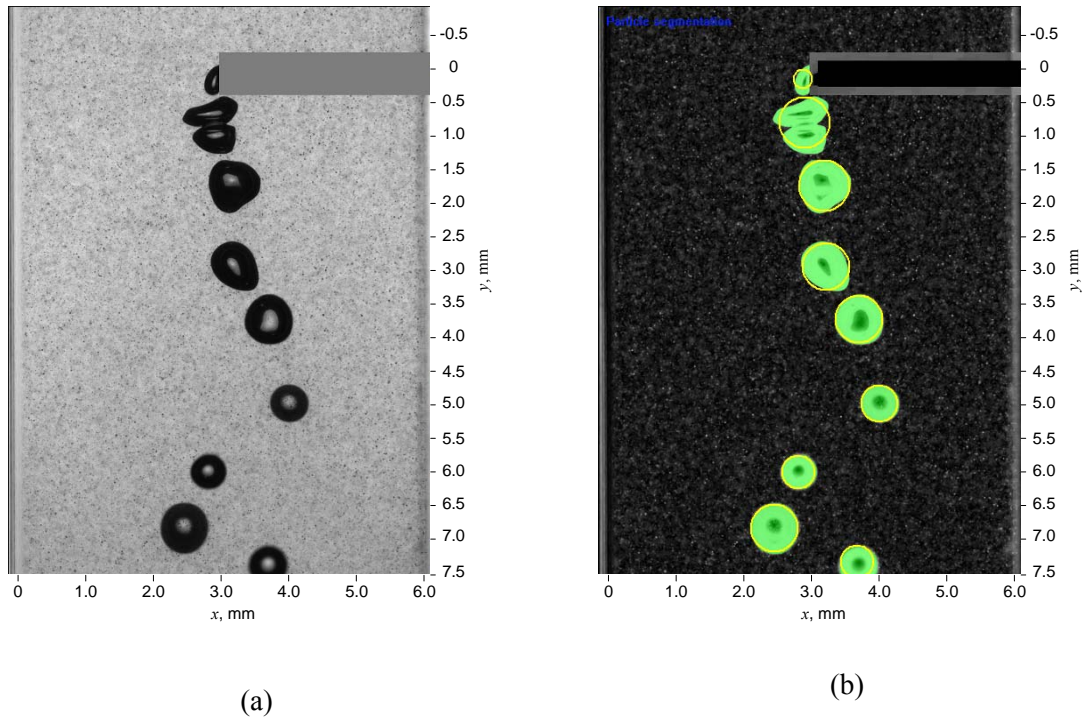
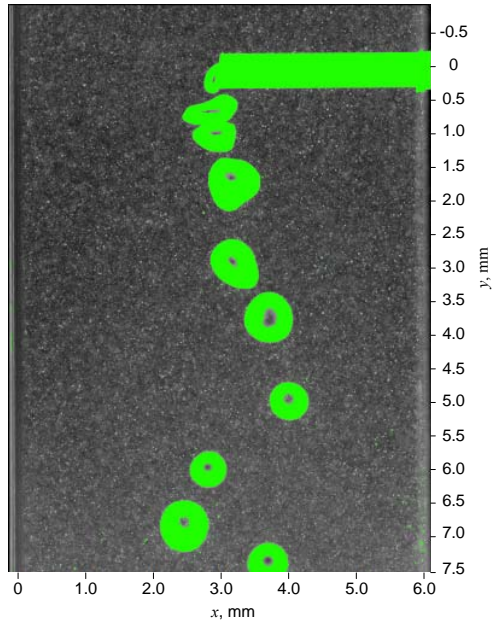
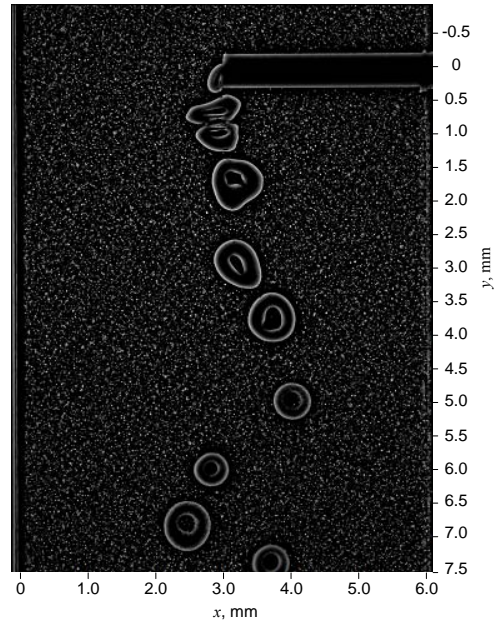


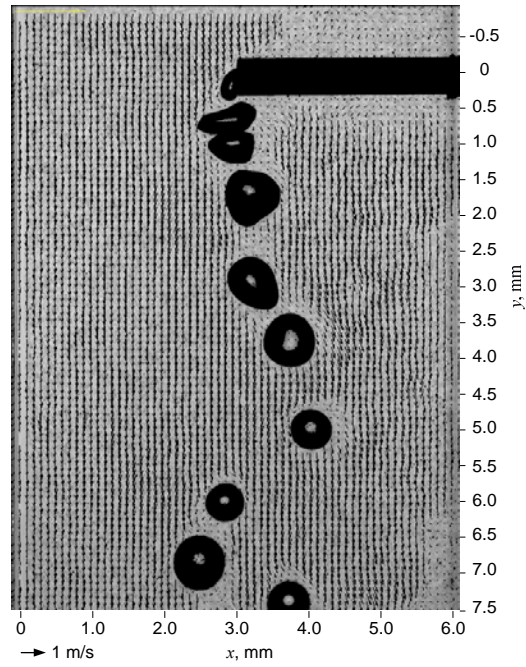
Figure 3-11. The PTV process applied to the Shadow-PTV/PIV images (a) the micro-tube has been manually masked out (b) the bubbles area has been detected using the PTV algorithm.



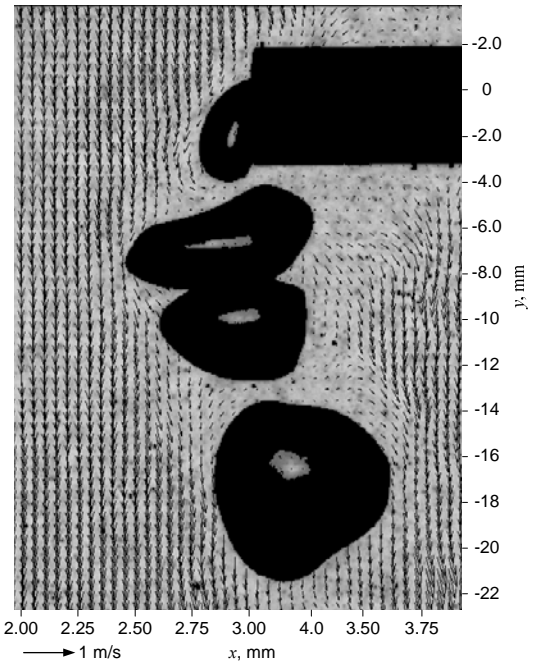
(a)



(b)



(c)



(d)

Figure 3-12. The PIV process applied to the Shadow-PTV/PIV images (a) the bubbles and the micro-tube are masked out (b) preprocessing algorithm has been applied to the images (c) the calculated vectors over the complete image field (d) calculated vector field around the micro-tube.

4. Assessment of Parameters for Distinguishing Droplet Shape in a Spray Field Using Image-Based Techniques

4.1. Introduction

Characterization of spray nozzle design and performance has typically been through characterization of spray field droplets and considerable effort has been devoted in the literature to develop suitable techniques for droplet size measurement [41, 42]. The most widely used droplet sizing systems are based on the Fraunhofer forward scattering principle and phase Doppler techniques which both assume droplets are spherical [43, 44]. This assumption can introduce considerable error in the measurement of droplet characteristics for non-spherical droplets [45]. In addition, droplet diameter is only a one-dimensional description of a three dimensional object and does not reveal many geometric features if the droplet shape is non-spherical.

There are several mechanisms that can result in the generation of non-spherical droplets in a spray field. Through the primary atomization process, liquid surface waves and aerodynamic forces break the liquid jet into ligaments and relatively large droplets which are typically non-spherical [19, 46]. These ligaments and droplets further break into smaller ones through the secondary atomization process [46]. The droplets formed in this process are also mostly non-spherical due to their initial conditions [47]. However, the existence of non-spherical droplets is not limited to the primary and secondary atomization processes and may exist throughout the spray field due to other mechanisms.

In general, the shape of a droplet is as a result of balance between surface forces and aerodynamic forces [47, 48]. Their interaction is usually characterized in terms of the Weber (We) number, which is the ratio of aerodynamic forces to surface forces [49]. If $We \ll 1$, surface forces dominate and spherical shapes are observed [47]. As aerodynamic forces increase, the We number becomes higher and droplet deformation takes place. Further increase in aerodynamic forces above $We \approx 6$ results in droplet break up [49]. Several breakup mechanisms such as vibrational breakup and bag breakup have been classified based on the We number [50-53]. Another mechanism which results in the formation of non-spherical droplets is collision between droplets. This leads to coalescence or breakup of the colliding droplets [49] based on their momentum. Experimental observations reveal that droplet shape is non-spherical over the period of both the breakup and coalescence mechanisms [23, 24, 49]. Therefore, the interaction of droplets with the surrounding air and each other may also result in non-spherical droplets.

Identifying droplet shape can reveal many characteristics of a spray field. In a recent review on spray diagnostic, Bachalo [10] stated that there are gaps in our knowledge of the breakup and dense regions of the spray and phenomena such as drop deformation, collision, and breakup have escaped characterization in spite of the modern diagnostic systems. Droplet shape identification can provide further insight into the primary and secondary atomization processes, increases the accuracy of droplet sizing by removing the assumption of spherical droplets, expresses the stability of droplets [54], and can be used to calculate drag force and the dynamic shape factor [55]. Therefore, characterization of droplet shape has a variety of applications in spray and atomization technology and requires development of appropriate measurement techniques.

Among droplet analyzers, image-based techniques have the capability to visualize droplet shape. An automated shadowgraph droplet sizing technique was developed to measure droplet size by Simmons and Gaag [28] and has been applied to investigate sprays [29-32]. This system was not recognized as a viable technique during that period due to limitations in computational and optical systems. However, recent advances in computers, CCD sensors, and image processing techniques have raised this approach to a practical means for investigating spray fields [10]. While hardware capabilities have

increased, suitable data processing algorithms and approaches are required to identify droplet characteristics.

Determination of the shape of a projected image of an object is typically identified based on comparison with a reference shape such as a circle or an ellipse. The comparison is quantified using a “shape parameter” which is obtained by measuring a number of geometric features of the object and comparing with the reference shape [44]. Shape parameters have been extensively applied and investigated in several applications. Eriksson et al. [56], Podczeczek et al. [57], and Bouwman et al. [58] have studied the applicability of different shape parameters for assessment of pellet and granule shapes for pharmaceutical applications. Carosone et al. [59] have investigated shape parameters to identify partially overlapped particles in particle tracking velocimetry (PTV) images. Iwano et al. [60] have applied shape parameters to classify pulmonary nodules. Some researchers have used a combination of several shape parameters to improve object shape identification [33, 60-70]. This has led to a wide variety of parameters being used to characterize object shape and so far no standard approach has been developed.

Several shape parameters have been used through the literature to characterize object shape which makes it difficult to compare the results of different research groups. Podczeczek and Newton [71] and Almeida-Prieto et al. [72] have attempted to resolve this confusion by suggesting new parameters. However, their suggested parameters were especially developed to identify characteristics of pharmaceutical particles and may not be suitable for other applications. Solid particles usually have a rough surface which is one of the major characteristics of particles in pharmaceutical and sediment applications and has been implemented into some shape factors [71, 73]. Liquid droplets generated in a spray field are affected by surface tension and their shape characteristics are diverse from solid objects. As a result of surface tension, droplets have smooth surfaces. Droplet shape can be identified using shape parameters which are less sensitive to surface roughness and consequently have lower error due to image discretization. Another important feature of droplets is their tendency to keep spherical shapes. As discussed earlier, a fully-formed droplet with a small We number tends to adapt the spherical shape. This makes a sphere an ideal shape and can be used as a reference in the shape parameter to quantify droplet shape as a deviation from it. Therefore, in quantifying the shape of

droplets, shape parameters should be used that can efficiently take advantage of the droplet shape features.

There are only a limited number of works on droplet shape identification in a spray field. Sudheer and Panda [74], Kashdan et al. [75], and Lecuona et al. [33] have adapted shape parameters from other fields and only used them as a filtering criteria to discriminate droplets from other objects in data images. Kashdan et al. [76] have measured droplet non-sphericity in a spray field using an adapted shape parameter and for their conditions droplets larger than 40 μm were observed to be mostly non-spherical. Malot et al. [54] on the other hand, investigated droplet shapes of a low density spray and defined a new shape parameter. For further progress in the development of droplet shape identification methods, a standard approach and the classification of the performance of different shape parameters is required.

In this chapter several shape parameters that have been used in the literature are presented. A survey of the literature has gathered the mathematical definitions and main features of several shape parameters for assessment. These have been used by researchers who have dealt with the identification of object shape in applications such as pharmaceutical, medical, food, biological, and spray industries. The Shadow-PTV system has been used to provide visual evidence of droplet shapes in a spray field. The acquired droplet images have been categorized into three classes based on their main visual features. The applicability of a selected number of shape parameters in distinguishing shapes of these three droplet classes has been investigated to indicate an optimum parameter for droplet shape identification in sprays.

4.2. The Experiment

To investigate the applicability of the shape parameters to determine droplet shape a series of experiments have been conducted to collect data images of droplets in a spray field. In this section, the effervescent atomizer Mark I which is described in section 2.3.1 has been used to generate the spray field. The atomizer operated at an air flow rate of 5 L/min and a water flow rate of 150 mL/min at standard temperature and pressure of 25°C and 1 atm in this experiment. This condition results in GLR of 0.04

The Shadow-PTV system described in section 3.1 is used to image the droplets. The camera imaged a field-of-view of $314 \times 237 \mu\text{m}$ with depth-of-field of $50 \mu\text{m}$. Image acquisition was conducted at an axial location of $z/d=37.5$ downstream from the discharge orifice.

4.3. Droplet Shape in a Spray Field

Non-spherical droplets in a spray field form as a result of initial conditions, aerodynamic forces and collisions [47-49]. Figure 4-1 and Figure 4-2 show the primary and secondary atomization processes, respectively. It is demonstrated in Figure 4-1 that the liquid jet breaks into ligaments and large droplets which are non-spherical. In Figure 4-2 the ligaments and large droplets break into smaller ones through the secondary atomization process. It is observed that most of these newly formed droplets are non-spherical.

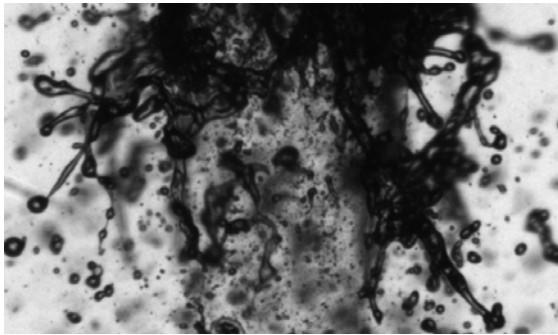


Figure 4-1. Liquid jet disintegration at the nozzle location.

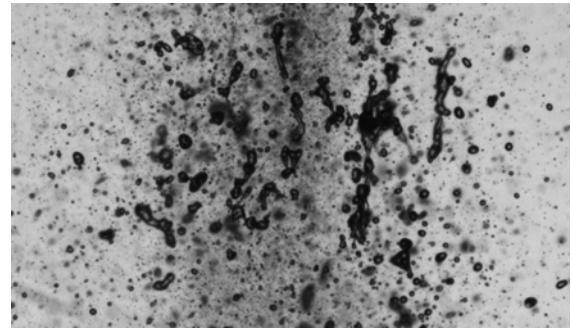


Figure 4-2. Disintegration of ligaments and droplets at $z/d=10$.

Aerodynamic forces result in deformation or breakup of droplets. Two of the breakup mechanisms known as vibrational breakup and bag breakup have been observed through the obtained shadowgraphy images [50-53]. Examples are presented in Figure 4-3 to Figure 4-8 from the investigated spray field. In these figures, two images of the same spray field are captured at a known $\Delta t = 0.6 \mu\text{s}$ apart. Figure 4-3 and Figure 4-4 show droplet breakup into smaller droplets as a result of vibrational breakup. It is observed that during this breakup the droplet is stretched and prospective droplets are connected through a liquid bridge which will eventually break. Figure 4-5 and Figure 4-6 illustrate the bag breakup mechanism. Through this process the droplet deforms into a hollow bag as a result of high aerodynamic forces. This thin bag will eventually burst and breakup into many small fragments. The images also reveal that droplet shapes are non-spherical when vibrational and bag breakup mechanisms are occurring.

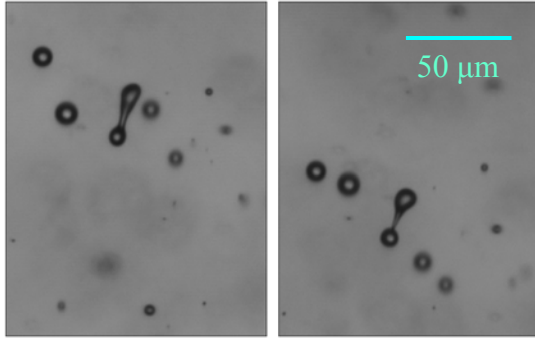


Figure 4-3. Two images of an example of droplet breakup into two droplets through the vibrational mechanism at (a) $t = t_0$. (b) $t = t_0 + 0.6 \mu\text{s}$.

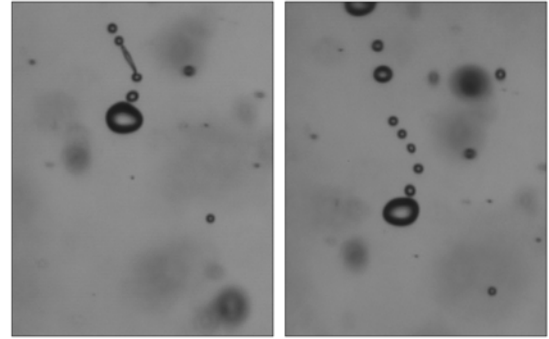


Figure 4-4. Two images of an example of droplet breakup into fragments through the vibrational mechanism at (a) $t = t_0$. (b) $t = t_0 + 0.6 \mu\text{s}$.

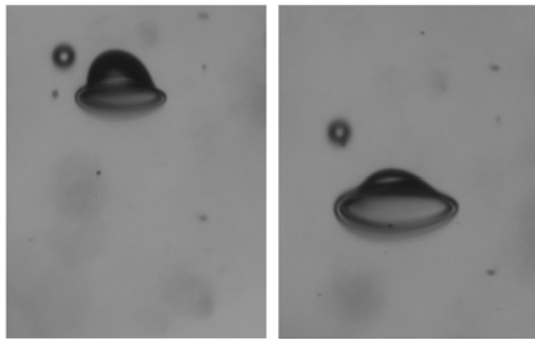


Figure 4-5. Two images of the breakup of a droplet into many fragments through the bag breakup mechanism at (a) $t = t_0$. (b) $t = t_0 + 0.6 \mu\text{s}$.

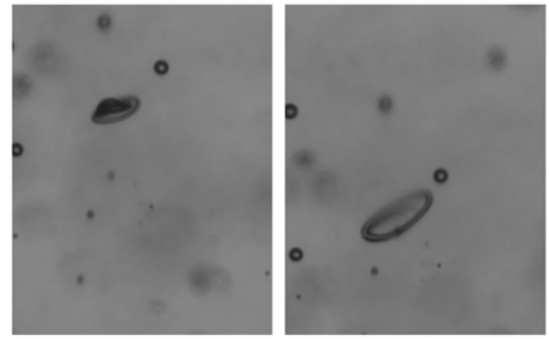


Figure 4-6. Two images of the breakup of a droplet into many fragments through the bag breakup mechanism at (a) $t = t_0$. (b) $t = t_0 + 0.6 \mu\text{s}$.

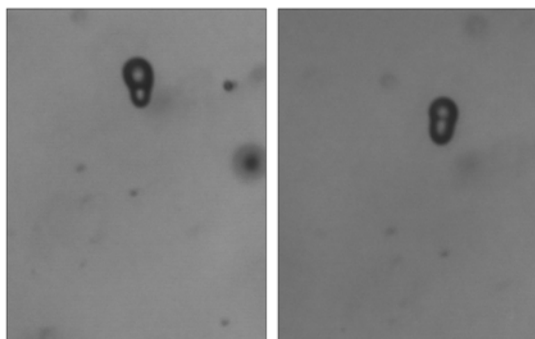


Figure 4-7. Collision of droplets that leads to droplet coalescence; (a) $t = t_0$. (b) $t = t_0 + 0.6 \mu\text{s}$.

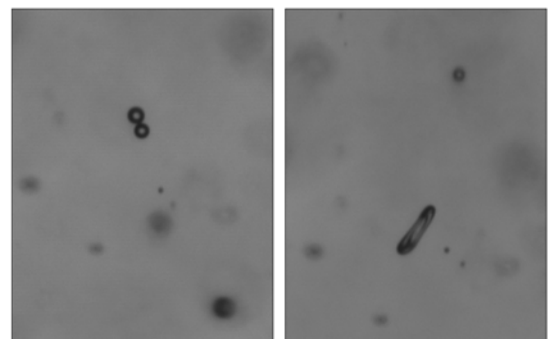


Figure 4-8. Collision of droplets that leads to droplet breakup into fragments (a) $t = t_0$. (b) $t = t_0 + 0.6 \mu\text{s}$.

The other source of non-spherical droplets is breakup or coalescence as a result of the collision of droplets. Coalescence of droplets occurs when two or more droplets collide with each other and merge to form a larger droplet as a result of surface tension. In Figure 4-7(a) two droplets are observed colliding and in Figure 4-7(b) after a time interval of $\Delta t = 0.6\mu\text{s}$ the droplets are observed to merge and coalesce to form a single droplet. Figure 4-8(a) and Figure 4-8(b) show a second example of colliding droplets which are breaking after collision. These figures confirm that collision of droplets may result in coalescence or breakup and that the droplets are non-spherical over the period of these mechanisms.

Examples of images of droplets with different shapes are shown in Figure 4-9. Figure 4-9(a) and (b) demonstrate spherical droplets. For these droplets surface tension plays the dominant role relative to aerodynamic forces and the droplets become spherical. Spherical shapes show that the droplets are stable, fully atomized, and are not prone to disintegration. Figure 4-9(c) - (f) illustrate droplets that have shapes that are deformed by aerodynamic forces. In these cases, the aerodynamic forces are not high enough to result in the breakup process and only result in shape deviation from spherical to elliptical. Droplets shown in Figure 4-9(g) - (t) consists of ligaments. These ligaments reveal occurrence of the breakup or coalescence phenomena in the spray field which depict that the atomization process is still occurring and droplet size changes. These processes affect droplet mean equivalent diameter in the spray field. As it is observed in Figure 4-9(g) - (t), the common feature of these droplets is concavity of their outer boundaries. This feature can be used to distinguish them from the other two classes of droplets. Therefore, the images of Figure 4-9 reveal that droplets based on their shape can be categorized to three droplet classes consisting of (i) spherical, (ii) deformed spheres, and (iii) ligaments. It is evident from these images that any shape parameter for droplet shape quantification will need to be able to distinguish between these different shape classes.

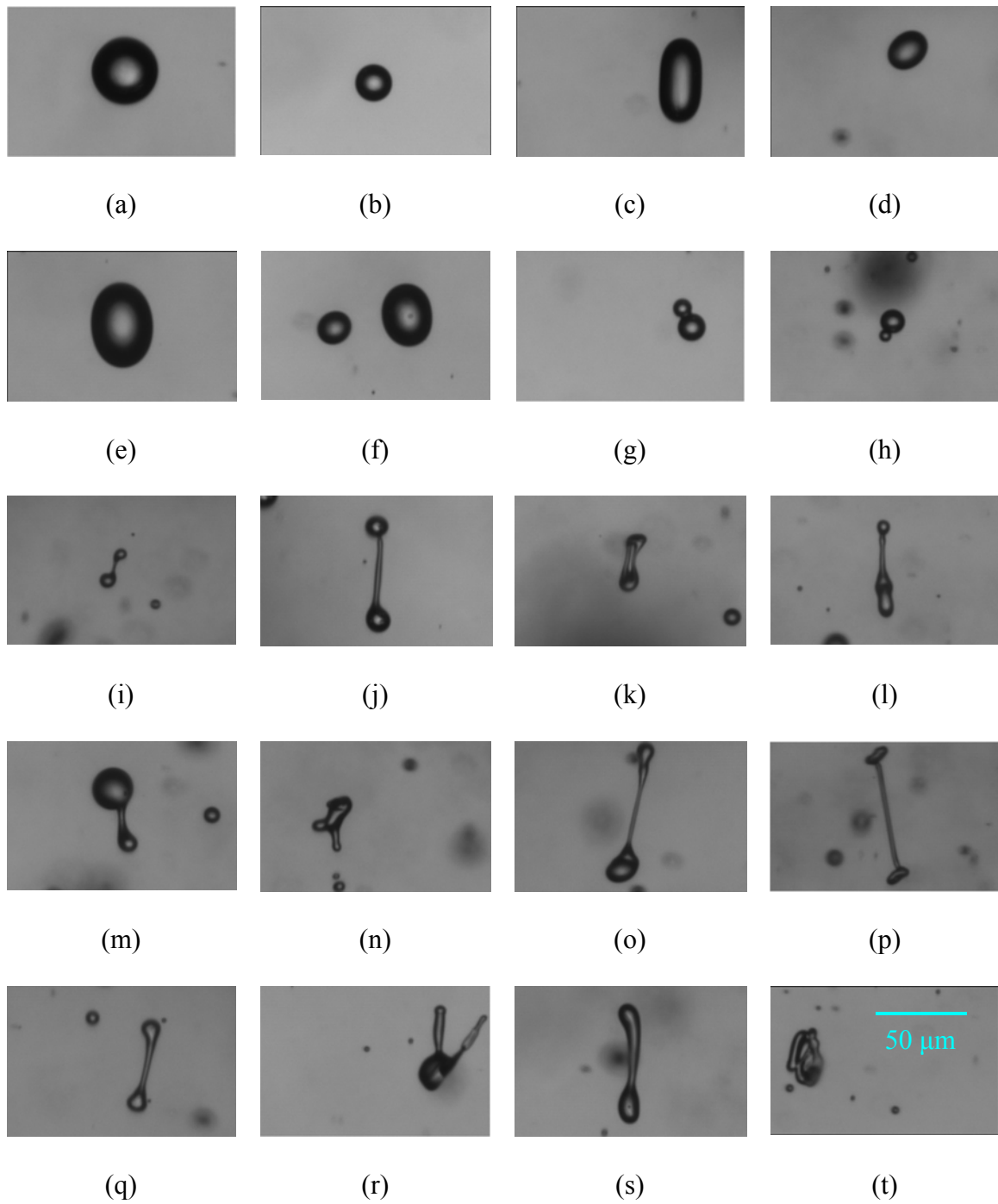


Figure 4-9. Droplet shapes at a spray field. (a)-(b) spherical droplets, (c)-(f) elliptical droplets, and (g)-(t) ligaments.

4.4. An Overview of Shape Quantifying Parameters

Identification of object shapes has been of interest in many applications ranging from pharmaceutical [56 - 58, 71, 72, 77, 78], medical [60 - 62, 79-81], fluids mechanics [23, 24, 33, 54, 59, 74 - 76, 82], material science [67 - 69, 98], historic art images [84], microbiology [85], geology [86], and food industry [63 - 66, 70, 87, 88]. An overview of the mathematical definitions and the features of shape parameters used in these fields to quantify shape of two-dimensional objects are presented in this section. The parameters along with associated names and the applied research areas are presented in Table 4-1.

Parameter 1 is the most common parameter discussed in the literature and has been applied with various names. This parameter has been suggested by Cox [83] to compare the ratio of area over the square of perimeter of the object to a circle. Since perimeter is included in this parameter it would be sensitive to the roughness and splashes of image periphery [58]. This parameter ranges from 0 to 1 and is theoretically 1 for a projected sphere. As the image outline deviates from a perfect circle the parameter value decreases toward zero for a line. This parameter has also been presented as the ratio of area equivalent diameter, D_a , over perimeter equivalent diameter, D_p , [69, 75, 76] where

$$D_a = \sqrt{\frac{4A}{\pi}} \text{ and } D_p = \frac{P}{\pi}. \quad 4-1$$

Parameter 2 is mostly known as the aspect ratio and expresses the ratio of width, b , over length, a , of the object image and ranges from 0 to 1. In spite of the apparent simplicity of the parameter's definition, various methods have been used in calculating this parameter, including:

(I) where a is the distance between two most distant points on the image periphery and b is the maximum distance between two points connected by a line perpendicular to a [57, 58, 63, 70, 72, 89 - 91].

(II) where a is the maximum Feret diameter and b is the Feret diameter perpendicular to a [56, 85]. The Feret diameter is defined as the longest distance between two parallel lines that do not intersect with the image outline [69]. Gonzalez et al. [92] method of *basic rectangle* can be used to obtain a and b based on this definition.

(III) where a is the maximum Feret diameter and b is the width of a rectangle which has the same length as the estimated Feret diameter and the same area as the object [69].

(IV) where a and b are the major and minor axis of a fitted ellipse, respectively. The fitted ellipse may be obtained by the second moment method [93, 94] or the least mean square method [86].

(V) where a and b are the longest and shortest lines passing through the center of the image and connecting two points on the image outline [23, 24, 35]. The lines are not required to be perpendicular.

(VI) where a and b are the length and width of the smallest enclosing rectangle. This is the approach used in the *BoundingBox* method in MATLAB [93].

The main purpose of *Parameter 2* is to identify the elongation of an object and does not address other object characteristics. For example, a circle and a square both have an aspect ratio of one [71].

Parameter 3 was introduced by Pentland [95] as projection sphericity to describe object shape. The length a can be the distance between two most distant points [57, 59, 65, 67, 70] or the Feret maximum diameter [69]. Mayor et al. [63, 70] has applied the square root of this parameter. This parameter ranges from 0 to 1 and is theoretically unity for a circular disc.

Parameter 4 is known as e_r and has been derived by Podczeczek and Newton [71] to express both shape deviation from a circular disc and surface roughness in one parameter. r_m is the mean radius drawn from the center of the area to the perimeter. Different number of radii have been used to calculate r_m in the literature including, 360 [56, 71] or 72 [57, 58, 72, 78] radii. The first term of this shape parameter is the ratio of the perimeter of a circle with mean radius over the actual perimeter of the object shape and reflects the effect of surface roughness. A correction factor is added to this term to eliminate the effect of major shape deformations. This factor, f , is suggested by Podczeczek and Newton [78] as

$$f = 1.008 - 0.231 \left(1 - \frac{b}{a} \right). \quad 4-2$$

The second term in the definition of *Parameter 4* is the square of eccentricity of an ellipse which depicts deviation from a circular shape [71]. This parameter also ranges from 0 to 1 and is theoretically unity for a circular disc.

Parameter 5, 6, and 7 all compare features of the smallest enclosing convex hull with the object [33, 59, 61, 64, 66]. Comparison between the area of the convex hull,

ACH , and the object area has been used by Pouletaut et al. [61] and Dickson et al. [64] as present by *Parameter 5* and *7*. The ratio of the perimeter of the convex hull, PCH , over perimeter of the region, *Parameter 6*, has also been used by Dickson et al. [64]. *Parameters 6* and *7* theoretically result in unity for any convex region. As the image boundary becomes concave these parameters reduce towards zero.

Parameters 8 and 9 have been developed by Almedia-Prieto [72] to express shape and boundary roughness, respectively. *Parameter 8*, known as V_r is theoretically zero for a circular disc and increases toward infinity with deviation from that shape. Since the absolute value of the difference between the local and mean radii is used, the parameter is less sensitive to surface roughness and mainly expresses shape [72]. *Parameter 9*, V_p , expresses surface roughness using the percentage of the difference between perimeter of the object and perimeter of a perfect circle with radius r_m . This parameter is also theoretically zero for a circle and increases towards infinity with shape deviation.

Parameter 10 is a normalized second central moment used by Iwano et al. [60] to characterize shape of pulmonary nodules. The mathematical definition of this parameter is based on the assumption of unit area for a pixel. Coordinates of the considered pixel and the centroid pixel are presented by (i, j) and (i_G, j_G) , respectively. This non-dimensional parameter gives a measure of how dense an object is packed around its centroid. As the shape of the object deviates from a circular disc this value increases. *Parameter 10* can also be used in the form of

$$\frac{A^2}{2\pi \sum_i \sum_j \{(i - i_G)^2 + (j - j_G)^2\}} \quad 4-3$$

Equation 3 theoretically results in unity for a projected sphere and as the shape deviates from a circle it decreases toward zero. Moments of other orders and forms have been applied by Dickson et al. [64]. The corresponding equations are discussed by Gonzalez et al. [70].

Parameter 11 demonstrates the percentage of the common area between the object and a circular disc of the same area located at the centroid of the object image. This parameter theoretically results in 1 for a circular disc. Any type of deviation from a circular disc such as boundary roughness and shape deviation reduces the common area and the parameter tends to zero.

Parameter 12 is used by Malot and Blaisot [54] and is the non-common area between the object image and a circular disc of the same area to depict shape deviation from a circular disc. The non-common area can be mathematically expressed as the difference between the union and intersection areas of the object image and the circular disc. The parameter is divided by the object area to become non-dimensional. This parameter ranges from 0 to 2 where the zero corresponds to a circular disc.

Parameter 13 presents the ratio of the object area over the area of the minimum enclosing rectangle. This parameter ranges from 0 to 1 and theoretically results in unity for a rectangular shape. **Parameter 13** allows comparison of the object shape against a rectangle and is limited to applications in which rectangular objects exist such as crystals [68]. The sides of the enclosing rectangle can be parallel to a selected set of x-y axis or parallel to the major and minor axis of the object image [64].

Parameter 14 allows comparison of the object shape against an ellipse using the ratio of the area of an object to the area of a fitted ellipse. The parameter ranges from 0 to 1 and theoretically results in unity for an elliptical shape. Different methods such as the second moment method [93, 94] or the least mean square method [86] can be used to fit the ellipse.

Parameters 15 and 16 express the ratio of area over square of thickness and the ratio of perimeter over thickness, respectively. Thickness, T , is defined as the number of steps necessary to disappear the object by removing a layer of boundary pixels at a time [64]. This process is known as erosion and is explained by Parker [96]. An elongated object will disappear with lower number of steps through the erosion process. Therefore, a high value of **Parameters 15 and 16** represents an elongated object.

Parameter 17 is the definition of eccentricity of an ellipse based on mathematics literature [97] which has been used to quantify shapes. The length, a , and width, b , can be determined with the methods explained for **Parameter 2**. This parameter ranges from 0 to 1 where zero is theoretically associated to a circular disc.

Table 4-1. An overview of shape quantifying parameters

Parameter number	Formula	Associated name(s)	Application(s)
1	$\frac{4\pi A}{P^2}$	Circularity [2, 57, 58, 60-62, 64, 65, 72, 77, 79, 81, 84] Roundness [63, 70, 97] Compactness [66, 74] Shape Factor [74, 82] Sphericity [68, 69, 75, 76] Degree of Splash [67] Third Circularity Measure [59] Imaging Factor [91]	Pharmaceutics [57, 58, 72, 76] Medical [60-62, 79, 81] Food [64-66, 88] Bubbles [82] Sprays [33, 74-76] Crystals [68, 69] Aggregate [98] Historic art images[84] PTV [59] Material [27]
2	$\frac{b}{a}$	Aspect Ratio [56-60, 65, 69, 72, 77] Height Deficiency Factor [61] Circularity [85] Elongation [63, 66, 70] Diameter Ratio [87] Centricity [23, 24] Anisometry Factor [91]	Pharmaceutics [56-58, 72, 76] Medical [60, 61, 81] Food [63, 64, 66, 70, 87] PTV [59] Microbiology [85] Crystals [69] Sprays [23, 24]
3	$\frac{4A}{\pi a^2}$	Projection Sphericity [57] Compactness [63, 70] Spatial Ratio [65] Elongated Factor [67] Second Circularity Measure [59] Circularity [69] Density Factor [91]	Pharmaceutics [57] Food [63, 65, 70] Material [87] PTV [59] Crystals [69]
4	$\frac{2\pi r_m}{P f} - \sqrt{1 - \left(\frac{b}{a}\right)^2}$	e_r [56 - 58, 71, 72, 77, 78]	Pharmaceutics [56 - 58, 71, 72, 77, 78]
5	$\frac{ACH - A}{ACH}$	Convex Deficiency Factor [61]	Medical [61]
6	$\frac{PCH}{P}$	Perimeter based convexity [64] Roughness [66] Convexity [33, 59]	Food [64, 66] Sprays [33] PTV [34]

Table 4-1. (continue) An overview of shape quantifying parameters

Parameter number	Formula	Associated name(s)	Application(s)
7	$\frac{ACH}{A}$	Area based convexity [64]	Food [64]
8	$\frac{\sum_{i=1}^n r_i - r_m \times 100}{r_m n}$	V_r [72, 77]	Pharmaceutics [72, 77]
9	$\frac{ 2\pi r_m - P }{2\pi r_m} \times 100$	V_p [72, 77]	Pharmaceutics [72, 77]
10	$\frac{\sum_i \sum_j \{(i - i_g)^2 + (j - j_g)^2\}}{A^2}$	Second central moment [60, 64]	Medical [60] Food [64]
11	$\frac{A \cap A_{circle}}{A_{circle}}$	Circularity index [80]	Medical [80]
12	$\frac{(A \cup A_{circle}) - (A \cap A_{circle})}{A}$	Shape parameter [54]	Sprays [54]
13	$\frac{A}{A_{rect}}$	Rectangularity [64]	Food [64]
14	$\frac{A}{A_{ellipse}}$	Ellipticality [64] Ellipse Factor [91]	Food [76]
15	$\frac{A}{T^2}$	Elongatedness [64]	Food [64]
16	$\frac{P}{T}$	Perimeter/thickness [64]	Food [64]
17	$\sqrt{1 - \frac{b^2}{a^2}}$	Eccentricity [87]	Geology [86]

4.5. Assessment of Shape Parameters

To investigate the performance of the different shape parameters in distinguishing the three droplet groups, their capability has been compared with droplet shape determined using manual classification. The droplet images obtained in the experiment have been manually categorized to the three droplet classes of spherical, deformed, and ligaments. This classification has been conducted visually and based on the shape characteristics of each droplet class as shown in Figure 4-9. Next, these images have been processed using a code developed in MATLAB. The grey scale of the image is inverted and normalized and then processed to identify droplet image regions using a 70% threshold level. The geometric characteristics of each droplet image region such as boundary, perimeter, and area are calculated to obtain the desired shape parameters.

Parameters 1, 2 (methods (IV) and (VI)), *3, 4, 8, 9, and 10* have been selected to investigate their performance. This selection has been based on the availability of a clear definition in the literature, the frequency of use of the parameter in the literature and the potential suitability of the parameter for droplet shape quantification. This has limited the set of parameters for comparison to those selected.

Investigation has highlighted that the shape parameters all have difficulty in distinguishing between the second (deformed spheres) and third class (ligaments) of droplet shapes. To address this issue a parameter has been developed as concavity parameter (*con*) which is a modification of *Parameter 7* and discriminates the third class of droplets (ligaments) from the other two droplet classes. This classification is based on concavity of the shape of the third group and convexity of the shape of the first and second groups of droplets and is defined as

$$con = sign \left[\frac{A}{ACH} - 1 + e \right]. \quad 4-4$$

This parameter results in value of 1 for the first and second groups of droplets which are convex and results in -1 for the third group of droplets which are concave. Due to the discretization error the area of the convex region is slightly higher than the discretized image area. The correction factor, *e*, has been added to compensate for this error caused by image discretization. A value of 0.025 is suggested based on the experimental results.

All of the selected shape parameters are multiplied by the *con* parameter to discriminate the third group of droplets.

The calculated values of the modified shape parameters for the obtained droplet images are plotted in Figure 4-10 - Figure 4-17. The plots are generated to compare the capability of the shape parameters in distinguishing the three groups of droplet shape through comparing them with the manual classification of droplet shape. In these figures it is specified that each droplet belongs to which class of droplets based on the manual classification. The parameters have been plotted versus droplet diameter in units of pixels removing the influence of the magnification of the imaging system used and to enable direct application of the results to future works.

The data presented in Figure 4-10 - Figure 4-17 reveal that the *con* parameter enables most of the shape parameters to distinguish the third group of the droplets. As expected, the obtained value for the third group of droplets falls in the range of negative numbers which separates them from the other two groups. It is only observed in Figure 15 that a relatively high number of the third group of droplets have positive values. This is because *Parameter 4* itself results in negative values for some ligaments.

A number of discretized small size droplets of the first and second group of the droplets with negative values are observed among the third group of droplets in Figure 4-10 - Figure 4-17. This is explained through the impact of image discretization effects on small droplets which results in higher *ACH/A* and negative *con* values. The error caused by discretization of digital image has a high impact in limiting the capability of the shape parameters in discriminating the three droplet groups. Preventing the error by considering a lower limit for droplet size in pixels necessitates application of an imaging system with sufficient magnification. High magnification lenses reduce the measurement depth-of-field and field-of-view which increases the spatial resolution of the measurement. A consequence of this is that a high number of images should be acquired and processed given that only a small number of droplets will typically be present in the image data.

Investigation of Figure 4-10 shows that the corresponding data of *Parameter 1* for the first and second groups of droplets are close to each other and can not be distinguished. *Parameters 2* (methods (IV) and (VI)), and *3* of Figure 4-11, Figure 4-12,

and Figure 4-13 provide relatively enough resolution to distinguish between the first and second group of droplets. The calculated data for *Parameter 4* presented in Figure 4-14 demonstrates that some of the first and second groups of droplets occupy the same region of the plot which eliminates it as a parameter for differentiating shape. It is also observed that *Parameter 4* results in discrete lines of values for spherical droplets which is contributed to the image discretization effect in measuring the a and b values. *Parameter 8* of Figure 4-15 results in three discrete regions of positive, around zero, and negative values for the shape classes of deformed, spherical, and ligaments, respectively. *Parameters 9* and *10* of Figure 4-16 and Figure 4-17 do not provide enough resolution to distinguish between the first and second group of droplets.

Among the investigated parameters, *Parameter 8* revealed the highest capability in discriminating spherical and deformed droplets. The data for each shape class occupy separate regions in Figure 4-15 and appropriate boundaries can be specified to distinguish droplets of the three groups. Deformed droplets of the second group have values larger than +2. The spherical droplets are located between values of -2 to 2. The ligaments of the third group have negative values and by reduction toward minus infinity their shape deviation is intensified.

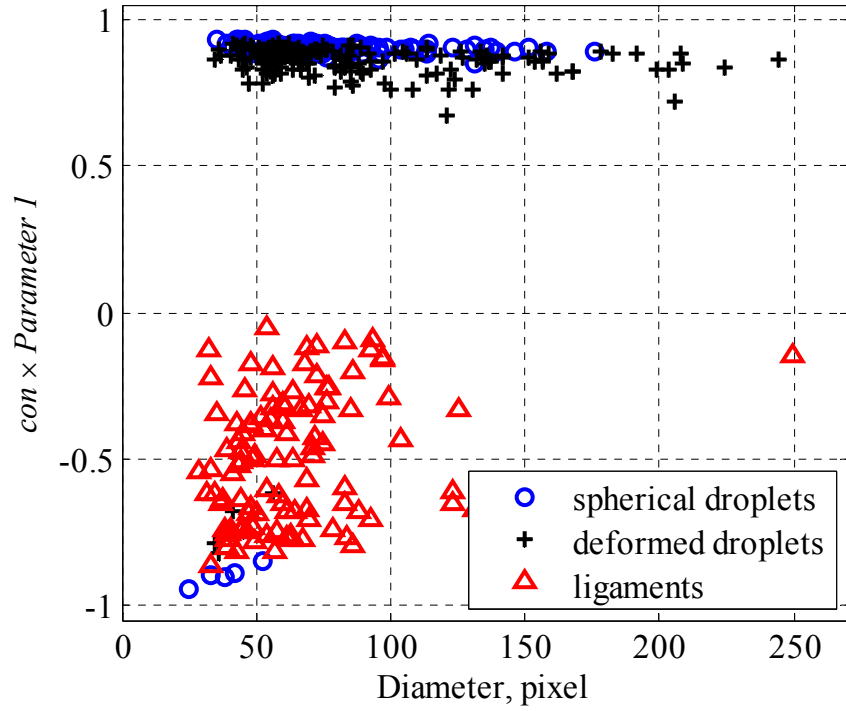


Figure 4-10. Assessment of shape identification using *Parameter 1*.

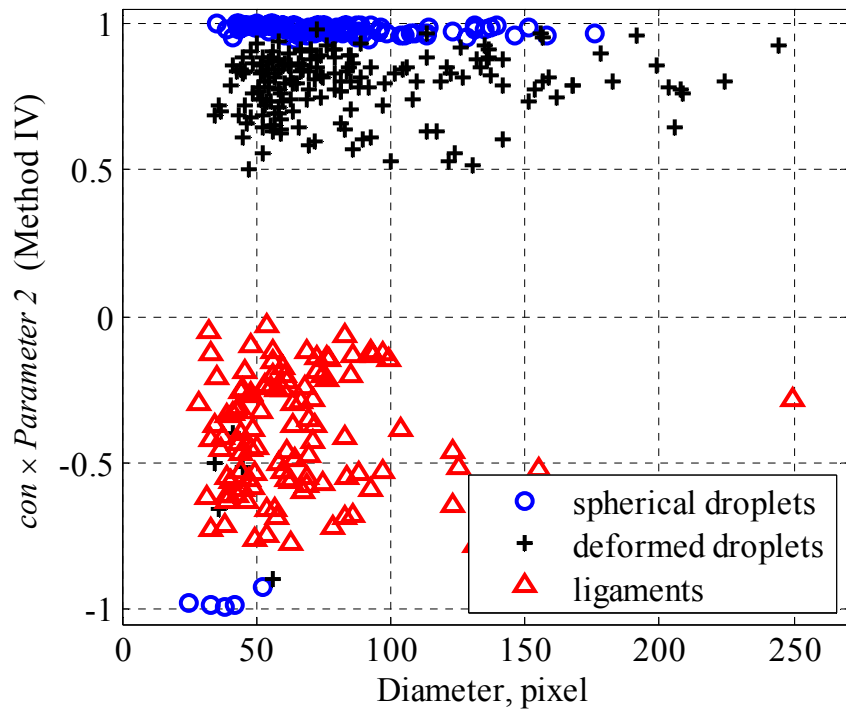


Figure 4-11. Assessment of shape identification using *Parameter 2*, method (IV).

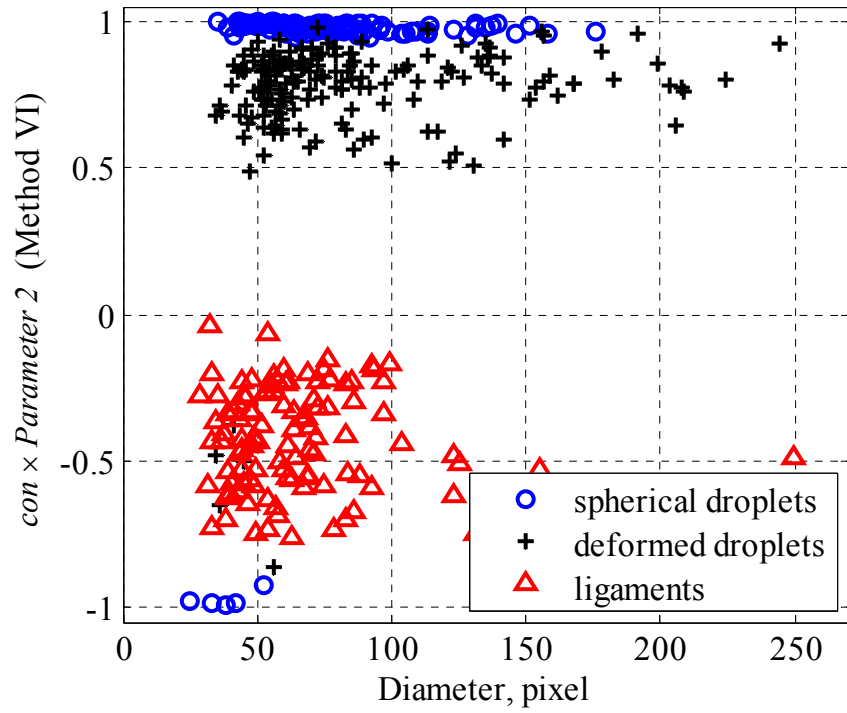


Figure 4-12. Assessment of shape identification using *Parameter 2*, method (VI).

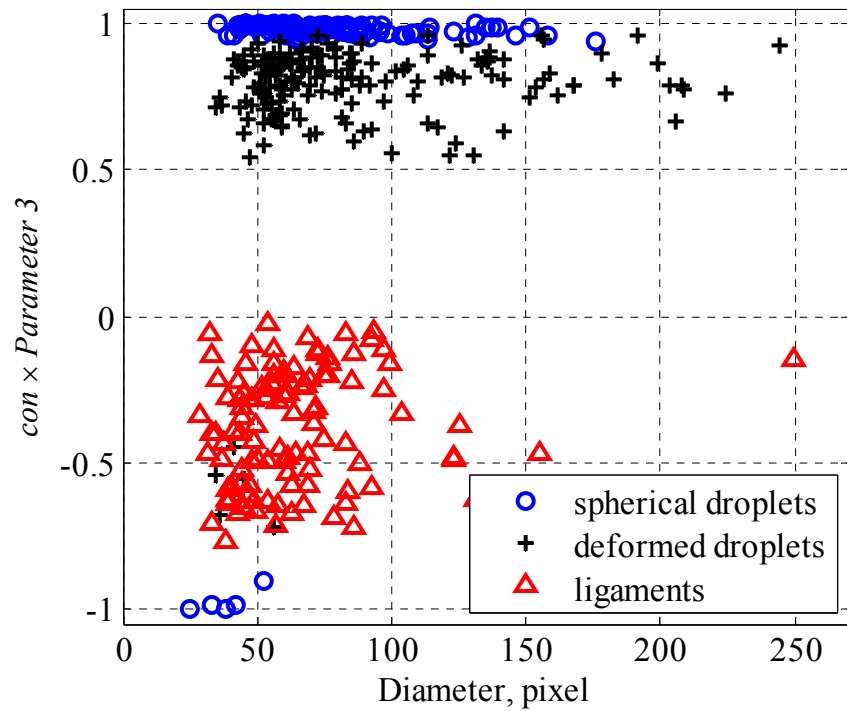


Figure 4-13. Assessment of shape identification using *Parameter 3*.

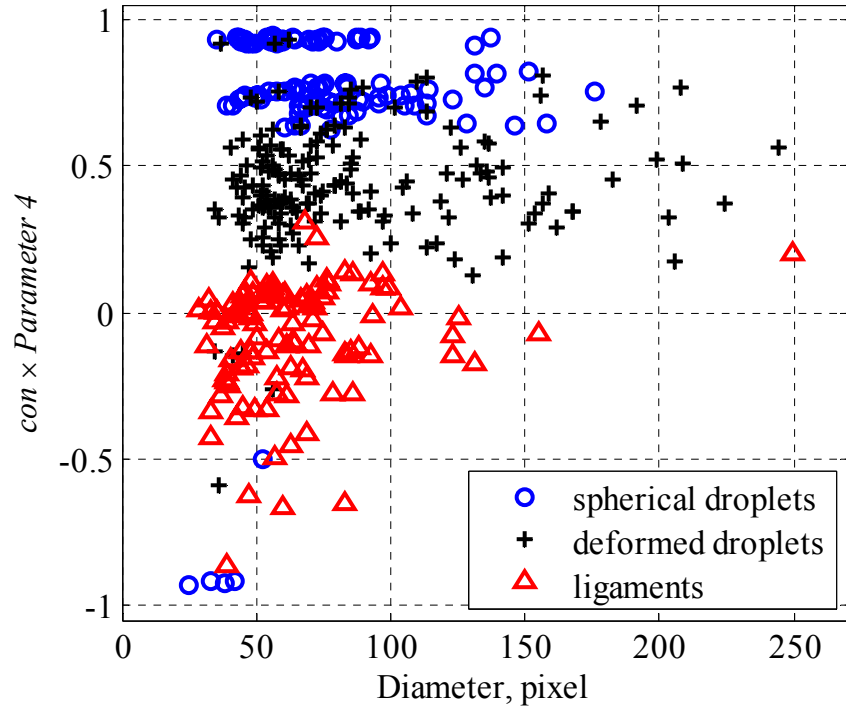


Figure 4-14. Assessment of shape identification using *Parameter 4*.

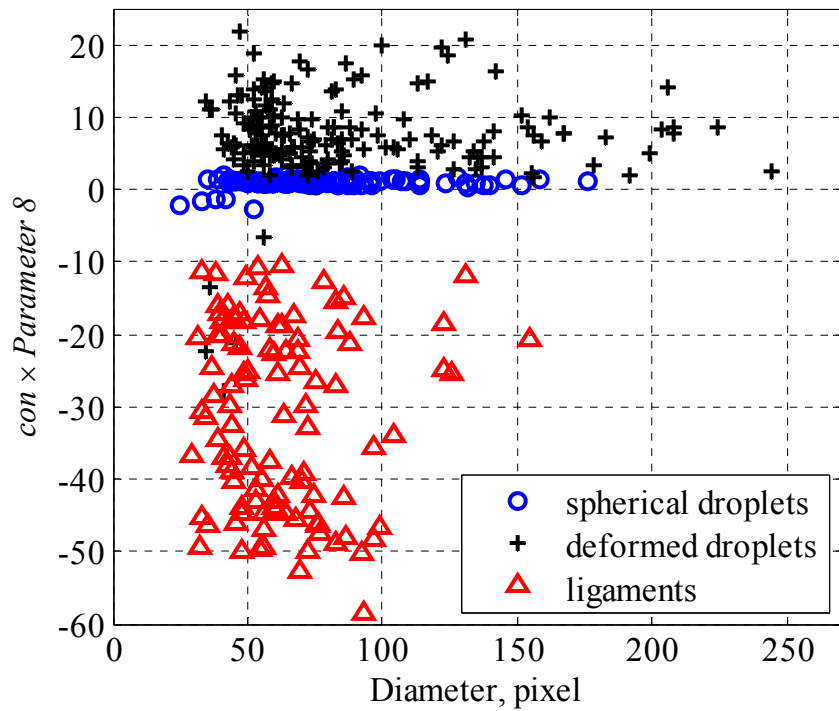


Figure 4-15. Assessment of shape identification using *Parameter 8*.

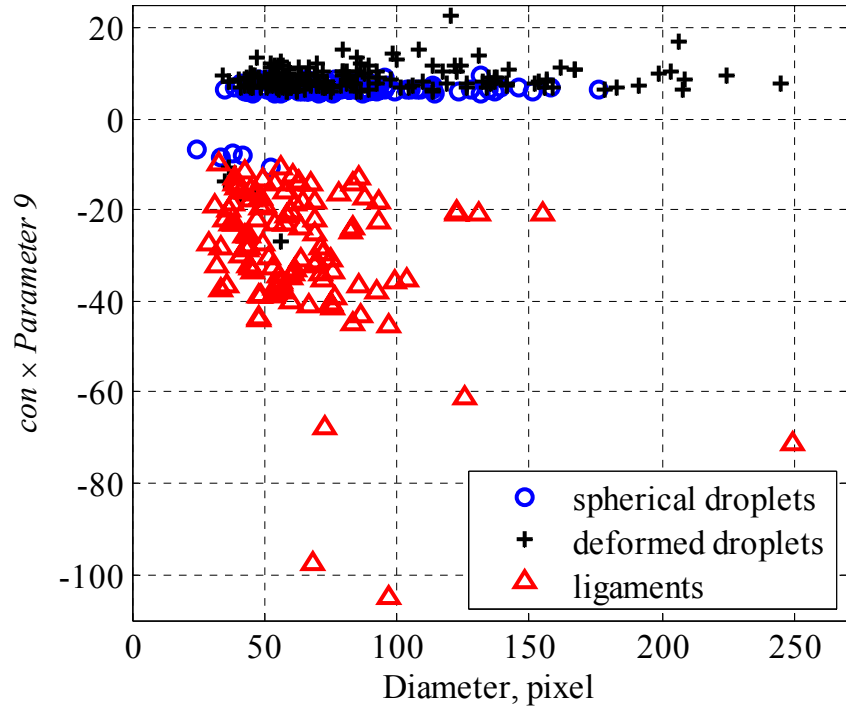


Figure 4-16. Assessment of shape identification using *Parameter 9*.

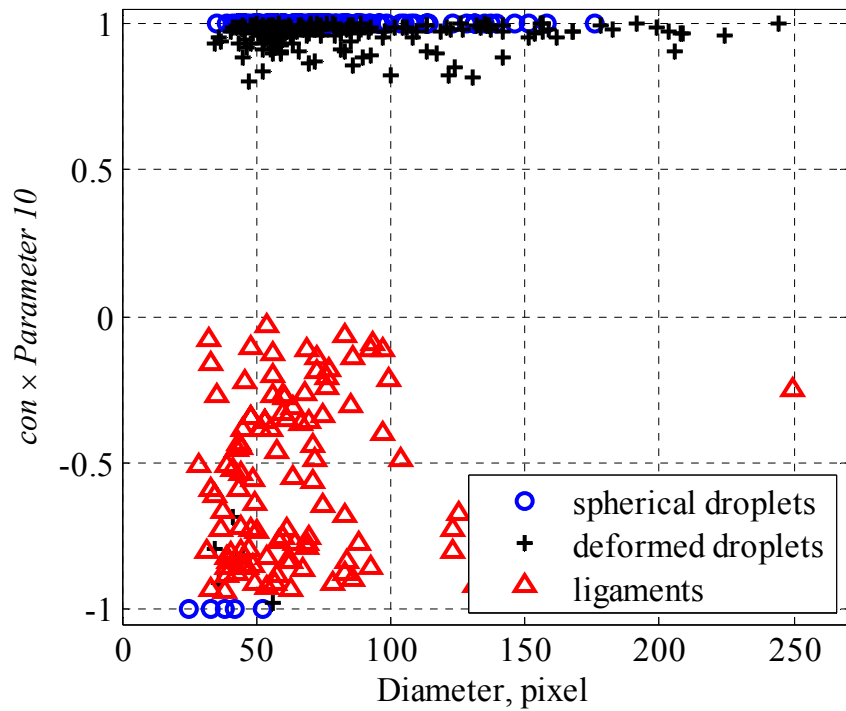


Figure 4-17. Assessment of shape identification using *Parameter 10*.

4.6. Conclusion

A review of the literature has been conducted on several shape parameters applied in various applications to identify object shape in image data. The gathered information consists of a mathematical definition, calculation procedure, application, and major characteristics of the shape parameters. This study showed that several names are associated with one mathematical definition and also different procedures have been observed for calculating the same geometric properties.

A shadowgraph droplet analyzer has been applied to provide visual images of droplets of different shapes existing in a spray field. The images revealed that different types of droplet shapes are present in the spray and these droplets can be classified into three distinct categories of (i) spherical, (ii) deformed spheres, and (iii) ligaments based on their shape.

The obtained images from the shadowgraph droplet analyzer have also been used to investigate the ability of a selected number of shape parameters in distinguishing the three droplet groups. Since most of the selected shape parameters had difficulty in distinguishing between the third group (ligaments) and the second group (deformed spheres) of droplets, a concavity parameter, *con*, has been suggested to distinguish the third group based on their shape concavity. The selected shape parameters have been multiplied by the *con* parameter which, except for *Parameter 4*, makes them capable of distinguishing the third group of droplets.

Investigating the performance of the shape parameters in distinguishing the first and second groups of droplets shows that *Parameters 1, 4, 9, and 10* do not provide a separate range of values to discriminate between the first and second group of droplets. *Parameters 2* (methods (IV) and (VI)), *3, and 8* provided enough resolution to distinguish between the spherical and the deformed droplets. Among them, *Parameter 8* is the most appropriate one for distinguishing spherical and deformed droplets. With the use of *Parameter 8* multiplied by the *con* factor, $con \times \text{Parameter } 8$, the captured spherical droplets from the experimental data images were located between values of -2 to 2. As the $con \times \text{Parameter } 8$ value increases toward positive or negative infinity deviation of droplet shape occurs toward the deformed sphere and the ligament groups, respectively.

5. Evaluation of Digital Image Discretization Error in Droplet Shape Measurement Using Simulation

5.1. Introduction

Among droplet analyzers, image-based techniques are capable of visualizing droplet shape by capturing a two-dimensional projected image of the droplets. These systems have recently become popular due to advances in computer and imaging technology [10]. However, the literature shows that their application has been mostly limited to characterizing droplet size based on an equivalent diameter [12, 33, 74, 75] and their capability in quantifying droplet shape has only been used in limited applications. This can be attributed to the uninvestigated sources of error in image-based techniques which prevents researchers from applying them. Two main sources of errors in image-based techniques are caused by measurement depth-of-field [99] and image discretization [57].

The measurement depth-of-field can lead to considerable error in image-based techniques. When a droplet is located outside the depth-of-field, its image becomes out-of-focus. The out-of-focus droplet image has a vague boundary which reduces the accuracy of boundary detection. This error has been addressed by previous researchers and can be prevented by applying efficient algorithms [73, 99-101] to only select in-focus droplets with sharp boundaries for data analysis.

The other source of error is caused by discretization of the image by the camera's two-dimensional digital CCD sensor which is typically an array of square pixels. Digital image discretization results in object images to have a jagged boundary and as a result the discretized image has a shape deviation from the real image. Object image properties such as area, perimeter, and diameter are calculated from the discretized images and can result in values that differ from the actual values, reducing measurement accuracy. This

error has been frequently observed in applications that involve shape quantification through digital images such as pharmaceutical [57, 72, 102], medical [60-62], and food industries [64-66].

In various applications, object shape is typically identified using shape parameters. A shape parameter compares the object shape with a reference shape through measuring a number of the objects geometric features. It has been observed in previous experiments that the applied shape parameters do not result in the expected theoretical values. For example, the shape parameters used by Podczec et al. [57], Hileman et al. [102], Hellen and Yliruusi [103], Wan et al. [104] should theoretically result in value of unity for a circular disc. However, they have considered values as low as 0.83 to 0.93 as a criterion for circular objects. For another shape parameter Podczec and Newton [59], Podczec et al. [57], Baert et al. [105], Vervaet and Remon [106], Vervaet et al. [107], Hellen and Yliruusi [103] have considered values of 1.002, 1.02, 1.2, 1.2, 1.2 and 1.06, respectively instead of theoretical value of unity for circular objects. Malot et al. [54] have considered droplet images with a value of 0 to 0.2 as circular for their shape parameter in spite of the theoretical value of zero for a circular disc. Almedia-Prieto et al. [72] have also suggested a value of 0 to 2 instead of theoretical value of zero for circular shapes measured using their shape parameter. These deviations are all attributed to image discretization error [23, 54, 57, 72, and 102], however, no direct investigation has been carried yet on image discretization in relation to the shape parameters used in droplet and particle shape measurement.

In a recent paper by Pavlova et al. [108], the applied shape measurement (their Figure 17) shows reduction of droplet circularity with reduction of image size and lead to the authors misleading conclusion of less sphericity for smaller droplets. This trend is against what is conduced from the We number and is caused by the image discretization error. In addition, the commercial systems, e.g. LaVision Inc., still apply an arbitrary shape parameter with unknown level of error due to image discretization. Although image discretization is well known in image processing literature, the lack of investigation of this error in relation to droplet and particle shape measurement results in misleading conclusions and limitation of the measurement.

The discretization error can be mitigated by increasing magnification and consequently the number of pixels used to characterize the object. Podczec et al. [57] suggested at least 40 pixels across the object image for accurate shape measurement using their applied parameters. Almeida-Prieto et al. [77] suggested minimum scaling factor of 20 $\mu\text{m}/\text{pixel}$. Almeida-Prieto et al. [72] suggested a minimum diameter of 50-60 pixels for their considered parameters. High optical magnification lowers the depth-of-field and field-of-view which necessitates processing a higher number of object images [77]. This will result in a majority of images having no data, especially in sparse regions of a spray field where droplet frequency in the field-of-view is low. Except for Almeida-Prieto et al. [72] who made their suggestion based on a simulation of 15 circles with diameter of 20 to 180 pixels, other suggestions for defining the level of discretization were based on experimental samples. Hence, it is important to conduct a complete investigation of the error caused by image discretization and clarify the limitations caused by that on different shape parameters.

The main aim of this chapter is to investigate the effect of image discretization error on shape measurement for a selection of shape parameters through a simulation. The investigation specifies the shape parameter which has the minimum error due to digital image discretization and also provides the highest resolution in identifying different droplet shapes. As the first step, image discretization, the involved factors, the selected shape parameters, and the simulation procedures are described. The simulation results are used to investigate the discretization error in calculating area, perimeter and the selected shape parameters. Finally, a factor is suggested to rank the shape parameters based on their capability in discriminating object shapes in the presence of the effect of digital image discretization.

5.2. Digital Image Discretization

In order to clarify the discretization error and the affecting factors, consider a digital image which is formed by a two-dimensional array of CCD pixels. These pixels obtain different gray level values based on the incident light. The object image is, then, discerned from its surrounding by selecting the pixels which have a gray value higher or lower than a selected threshold. Figure 5-1(a) - (i) show a simulation of digital images of the projected view of a sphere which forms a circular disc in the two-dimensional image with different sizes and positions relative to the pixels grid. The images are generated by considering a circle and selecting the pixels which are completely inside that circle. This assumption is equivalent to assuming that only pixels which are completely inside the circle have enough intensity to pass the threshold level used to select in-focus droplets. The boundary pixels obtained using two methods of 4-connected and 8-connected to the background are also shown in Figure 5-1(a) and (b), respectively. These methods of boundary detection are discussed in section 5-4.

The images shown in Figure 5-1(a)-(i) demonstrate that instead of smooth boundaries, digital images have jagged boundaries formed by the sides of the rectangular CCD pixels. This results in considerable deviation of the digital image from the real object shape. In Figure 5-1(a)-(h) the center location of the assumed circles, highlighted by a cross symbol at the circle origin, has been shifted relative to the pixel grid. Following the patterns of the discretized images reveals that the location of the assumed circle relative to the pixels grid may result in addition or elimination of pixels to the digital image and consequently change in the digital image pattern. Figure 5-1(i) shows a discretized image of a circular disc with twice the diameter of the circular discs in Figure 5-1(a)-(h). Comparison of this image with the others depicts that the relative size of the image to the pixels can also affect the shape deviation of the discretized image. Therefore, the location of the circular disc relative to the pixels grid and also image/pixel size ratio may result in formation of different digital image patterns. These deviations affect geometric features of the images, such as area and perimeter, and consequently the shape parameters.

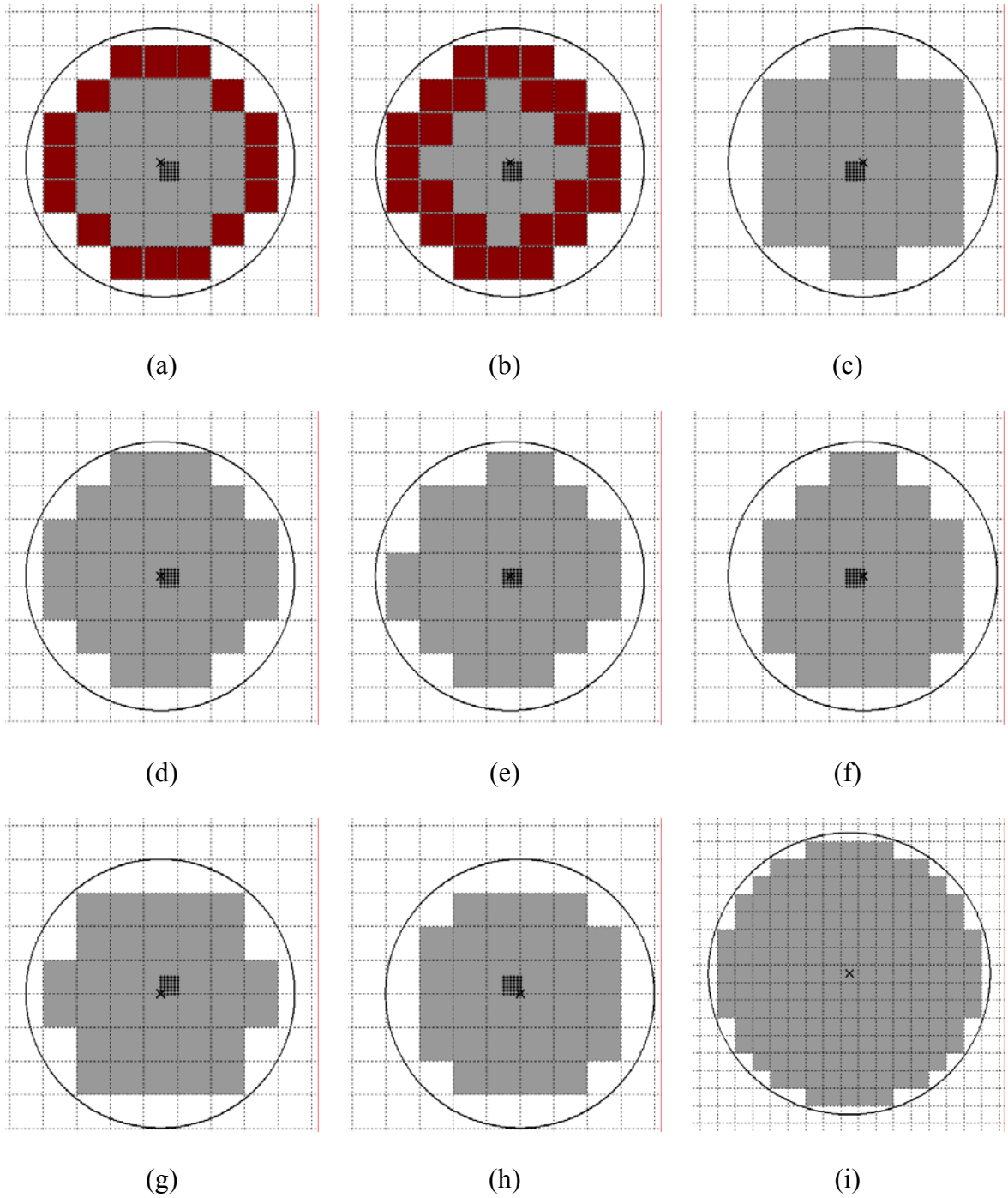


Figure 5-1. Formation of discretized images on the CCD grid. (a) Center of the assumed circle is at the centroid of the central pixel. Boundary pixels are 4-connected to the background. (b) Center of the assumed circle is shifted $1/6$ pixel to right. Boundary pixels are 8-connected to the background. Center of the assumed circle is shifted (c) $1/2$ pixel to right (d) $1/6$ pixel downward (e) $1/6$ pixel to right and $1/6$ pixel downward (f) $1/2$ pixel to right and $1/6$ pixel downward (g) $1/2$ pixel downward (h) $1/2$ pixel to right and $1/2$ pixel downward. (i) The diameter of the assumed circle is twice that of other images.

5.3. Simulation of Digital Images

In this work, a simulation has been conducted to assess the effect of discretization error in calculating main geometric features of an object and the selected shape parameters. Circular and elliptical discs have been generated as the investigated shapes of this simulation. Circular discs are especially important since all the shape parameters consider a circular disc as the reference shape and a considerable portion of droplets in a spray field are spherical [23]. The elliptical shape is also important since it is one of the prevalent shapes for non-spherical droplets in a spray field and can assess the capability of shape parameters in distinguishing droplet shape deviation in the presence of image discretization.

The digital images of circular and elliptical discs have been generated with the same method of Figure 5-1 in MATLAB. The discretized images of circular discs have been produced by assuming circles with diameters ranging from 5 to 160 pixels to investigate the affect of image/pixel size ratio on the discretization error. In addition, for each diameter, the simulated circular discs have been positioned at 36 locations to investigate the effect of image location relative to the pixels grid. The center locations are spread evenly on a quarter of a pixel, see Figure 5-1(a). This results in total number of 5976 simulated circular discs. Two types of elliptical discs with aspect ratio of $b/a = 0.7$ and 0.4 have been generated which are shown in Figure 5-2. The major axis, a , ranges from 5 to 240 pixels and the centers have also been positioned at the same 36 locations on a quarter of a pixel which results in a total number of 16992 elliptical discs.

After the simulated images of circular discs and elliptical discs have been generated, their area equivalent diameter is calculated using:

$$D = \sqrt{\frac{4A}{\pi}}. \quad 5-1$$

The calculated area equivalent diameters are used as their diameter through this investigation instead of the diameter of the preliminary assumed circles. Finally, area, perimeter and the shape parameters are calculated for the images using a code written in MATLAB. Area and perimeter are calculated using the method described by Gonzalez [92] which is discussed below. In this work, *Parameters 1, 2, 3, 4, 8, and 9* have been selected from Table 4-1.

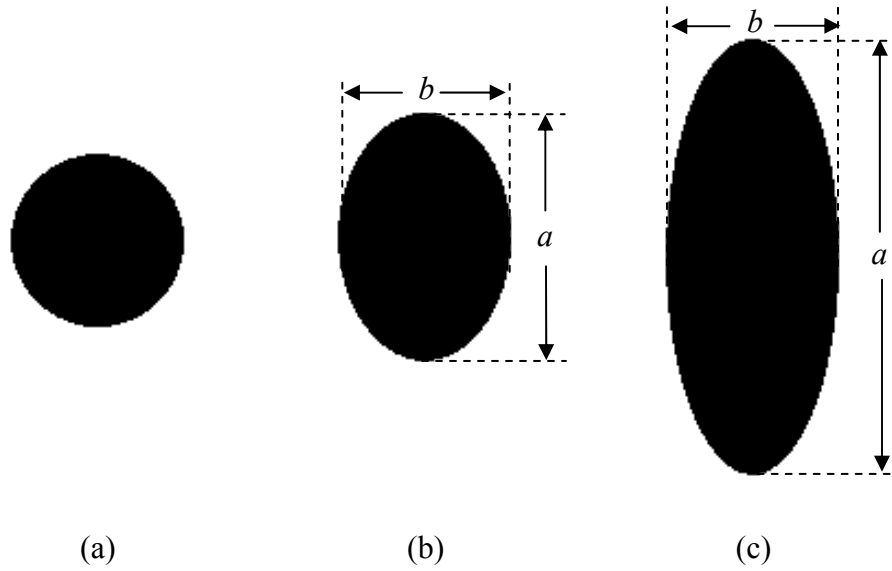


Figure 5-2. Two-dimensional discretized images of used in the simulation. (a) simulated circular disc, (b) simulated elliptical disc with $b/a = 0.7$, and (c) simulated elliptical disc with $b/a = 0.4$.

5.4. Effect of Image Discretization on Area and Perimeter

Any error caused by digital image discretization appears in the calculated shape parameter through the measurement of geometric features of the object being imaged. In this section, the effect of image discretization on area and perimeter which are the two main geometric features used in the shape parameters is investigated.

Area of a region in a digital image is typically measured by counting the number of pixels covering the region that are above a pre-specified value. In order to investigate the discretization error, the ratio between the area of the simulated circular disc to their real area is calculated as

$$\frac{A_{discretized}}{A_{real}} = \frac{\text{number of pixels}}{\pi r^2} \quad 5-2$$

where r is the radius of the assumed circle before image discretization.

Figure 5-3 shows the calculated values of Equation 5-2 for a size range of 5 to 160 pixels across the object. It is observed that at small diameters there is a sharp-drop off in the calculated values. This expresses a high error caused by image discretization in the measurement of the area of low resolution digital images. The data is also scattered due to change in digital image area caused by shifting the location of the assumed circle relative to the pixels grid. As the number of pixels used to discretize the diameter increases, the values approach unity and become uniform. In a digital image the minimum measurable area is equal to the size of a pixel. Increase in discs diameter results in reduction of the relative area of a pixel to the image area. Consequently, discretization error reduces and the values of Figure 5-3 approach unity. Results show that the error can be as high as 5% for a circle of 70 pixels in diameter.

Image discretization can also affect the perimeter of the object image. The first step in measuring the perimeter of an object in a digital image is to specify the boundary or the boarder of the region. The boundary consists of a set of object image pixels which are connected to at least one background pixel [92]. The pixels which are not in the object image are called background pixels [92]. There are two different approaches regarding connectivity of boundary pixels to background pixels: 4-connected and 8-connected. Boundary pixels are 4-connected to the background if they are horizontally or vertically connected to them. Boundary images are 8-connected if they are horizontally,

vertically, or diagonally connected to the background pixels [109]. Examples of the two boundary connectivity possibilities are shown in Figure 5-1(a) and (b).

The second step in estimating the perimeter of an image is to measure the length of the specified boundary contour. Again, different procedures have been reported in the literature [33, 57, 75]. Kashdan et al. [75] have measured perimeter as the number of pixels on an images boundary. Measuring perimeter by the number of pixels should be avoided because number of pixels represents area and not length [109]. Lecouna et al. [33] estimated perimeter as the total length of straight lines connecting all the external pixel vertices. Podczeck et al. [57] have estimated perimeter as the perimeter of the polygon obtained from 72 evenly distributed lines from the center of the image to the image boundary. The most common method of calculating perimeter is based on whether the perimeter cuts horizontally, vertically or diagonally through a pixel [92]. This method is equivalent to the total distance between centers of successive pixels of the boundary and has been used in this paper as the standard method for measuring perimeter length.

In order to investigate the discretization error in measuring image perimeter, the ratio of the perimeter of discretized images of circular discs to their real perimeter has been calculated by

$$\frac{P_{discretized}}{P_{real}} = \frac{\text{length of boundary}}{2\pi r} \quad 5-3$$

The calculated values of Equation 5-3 obtained through 4-connected and 8-connected boundary pixels to the background pixels for the simulated circular discs are shown in Figure 5-4. For both methods, scattered values with sharp drop-off are observed at small diameters. At 100 pixels in diameter, the 4-connected and 8-connected methods result in 3.5% and 24.8% error. Therefore, the 4-connected method results in a better estimation of the perimeter than the 8-connected method. In addition, over the investigated diameter range the error does not tend to zero with increase of the number of pixels and the perimeter ratio does not approach unity. Therefore, shape parameters which use the image perimeter in their mathematical definition are expected to have relatively high error.

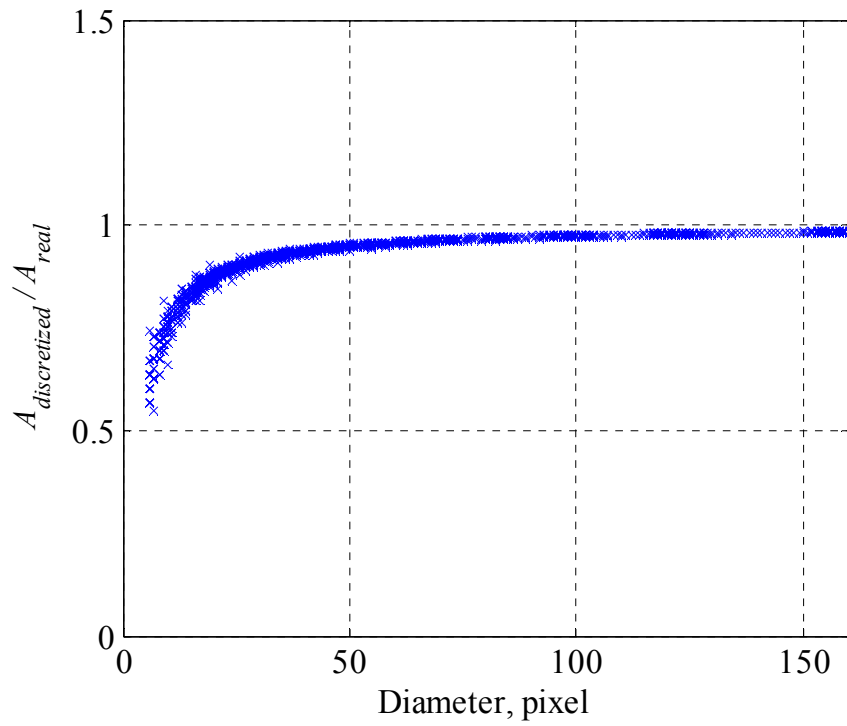


Figure 5-3. Image discretization effect on area measurement.

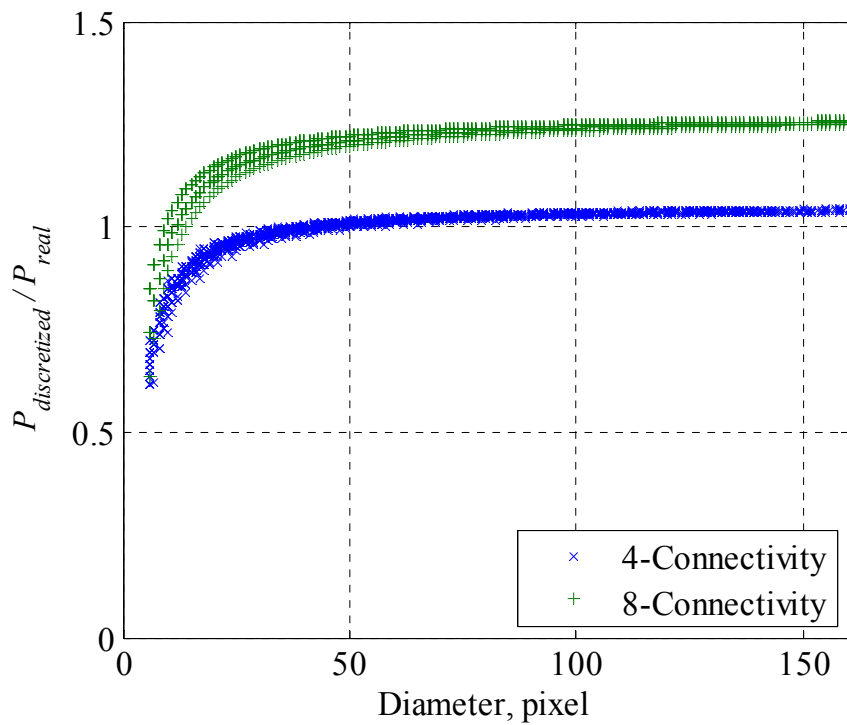


Figure 5-4. Image discretization effect on perimeter measurement.

5.5. Effect of Image Discretization on the Performance of Shape Parameter

The described simulation has been conducted to show the effect of discretization on the capability of a selected number of shape parameters in distinguishing different shapes. The simulation has been conducted through generating digital images of circular and elliptical discs and calculating the selected shape parameters. The results are presented in Figure 5-5 - Figure 5-10 and demonstrate the calculated shape parameters versus area equivalent diameter, d , for the simulated circular and elliptical discs of 0.7 and 0.4 aspect ratios. The expected theoretical values for the parameters have also been calculated and are presented in the figures with solid and dashed lines. In the calculation of the theoretical values the method of Ramanujan has been used to obtain ellipse perimeter [110]. Some regular patterns are observed in the data presented in Figure 5-5 - Figure 5-10. These regular patterns which are observed as batches of data are caused by the selected method for generating the digital images, mainly, increase of diameter through 1 pixel steps and the 36 locations for the center of the simulated shapes.

It is observed in Figure 5-5 that for small diameters of approximately less than 30 pixels, *Parameter 1* results in scattered values for circular and elliptical discs. In this region, the values for circular and elliptical discs of $b/a = 0.7$ are also cluttered into each other which incapacitates this parameter in discriminating them. The clearance between the two groups of $b/a = 0.7$ and 0.4 elliptical disc is enough to make them distinguishable which shows higher capability of *Parameter 1* in distinguishing highly deformed shapes instead of slightly deviated shapes. As diameter increases beyond 30 pixels, the values for circular discs reduce and become less than theoretical value of unity. This underestimation can be explained through the observed trends of area and perimeter described for Figure 5-3 and Figure 5-4. Image discretization results in underestimation of both perimeter and area but the presence of P^2 makes it a dominant factor at larger diameters. In spite of the popularity of this parameter in the literature, it doesn't result in the theoretical value of 1 even for a circular disc of 160 pixels in diameter. The data for the 0.7 and 0.4 elliptical discs are also different from theoretical values at 160 pixels diameter. In general, *Parameter 1* does not result in the expected theoretical values even

for diameters as large as 160 pixels and its resolution in distinguishing different shapes is small.

The calculated values for *Parameter 2* using the smallest bounding box method of MATLAB [93] are demonstrated in Figure 5-6. In this figure it is observed that *Parameter 2* results in unity except for a discrete line of values for the simulated circular discs. The discrete line of values in Figure 5-6 is as a result of the minimum measureable length being equal to the length of a pixel. The separate line is formed by the images in which the length is one pixel longer than the width. As the images get larger the b/a length ratio increases toward unity and the difference between the values reduces. It is also observed in Figure 5-6 that the values for the elliptical discs are scattered for diameters smaller than 50 pixels. However, the difference between circular and the two elliptical discs is sufficient that the groups are distinguishable. In addition, the values for the three groups of simulated discs are asymptotic to the theoretical values as diameter increases. The deficiency of *Parameter 2* is its limited ability in distinguishing many geometric features because it only consists of the length of two lines of the object image. For example, a circle and a square theoretically result in the same value according to this parameter. In Figure 5-1, images (a), (e), and (h) have different patterns but all result in unity for *Parameter 2* because they have equal length and width. Images (c), (f), and (g) of Figure 5-1 are also different but result in equal values because in all of them length is one pixel longer than width. This limited ability in revealing geometric features makes this parameter unsuitable for identifying various droplet shapes.

The result of the calculation for *Parameter 3* is shown in Figure 5-7. For diameters smaller than 30 pixels, *Parameter 3* is overestimated for circular discs. This is due to the higher area of the circular disc with diameter equal to the longest axis than the area of the disc. For diameters smaller than 50 pixels, the values for $b/a = 0.4$ and 0.7 elliptical discs is scattered. In spite of the scattered data, there is enough resolution between the three groups to distinguish between them. As diameter increases the *Parameter 3* values tend towards the theoretical values and the discretization error is minimized. In general, this parameter provides clearance between the simulated discs of this investigation and is capable of distinguishing them for diameters larger than 10 pixels.

The simulation result for *Parameter 4* is shown in Figure 5-8. A separate line of values for circular discs similar to Figure 5-6 is also observed in Figure 5-7 which is due to the existence of b/a , in *Parameter 4*. The parameter is also highly sensitive to discretization and for small circular discs values as low as 0.5 instead of the theoretical value of unity are observed. For small diameters the data for the elliptical discs is *Parameter 3* scattered. As diameter increases up to 160 pixels, the parameter does not result in the theoretical value of unity for circular discs and the discrete line is still present. The values are also different from the theoretical values for the 0.4 and 0.7 elliptical discs at 160 pixels diameter. There is a larger difference between the values for the circular discs and 0.7 elliptical discs than the two groups of 0.7 and 0.4 elliptical discs. The ability of this parameter to distinguish between different shapes is relatively limited by its high sensitivity to image discretization.

The simulation result for *Parameter 8* is demonstrated in Figure 5-9. For small circular and elliptical discs with diameter less than 50 pixels, the values are scattered as a result of image discretization. *Parameter 8* also reveals high sensitivity to shape deviation and provides enough difference between the three groups to make their discrimination feasible. As diameter increases up to 160 pixels the data for circular discs and the 0.7 elliptical discs tend toward the theoretical values. The data of the 0.7 elliptical discs also becomes uniform but deviation from the theoretical value is observed at 160 pixels diameter. The difference between elliptical discs of 0.4 and 0.7 aspect ratio is relatively high which reveals sensitivity to shape deviation for highly deformed shapes. In spite of *Parameter 8* being highly sensitive to image discretization, it reveals a good compromise between sensitivity to image discretization and shape deviation which makes different shapes distinguishable.

The simulation result for *Parameter 9* is shown in Figure 5-10. This parameter has been especially developed to measure surface roughness [72]. For this reason, perimeter and mean radius are used in the mathematical definition of this parameter which are both sensitive to surface roughness. However, this characteristic results in a high sensitivity to discretization error which also appears as roughness on the outer boundary of the image. For diameters less than 70 pixels the data of the three groups of simulated discs are scattered due to the sensitivity of this parameter to image discretization. At diameters

less than 40 pixels the data for the circular and 0.7 elliptical discs are cluttered into each other and are not distinguishable. With increase of diameter the scatter in the data decreases but the effect of discretization error is still present; the values of the circular and elliptical discs do not tend to the theoretical value with increase of diameter. The difference between the data and the theoretical values indicates high sensitivity of this parameter to image discretization. The simulation shows that this parameter is also affected by shape deviation as well as the effect of surface roughness. The difference between the values increases for higher deformed shapes of 0.4 and 0.7 elliptical discs. In general, *Parameter 9* amplifies the discretization error and is not efficient in distinguishing shape deviations.

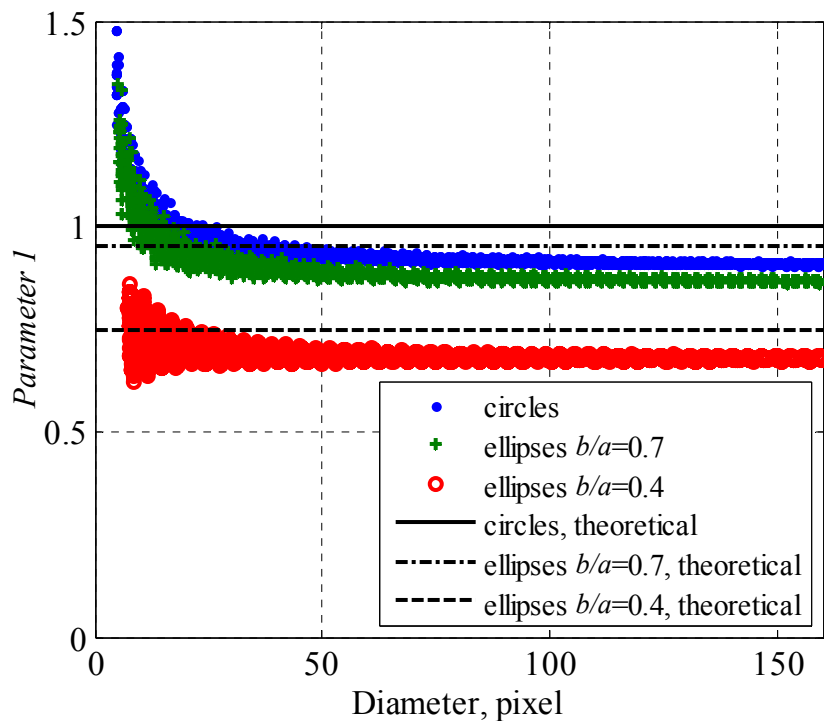


Figure 5-5. Effect of image discretization on shape quantification using Parameter 1.

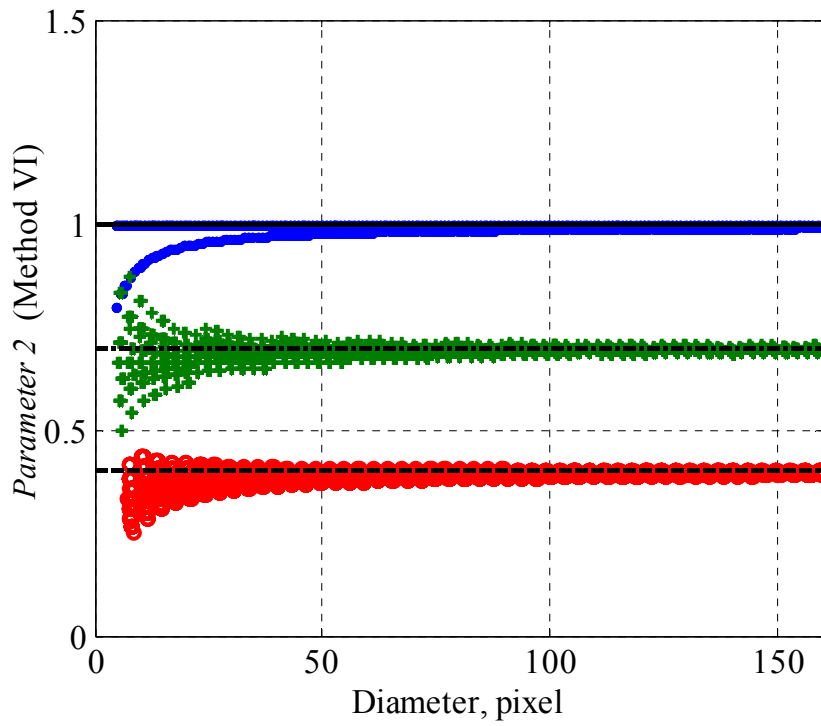


Figure 5-6. Effect of image discretization on shape quantification using Parameter 2.

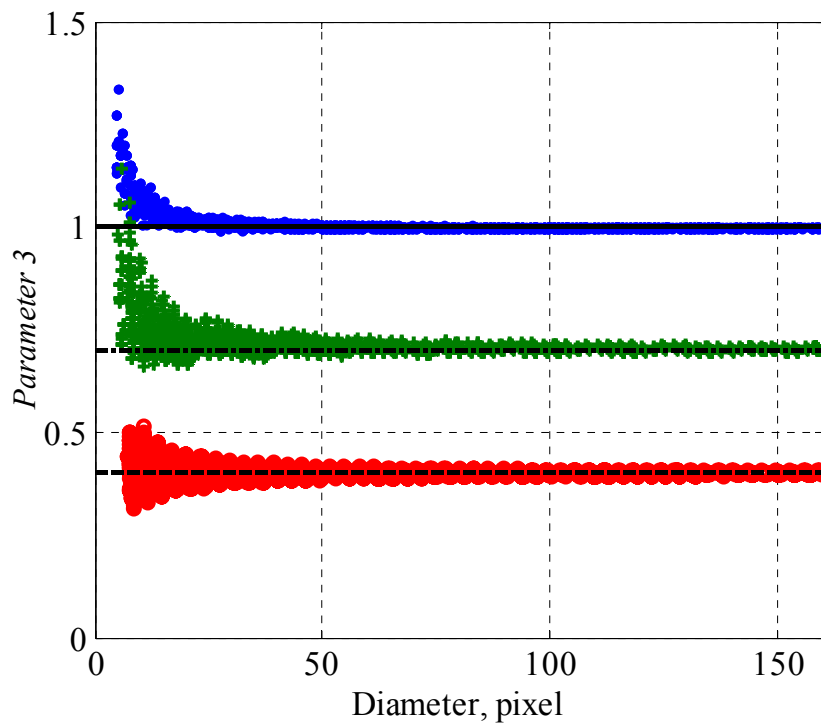


Figure 5-7. Effect of image discretization on shape quantification using Parameter 3.

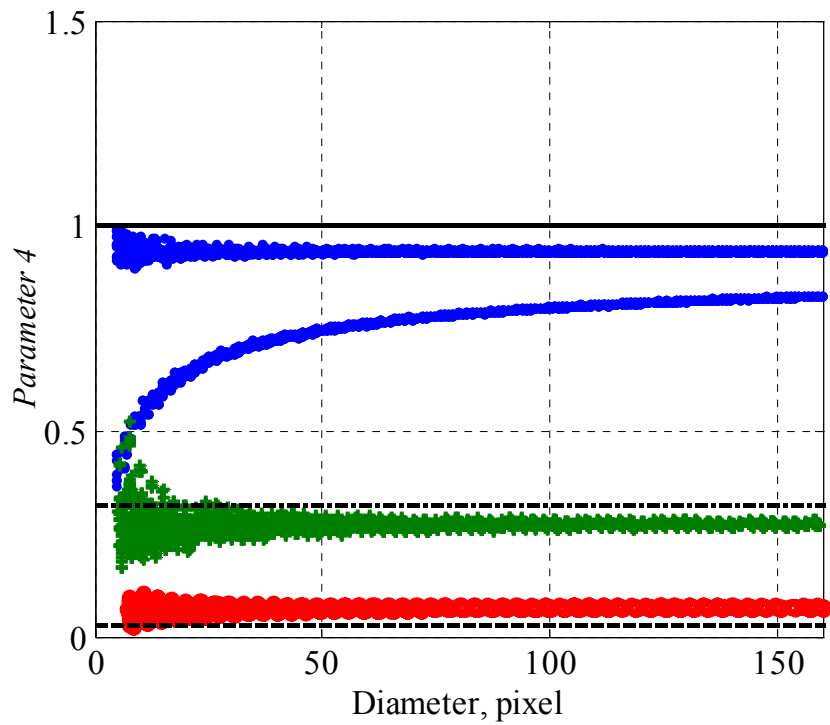


Figure 5-8. Effect of image discretization on shape quantification using Parameter 4.

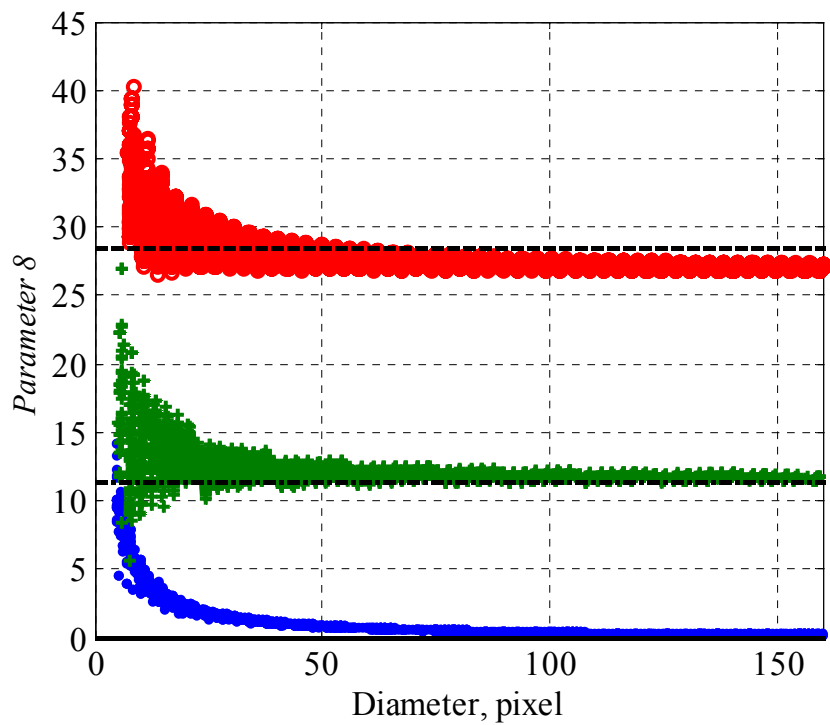


Figure 5-9. Effect of image discretization on shape quantification using *Parameter 8*.

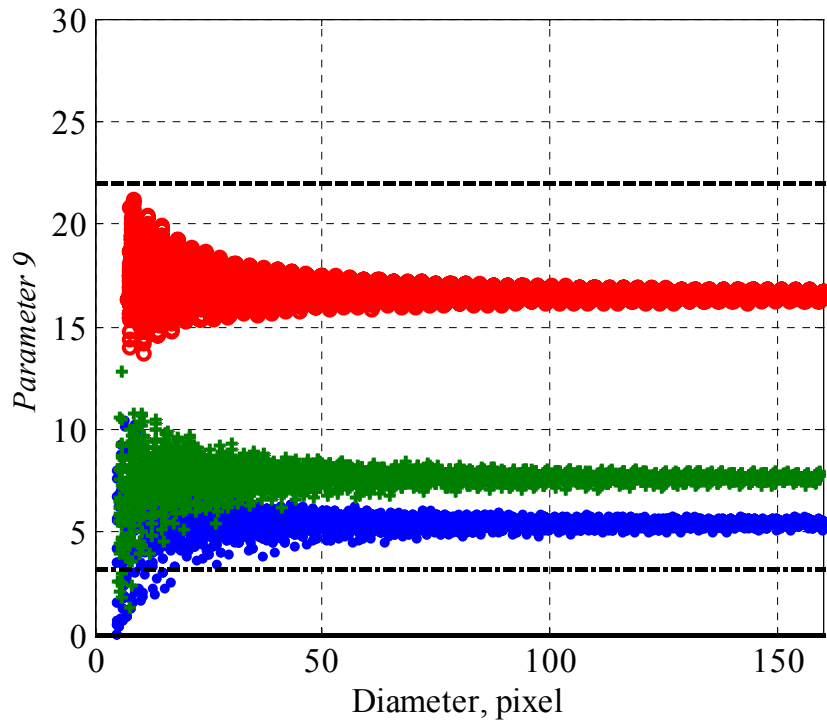


Figure 5-10. Effect of image discretization on shape quantification using Parameter 9.

It has been observed that the spread in data and consequently the image discretization error decreases with increase of the relative size of image/pixel. The error tends to approach zero for the simulated circular discs with increase of diameter for *Parameters 2, 3, and 8*. However, *Parameters 1, 4, and 9* do not approach to their theoretical values even at 160 pixels diameter and a considerable discretization error has been observed. This is due to existence of perimeter in the mathematical definition of these shape parameters. As in Figure 5-4, the discretization error in calculating perimeter does not approach zero with increase of image diameter over the investigated range.

The previous figures demonstrated that the shape parameters have different degrees of sensitivity to shape deviation and image discretization. For example, the obtained values of *Parameter 1* and *9* for small circular and elliptical discs are scattered because of image discretization and are also so close that it is difficult to distinguish between them. *Parameters 4* and *8* are also highly sensitive to image discretization but they are also highly sensitive to shape deviation enough resolution is available to distinguish between

different shapes. Therefore, both the sensitivity to image discretization and shape deviation is important to determine the best shape parameter.

In order to quantitatively express the capability of the shape parameters in distinguishing different shapes and consider both the scatter in data caused by image discretization and also the difference between them a “clearance factor” has been developed. This factor is defined as

$$\frac{0.5 \times [(\max - \min)_{group1} + (\max - \min)_{group2}]}{|\text{mean}_{group1} - \text{mean}_{group2}|} \quad 5-4$$

The terms used in 5-4 are described in Figure 5-11 for groups 1 and 2 which refer to the two groups of the simulated shapes such as the circular discs and 0.7 elliptical discs. The minimum, maximum and mean values are calculated for moving intervals of approximately 10 pixels in diameter of each data group. The (max-min) terms in the numerator express the spread of the data in each group due to image discretization. The denominator expresses the distance between the mean of the two groups of the data which depicts sensitivity to shape deviation. The factor 0.5 is added to the nominator to only consider that portion of the data band which is between the mean values.

If the clearance factor is higher than unity, it reveals that the data for the two considered groups has overlap and it is not feasible to distinguish them. Clearance factors smaller than unity reveal that there is no overlap between the two groups of data. The lower is the clearance factor, the higher is the difference between the data therefore the shape parameter provides higher resolution in distinguishing shape deviation.

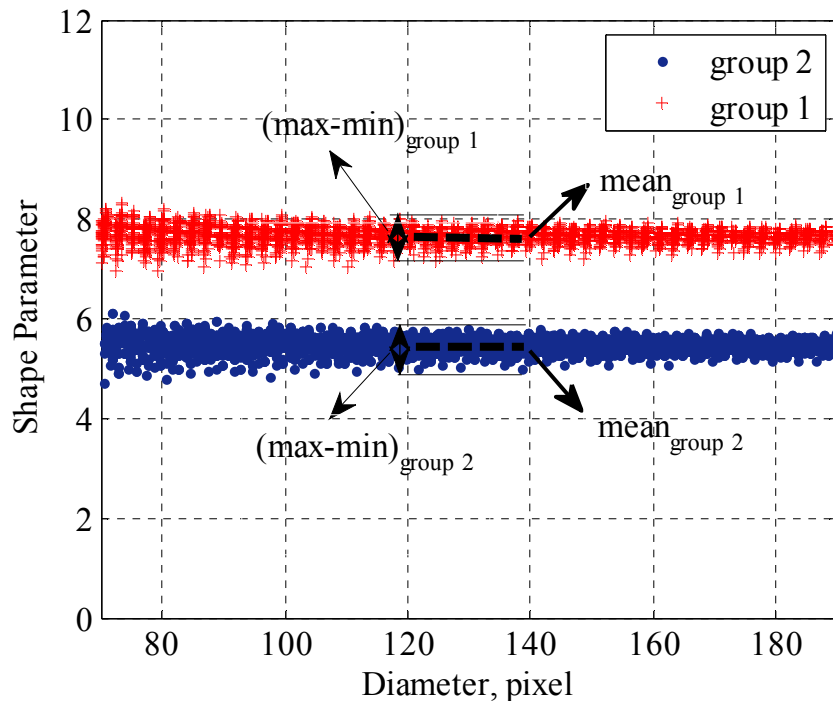


Figure 5-11. Definition of the terms used in the “clearance factor”.

Figure 5-12 shows the clearance factor calculated for the circular discs and the 0.7 elliptical discs. It is observed that for small diameters the clearance factor is high and reduces with increase of diameter. *Parameter 1* and *9* result in clearance factor higher than 1 for diameters smaller than 50 pixels which shows their incapability in distinguishing between the circular and 0.7 elliptical discs. *Parameters 2, 3, 4, and 8* result in lower clearance factor and provide better resolution to discriminate between the investigated shapes. Among them, *Parameter 8* results in the lowest clearance factor and consequently the highest resolution to distinguish between the considered shapes.

The clearance factor calculated for the 0.7 and 0.4 elliptical discs are shown in Figure 5-13. In contrary to the Figure 5-12, the clearance factor values for all the shape parameters at the investigated diameters are less than unity which demonstrates better resolution of these shape parameters for distinguishing highly deviated shapes. It is observed that the clearance factors decrease with increase of diameter. Similar to Figure 5-12, *Parameters 1* and *9* have the highest clearance factor values and result in the lowest resolution in distinguishing the two groups. However, *Parameters 1* and *9* have lower clearance factor in comparison to Figure 5-12 which indicates their higher efficiency in

distinguishing highly deformed objects instead of deviations from circular shape. *Parameter 8* has the lowest clearance factor in Figure 5-13, therefore, the highest resolution among them.

In order to keep the clearance factor lower than 0.25 for *Parameters 2, 3, 4, and 8*, it is suggested to consider a minimum equivalent area diameter of 30 pixels. For *Parameters 1 and 9* which have higher error it is suggested to have at least 100 pixels diameter to keep the clearance factor lower than 0.5. However, these limits depend on the application of the shape parameter and the required accuracy. It is suggested as future work to investigate the capability of different shape parameters in distinguishing droplet shape using experimental images and indicate the required clearance factor for this application.

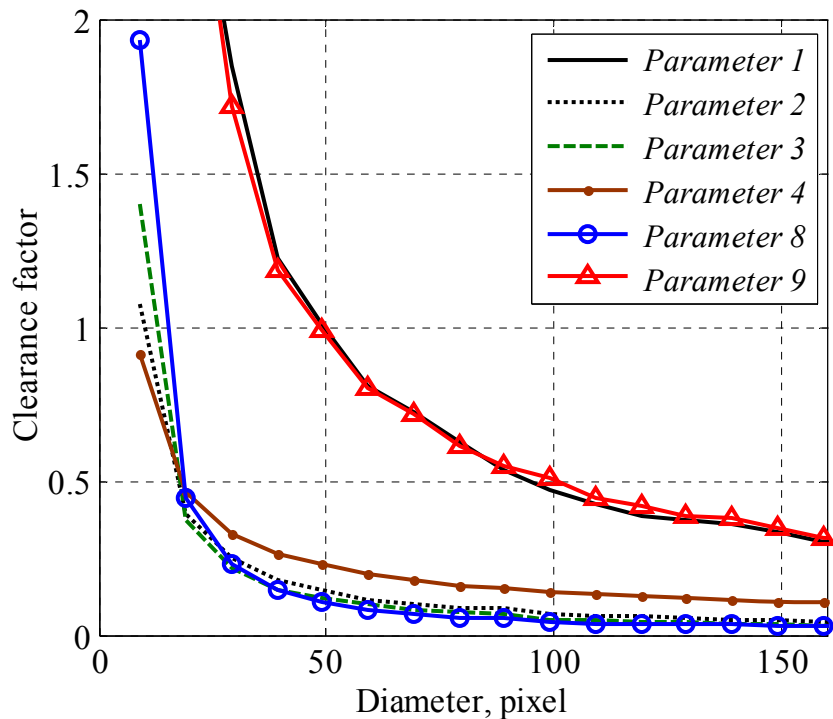


Figure 5-12. The clearance factor expressing the capability of shape parameters to distinguish circular discs and 0.7 elliptical discs.

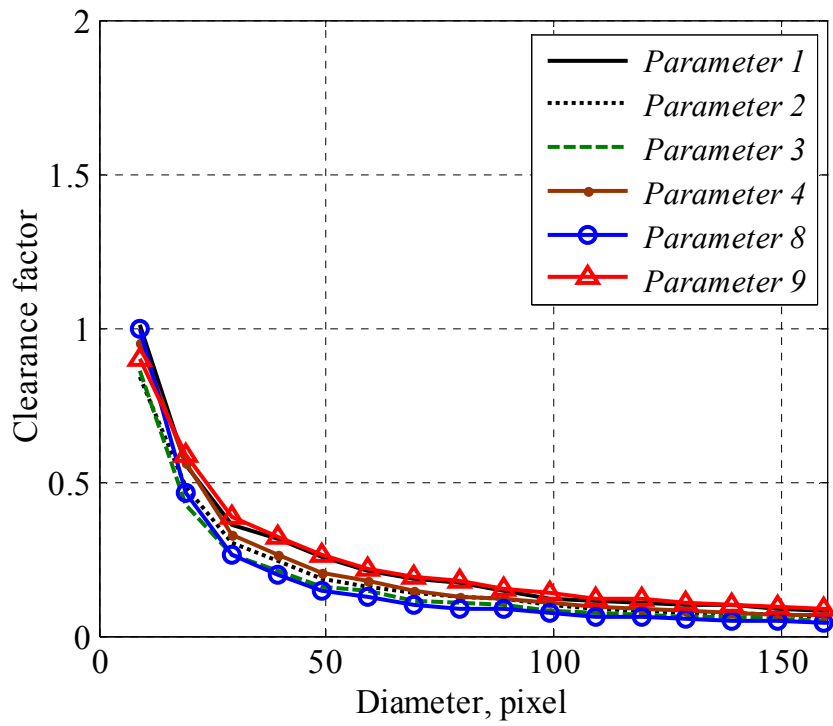


Figure 5-13. The clearance factor expressing the capability of shape parameters to distinguish 0.7 and 0.4 elliptical discs.

5.6. Conclusion

A simulation has been conducted to investigate the effect of digital image discretization in quantifying droplet shape. Digital images have been simulated by generating discretized images of circular and elliptical discs of 0.7 and 0.4 aspect ratios. The simulated images have been generated by varying two factors of size and location of the image relative to the pixels.

The simulation results showed that discretization error considerably affects image area and perimeter calculations. The discretization error decreases toward zero in calculating area with increase of image size. For calculating image perimeter, the discretization error does not approach zero with increase of image size over the investigated range of 5 to 160 pixels area equivalent diameter.

The simulation demonstrated that the shape parameters are influenced by image discretization with different degrees. Generally, discretization effect decreased as the ratio of image size to pixel size increases. Shape parameters which contain the geometric feature of perimeter in their mathematic definition did not approach to their theoretical values and the discretization error remained constant as the images size increased up to 160 pixels area equivalent diameter. The parameters also demonstrated different sensitivity to shape deviation. Some shape parameters introduce relatively low error due to image discretization effect but simultaneously low resolution to distinguish between different shapes. This highlights that both the sensitivity to image discretization and shape deviation should be considered to determine the most efficient shape parameter.

A “clearance factor” has been suggested to rank the parameters based on lower sensitivity to image discretization and higher sensitivity to shape deviation. The lower the clearance factor, the more efficient is the shape parameter for distinguishing shape change. A minimum equivalent area diameter of 30 pixels is suggested for *Parameters 2, 3, 4, and 8* to result in a clearance factor of lower than 0.25. For *Parameters 1 and 9*, it is suggested to have at least 100 pixels diameter to keep the clearance factor lower than 0.5. Results revealed that *Parameter 8* had the lowest clearance factor for a considered diameter and provides the highest resolution in distinguishing shape deviation in the presence of image discretization effect.

6. Evaluation of StereoPIV Measurement of Droplet Velocity in an Effervescent Spray

6.1. Introduction

Successful design and utilization of atomization systems depend on the capability of characterizing the spray structure. One of the fundamental characteristics of the spray structure is the droplet velocity field. Droplet velocity determines the required length for complete evaporation and combustion of droplets in spray combustors [111]. Droplet velocity at the vicinity of chamber wall in diesel engines affects the impingement phenomenon which contributes to the atomization performance and also the exhaust emissions [112]. The flow structure of combustion chambers can also be investigated by characterizing the droplet velocity field [113, 114]. The finish quality in paint sprays is also affected by droplet velocity [115]. In addition, droplet velocity changes deposition and driftability in agricultural sprays [116]. As a result, the need for accurate and fast measurement of spray droplet velocity in various applications has led to the development of several measurement techniques including laser Doppler anemometry (LDA), phase Doppler particle analyzer (PDPA) and particle tracking velocimetry (PTV).

Spatially correlated measurement of a spray velocity field over a plane can reveal important characteristics of the flow such as large-scale turbulent structures, mixing phenomenon, entrainment of ambient air, and transient flow structure [117-121]. One of the systems that can conduct planar measurement of velocity is PIV [36, 38]. In typical applications of PIV, an appropriate number of equal size seeding particles are added to the flow and these are tracked in images using a group correlation algorithm over sub-regions. These seeding particles scatter an equal amount of light and contribute evenly in the velocity field calculations. The PIV system has successfully been applied to

numerous experiments such as flow over airfoils [122], turbulent flows [123], and flow structure in combustion chambers [112-114].

The application of a PIV system to measure droplet velocity in sprays is, however, different from the typical applications of PIV. In the measurement of a spray velocity field using the PIV technique, droplets play the role of the seeding particles. The droplet characteristics of velocity and size depend on the atomizer design and the spatial location within the spray field. Consequently from a PIV processing view point, the spray droplets may not be the optimum choice of seeding particles and may result in different levels of accuracy in the measurement of spray droplet velocity field.

Some of the difficulties in utilization of PIV systems for the measurement of spray velocity have been addressed in the literature. Ikeda et al. [124] and Palero et al. [125] have investigated the applicability of two-dimensional PIV and StereoPIV to spray velocity measurement, respectively. In both works the effect of droplet size spectrum has been investigated through comparison with size-classified droplet velocity measurement using a PDPA. Agreement between the PIV and PDPA measurements has been observed for the velocity of droplets in the 20-30 μm range. Palero and Ikeda [117] used PIV to characterize turbulent mixing zones and recirculation areas within an oil burner spray. Ikeda et al. [126] developed a new PIV data processing algorithm, introduced as multi-intensity-layer PIV, to also provide droplet size information. Palero and Ikeda [127] extended this processing algorithm to StereoPIV and investigated three dimensional velocity vector map of a spray field.

The works discussed in the literature have identified a relatively high error of the PIV measurement at the vicinity of the atomizer nozzle. Droplet velocity at this region is of special importance as it directly affects mechanisms such as droplet breakup and evaporation. The vector plots of Ikeda et al. [124] and contours of Palero et al. [125] reveal disagreement between PIV and PDPA velocity measurement in this region. Palero and Ikeda [127] have also recorded discrepancy between StereoPIV and PDPA size classified velocity measurement at the near nozzle high droplet number density region and suggested investigation of the discrepancy as future works. As a result, a clear understanding of the sources of error involved in the PIV measurement in dense regions of the spray is necessary to extend the measurement range to this area. The literature has

also identified agreement between PIV measurement and the velocity of the 20-30 μm droplets at the far-field of the spray [124, 125]. This conclusion corresponds to a specific spray field with a certain droplet size distribution. Implementation of this as a general conclusion to other sprays and atomization conditions requires further investigation.

The aim of this chapter is to investigate the factors which affect the accuracy of the StereoPIV droplet velocity measurement in a spray field. In order to identify the regions where relatively high error is introduced, a shadowgraph particle tracking velocimetry (Shadow-PTV) has been applied to allow comparison with StereoPIV results. The Shadow-PTV system is an image-based droplet analyzer which provides droplet velocity measurement of individual droplets in a spray field. This system is also suitable for measurement at dense regions because it does not encounter the multi-scattering issue of the laser beam [44] and also measurement is not restricted to the assumption of spherical droplets [128]. In this investigation, the effects of droplet number density, droplet velocity profile, and droplet size spectrum on StereoPIV measurement have been investigated as potential factors that can introduce error in the measurement.

In order to identify the situations in which considerable error is introduced in the StereoPIV droplet velocity measurement, the StereoPIV results are compared with droplet velocity measurement using the Shadow-PTV system. This comparison is conducted along the spray centerline and at three different GLRs. The comparison is followed by investigating the characteristics of the spray field that provide the essential information needed to identify the sources of error in the StereoPIV measurement. The studied characteristics include droplet number density, droplet axial velocity profile, and droplet size distribution. To further elucidate the effect of droplet size distribution, the StereoPIV velocity measurement is also compared with size-classified droplet velocity measurement using Shadow-PTV.

6.2. *The Experiment*

The spray field utilized for this experiment is generated by the effervescent atomizer Mark I. The experiments of this chapter have been conducted at GLRs of 0.054, 0.085, and 0.198. These three different GLRs have been considered to further elucidate the effect of droplet number density. Constant air flow rate of 5 L/min has been applied at standard temperature and pressure of 25°C and 1atm. Water flow rates of 30, 70, and 110 mL/min have been used to vary the GLR to the indicated values. The selected GLRs result in an annulus film of water surrounding the central air stream in the conic area just before the exit nozzle, see Figure 2-5 Detail A. The selection of annular flow regime was based on improved spray quality in terms of smaller droplet SMD [12] and steadiness [26].

The StereoPIV system which has been described in section 3.2 has been implemented in this experiment. In order to generate the laser sheet, the laser beam is passed through a set of two spherical lenses (a telescope) to focus the beam at the center of the field-of-view and is expanded in one dimension using a cylindrical lens. Although an expanded laser beam can be converted to a thinner laser sheet by the spherical lens, the minimum feasible laser sheet thickness is limited by the quality of the initial laser beam [39]. This is characterized by the M^2 factor of the laser [39]. The minimum laser sheet thickness is also obtained only at a small region and the practical thickness is its average over the field-of-view of the PIV system. The laser utilized in this experiment has an M^2 factor of 9 which results in the minimum laser sheet thickness of 0.5mm averaged over the field-of-view [35]. The field-of-view is 50×38mm which results in 36 $\mu\text{m}/\text{pixel}$ magnification. The StereoPIV images have been obtained at 7 consecutive axial locations downstream of the nozzle exit orifice.

In order to provide the necessary data for comparison of the StereoPIV measurement, a Shadow-PTV system has been applied. The Shadow-PTV system is described in section 3.1. The camera captures images of a field-of-view of 237×314 μm with depth-of-field of 50 μm . Measurements have been conducted at 7 axial locations along the centerline and 4 radial locations. The minimum distance of the Shadow-PTV measurement location relative to the nozzle is limited by large ligaments and overlapped droplets which are observed in the Shadow-PTV image of the nozzle vicinity. In this

work, axial positions were located at $z/d = 50, 75, 100, 125, 150, 175,$ and 200 downstream from the discharge orifice. Two of the radial positions were located at $r/d = 3.5$ and 6.1 from the centerline at $z/d = 50$ downstream location. Two other radial points were located at $r/d = 6.1$ and 12.3 across $z/d = 100$. Depending on the droplet density at the selected locations 5000 to 23,000 image pairs have been taken at each investigated location. The number of images at each location has been chosen to record large enough data set to obtain reliable statistical results.

6.3. Comparison of StereoPIV and Shadow-PTV Velocity Measurement

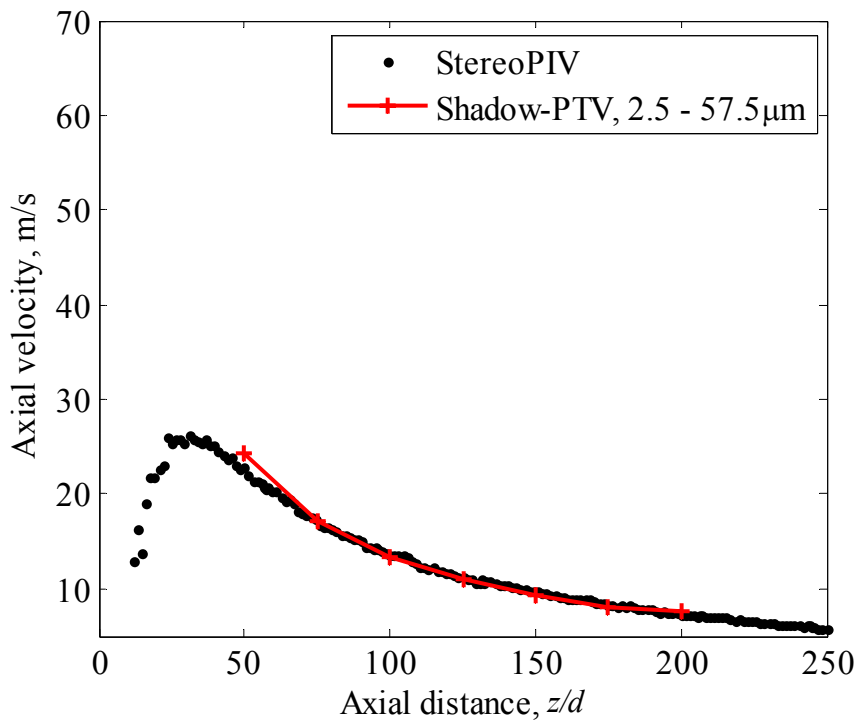
Decay of axial droplet velocity, measured using the StereoPIV and Shadow-PTV systems, is shown in Figure 6-1 for the three different GLRs. The Shadow-PTV data show droplet velocity averaged for all the droplets in the size range of 2.5 - 57.5 μ m. Investigating the Shadow-PTV data shows a continuous reduction in droplet velocity along the spray centerline. In these figures, the rate of droplet velocity reduction along the spray centerline decreases with increase of axial distance. As expected, lower droplet velocity is observed for the higher GLRs as a result of lower liquid flow rates through the nozzle. At $z/d = 50$ droplet velocities are 25, 35, 46 m/s for GLR = 0.198, 0.085, and 0.054, respectively.

The measurement using StereoPIV shows initial increase of droplet velocity close to the nozzle with increase of axial distance. The droplet velocity reaches its maximum at approximately $z/d = 30, 50,$ and 70 in Figure 6-1 (a), (b), and (c), respectively. The slope of this velocity increase is the highest for the lowest GLR of 0.198 in Figure 6-1(a) and decreases with reduction of GLR in Figure 6-1(b) and (c). In addition the maximum velocity at the peak increases with reduction of GLR. Maximum velocities of 26, 29, and 37 m/s are observed for GLR of 0.198, 0.085, and 0.054, respectively. After these peaks, a sharp reduction of droplet velocity followed by a gradual decrease is observed over the range of investigation.

Comparison of the StereoPIV measurement to Shadow-PTV measurement in Figure 6-1 demonstrates that the StereoPIV system under-measures droplet velocity at $z/d < 70$ region. The under-measurement is relatively low in Figure 6-1 (a) for the highest GLR but is amplified for lower GLRs of Figure 6-1 (b) and (c).

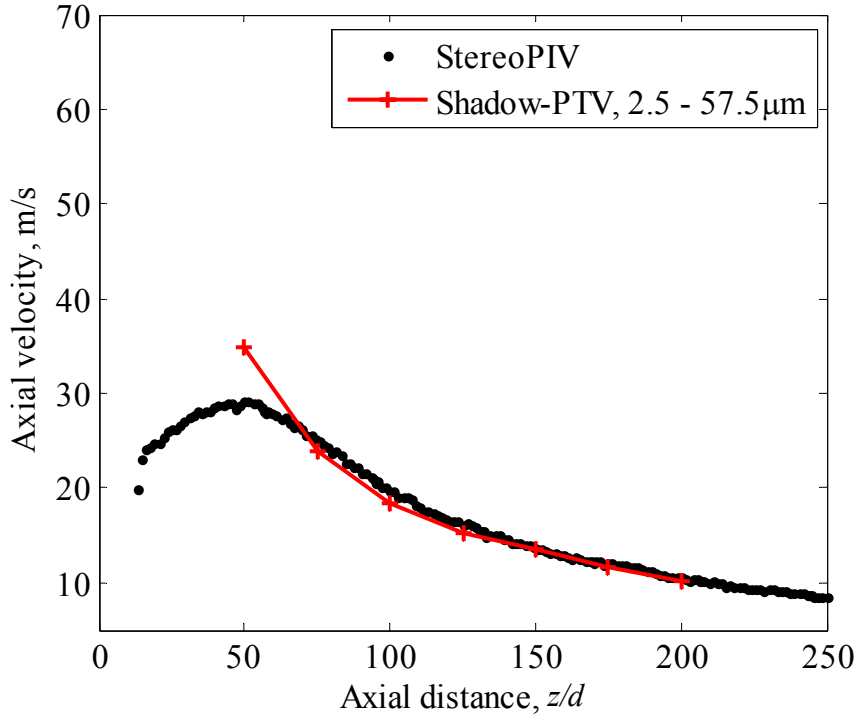
Comparison of the StereoPIV and Shadow-PTV measurements at $z/d > 70$ region of Figure 6-1 (a) shows that the StereoPIV velocity measurement is in agreement with the Shadow-PTV. For the two lower GLRs of Figure 6-1(b) and (c), the StereoPIV velocity is higher relative to the Shadow-PTV. This over-measurement reduces as the axial distance increases and the StereoPIV approaches Shadow-PTV droplet velocity measurement. Agreement between the StereoPIV and Shadow-PTV is observed at $z/d > 150$ and $z/d > 200$ in Figure 6-1(b) and (c), respectively.

Investigation of Figure 6-1 demonstrates that two different types of error have been observed for StereoPIV measurement at $z/d < 70$ and $z/d > 70$. First, under-measurement by StereoPIV at $z/d < 70$ is observed which is shown to be higher for lower GLRs. Second, over-measurement of StereoPIV measurement is observed at $z/d > 70$ for GLR = 0.085 and 0.198. This over-measurement reduces with increase of axial distance resulting in final agreement between the two systems. In order to examine the observed trends of the StereoPIV measurement, the main spray characteristics which can affect the measurement are investigated.

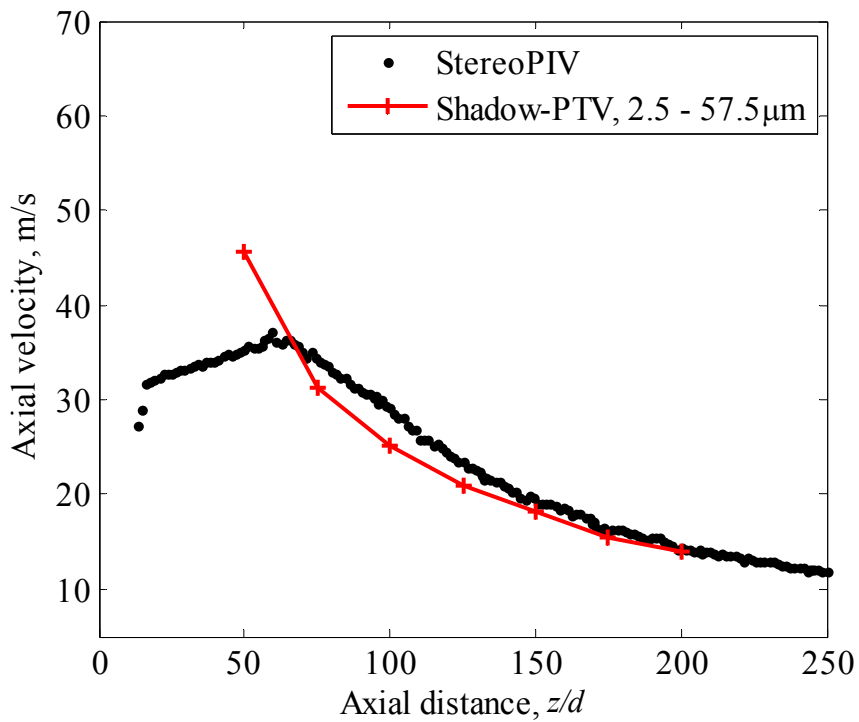


(a)

Figure 6-1. Droplet axial velocity decay along the spray centerline measured by the StereoPIV and Shadow-PTV systems at (a) GLR=0.198 (b) GLR=0.085 (c) GLR=0.054.



(b)



(c)

Figure 6-1. (continued) Droplet axial velocity decay along the spray centerline measured by the StereoPIV and Shadow-PTV systems at (a) GLR=0.198 (b) GLR=0.085 (c) GLR=0.054.

6.4. Effect of Droplet Number Density

Droplet number density in a spray field is a function of the atomizer design and varies throughout the spray field. A sample StereoPIV image at the vicinity of the atomizer nozzle, $z/d = 0 - 40$ is shown in Figure 6-2(a) which demonstrates a dense accumulation of large droplets in this region. In this relatively small region close to the nozzle, the liquid jet disintegrates into ligaments and droplets before dispersing further downstream. Figure 6-2(b) shows a StereoPIV image of droplets at further downstream location of $z/d = 150 - 190$. In this region, a lower number of discrete and relatively smaller droplets are observed mainly due to spread of droplets into a larger volume at the downstream location, and also disintegration and evaporation of droplets.

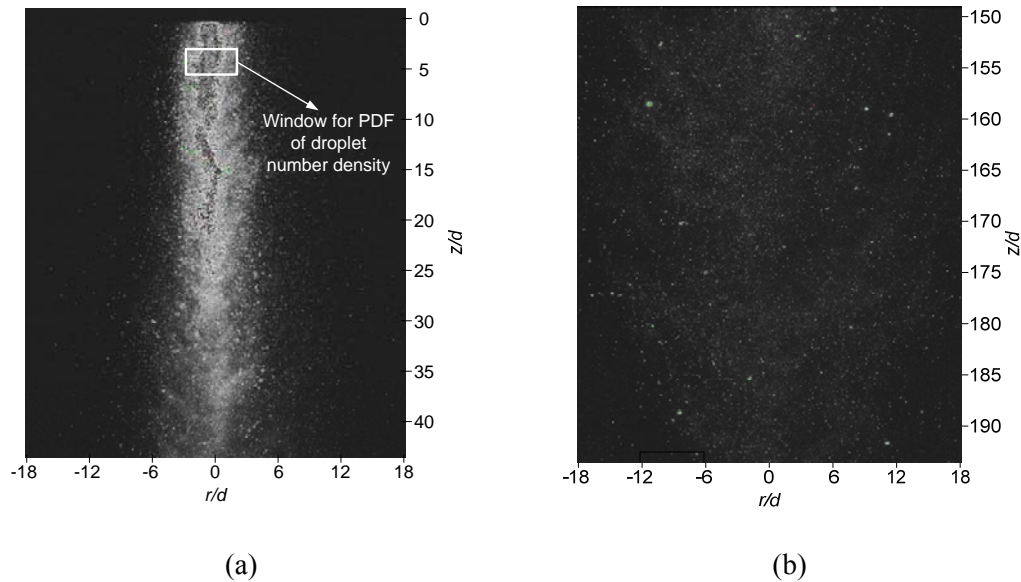


Figure 6-2. StereoPIV image (a) at the nozzle vicinity, $z/d = 20$ (b) at the far field, $z/d = 140$. The images have the same level of gray-scale.

The droplet number density within the flow field can be characterized using images collected with the StereoPIV system. The percentage of the pixels which have intensity higher than 2.45 percent (100 counts) of the maximum count (4096 counts for the 12-bit camera) has been calculated in selected windows of the StereoPIV images. A sample of these windows which have height and width of 50 and 120 pixels, respectively, is shown in Figure 6-2(a). The height is along the z axis and the windows are located symmetrically with respect to the z axis. The results are presented in Figure 6-3 as a

probability density function (PDF) versus axial distance along the spray centerline for the three investigated GLRs.

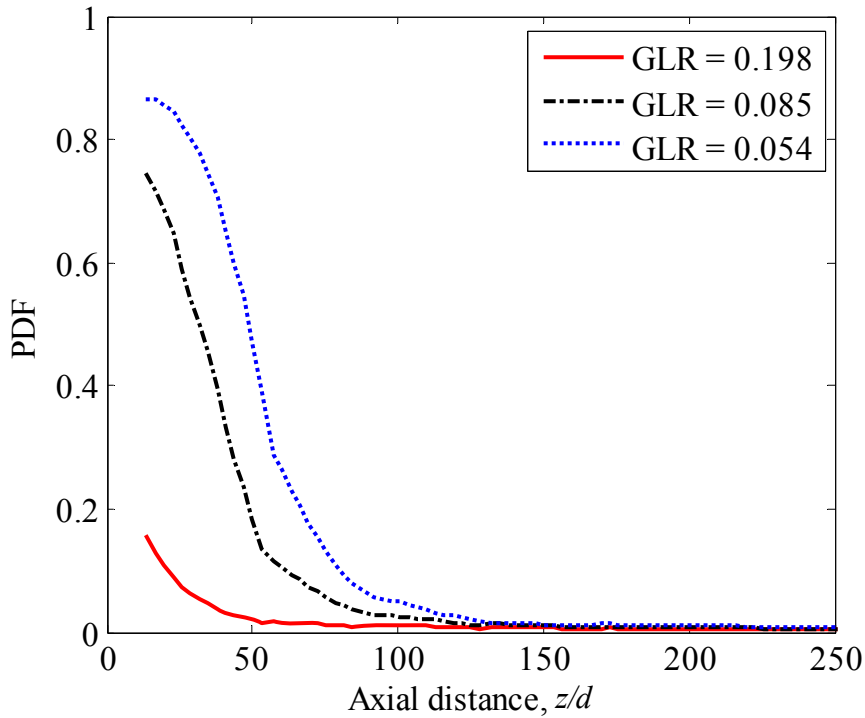


Figure 6-3. PDF of pixels in the StereoPIV images with intensity higher than 2.4 percent of the maximum count along the spray centerline.

It is observed in Figure 6-3 that high PDF values exist at the vicinity of the nozzle. The high PDF values represent high droplet number density in this region which is consistent with the image of cluttered and large droplets of Figure 6-2(a). A drop-off in the PDF values is observed with increase of axial distance which is followed by a region of low PDF values due to disintegration, evaporation, and spread of droplets into a larger volume.

Higher PDF values which depict higher droplet number density are observed at lower GLRs of Figure 6-3. At $z/d = 25$, the PDF values are 0.8, 0.6, and 0.07 for GLR = 0.054, 0.085, and 0.198, respectively. This variation of droplet number density with GLR is non-linear. If regions with PDF higher than 0.05 are considered as the near-field and regions with PDF lower than 0.05 are considered as the far-field region of the spray, locations of $z/d = 30, 80,$ and 100 separate the near-field and far-field regions for GLR =

0.198, 0.085, and 0.054, respectively. This shows that the region of high droplet number density is extended further downstream for the lower GLRs.

The PDF values of Figure 6-3 can be compared to the optimum values for seeding suggested for PIV measurement in the literature. Keane and Adrian [37] have shown that for single-exposure double-frame PIV measurement at least 6 particles per interrogation window are necessary. Raffel et al. [46] have also recommended an optimum particle diameter of approximately 2 pixels. Assuming 6 particles of 2×2 pixels in an interrogation window of 32×32 pixels results in a PDF of 0.023 for optimum size and number density of PIV seeding particles. Investigation of Figure 6-3 shows that the PDF values at the spray near-field is higher than this for three GLRs of 0.054, 0.085, and 0.198 and that the criterion is satisfied at $z/d = 125$, 110, and 45, respectively. Consequently, in the near field of the spray, droplet number density is higher than the optimum density of seeding particle required for the PIV algorithm and this region of extra droplet number density is extended further downstream for lower GLRs. The increased number of seed particles will result in reduction of the accuracy of the PIV processing algorithm. In addition, the high droplet number density at this region generates a significant amount of multi-scattering of the laser sheet which affects out-of-plane resolution of the StereoPIV measurement.

6.5. Effect of Droplet Axial Velocity Radial Distribution

In a PIV measurement, droplet velocity is averaged over the measurement depth-of-field. Therefore, variation of droplet velocity in this volume can affect the accuracy of the results. Droplet velocity profiles in the radial direction are presented to investigate the effect of depth-of-field in the StereoPIV measurement. Radial profiles of droplet axial velocity at two axial locations of $z/d = 50$ and 100 at $GLR = 0.085$ are measured using the Shadow-PTV system. These velocity profiles along with laser sheet half thickness are shown in Figure 6-4. In this figure, $z/d = 50$ is considered to be at the near-field high droplet number density region of the spray while $z/d = 100$ is considered at the far-field low droplet number density of the spray according to the droplet number density plot of Figure 6-3.

It is observed in Figure 6-4 that the peak velocities are 34 and 18 m/s at $z/d = 50$ and 100 respectively and droplets at both near-field and far-field have the highest axial velocity at the spray centerline. As the radial distance from the spray centerline increases, droplet axial velocity decreases. The drop-off in axial velocity with increase of radial distance is higher for $z/d = 50$ in comparison to $z/d = 100$. As a result, droplet velocity in the radial direction has a higher gradient in the near-field than the far-field of the spray.

Averaging droplet velocity over a thick depth-of-field can result in under-measurement of the velocity of the centerline droplets by accounting for the low velocity droplets of radial locations. This highlights the importance of the measurement depth-of-field at the near-field region of sprays where multi-scattering of the laser sheet from high seeding will act to increase the image depth-of-field. The under-measurement reduces in the far-field of the spray because of lower seeding density and also lower droplet velocity gradient in the radial direction. In the far-field, the StereoPIV accuracy is less sensitive to the measurement depth-of-field and a wider depth-of-field introduces less error in comparison to the spray near-field.

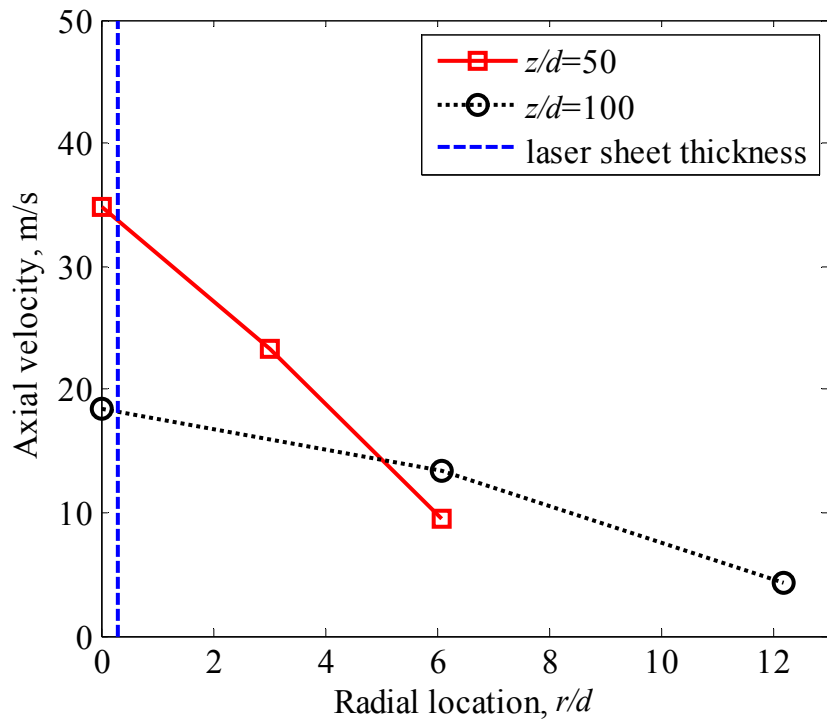
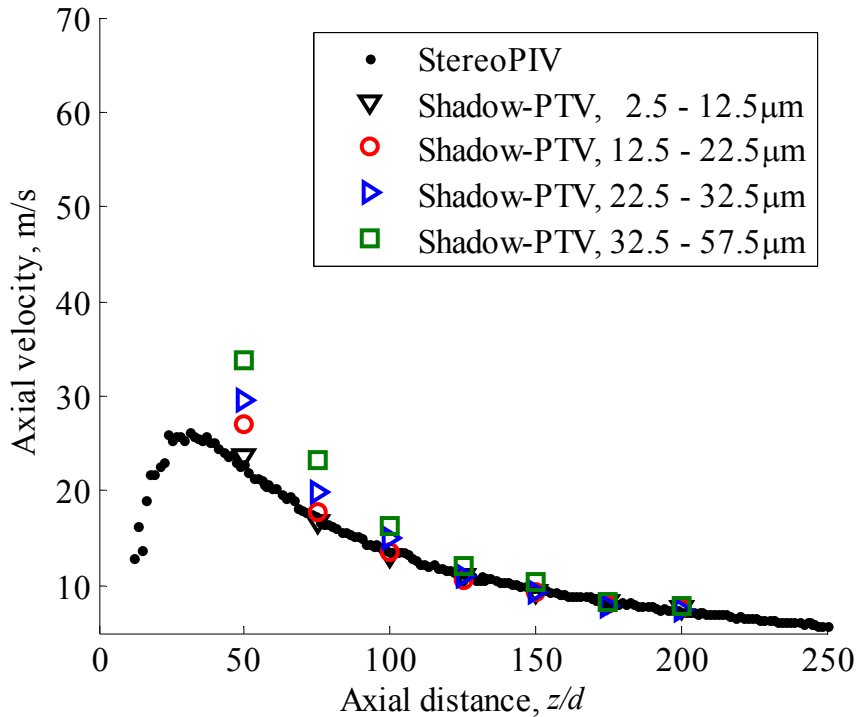


Figure 6-4. Droplet velocity profile at two axial locations for GLR of 0.085. Half of the laser sheet thickness is also shown in this plot.

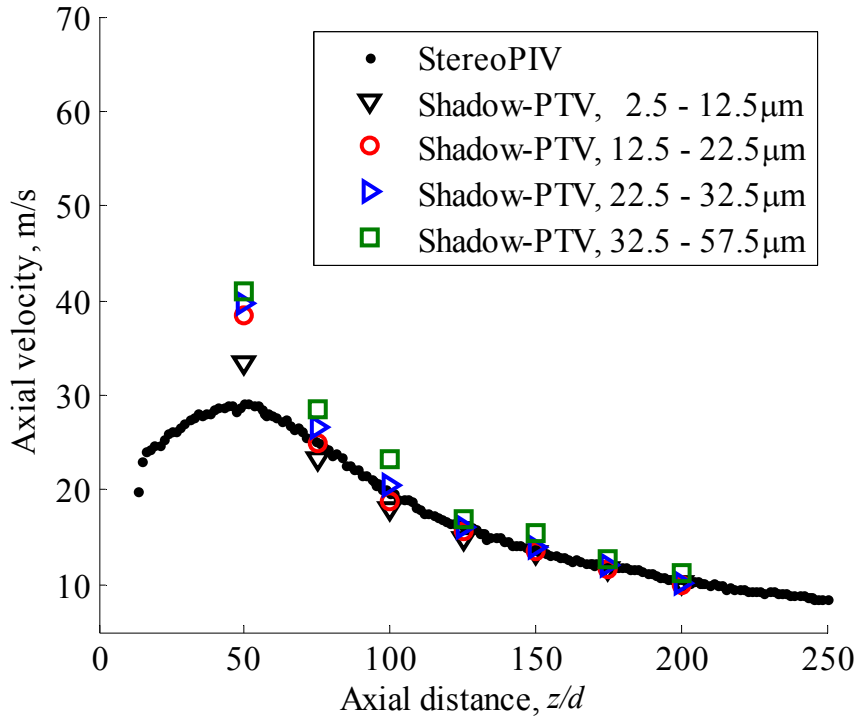
6.6. Effect of Droplet Size Distribution

Droplets of different size and velocity play the role of the seeding particles in the PIV measurement of a spray field. To investigate the effect of droplet size on the PIV measurements, the Shadow-PTV velocity measurement is binned into four droplet size classes of 2.5-12.5, 12.5-22.5, 22.5-32.5, and 32.5-57.5 μm and compared with StereoPIV measurement. The decay of axial velocity of the size-classified droplets measured by the Shadow-PTV along with the StereoPIV are shown in Figure 6-5 (a), (b), and (c) for GLR=0.198, 0.085, and 0.054, respectively. The Shadow-PTV measurement of these figures shows that droplets of different size classes have different averaged velocities and smaller droplets are observed to have lower velocity. This trend is observed more clearly in Figure 6-5 (c) in which, due to higher liquid flow rate the difference between velocities of the four size-classified groups is higher. The size-classified droplet velocities and the difference between them tend to decrease with increase of axial distance as a result of reduction in droplet velocity toward their individual terminal velocity.

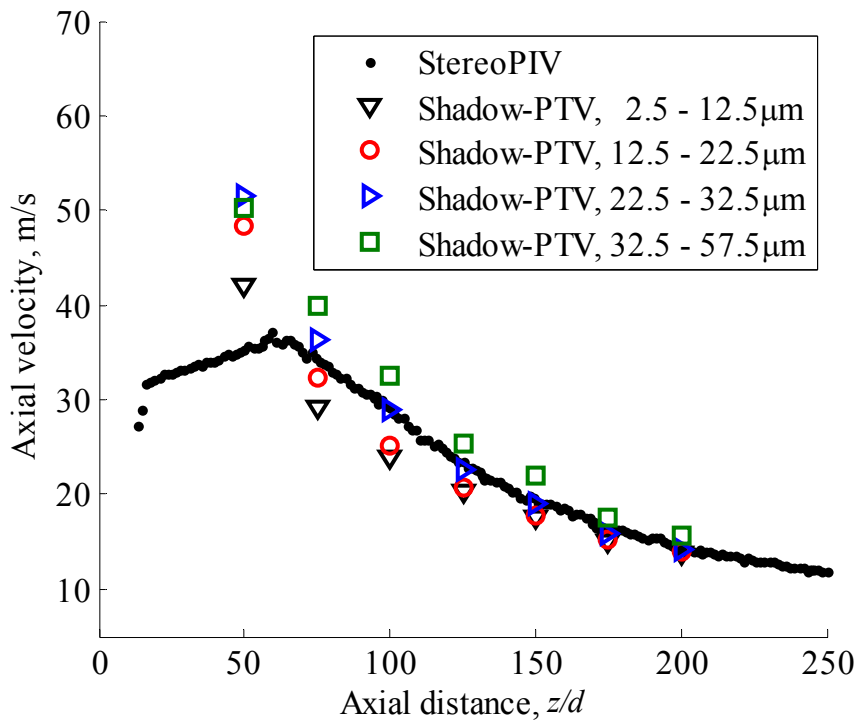


(a)

Figure 6-5. StereoPIV and size-classified Shadow-PTV measurement of axial velocity of spray droplets at (a) GLR=0.198 (b) GLR=0.085 (c) GLR=0.054.



(b)



(c)

Figure 6-5. (continued) StereoPIV and size-classified Shadow-PTV measurement of axial velocity of spray droplets at (a) GLR=0.198 (b) GLR=0.085 (c) GLR=0.054.

It is observed in Figure 6-5(a) that at $z/d = 50$ the StereoPIV measurement is lower than the Shadow-PTV velocity of all the four droplet size-classified groups. With increases of axial distance the StereoPIV velocity measurement increases relative to the Shadow-PTV velocity and at $z/d = 75$ and 100 the StereoPIV measurement is in agreement with velocity of $12.5 - 22.5\mu\text{m}$ size class. At larger axial distances of $z/d = 125$ and 150 agreement is observed with $22.5 - 32.5 \mu\text{m}$ droplets. Investigation of Figure 6-5(b) demonstrates that at $z/d = 50$ the StereoPIV measurement is lower than the Shadow-PTV velocity of all the four droplet size-classified groups. At $z/d = 75$, the StereoPIV measurement is in agreement with $12.5 - 22.5 \mu\text{m}$ droplet size classes. At larger axial distances, the difference between the velocities of the four droplet classes are small, however, the StereoPIV measurement is closer to the velocity of $22.5 - 32.5 \mu\text{m}$ droplet size class. Similar to Figure 6-5(a) and (b), comparison in Figure 6-5(c) shows under-measurement of the StereoPIV relative to the size-classified Shadow-PTV droplet velocity measurement at $z/d = 50$. The StereoPIV measurement increases relative to the Shadow-PTV and falls between droplet velocity of $12.5 - 22.5$ and $22.5 - 32.5 \mu\text{m}$ droplet size classes at $z/d = 75$. At further downstream locations agreement is mostly observed with $22.5 - 32.5 \mu\text{m}$ droplets.

To address the observed bias in the StereoPIV measurement, droplet size distribution has been investigated and data is presented in Figure 6-6(a) - (e). Since in a PIV measurement of a spray field both droplet size distribution and droplet cross-sectional area are influential, in Figure 6-6(a) - (e) both number frequency, N_f , and droplet number frequency times droplet cross section area, $N_f \times A$ have been presented through the left and right vertical axes, respectively. The results for axial distance of $z/d = 75$ for $\text{GLR} = 0.198$, 0.085 , and 0.054 are shown in Figure 6-6(a) - (c), respectively, and the results for $\text{GLR} = 0.054$ at $z/d = 125$ and 175 are shown in Figure 6-6(d) and (e). In these plots, droplets have been categorized into bins of $5\mu\text{m}$ in size which cover droplet diameter of 2.5 to $57.5\mu\text{m}$. To generate the number frequency plots, the number of droplets in each bin has been divided by the total number of droplets. In these plots, mean diameter based on the N_f plots is calculated according to

$$D_{mean, N_f} = \frac{\sum_{i=1}^n (N_f)_i \times D_i}{\sum_{i=1}^n (N_f)_i} \quad 6-1$$

where $(N_f)_i$ and D_i represent droplet number frequency and droplet diameter for a droplet bin. The mean diameter based on Eq.1 is calculated and shown in Figure 6-6 by a circular symbol. Mean diameter based on $N_f \times A$ plot is calculated by

$$D_{mean, N_f \times A} = \frac{\sum_{i=1}^n (N_f \times A)_i \times D_i}{\sum_{i=1}^n (N_f \times A)_i} \quad 6-2$$

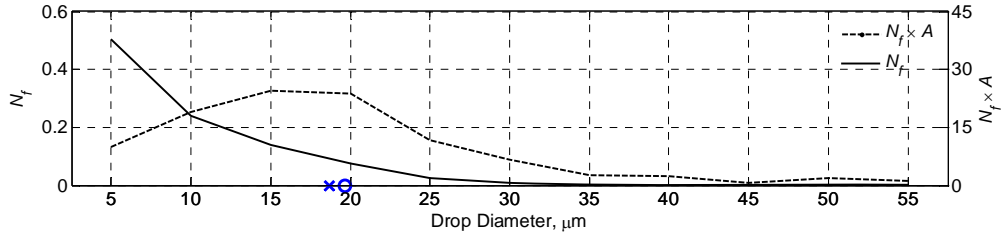
where $(N_f \times A)_i$ represents droplet number frequency times droplet cross-sectional area for a selected droplet bin. The calculated values of mean diameter based on Eq.2 are shown in Figure 6-6 by a cross symbol.

It is observed in the N_f plots of Figure 6-6(a) - (e) that most of the droplets are in the 2.5 - 12.5 size class and in general droplets in the 2.5 - 12.5, 12.5 - 22.5, 22.5 - 32.5, and 32.5 - 57.5 μm have the highest to lowest number frequency, respectively, at the different locations and GLRs. Comparison of Figure 6-6(a), (b), and (c) depicts the negligible effect of GLR variation on droplet size distribution at $z/d = 75$. Only a slight increase of number frequency of droplets in the 2.5 - 12.5 and 12.5 - 22.5 μm classes is observed with reduction of GLR. Figure 6-6(c), (d), and (e) show that increase of the axial distance results in a slight shift of the number frequency plots toward larger droplets. With increase of axial distance, number frequency of droplets in 2.5 - 12.5 μm range reduces and number frequency of the droplets in the other size classes of 12.5 - 22.5, 22.5 - 32.5 and 32.5 - 57.5 μm increases. Therefore, the presence of most of the droplets in the size class of 2.5 - 12.5 μm does not address the StereoPIV relative agreement with the 12.5 - 22.5 or 22.5 - 32.5 μm droplets at $z/d \geq 70$ of Figure 6-5(a)-(c).

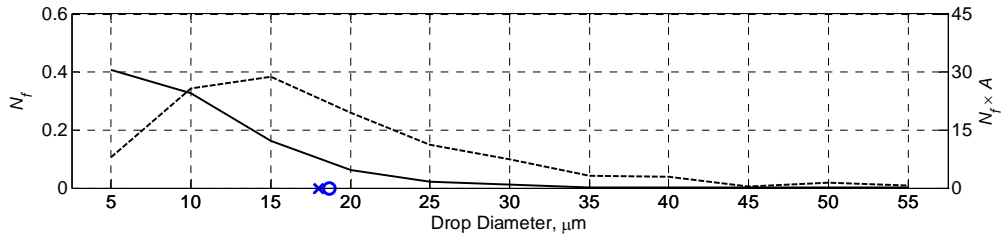
The mean droplet diameter based on N_f in Figure 6-6(a), (b), and (c) are 19.6, 18.7, and 19.3 μm , respectively, which show negligible change of droplet mean diameter with GLR variation. This is explained through the concept of a “tree” regime, introduced by Santangelo and Sojka [19], which describes the atomization mechanism of effervescent atomizers at high GLRs. In this concept the liquid exits the nozzle as a short annular jet or “trunk” with a number of attached limbs. The change in the flow structure, which is

mainly in terms of the length of the liquid trunk, at these high GLRs is small and consequently droplet mean diameter remains constant over a range of GLRs [19]. The mean droplet diameter based on N_f in Figure 6-6(c) - (e) is 19.3, 23.9, and 28.0 μm , respectively. This trend shows increase of droplet mean diameter based on N_f with increase of axial distance which has been attributed to droplet evaporation, entrainment of larger droplets from radial locations and droplet coalescence [21].

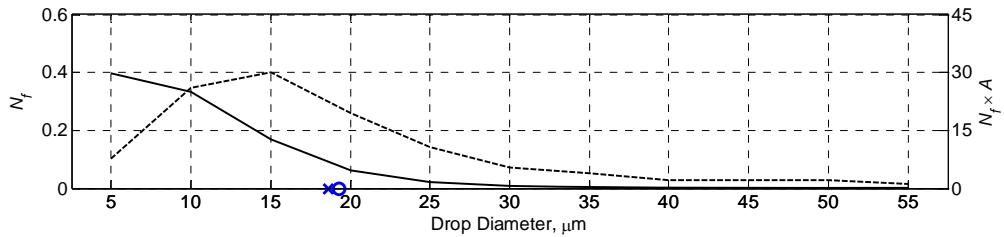
It is observed in Figure 6-6(a) - (c) that the $N_f \times A$ peak is at the 12.5 - 22.5 μm droplet group for the considered GLRs. The mean diameter based on $N_f \times A$ is also approximately located at 18 μm . Hence, negligible change in the location of the $N_f \times A$ peak and mean diameter based on $N_f \times A$ has been observed at $z/d = 75$ with GLR variation. The $N_f \times A$ plot of Figure 6-6(c) which corresponds to $z/d = 75$ and $\text{GLR} = 0.054$ shows that the 12.5 - 22.5 μm droplet group has the highest $N_f \times A$. The mean diameter based on $N_f \times A$ is also located at 18.6 μm . At $z/d = 125$ and $\text{GLR} = 0.054$, the $N_f \times A$ plot of Figure 6-6(d) shows that the highest $N_f \times A$ value has shifted toward larger droplets, however, the peak is still at 12.5 - 22.5 μm droplet class and the mean $N_f \times A$ is located at 22.8 μm . With further increase of axial distance to $z/d = 175$ of Figure 6-6(e) the $N_f \times A$ peak is at the 22.5-32.5 μm droplet group and the $N_f \times A$ mean diameter is located at 26.5 μm . Therefore, the location of the $N_f \times A$ peak and the mean diameter based on $N_f \times A$ have shifted toward larger droplets with increase of axial distance.



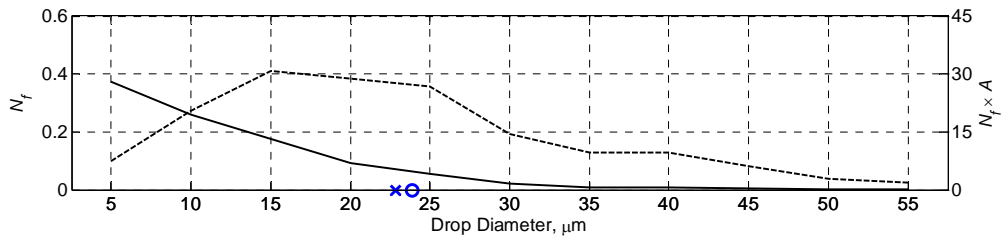
(a) GLR=0.198 and $z/d=75$.



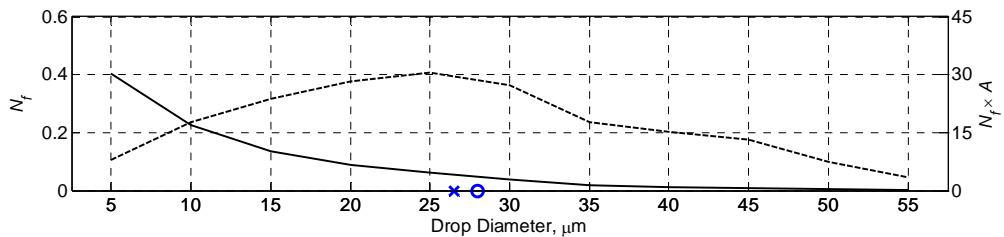
(b) GLR=0.085 and $z/d=75$.



(c) GLR=0.054 and $z/d=75$.



(d) GLR=0.054 and $z/d=125$.



(e) GLR=0.054 and $z/d=175$.

Figure 6-6. N_f and $N_f \times A$ at different GLRs and locations along the spray centerline. The cross sign (\times) shows the mean diameter based on the $N_f \times A$ plot and the circular sign (\circ) shows the mean diameter based on N_f .

It has been observed in Figure 6-5(a) that at $z/d = 75$ the StereoPIV measurement is relatively close to the velocity of 12.5 - 22.5 μm droplet size class. This is consistent with the location of the $N_f \times A$ peak which is at 12.5 - 22.5 μm droplet size class and also the mean droplet diameter based on $N_f \times A$ and N_f which is at 18.7 and 19.6 μm , respectively, in Figure 6-6(a). At $z/d = 75$ of Figure 6-6(b), agreement is observed between StereoPIV and Shadow-PTV measurement of 12.5 - 22.5 μm droplet size class. This bias is also supported by the evidence of the highest $N_f \times A$ at 12.5 - 22.5 μm droplet size class and the mean diameter based on $N_f \times A$ and N_f which is at 18.0 and 18.7 μm , respectively, in Figure 6-6(b). The Shadow-PTV size classified measurement at $\text{GLR} = 0.054$ of Figure 6-5(c) showed that the StereoPIV falls between 12.5 - 22.5 and 22.5 - 32.5 μm size classes at $z/d = 75$ and agrees with 22.5 - 32.5 μm at $z/d = 125$ and 175. Again this bias can be justified by the location of $N_f \times A$ peak. The bias is also in agreement with the mean diameter based on $N_f \times A$ which is at 18.6, 22.8, and 26.5 μm and mean diameter based on N_f which is at 19.3, 23.9, and 28.0 μm in Figure 6-6(c), (d), and (e), respectively. Therefore, the bias in the StereoPIV measurement can be estimated using the location of the $N_f \times A$ peak and also the mean droplet diameter based on $N_f \times A$ and N_f .

In summary, it has been observed in Figure 6-5 that the StereoPIV system under-measures droplet velocity at $z/d = 50$ in comparison to all the four size-classified droplet groups. This is similar to what has been observed in Figure 6-1 from comparison of StereoPIV and Shadow-PTV results averaged over all droplet sizes. As explained in the last section, this under-measurement is due to averaging droplet velocity over a thick depth-of-field which results in accounting for the low velocity droplets at the radial locations. At $z/d > 70$, it has been observed that the StereoPIV measurement is biased toward 12.5 - 22.5 and 22.5 - 32.5 μm droplet size classes. This bias in the StereoPIV measurement can be addressed using the $N_f \times A$ plots presented in Figure 6-6 and the resolution of the StereoPIV cameras. Magnification of the StereoPIV setup is 36 $\mu\text{m}/\text{pixel}$ and the scattered light of the small droplet groups would spread over a single pixel area. As a result, the smallest droplets which are present in the 2.5 - 12.5 μm droplet size class will have considerably lower intensity peak and lower weight in the StereoPIV processing algorithm. Results also showed that this bias can be estimated using the mean droplet diameter based on $N_f \times A$ and N_f .

6.7. Conclusion

In this chapter, the effect of main characteristics of spray droplets which play the role of seeding particles in StereoPIV measurement on the accuracy of the spray droplet velocity measurement has been investigated. The spray measurement of droplet velocity has been compared with Shadow-PTV measurement to identify the regions where relatively high error is introduced. The StereoPIV and Shadow-PTV results have been used to investigate the effect of droplet number density, droplet velocity profile, and droplet number frequency. The investigation has been carried out at both dense and dilute regions of the spray and also at three different GLRs.

In the near-field dense spray region of $z/d < 70$, StereoPIV system under-measures the droplet velocity in comparison to Shadow-PTV measurement. This under-measurement is exacerbated by increasing the spray liquid flow rate which results in higher droplet number density. High droplet number density at this region causes multi-scattering of the laser sheet and the measurement would be the average over a wider depth-of-field. This wide depth-of-field will include the droplets outside the integration volume which have lower velocity than the centerline droplets. Therefore, StereoPIV measurement at the near-field region of the spray is limited by (1) wider measurement depth-of-field and (2) higher droplet velocity gradient in the radial direction. Since it is difficult to prevent the scatter of the laser sheet at high droplet number density regions of the spray field, use of lenses with thin depth-of-field is suggested to restrict the measurement to the desired region and obtain more accurate results.

The StereoPIV under-measurement reduces with increase of axial distance and disappears at around $z/d = 70$. With increase of axial distance, the spray becomes dilute and droplet number density decreases. This results in reduction of multi-scattering of the laser light and thinner image depth-of-field. In addition, lower droplet velocity gradient toward radial direction exist at the spray far-field. The alleviation of these two factors results in a decrease of the StereoPIV under-measurement.

In the far-field dilute region of the spray, the StereoPIV over-measures droplet velocity in comparison to Shadow-PTV measurement of 2.5 - 57.5 μm droplet size class. Comparison to the size-classified measurement also reveals that it is generally biased toward the 12.5 - 22.5 and 22.5 - 32.5 μm droplet size classes depending on the axial

location. This bias is due to the droplet/pixel size ratio and also the combined effect of droplet number frequency and droplet cross-sectional area. If a droplet is considerably smaller than the area viewed by a single CCD pixel, the scattered light of the droplet would spread over the pixel which results in lower intensity peak and consequently lower weight for that droplet in the StereoPIV processing algorithm. The droplet number frequency times droplet cross-sectional-area, $N_f \times A$ plots, also demonstrated that the 12.5 - 22.5 and 22.5 - 32.5 μm droplets have the best combination of droplet number frequency and cross-sectional area at $z/d = 75$, 125 and $z/d = 175$, respectively. The StereoPIV measurement would be biased toward the droplet mean diameter based on $N_f \times A$ at the far-field dilute region of the spray.

7. The Effect of Gas-Injector Location on Bubble Formation in Liquid Cross-Flow

7.1. Introduction

The capability to generate and maintain a mixture of micro-size bubbles in a liquid flow is an essential process in many applications such as medical, heat exchangers, chemical plants, biological fluids, and wastewater treatment. Artificial oxygenators are used during open heart surgery to inject micro-size oxygen bubbles into blood using a gas sparger [129]. Heat exchangers apply two-phase flows as an effective means for thermal transport in power plants [130] and spacecrafts [131]. In the processes of refining molten metals, argon gas is injected for liquid stirring, and avoiding reoxidization and clogging [132, 133]. In wastewater treatment aeration systems are used to deliver oxygen to micro-organism metabolism [134]. In relation to this thesis, the generation of a population of micro-size bubbles was of interest for application in effervescent atomizers [9]. In all of these applications, the size of the generated bubbles affects the total area of the gas-liquid interface and consequently affects the mixing and mass transport processes. Hence, the generation of smaller bubbles in a controlled fashion is a critical process in many industrial applications which has drawn considerable attention.

Several techniques have been introduced to generate micro-bubbles. Micro-fluidic techniques such as capillary flow focusing [135 - 137] and T-shaped microchannels [137, 138] have the potential to produce micro-size bubbles. However, these devices require significant scale-up or multiplexing in order to be applied to industrial applications. A common method in industrial applications is gas injection from an orifice(s) into the liquid flow. Gas injection from an orifice can be conducted in different configurations which significantly affects the characteristics of the generated bubbles [138]. The

direction of the nozzle with respect to the flow can be varied to result in co-flow, cross-flow, or counter-flow configurations. The nozzle can be submerged from top, bottom, or side of the channel. The nozzle outlet can be flush aligned with the wall (wall injection) or submerged into the liquid (nozzle injection) [131]. The orientation and the size of the nozzle can also be different.

Among the different configuration of bubble generation from an orifice, gas injection into liquid cross-flow has been proved to generate the smallest bubbles [139, 140]. It is also hypothesized that in this configuration the bubbles are swept away from the vicinity of the nozzle and the probability of bubble coalescence is reduced [138, 139]. This configuration can also be applied to different scenarios because a bulk liquid motion is typically present in most industrial applications such as distillation columns, floatation cells, and aerated stirred tanks.

There has been a number of experimental works which have investigated bubble formation during gas injection into liquid cross-flow. Maier [140] first showed that in order to obtain the smallest bubbles the direction of air injection should be normal to the liquid cross-flow. Sullivan et al. [141] have investigated the formation of gas bubbles in a laminar horizontal liquid flow using nozzles of 1.59 to 3.18 mm in diameter which were submerged 76.2 mm (3") into the liquid. Tsuge and Hibino [142] used a submerged nozzle configuration and showed that smaller bubbles are obtained at higher liquid flow rates and lower gas flow rates. Forrester and Rielly [143] have investigated bubble formation during gas injection from an orifice located on different blade sections. Nahara and Kamotani [131] have investigated bubble formation from a wall orifice into liquid cross-flow at both normal and reduced gravity. Bai and Thomas [133] also investigated the effect of several parameters such as liquid velocity, gas injection flow rate, injection hole diameter, and gas composition on the bubble formation process. Zhang and Tan [144] studied liquid weeping phenomenon during gas injection from a wall orifice. Loubiere et al. [134] used a flexible membrane sparger to inject the gas phase into the liquid cross-flow.

Few analytical models for bubble formation in liquid cross-flow have also been developed in the literature. The models typically use a force-balance equation of the involved forces to model the process. These models which are extended from those

developed for bubble formation in stagnant liquids incorporate an additional term for the drag force due to liquid cross-flow [133, 145]. The drag force is calculated by estimating the average velocity across the channel [139, 144, 146, 147], the superficial velocity [148], the velocity profile across the channel [131, 133], or the liquid velocity at a specific height above the orifice [141].

It is essential in the design of two-phase gas-liquid systems to clarify the effects of the various parameters so that the bubbles are generated in the desired size range and maintain that throughout the process. The formation of bubbles during air injection from a wall orifice or an injection nozzle are both influenced by the shear force of the cross-flow, however, they differ in some important respects. In the wall orifice configuration, the bubble initial formation steps occur within the boundary layer. The bubble motion is also restricted by the wall and its surface may touch the wall [131, 133]. In contrast, for the nozzle injection configuration, the bubble formation can be affected by the change in the liquid velocity field due to the intrusion of the nozzle injector.

There are some gaps in the previous experimental investigations on bubble formation in liquid cross-flow. The investigations have been conducted using both the wall orifice [131, 133, 134, 140, and 144] and the nozzle injection [141, 142] configurations. However, these experiments have been conducted at different conditions which prevent the comparison between the two air injector configurations.

A number of the previous works calculated average bubble size based on the measurement of gas flow rate and bubble frequency [141, 142, and 144]. The other works have measured the size of the individual bubbles but they have only recorded the average size [131, 133] or the minimum and maximum of the bubbles size [134]. Bubble size distribution is of considerable importance in most industrial applications since not only the average size but also the size distribution should be in the required range. It also provides evidence on the formation mechanism of the bubbles.

The developed analytical models typically use empirical parameters which make them limited to a specific condition. The models are also based on the assumptions of (a) uniform, inviscid and irrotational liquid cross-flow and (b) the bubbles flow away from the injector and have no effect on the other bubbles [144, 147]. These assumptions need

further investigation for the nozzle injector configuration. The intrusion of the nozzle injector can disturb the liquid flow field and invalidate the assumptions.

In this chapter, bubble generation via gas injection from the two configurations of wall orifice and nozzle injection is experimentally investigated and compared. Bubble size, shape and velocity and also the liquid velocity field is simultaneously measured using a backlight imaging technique followed by PIV and PTV processes. The results also enhance the understanding of the bubble formation in liquid cross-flow and provide the experimental backup required to improve the available analytical models of bubble formation in liquid cross-flow.

7.2. The Experiment

The micro-bubble generator which is described in section 2.2 has been used in this experiment. The experiment has been conducted at liquid flow rate of 1,400 ml/min and gas flow rate of 4 ml/min. The micro tube has OD and ID of 0.02 and 0.01 inch, respectively. The tip of the micro-tube has been located at four positions of: $x/w=0$ (wall orifice) and $x/w=1/6$, $1/3$, and $1/2$ (nozzle injection).

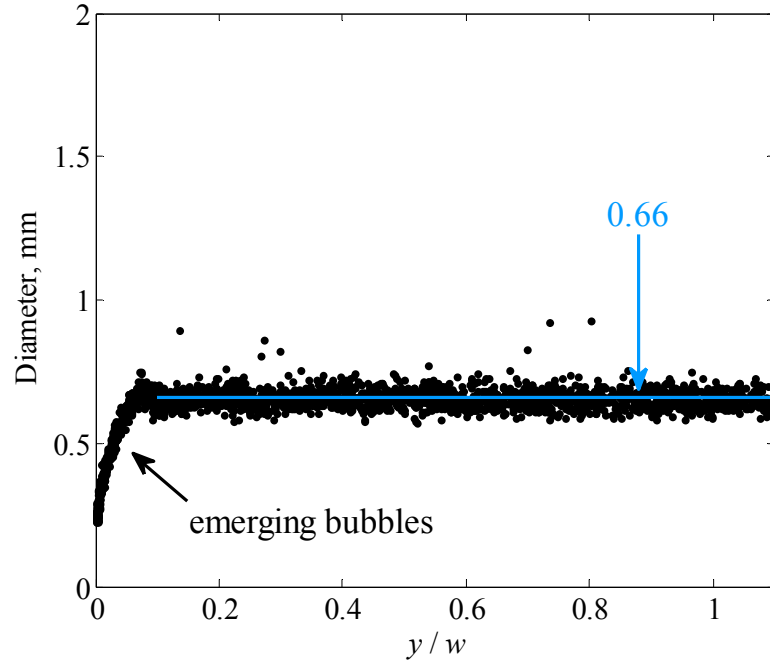
The Shadow-PIV/PTV technique has been applied to measure the size, shape, and velocity of the generated bubbles and also the liquid field velocity. This technique is described in section 3.3. The lens configuration has been set to a field-of-view of 8.44×6.29 mm and magnification of $6.1 \mu\text{m}/\text{pixel}$. Image acquisition has been conducted at the vicinity of the micro-tube. A set of 500 double-frame images have been recorded for each nozzle configuration.

7.3. Bubble Size

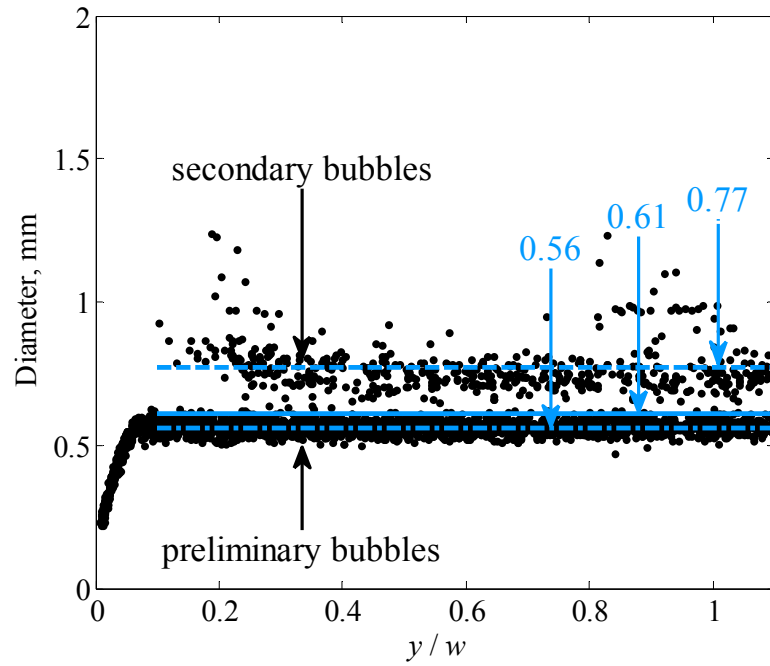
Data of the bubble size measurement for the different nozzle positions obtained by the PTV process are plotted in Figure 7-1 as bubble diameter versus the y/w location of the centroid of the bubble image. The data are ensembles of the size and location of the bubbles detected in each image set. The tip of the air injector tube is located at $x/w = 0, 1/6, 1/3,$ and $1/2$ across the channel in Figure 7-1(a), (b), (c), and (d), respectively. In all the figures, a sharp increase in bubble size from the location of the air injector, $y/w = 0$, is observed. The increase in bubbles size continues till approximately $y/w = 0.05$ where the bubbles size becomes constant. These bubbles are termed “emerging” bubbles and are highlighted in Figure 7-1(a). The emerging bubbles correspond to the partial appearance of bubbles from the tip of the air injector tube. As the bubbles emerge from the nozzle they continue to grow until they pinch-off and become separated. The data show separation at about $y/w = 0.07$ and $y/w = 0.05$ for the wall orifice and the nozzle injection configurations, respectively.

The average bubble size over the axial range of $y/w = [0.1 \ 1.1]$ is 0.66 in Figure 7-1(a) which corresponds to the wall orifice configuration. The average bubble size is 0.61, 0.60, and 0.60 in Figure 7-1(b), (c), and (d), respectively, which correspond to the nozzle injection configuration. Therefore, the average bubble size is larger for the wall orifice configuration. The variation in the average bubble size is also negligible for the air injector locations of $x/w = 1/6, 1/3,$ and $1/2$.

The size distribution of the bubbles in Figure 7-1(a) shows a single group of data. This group consists of bubbles with relatively uniform size distribution along the axial distance. The data of Figure 7-1(b), (c), and (d) show two distinct groups of bubbles. One of the groups consists of smaller bubbles with relatively uniform size distribution. The other group consists of larger bubbles with more scatter in the data. These two groups of small and large bubbles are called “preliminary” and “secondary” bubbles in this chapter and are specified in Figure 7-1(b).

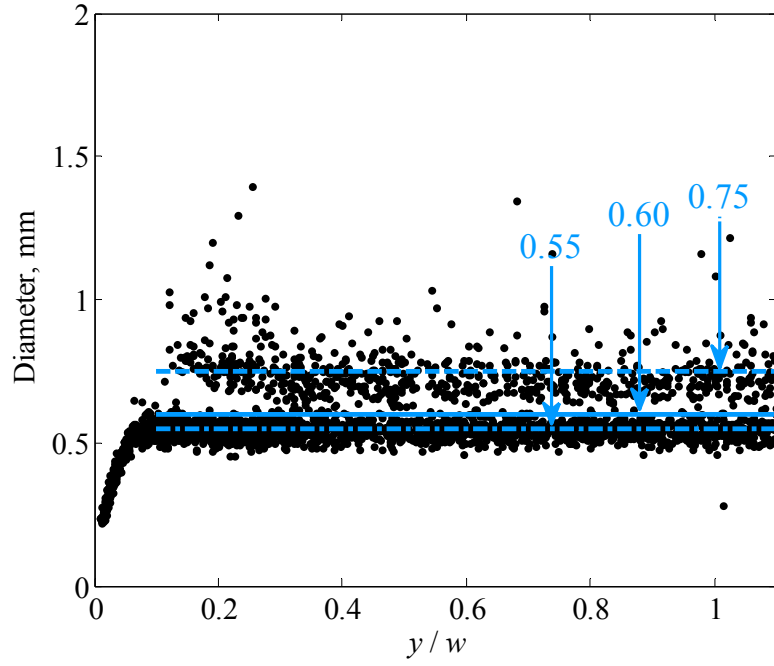


(a)

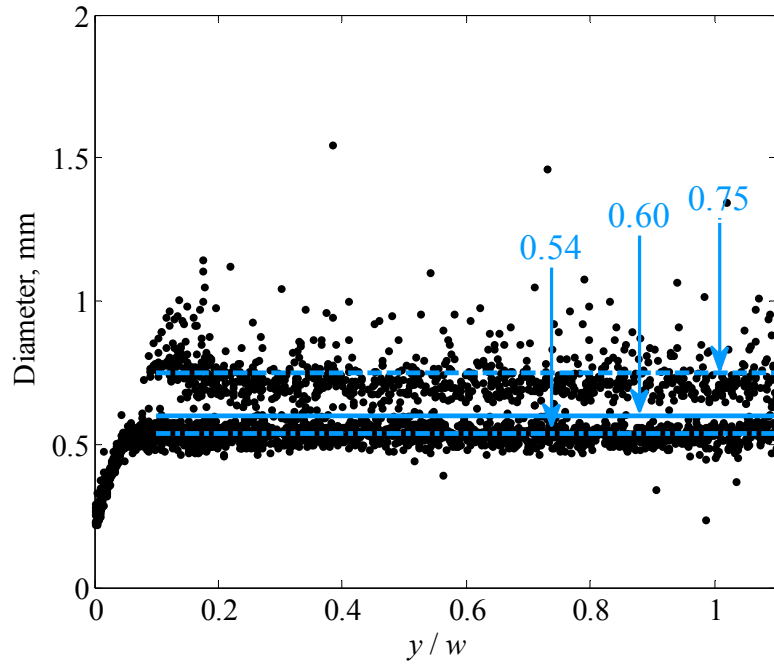


(b)

Figure 7-1. Bubble size versus y distance for four different location of the air injector tip of (a) $x/w = 0$, (b) $x/w = 1/6$, (c) $x/w = 1/3$, and (d) $x/w = 1/2$. The average of the size of the bubbles, the preliminary bubbles and the secondary bubbles in the axial range of $y/w = [0.1 \ 1.1]$ are shown by ‘—’, ‘- -’, and ‘- -’, respectively.



(c)



(d)

Figure 7-1. (continued) Bubble size versus y distance for four different location of the air injector tip of (a) $x/w = 0$, (b) $x/w = 1/6$, (c) $x/w = 1/3$, and (d) $x/w = 1/2$. The average of the size of all the bubbles, the preliminary bubbles and the secondary bubbles in the axial range of $y/w = [0.1 \ 1.1]$ are shown by ‘—’, ‘- -’, and ‘- · -’, respectively.

It is observed in Figure 7-1(b), (c), and (d) that the emerging bubbles are immediately followed by the data group of the primary bubbles as diameter increases. This attachment between the two data groups shows that the preliminary bubbles are directly formed by the process of bubble pinch-off from the air injector. The bubbles of Figure 7-1(a) can also be considered as preliminary bubbles because of the attachment between their data and the emerging bubbles. The average size of the preliminary bubbles over the range of $y/w = [0.1 \ 1.1]$ is 0.66, 0.56, 0.55, and 0.54 in Figure 7-1(a), (b), (c), and (d), respectively. Therefore, the average size of the preliminary bubbles is larger for the wall orifice. For the nozzle injection, the average size slightly reduces as the air injector penetrates into the liquid cross-flow.

The group of the secondary bubbles consists of larger bubbles and is only observed in Figure 7-1(b), (c), and (d). These bubbles form a separate set of data starting at further downstream of the pinch-off location. The average of bubble size over the range of $y/w = [0.1 \ 1.1]$ for this group of bubbles is 0.77, 0.75, and 0.75 in Figure 7-1(b), (c), and (d), respectively. The average size of the secondary bubbles reduces slightly with the displacement of the air injector tip toward the center of the channel. Comparison of the figures also shows higher number of secondary bubbles as the air injector tip is moved toward the center of the channel.

In general, smaller average bubble size is observed for the three nozzle injection configurations in comparison to the wall orifice configuration. The average bubble size was relatively constant for the three nozzle injection configurations. The bubble size distribution plots also revealed a major difference between the wall orifice and the nozzle injection. The wall orifice results in a relatively uniform distribution of bubble size. These bubbles are termed preliminary bubbles and are directly formed by the pinch-off of the air bubbles from the air injector tip. The nozzle injection configurations result in two groups of preliminary and secondary bubbles. The secondary bubbles are larger, have a wider size distribution, and are formed at further downstream of the pinch-off location. For the nozzle injector, the displacement of the air injector toward the center of the channel resulted in slight reduction of the size of the preliminary and the secondary bubbles. The displacement of the air injector into the liquid cross flow also increases the number of the secondary bubbles.

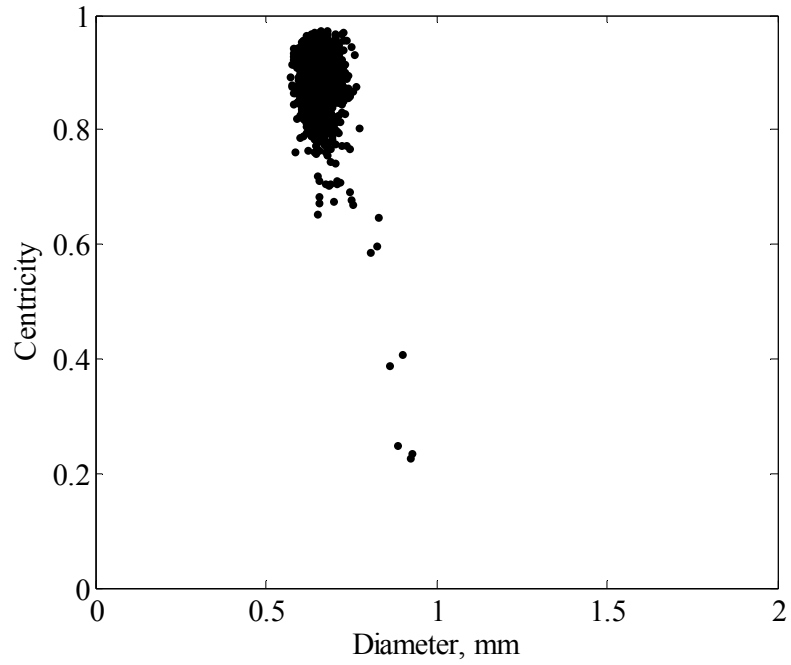
7.4. Bubble Shape

The geometric features of the bubbles can be used to study their formation mechanism. In this investigation, the shape of the bubbles is characterized by applying the PTV algorithm to calculate the centricity parameter. The calculated centricity parameter is plotted versus diameter in Figure 7-2(a) and (b) for the air injector locations of $x/w = 0$ and $1/2$, respectively. In these plots only the detected bubbles in the axial range of $y/w = [0.1 \ 1.1]$ have been considered and the emerging bubbles are not shown.

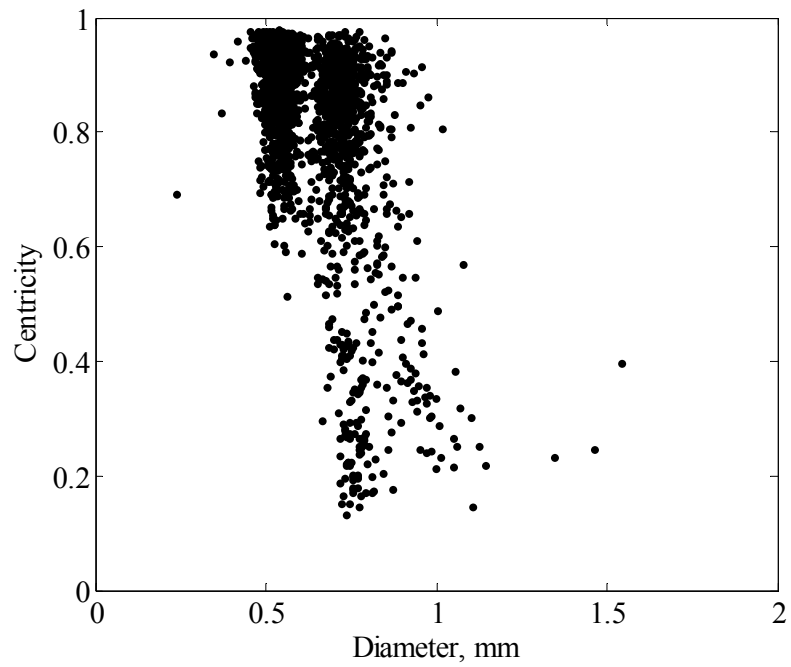
The preliminary bubbles generated by the wall orifice configuration are observed as a single batch of data in Figure 7-2(a). These bubbles have uniform size distribution. Their centricity is also high which represents a relatively circular shape. The two groups of preliminary and secondary bubbles for the nozzle configuration are observed in Figure 7-2 (b). The bubbles of the preliminary group have smaller size and relatively high centricity. However, the larger bubbles of the secondary group consist of both high and low centricity bubbles. Low centricity values of bubble shape indicate that the bubble has considerably deviated from being spherical.

Visual evidence of low centricity bubbles of the secondary group is illustrated in Figure 7-3(a) - (d). The images demonstrate that the low centricity shapes are formed as a result of coalescence of the bubbles. Figure 7-3(a) and (b) show two bubbles in the initial stages of coalescence in which they are colliding at a small distance downstream of the air injector. In the final stages of the coalescence process, the two bubbles will unify and form an elongated bubble. Samples of the elongated bubbles formed as a result of coalescence of two bubbles are shown in Figure 7-3(c) and (d). The unified bubbles of Figure 7-3(c) and (d) are still at the vicinity of the air injector which demonstrates a rapid unification process after the bubbles collision. The elongated bubbles would eventually form a large spherical bubble at further downstream in order to reduce the surface energy level.

The results of the shape measurement showed that the 2-D image of the preliminary bubbles is relatively circular. The secondary bubbles consist of both circular and non-circular images. The visual evidence of the bubbles illustrates that the highly non-circular bubbles of the secondary group are the bubbles which are in the process of coalescence.

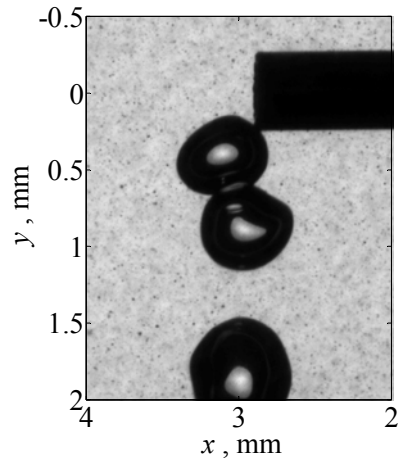


(a)

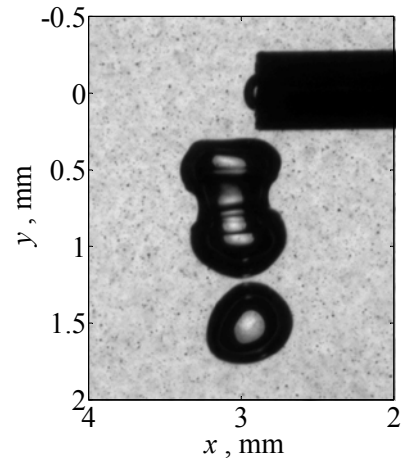


(b)

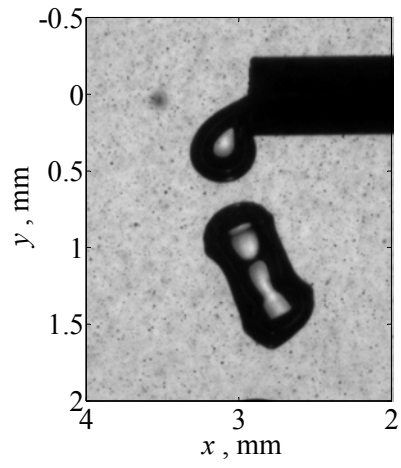
Figure 7-2. Bubble centricity versus diameter for two different location of the air injector tip of (a) $x/w = 0$ and (b) $x/w = 1/2$.



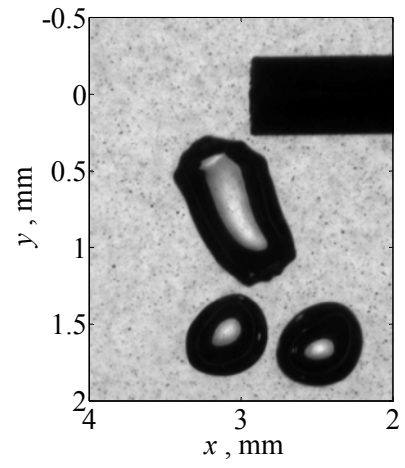
(a)



(b)



(c)



(d)

Figure 7-3. Samples of low centricity large bubble observed in the secondary group of bubbles.

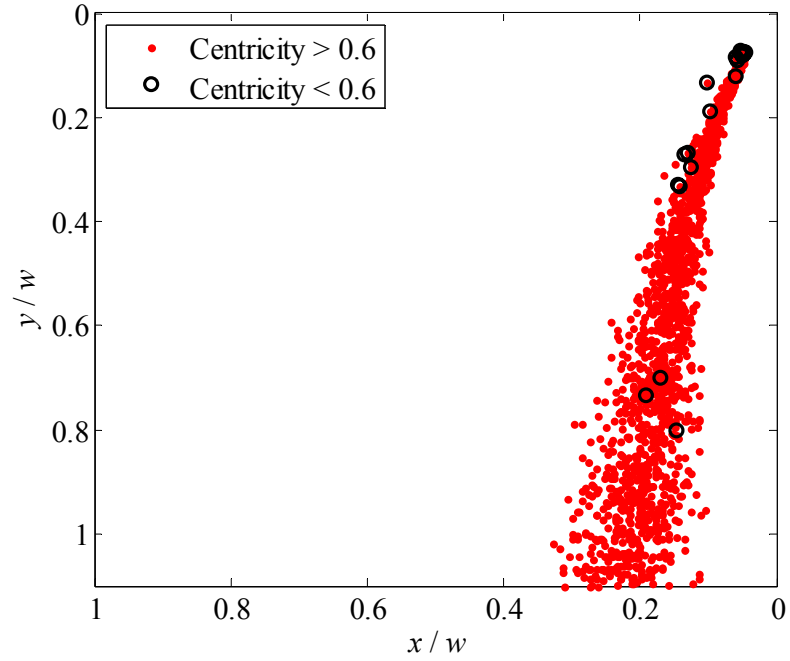
7.5. Bubble Location

The PTV algorithm can provide the location of the low and high centrlicity bubbles. The location of the centroid of the bubbles when the tip of the air injector is located at $x/w = 0$ and $x/w = 1/2$ are shown in Figure 7-4 (a) and (b), respectively. In these figures only the data for the bubbles in the axial range of $y/w = [0.1 \ 1.1]$ are presented and the emerging bubbles are removed. The data are divided into two groups of bubbles with centrlicity higher and lower than 0.6 to separate the coalescing bubbles from others.

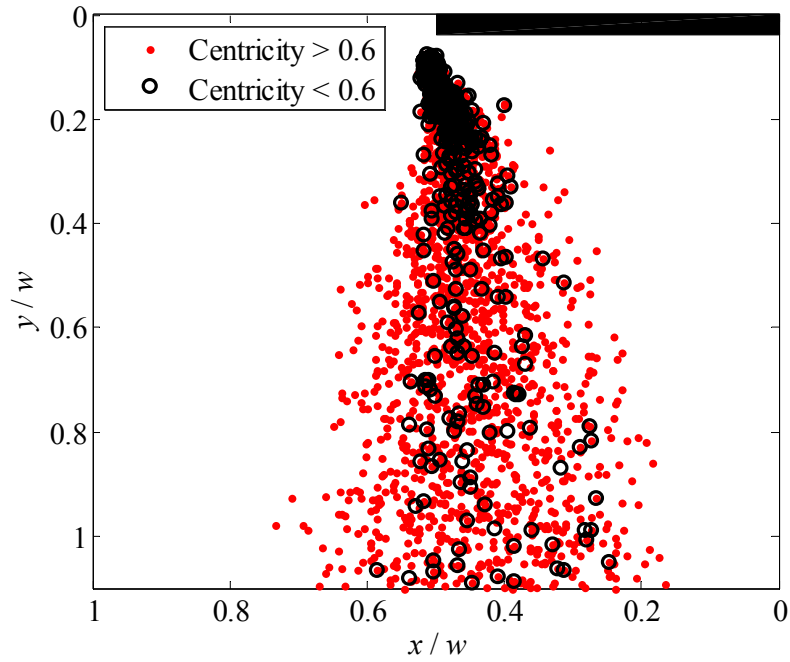
As it has been observed in the previous section the majority of the bubbles generated from the wall orifice configuration have a centrlicity higher than 0.6 as shown in Figure 7-4(a). Only a few bubbles with centrlicity lower than 0.6 are observed. The bubbles follow a narrow path starting from the wall orifice. The path of the bubbles becomes wider as they move downstream and covers about 20 percent of the channel width at $y/w = 1.1$. In the investigated axial distance, the location of the bubbles is still close to the orifice side and their path does not reach the centerline of the channel.

The location of the bubbles for the nozzle injection of Figure 7-4(b) shows that the high centrlicity bubbles exist at both upstream and downstream locations. However, the bubbles with low centrlicity which consist of coalescing bubbles mostly exist at the close vicinity of the air injector tube. The bubbles form a wider path and are covering about 50 percent of the channel width at $y/w = 1.1$. The path of the bubbles is also inclined toward the air injector wall.

The plots of bubble location showed that in the investigated axial distance the generated bubbles of the wall orifice configuration have a narrow path close to the wall orifice side. The bubbles of the nozzle injection configuration follow a wider path which is inclined toward the injector side. The location of the low centrlicity bubbles show that coalescence mostly occurs at the vicinity of the air injector tip. The occurrence of the coalescence phenomenon at the vicinity of the nozzle can be further investigated by studying the motion of the bubbles and the surrounding liquid flow.



(a)



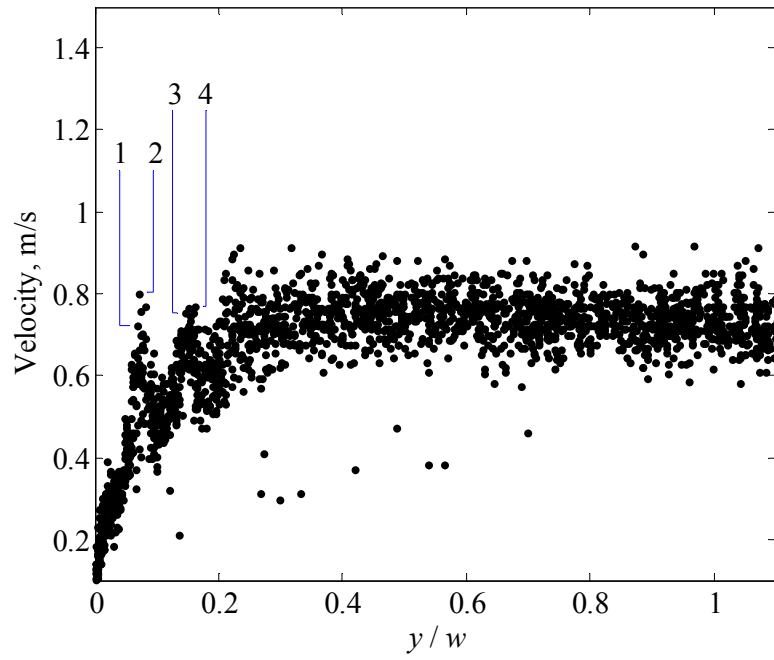
(b)

Figure 7-4. The location of high centrality (>0.6) and low centrality (<0.6) bubbles. The tip of the air injector tube is located at $x/w = 1/2$ and $y/w = 0$.

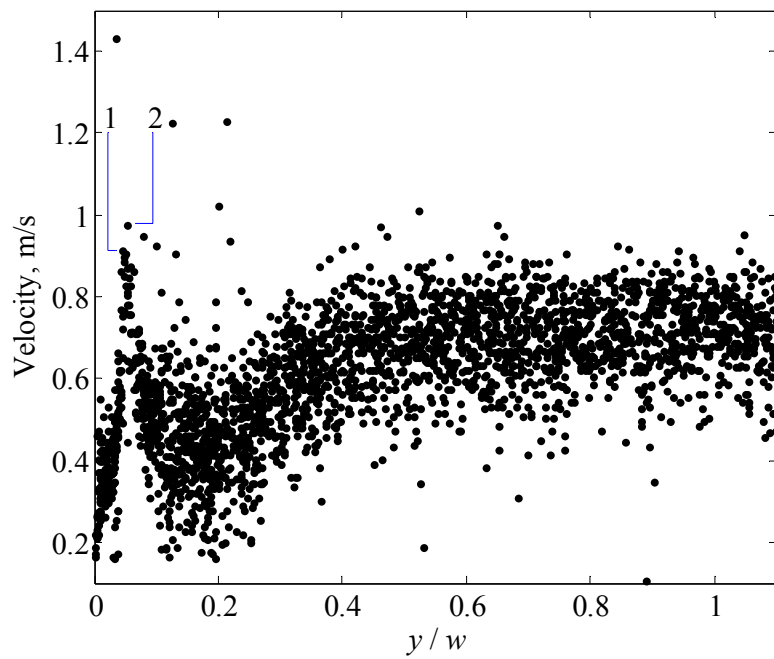
7.6. Bubble Velocity

In order to investigate the motion of the bubbles their velocity is measured by the PTV process. Axial velocity of the bubbles versus axial distance along the channel is shown in Figure 7-5(a) and (b) for the air injector locations of $x/w = 0$ and $x/w = 1/2$, respectively. The data consists of all the detected bubbles in the axial range of $y/w = [0 \text{ } 1.1]$.

A sharp initial increase in axial velocity is observed in the range of $y/w = 0$ to 0.07 in Figure 7-5(a). The observed increase in bubble velocity reaches a local maximum at about $y/w = 0.07$. The corresponding double-frame images of two bubbles at this local maximum velocity as highlighted by number 1 and 2 in Figure 7-5(a) are shown in Figure 7-6 and Figure 7-7, respectively. In these figures, the centroid of the bubble image is shown by the cross sign. The two bubbles are elongated and connected to the wall orifice in the first frame shown in Figure 7-6(a) and Figure 7-7(a). However, the bubbles are separated and have a truncated shape in the second frame illustrated in Figure 7-6(b) and Figure 7-7(b). The PTV measurement shows that the centroid of the bubble image has moved considerably in the time interval between the frames and the measured velocity is 0.72 and 0.80 m/s for bubble 1 and 2, respectively. Therefore, this local maximum in the bubble velocity demonstrates the pinch-off location of the bubbles from the orifice. A sharp drop-off in bubble velocity is observed after the pinch-off process.



(a)



(b)

Figure 7-5. Axial velocity of the bubbles versus axial distance. The air injector is located at (a) $x/w = 0$ (b) $x/w = 1/2$.

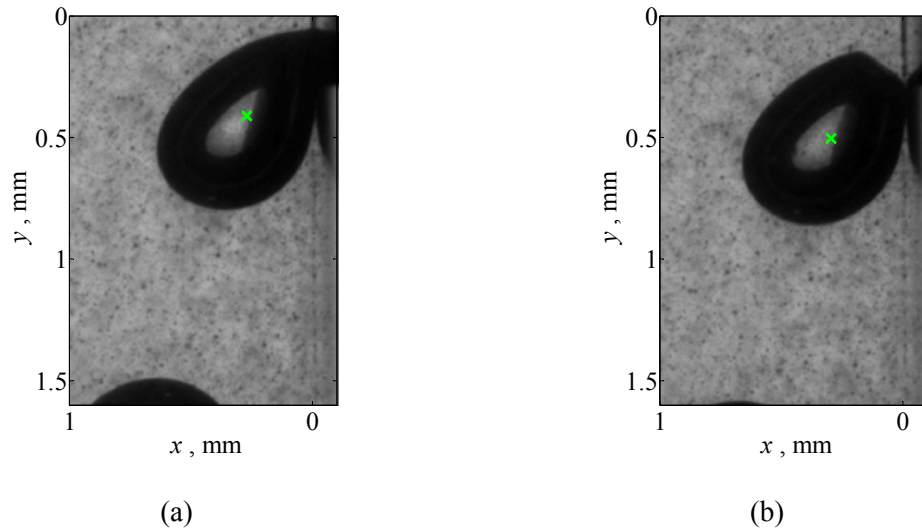


Figure 7-6. The double-frame image corresponding to data point 1 in Figure 7-5(a). (a) $t = t_0$. (b) $t = t_0 + 130 \mu\text{s}$. The centroid of the bubble image is shown with the cross sign.

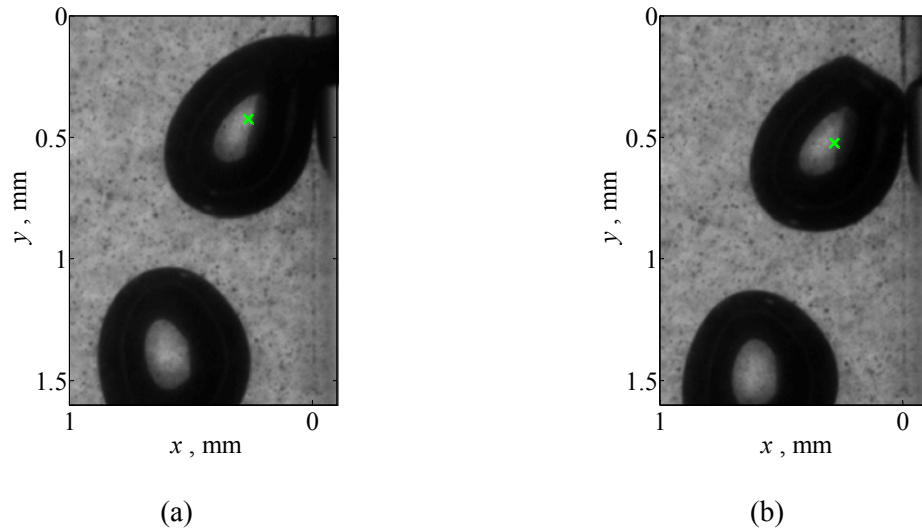


Figure 7-7. The double-frame image corresponding to data point 2 in Figure 7-5(a). (a) $t = t_0$. (b) $t = t_0 + 130 \mu\text{s}$. The centroid of the bubble image is shown with the cross sign.

A second peak is also observed in Figure 7-5(a) at $y/w = 0.15$. Two double-frames samples of the bubbles specified by 3 and 4 in Figure 7-5(a) are shown in Figure 7-8 and Figure 7-9, respectively. In the second frame of both images, a significant downward displacement is observed especially at the right side of the bubbles. The non-uniformity of the displacement for the two sides of the bubble causes a net rotation and/or

deformation of the bubble. The PTV calculation also shows high displacement of the centroid of these bubbles and their velocity is 0.75 and 0.77 m/s, respectively. Therefore, the bubbles are subject to significant rotation and translation upon passing this location.

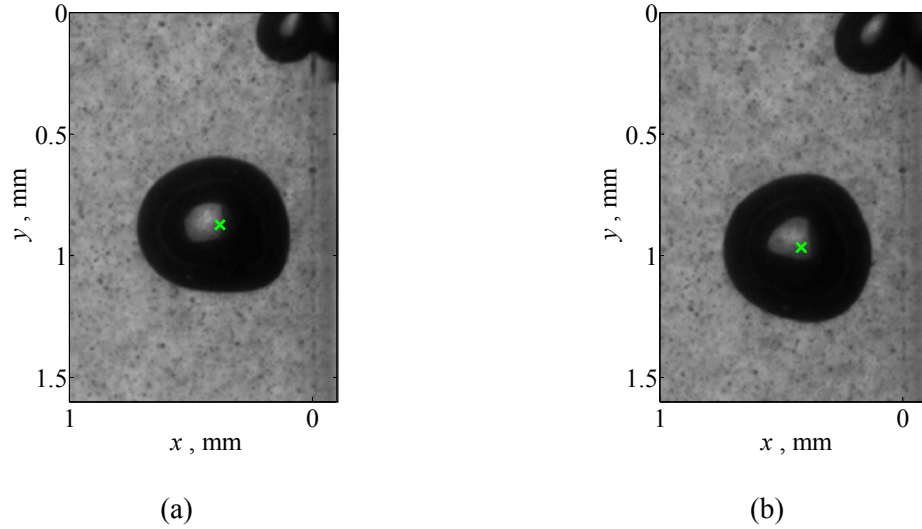


Figure 7-8. The double-frame image corresponding to data point 3 in Figure 7-5(a). (a) $t = t_0$. (b) $t = t_0 + 130 \mu\text{s}$. The centroid of the bubble image is shown with the cross sign.

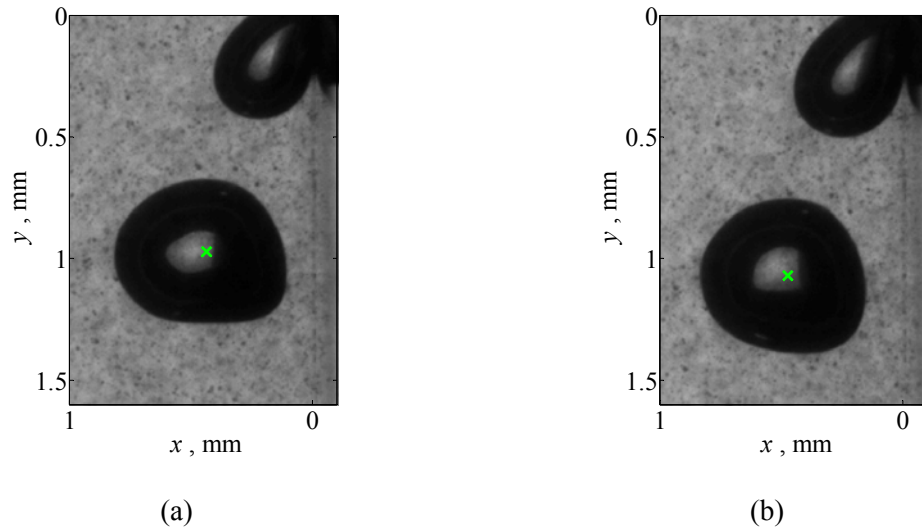


Figure 7-9. The double-frame image corresponding to data point 4 in Figure 7-5(a). (a) $t = t_0$. (b) $t = t_0 + 130 \mu\text{s}$. The centroid of the bubble image is shown with the cross sign.

After the second peak the bubbles velocity increases till about $y/w = 0.3$ in Figure 7-5(a) where it becomes constant. This acceleration is due to the drag force exerted on the bubbles by the surrounding liquid cross-flow. The average of the bubble velocity is observed to be relatively constant in the axial range of $y/w = [0.3 \ 1.1]$. The distribution of the bubbles velocity in this axial distance is in the range of 0.65 - 0.9 m/s.

Axial velocity data for the nozzle injection configuration shown in Figure 7-5(b) demonstrates a sharp initial increase in the velocity of the bubbles. This sharp increase is followed by a reduction which results in a local maximum in bubble velocity at about $y/w = 0.05$. The corresponding double-frame images of two arbitrary points, 1 and 2 selected on the local maximum, are illustrated in Figure 7-10 and Figure 7-11. These images demonstrate that bubble is elongated and attached to the air injector in the first frame. After the time interval the bubble is detached from the injector tip in the second frame. The detachment process is accompanied by considerable change in the bubble shape. The measurement shows significant change in the location of the centroid of the bubble during the time interval of the images. The velocity of bubble 1 and 2 is 0.98 and 0.91 m/s, respectively. It is also observed in Figure 7-5(b) that the bubbles immediately after detachment from the air injector have lower velocity.

The detached bubbles accelerate as a result of the drag force exerted on them by the surrounding liquid cross-flow and reach a constant velocity at about $y/w = 0.5$. The average of the bubble velocity is observed to be constant in the axial range of $y/w = [0.5 \ 1.1]$. In this region, the distribution of bubble velocity is relatively wide and the bubble velocity is spread over 0.5 - 0.9 m/s range.

The velocity of the bubbles which are attached to the wall orifice or the nozzle injector showed sharp with increase of axial distance. After this peak the bubbles pinch-off from the nozzle. The pinch-off location is earlier in the nozzle injection configuration. The newly detached bubbles have a lower velocity and are gradually accelerated by the liquid cross-flow. In the wall orifice configuration the detached bubbles are subject to a second velocity peak. The double-frame images contributed this velocity peak to the high rotation and displacement of the bubbles as they pass this location. The generated bubbles of the wall orifice configuration are subject to higher acceleration and reach the terminal velocity at a shorter distance. Comparison of the

plots also showed that the data are more scattered and the velocity distribution is wider for the nozzle injection configuration.

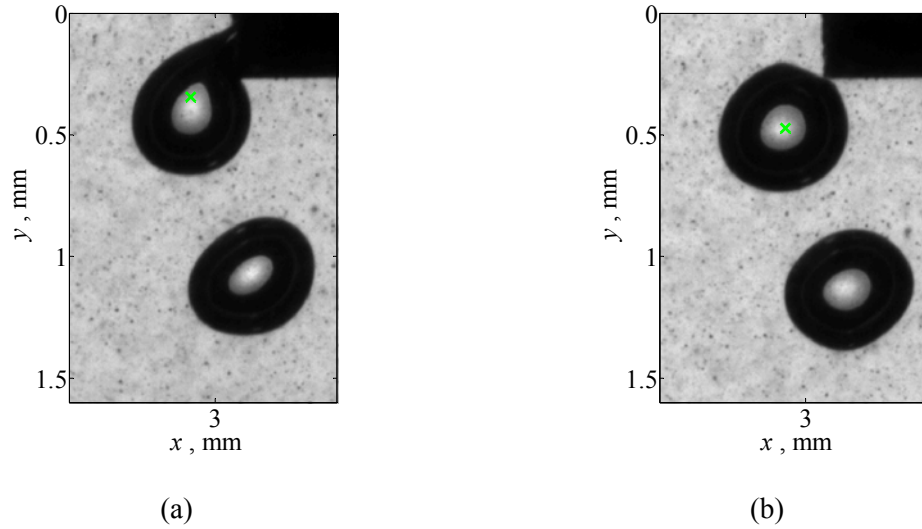


Figure 7-10. The double-frame image corresponding to data point 1 in Figure 7-5(b). (a) $t = t_0$. (b) $t = t_0 + 130 \mu\text{s}$. The centroid of the bubble image is shown with the cross sign.

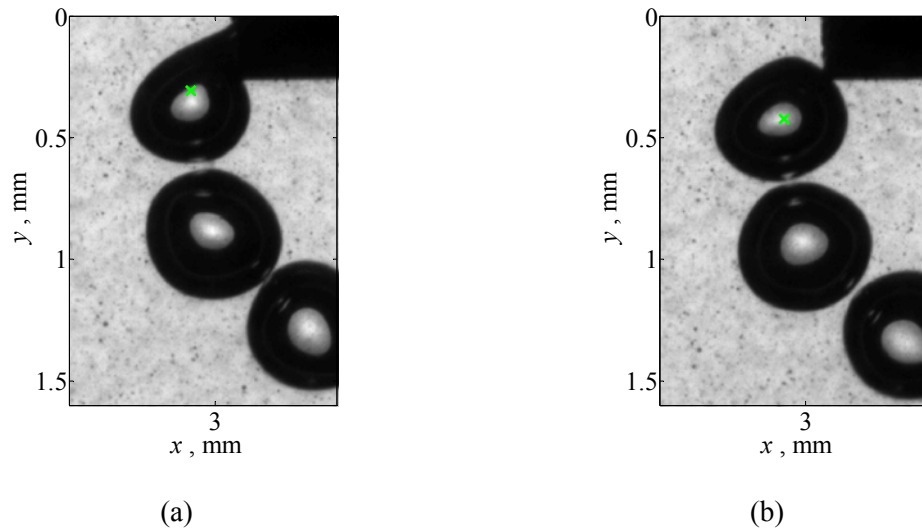


Figure 7-11. The double-frame image corresponding to data point 2 in Figure 7-5(b). (a) $t = t_0$. (b) $t = t_0 + 130 \mu\text{s}$. The centroid of the bubble image is shown with the cross sign.

7.7. *Liquid Velocity Field*

The PIV process has been applied to the data to measure the liquid velocity field for the wall orifice and the nozzle injection configurations. Figure 7-12 (a) and (b) show the average axial velocity contours of liquid flow along the channel for the two air injector locations of $x/w = 0$ and $x/w = 1/2$, respectively. The plots are accompanied by axial velocity profiles at four axial locations along the channel for the wall orifice and the nozzle injection configurations shown in Figure 7-13(a) and (b), respectively.

The boundary layer formed on both walls of the channel is observed in the velocity contour plot of Figure 7-12 (a) and Figure 7-13(a). The boundary layer on the wall orifice side is affected by the presence of the orifice and is thinner. This is observed clearer in the velocity profiles of Figure 7-13(a) which show a higher velocity gradient close to the orifice wall. There is a low velocity region at the vicinity of the wall initiating from the orifice location. This low velocity region is caused by the existence of the orifice and also the wake and the flow around the generated bubbles. The velocity profiles at $y/w = 0, 0.1, \text{ and } 0.4$ locations of Figure 7-13(a) show that the low velocity region gradually diminishes as it follows the path of the bubbles downward and inclined toward center of the channel.

The contour plot of the nozzle injector configuration is shown in Figure 7-12. Figure 7-12 (b) shows a small region of low velocity liquid at the immediate upstream of the span of the air injector tube. This region is also observed in the $y/w = -0.1$ velocity profile of Figure 7-13(b). A low velocity region is observed at the downstream of the air injector tube followed by a region of recovery to a higher velocity. A region of low velocity fluid is also observed at the vicinity of the tip of the air injector. The velocity profiles at $y/w = 0.1$ and 0.4 locations also demonstrate this region. This low velocity region can be contributed to both the wake and the surrounding flow of the bubbles and also the wake generated by the tip of the air injector. The low velocity region is inclined toward the air injector side and is diminishes as it extended toward downstream.

In order to characterize the flow unsteadiness in the channel, contours of RMS of the velocity field are shown in Figure 7-14(a) and (b) for the air injector locations of $x/w = 0$ and $x/w = 1/2$, respectively. Figure 7-14(a) shows a region of high velocity RMS starting

from the wall orifice location and follows the path of the bubbles. This unsteadiness is caused by the flow around the bubbles and their wake.

A region of high RMS is observed at the vicinity of the air injector tip at Figure 7-14(b). This region of high vorticity is caused by the unsteady wake formed by the air injector tip and also the flow around the bubbles and their wake. The region of high RMS is spread in a large region downstream of the air injector. It is also inclined toward the injector side and affects the flow passing over the injector tube.

The vorticity fields are also presented to further scrutinize the liquid flow field. Figure 7-15(a) and (b) show contours of instantaneous vorticity in the channel for air injector locations of $x/w = 0$ and $x/w = 1/2$, respectively. In these figures positive vorticity represents anti-clockwise rotation and is shown by bright band of the gray-scale spectrum. The dark band of the color spectrum corresponds to negative vorticity and clockwise rotation. The bubbles are observed as white regions of relatively circular shape. The area of the injector tube is also hatched in Figure 7-15(b).

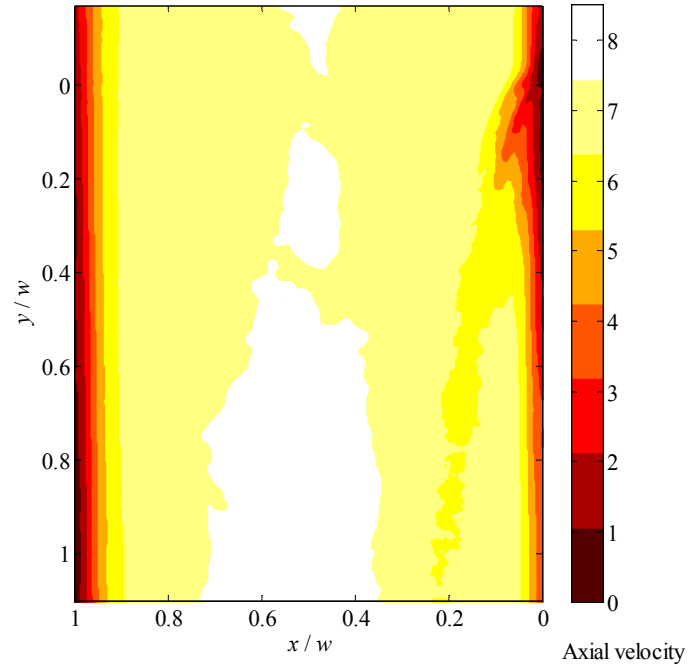
A region of anti-clockwise vorticity is observed in Figure 7-15(a) at the free side of the bubble which is connected to the wall orifice. Two regions of anti-clockwise and clockwise vorticity are observed on both sides of the last detached bubble next to the wall orifice. The vorticity contours around the other bubbles show that the clockwise vorticity side is strengthened as the bubbles flow toward downstream to balance the anti-clockwise vorticity. The final balance between these counter-acting vorticity fields prevents the bubbles rotation around their center.

The vorticity contours of Figure 7-15(b) shows anti-clockwise vorticity at both sides of the bubble which is attached to the air injector tube. This results in net anti-clockwise vorticity acting on the emerging bubbles which can help the bubble pinch-off process and generate smaller bubbles by early separation from the air injector tip. After the bubbles have separated a strong region of clockwise vorticity is also formed on the upper side of the bubble which balances the net vorticity acting on the flowing bubbles.

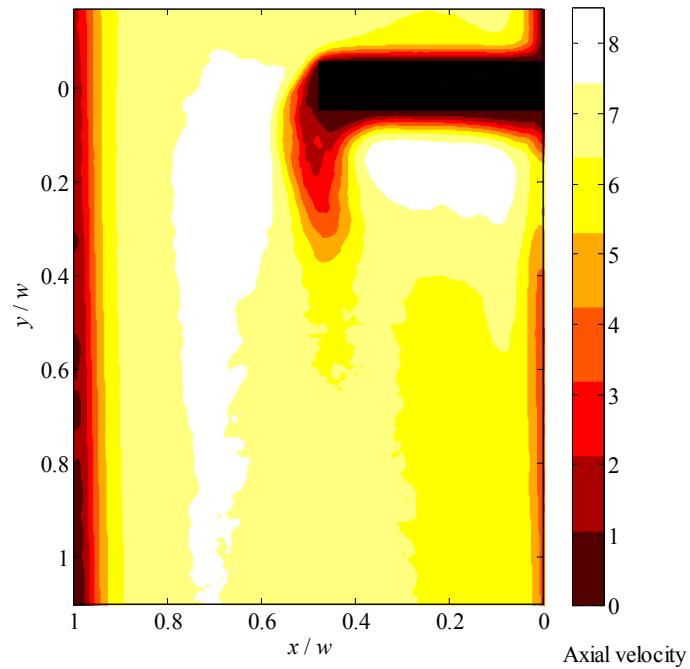
The PIV measurement of the liquid velocity field showed a low axial velocity region at the vicinity of the wall orifice and the nozzle injector. RMS of axial velocity is also observed to be high at this region which shows flow unsteadiness. In the wall orifice configuration, this unsteady low velocity region is formed by the wake and the

surrounding flow of the generated bubble. In the nozzle injection configuration, the wake formed by the tip of the air injector tube contributes to this region in addition to the wake and the surrounding flow of the bubbles. This results in a larger region of unsteady low velocity flow for the nozzle injection configuration. This region is extended downward and is inclined toward the injector side.

The instantaneous vorticity contours also showed that in the wall orifice configuration an anti-clockwise vorticity acts on the free side of the attached bubble. The effect of this vorticity is opposed by the contact between the other side of the bubble and the wall. A clockwise vorticity is formed on the wall-facing side of the bubble after detachment. This clockwise vorticity becomes stronger as the bubble flows toward downstream and balances the anti-clockwise vorticity. In the nozzle injection configuration anti-clockwise vorticity is observed on both sides of the elongated bubble which is attached to the tip of the air injector. This net anti-clockwise vorticity can result in earlier bubble breakup. A strong clockwise vorticity is formed on the right side of the bubble immediately after its separation which balances the anti-clockwise vorticity acting on the other side.

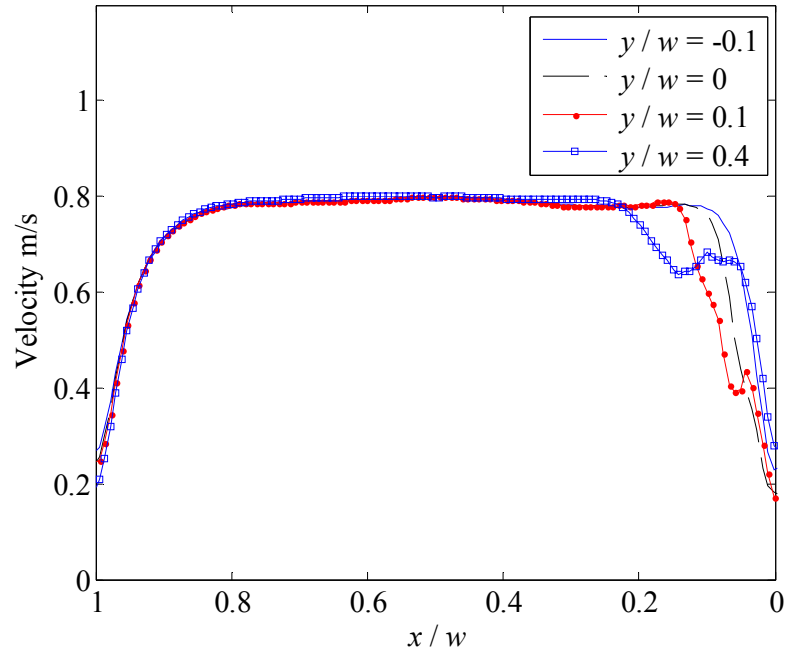


(a)

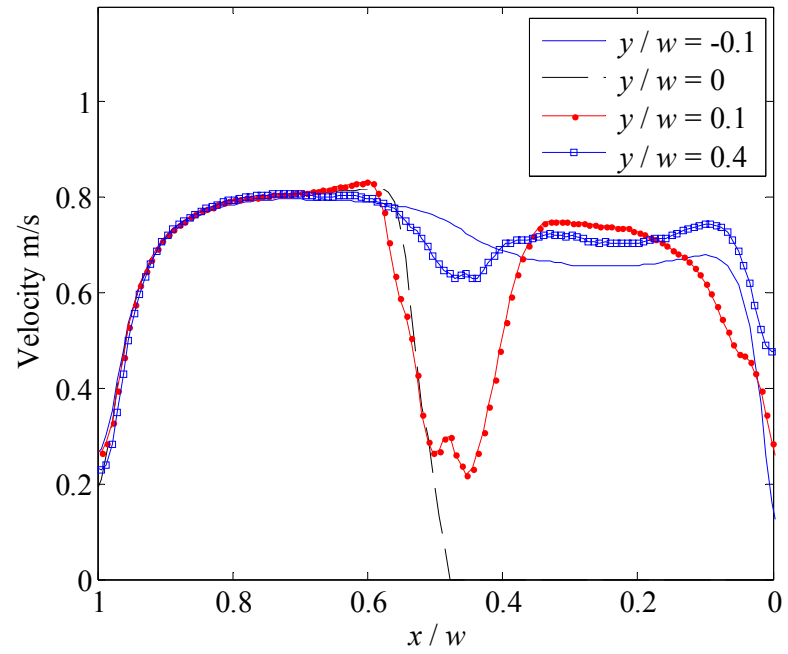


(b)

Figure 7-12. Contours of liquid axial velocity field in the channel. The tip of the air injector is located at (a) $x/w = 0$ (b) $x/w = 1/2$.

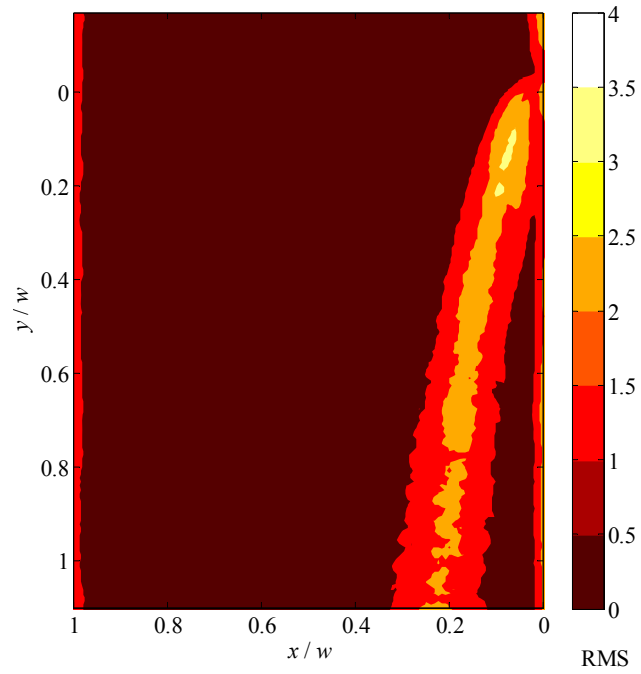


(a)

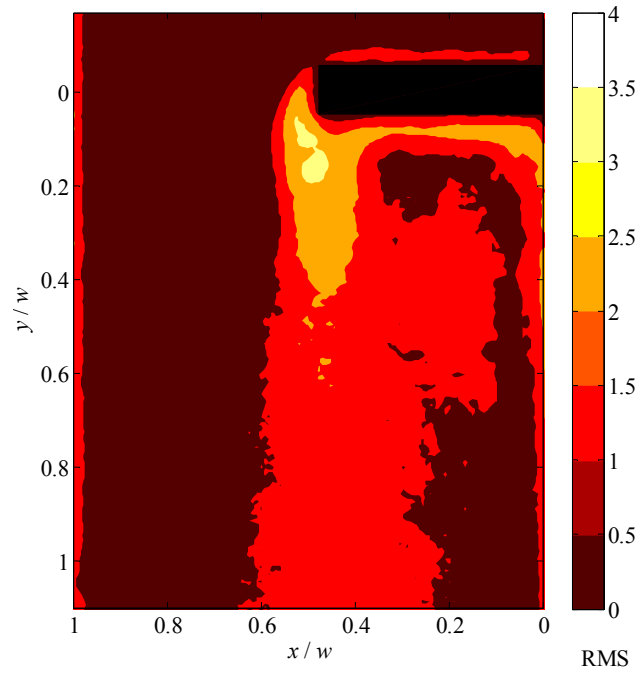


(b)

Figure 7-13. Profiles of water axial velocity at different locations in the channel.

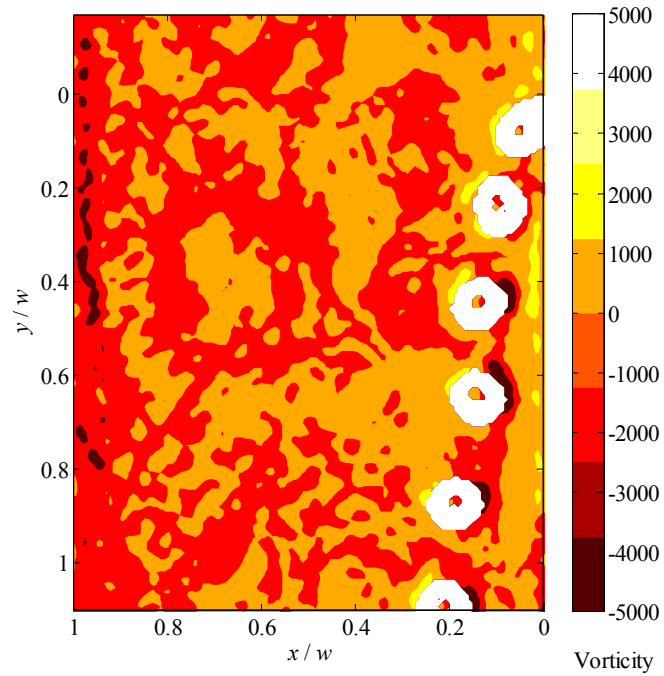


(a)

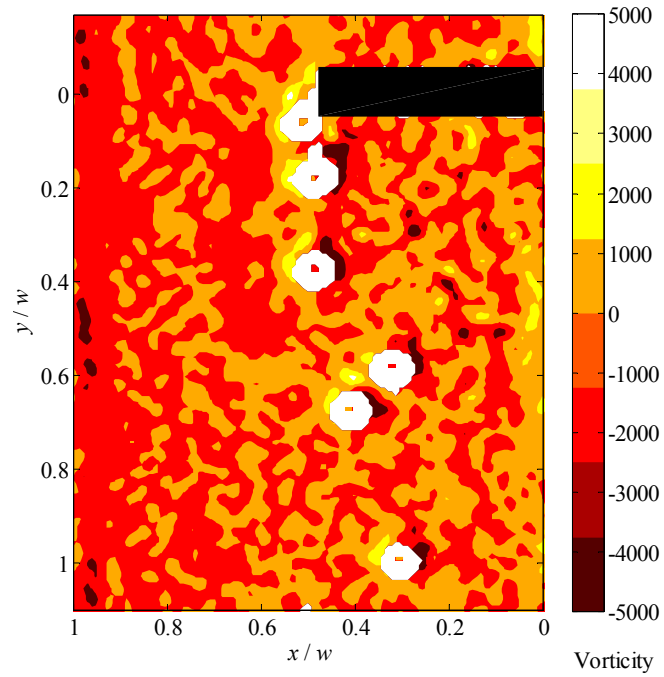


(b)

Figure 7-14. RMS of axial velocity field in the channel. The tip of the air injector is located at (a) $x/w = 0$ (b) $x/w = 1/2$.



(a)



(b)

Figure 7-15. Vorticity field in the channel. The tip of the air injector is located at (a) $x/w = 0$ (b) $x/w = 1/2$.

7.8. Discussion

Air injection from the wall orifice configuration results in generation of bubbles into the liquid cross flow. At the initial stages of bubble formation, the bubble appears partially from the wall orifice. An anti-clockwise vorticity acts on the liquid-gas interface of the attached bubble while the other side of the bubble is in contact with the micro-tube and the wall surfaces. Continued gas injection increases the bubble size and the liquid cross-flow pushes it in the downstream direction. The bubble velocity reaches its maximum and the bubble breakups from the orifice. The bubble has a low velocity immediately after detachment and is accelerated by the liquid cross-flow. A low velocity and unsteady liquid field exists at the vicinity of the wall orifice which is formed by the wake and the surrounding flow of the detached bubbles. A clockwise vorticity is formed on the wall-facing side of the bubble after its detachment. As the bubble flows downstream and toward the channel centerline, it exits the boundary layer. At this location the second local maximum in the velocity of the bubbles is observed which is accompanied by considerable rotation and displacement of the bubble. The clockwise vorticity also becomes stronger and balances the anti-clockwise vorticity of the other side. The generated bubble is still subject to acceleration and reaches a constant velocity at further downstream. These bubbles have the same size as the bubbles which have newly pinched-off from the air injector tip and are called preliminary bubbles. The preliminary bubbles have a narrow size distribution and are relatively spherical.

At the initial stages of bubble formation from the nozzle injector, the bubble is elongated in the flow direction and attached to the tip of the tube. The bubble, which is attached to the nozzle injector, is subject to high acceleration and its velocity increases sharply. An anti-clockwise vorticity is also observed on both sides of the elongated bubble which helps the breakup process. As the bubble becomes elongated, its velocity reaches its maximum and the bubble breakups from the tip of the tube. The newly detached bubble has a lower velocity and is accelerated by the liquid cross-flow. A strong clockwise vorticity is also observed immediately after the bubble separation. The bubbles follow a wide path which is inclined toward the injector side. The wake of the generated bubbles along with the wake of the tip of the air injector tube results in formation of an unsteady and low velocity region at the vicinity of the nozzle. This

region is extended downstream and is inclined toward the injector wall. The unsteady liquid flow results in wide distribution of bubbles velocity. As a result the high velocity bubbles may coalesce into the low velocity ones at a close downstream of the breakup location. During the coalescence process the bubbles are non-spherical. The bubble coalescence results in formation of secondary bubbles in addition to the preliminary bubbles. The secondary bubbles are larger and have a wider size distribution.

7.9. Conclusion

The investigations showed different mechanisms and features for the generated bubbles using the wall orifice and nozzle injection configurations. In general, the average size of the bubbles generated by the wall orifice configuration is larger than the nozzle injector configuration. However, the wall orifice configuration generated bubbles with narrower size distribution.

Air injection from a wall orifice configuration resulted in formation of a single group of bubbles termed preliminary bubbles. These bubbles were directly formed by the pinched-off process from the air injector tip, had a narrow size distribution, and were relatively spherical. The bubbles were subject to a high acceleration before separation from the orifice. The bubbles velocity drops-off after detachment from the orifice, reaches a local maximum as it passes the boundary layer and finally reaches a constant velocity. The velocity size distribution was also relatively narrow. A region of low liquid velocity and high velocity RMS has been observed at the vicinity of the wall orifice which is contributed to the wake and the fluctuations induced by the generated bubbles.

The investigation of the nozzle injection configurations demonstrated two distinct groups of bubbles: preliminary and secondary bubbles. The preliminary bubbles were smaller with a narrow size distribution and were relatively spherical. The group of secondary bubbles consisted of larger bubbles which had both spherical and non-spherical shapes. The non-spherical bubbles were caused as a result of bubble coalescence. The bubble velocity measurement also showed high acceleration of the bubbles attached to the air injector followed by a sharp drop-off as a result of detachment from the air injector. The separated bubbles were subject to a relatively low acceleration to reach the terminal velocity. The bubbles had a wide velocity distribution as a result of the unsteady liquid flow at the vicinity of the air injector. In the nozzle injection configurations, further displacement of the air injector toward the center of the channel results in slight reduction of the size of the preliminary and the secondary bubbles. The displacement of the air injector into the liquid cross flow also increases the number of the secondary bubbles.

8. The Effect of Internal Flow Structure on the Performance of Effervescent Atomization

8.1. Introduction

Effervescent atomization is a twin-fluid atomization mechanism which has been developed in 1980s by Lefebvre [149]. In this atomization mechanism a relatively low amount of gas is injected into the mixing chamber. The injected gas and liquid phases form a two-phase flow pattern in the mixing chamber which flows toward the discharge orifice. At the exit plane of the discharge orifice, the liquid phase disintegrates into ligaments and droplets mainly as a result of the sudden expansion of the gas phase.

Effervescent atomizers have specific advantages over other types of twin-fluid atomizers. Effervescent atomizers are capable of generating small droplets at injection pressures lower than other atomizers. The first experiments on effervescent atomizers revealed their capability to generate droplets with SMD as low as 20 μ m at operating pressures of about 5 psig [149 - 152]. The diameter of the exit orifice is also larger than other types of atomizers operating at a comparable flow rate [9, 11] and was observed to have a negligible effect on droplet SMD [150 - 152]. The relatively large exit nozzle of effervescent atomizers reduces the clogging problems and makes it suitable for atomizing liquids with impurities [149, 153 - 155]. The presence of air in the spray field may also reduce the production of pollutants in combustion applications [149]. Droplet SMD has also been found to be relatively insensitive to liquid viscosity [4]. These features make effervescent atomization suitable for many applications ranging from combustion engines [1-3], incineration [5], slurries [4], and consumer products [6] applications.

All the twin-fluid atomizers require a supply of atomizing gas which in some applications can result in difficulties due to the required space and the additional weight.

Effervescent atomizers can operate in a wide range of GLR and using less gas flow rates in comparison to most other types of twin-fluid atomizers [9, 149, 152]. However, there are some drawbacks in the characteristics of the generated spray by the effervescent atomizers during operation at their lowest GLR limit.

Larger droplet SMD has been observed when effervescent atomizers operate at GLRs less than 0.03 [149, 151, 152, 156]. It has also been recorded in the literature that droplet SMD increases with reduction of GLR in the operational range of 0.002 - 0.03 [149, 151, 152, 154, 156]. Unsteadiness and pulsation has also been observed in the generated spray field in the low GLR operation range [13, 19, 157].

Roesler and Lefebvre [152] recorded existence of a bubbly flow pattern in the atomizer mixing chamber at this low range of GLR. Santangelo and Sojka [19] described the atomization mechanism of effervescent atomization at this GLR range using the “single bubble expansion” process. In this process, the liquid jet is disintegrated into ligaments and droplets due to sudden expansion of the gas bubbles upon exiting from the discharge nozzle. Catlin and Swithenbank [13] have conducted simultaneous high speed imaging of the flow inside the mixing chamber and the external spray. They have also observed explosion-like events in the near-field spray for each bubble that passes through the atomizer discharge orifice. These explosion-like events in the liquid jet can cause pulsation and instabilities in the spray depending on the size and the arrival rates of the bubbles at the discharge orifice.

An extreme case of instability caused by these explosion events is observed at higher GLRs when the bubbles start to coalesce in the mixing chamber. In this condition, a slug flow is formed before the discharge orifice [13, 155]. Large bubbles with alternative liquid bridges pass through the discharge orifice and result in considerable pulsation and instabilities in the generated spray field [19, 155].

The instabilities and unsteadiness in the spray field are undesirable in combustion applications [11]. The pulsations may affect the atomization mechanism and result in incomplete atomization and formation of large ligaments and droplets [13, 19]. Spray unsteadiness can also cause combustion instability, noise, pollution, excessive load on the combustion chamber and also problems in the burner starting sequence [26, 157].

The previous measurements on effervescent atomization at GLR less than 0.03 which contributes to bubbly flow in the mixing chamber has been mostly conducted using forward scattering systems [2, 6, 150 - 152, 156, 158]. Whitlow and Lefebvre [156] have warned against use of the Malvern system when ligaments and large droplets are available in the spray field. They have recorded failure of the Malvern system in indicating the presence of the visually observed ligaments and large droplets within the spray field during the unsteady operation of the effervescent atomizer. Only Kim and Lee [154] have used an image-based droplet sizing system over a wide range of GLR and investigated the effect of internal flow pattern on spray characteristics. Their measurement shows droplets as large as 1000 μm in diameter when bubbly flow pattern exists in the mixing chamber. This highlights the necessity to consider the presence of large droplets and the ligaments during the instable operation of effervescent atomizers.

In this investigation, it has been hypothesized that if a large number of small bubbles are generated before the discharge orifice, the instabilities and pulsations of the effervescent atomizers at low GLR can be reduced. In order to test this hypothesis, an atomizer has been designed which applies a porous air injector to generate a population of small bubbles. The generated spray field of this atomizer has been compared with the spray field generated by another effervescent atomizer which uses a typical multi-hole air injector. The investigations have been carried out at low GLR of 0.0148, 0.0181, 0.0208, 0.0237, and 0.0267 which result in a bubbly flow pattern in typical effervescent atomizers. Investigation of the flow in the mixing chamber and the disintegration process of the liquid jet have also been qualitatively conducted using visual images. Measurement of droplet size has been conducted using shadowgraph droplet analyzer with a relatively large field-of-view to identify existence of any ligament or large droplet in the spray field.

8.2. The Experiment

The spray field utilized for this experiment is generated by the effervescent atomizer Mark II. A porous air injector and a multi-hole air injector have been used separately in this atomizer. The atomizer Mark II, the porous air injector, and the multi-hole air injector are described in section 2.3.2. The experiments of this chapter have been conducted at GLRs of 0.0148, 0.0181, 0.0208, 0.0237, and 0.0267. These five different GLRs have been achieved at different air and water flow rates illustrated in Table 8-1

In order to measure droplet size the Shadow-PTV system has been applied. This system is described in section 3.1. The camera captures images of a field-of-view of $670 \times 920 \mu\text{m}$. Measurements have been conducted at 5 axial locations along the centerline. In this work, axial positions were located at $z/d = 37.5, 50, 62.5, 75,$ and 87.5 along the spray centerline. A set of 5000 image pairs have been taken at each investigated location and GLR.

Table 8-1. The GLRs and the flow rates used in the experiment.

GLR	Water flow rate (mL/min)	Gas flow rate (mL/min)
0.0148	200	2500
0.0181	230	3500
0.0208	200	3500
0.0237	175	3500
0.0267	200	4500

8.3. Qualitative Investigation of Internal Flow and the Produced Spray

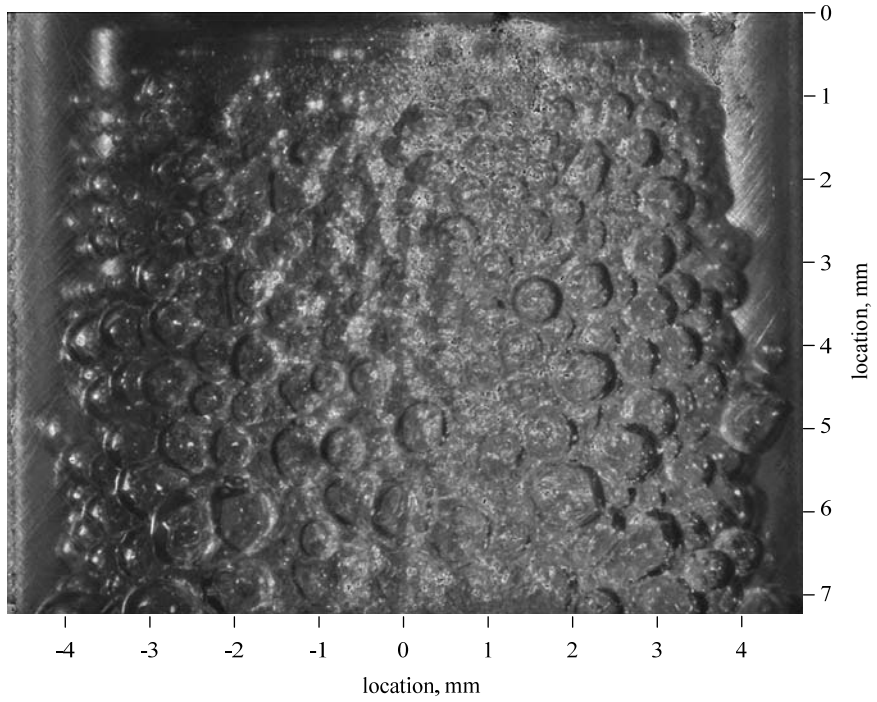
In this section, the recorded images of the internal flow and the near-field spray of the atomizers operating using the two air injectors are presented for qualitative comparison. The generated bubbles at the beginning of the porous section of the air injector are shown in Figure 8-1(a). In this figure, a large number of small bubbles in the order of 0.5 mm in diameter are observed in the vicinity of the porous part. The bubbles relatively have the same size and are spherical. The multi-hole air injector and the generated bubbles are shown in Figure 8-1(b). The images show that the multi-hole air injector introduces large bubbles. The bubbles are highly deformed and there is a relatively large distance between successive bubbles.

The air-water mixture generated by the porous media and the multi-hole air injectors prior to the discharge orifice are shown in Figure 8-2(a) and (b), respectively. A homogenous population of small bubbles is observed in Figure 8-2(a). These small bubbles are observed to deform and squeeze into the discharge orifice. The mixture in Figure 8-2(b) shows a number of large bubbles before the discharge orifice.

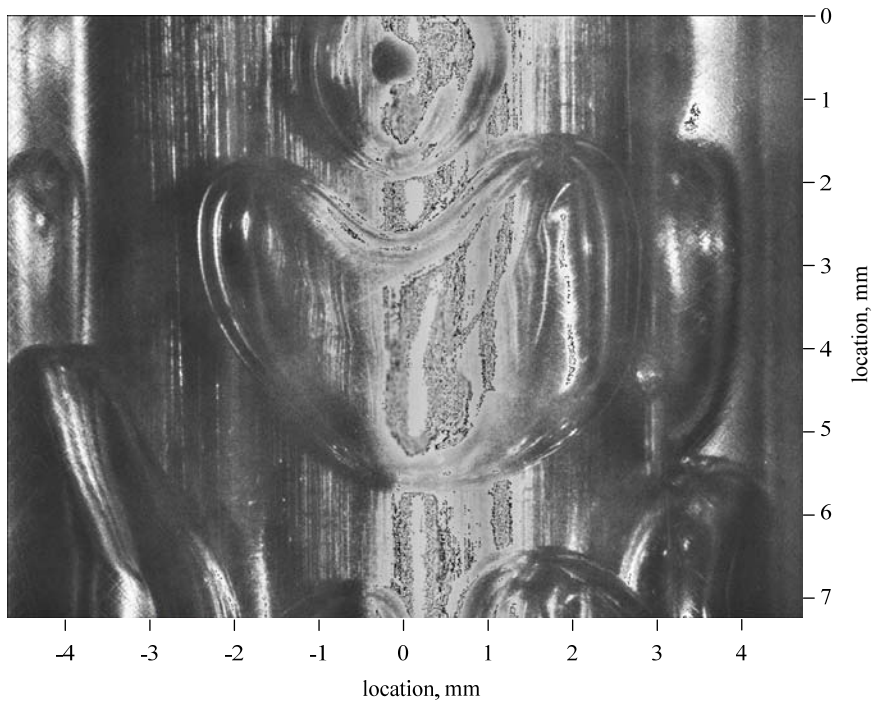
Two sample shadowgraphy images of the near-field spray generated by the porous air injector in the vicinity of the discharge orifice are shown in Figure 8-3(a) and (b). Investigation of the recorded image sets showed similar atomization mechanism as the two illustrated samples. The images show that the liquid phase exits the discharge orifice as a turbulent liquid trunk. The liquid trunk continues till about $3d$ distance downstream where it disintegrates into ligaments and droplets.

Shadowgraphy images of the near-field spray generated by the multi-hole air injector in the vicinity of the discharge orifice are shown in Figure 8-4. The images show samples of different atomization mechanism observed in the recorded images. The atomization mechanism of Figure 8-4(a) shows a liquid trunk extended $3d$ distance downstream before disintegrating into ligaments and droplets. This mechanism is similar to the atomization mechanism observed in Figure 8-3(a) and (b) corresponding to the porous air injector. Figure 8-4(b), (c), (d), (e), and (f) shows atomization mechanisms which result in non-fully atomization of the liquid jet. A large ligament which is spread in radial direction as a result of pulsation in the discharge orifice is observed in Figure 8-4(b). This ligament causes unsteadiness in the generated spray field. Figure 8-4(c) and

(d) also illustrate sample images of non-symmetric instabilities in the two-phase flow discharging from the nozzle. A non-disintegrated liquid jet is observed in Figure 8-4(e). The distortions on the surface of the liquid jet show that the flow is turbulent. However, the liquid jet has not disintegrated into smaller ligaments and droplets because of the lack of the gas phase in the discharge orifice. Figure 8-4(f) corresponds to the moment when a large bubble passes through the discharge orifice along with a small amount of liquid. This instantaneously high GLR through the discharge orifice results in fast disintegration of the liquid phase into small droplets.

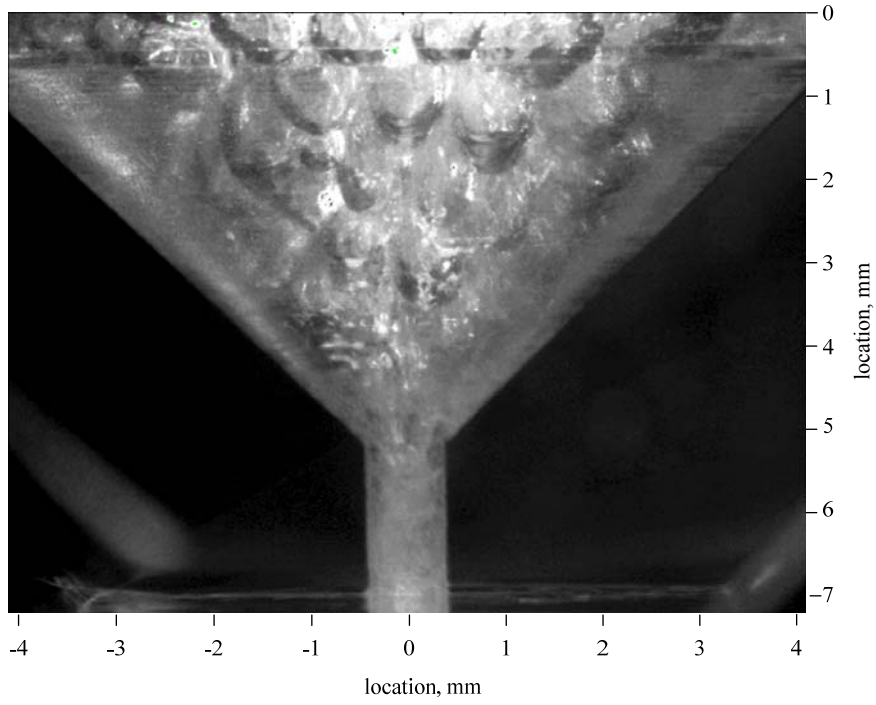


(a)

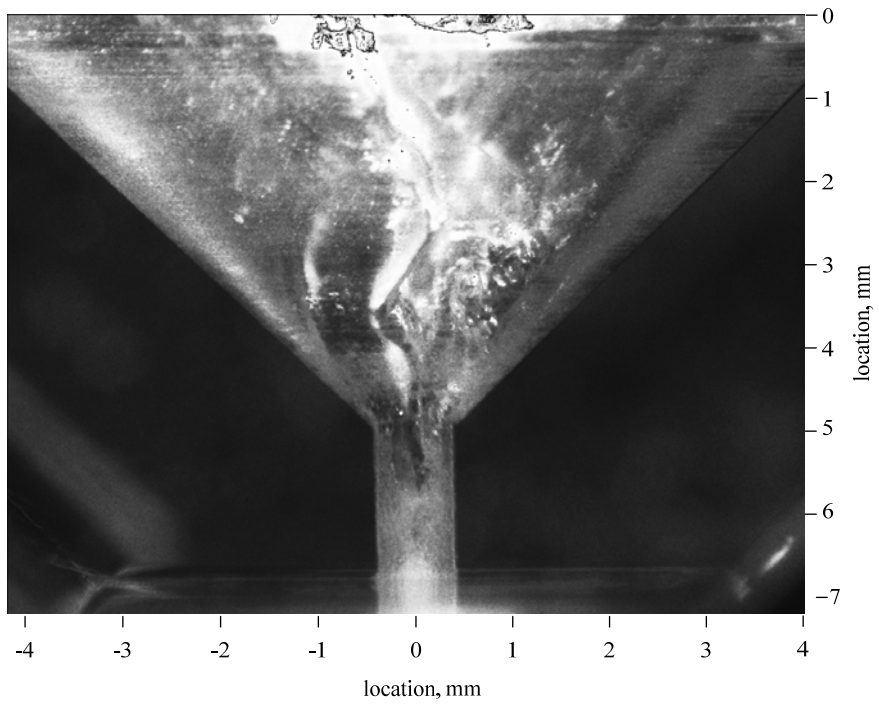


(b)

Figure 8-1. The generated bubbles in the mixing chamber by (a) the porous media air injector and (b) the multi-hole air injector. The liquid flow is downward.

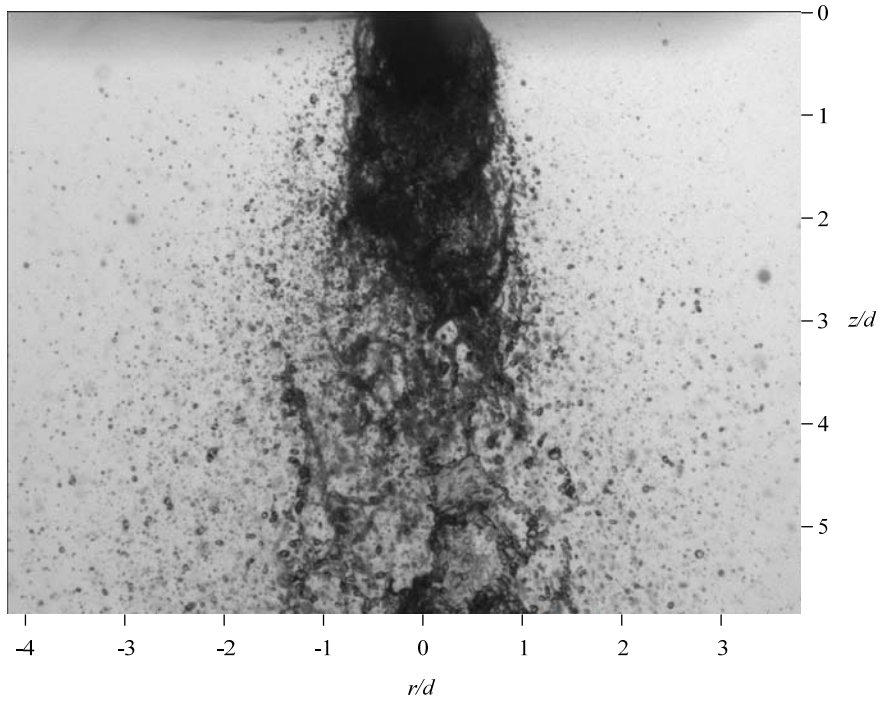


(a)

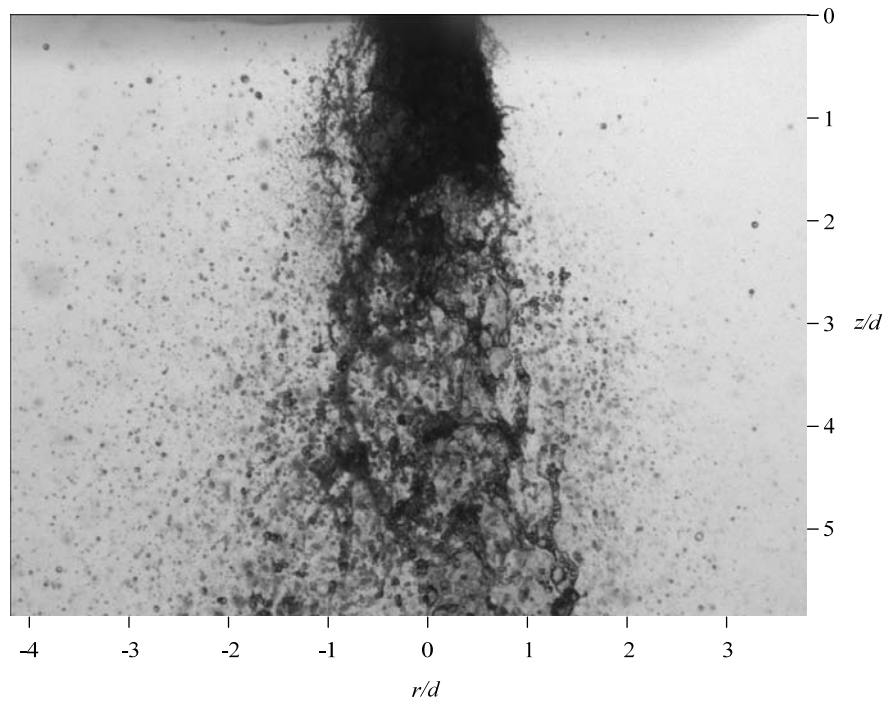


(b)

Figure 8-2. The air-water mixture near the discharge orifice produced by the (a) porous media air injector and (b) the multi-hole air injector.

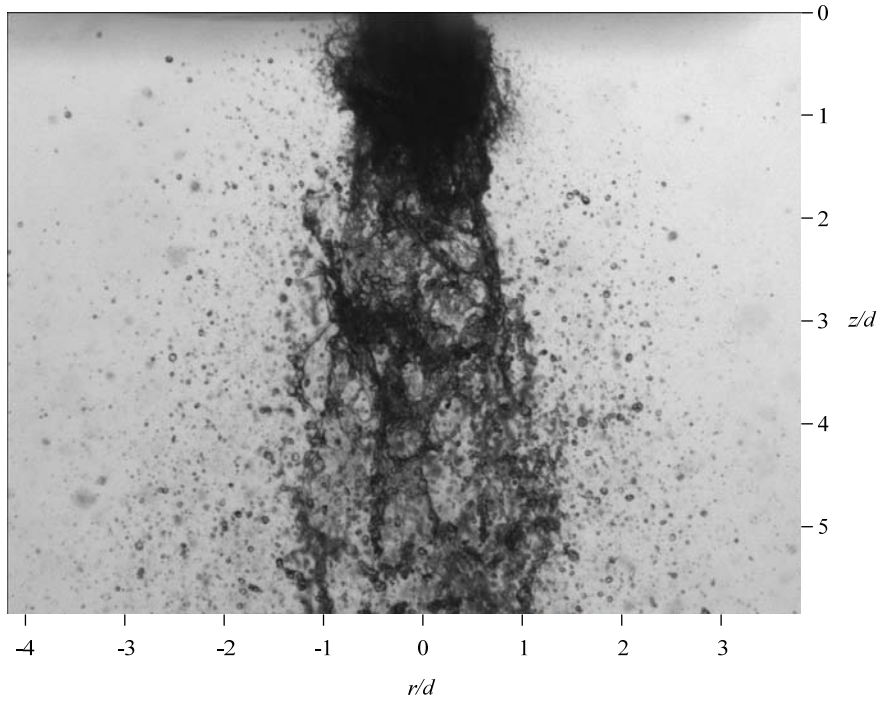


(a)

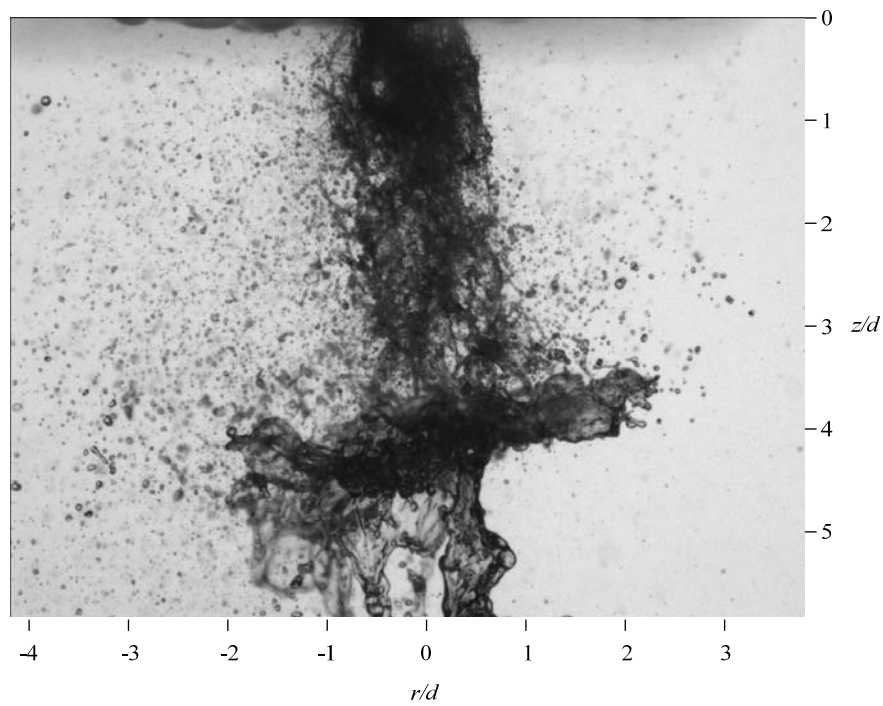


(b)

Figure 8-3. Shadowgraphy images of the spray produced by the effervescent atomizer applying the porous air injector.

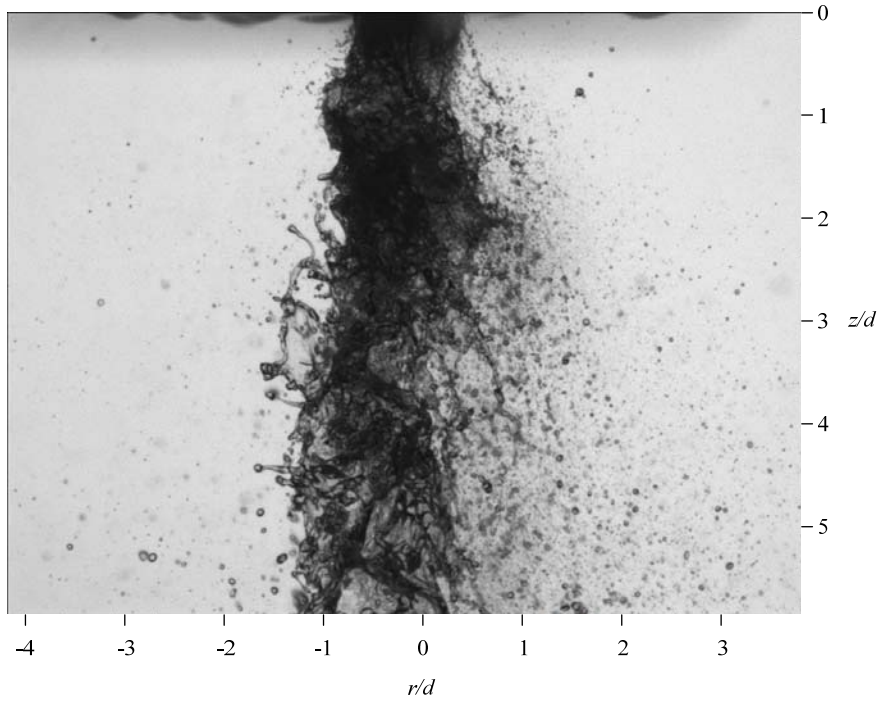


(a)

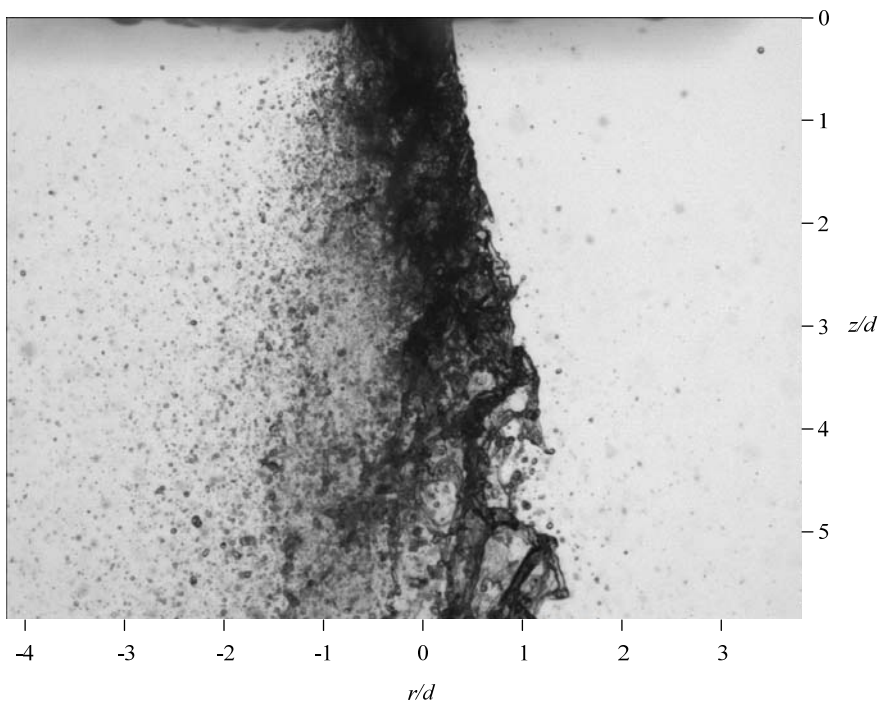


(b)

Figure 8-4. Shadowgraphy images of the spray produced by the effervescent atomizer applying the multi-hole air injector.

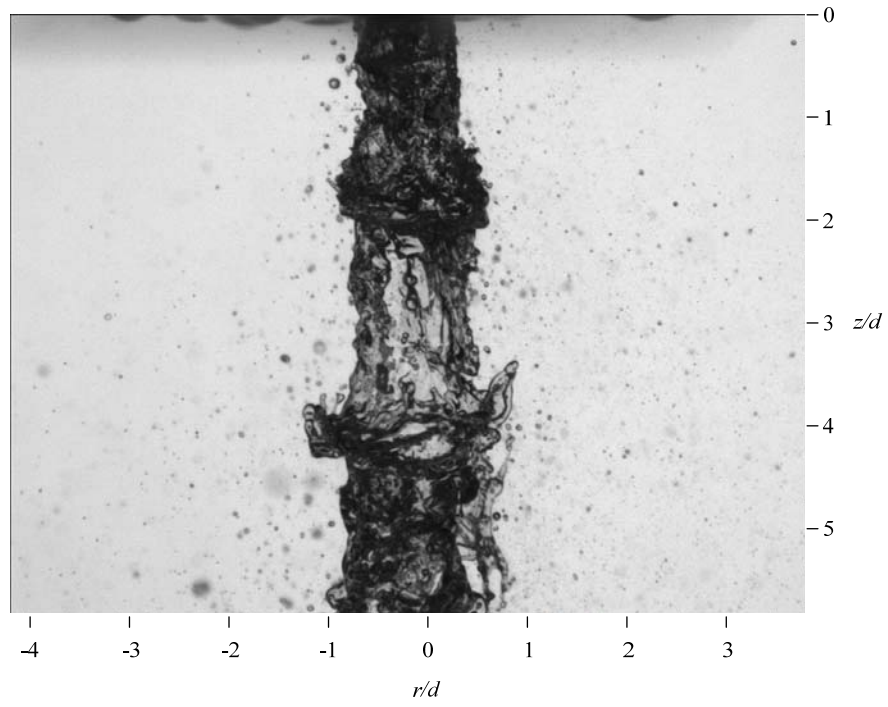


(c)

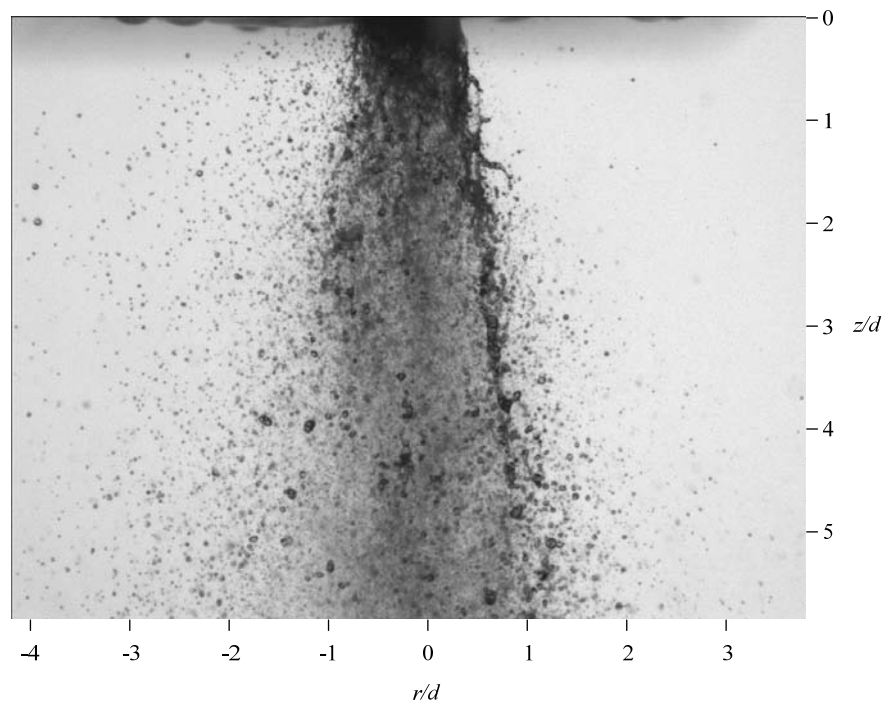


(d)

Figure 8-4. (continued) Shadowgraphy images of the spray produced by the effervescent atomizer applying the multi-hole air injector.



(e)



(f)

Figure 8-4. (continued) Shadowgraphy images of the spray produced by the effervescent atomizer applying the multi-hole air injector.

The qualitative comparison of the internal flow and the generated spray fields demonstrated major differences upon applying the porous or the multi-hole air injectors. The porous air injector generates a high number density population of small bubbles in the mixing chamber. This homogeneous mixture of gas and liquid feeds the discharge orifice with steady flow of air and liquid. The instantaneous GLR would be relatively constant through the discharge orifice and a single atomization mechanism has been observed. In this atomization mechanism, a liquid jet exits the discharge orifice and extends till $3d$ distance downward where it disintegrates into ligaments and droplets.

The multi-hole air injector generates bubbles of approximately 5 mm in diameter. The generated bubbles are a few millimeters apart from each other and highly deformed. This mixture results in a fluctuating instantaneous GLR in the discharge orifice. There are instances when the exit orifice would be occupied mostly by the liquid phase or mostly by the gas phase. This unsteady flow of gas and liquid through the discharge orifice results in pulsation and instability in the discharged flow. The atomization mechanism is deficient and generates relatively large ligaments and droplets.

8.4. Quantitative Investigation of the Generated Spray Field

In this section the characteristics of the spray droplets are quantitatively investigated and compared for the atomizers applying the porous and the multi-hole air injectors. First, droplet number frequency at five axial locations and five GLRs are investigated. Second, droplet SMD is investigated for the considered axial locations and GLRs. Finally, the number of ligaments and large droplets are investigated.

8.4.1. Droplet Number Frequency

The number frequency of droplets measured using the Shadow-PTV system is shown in Figure 8-5, Figure 8-6, Figure 8-7, Figure 8-8, and Figure 8-9 for GLR = 0.0148, 0.0181, 0.0208, 0.0237, and 0.0267, respectively. In each of these figures, the number frequency at $z/d = 37.5, 50, 62.5, 75, 87.5$ are specified by (a), (b), (c), (d), and (e), respectively. The plots show droplet number frequency in logarithmic scale versus droplet diameter in microns for the two atomizers operating using the multi-hole and the porous media air injectors. The droplets have been categorized into bins of $5\mu\text{m}$ size which cover from 5 to $600\mu\text{m}$ droplets. There are some gaps in the number frequency data which is due to lack of any droplet in the corresponding bin.

In all of the figures, reduction of droplet number frequency is observed with increase of droplet size for both the porous and the multi-hole air injectors. The initial sharp reduction in droplet number frequency is observed till about $100\mu\text{m}$ droplet size. After this point, the rate of reduction decreases and droplet number frequency becomes relatively constant. It is also observed that the majority of droplets are smaller than $40\mu\text{m}$ and only the number frequency of these droplets is less than 0.01.

The comparison between the multi-hole and the porous air injectors shows that in general the number frequency of droplets smaller than $200\mu\text{m}$ is lower for the multi-hole air injector. The multi-hole air injector also generates a considerable number of droplets larger than $300\mu\text{m}$ which are rare in the porous air injector data. Although the number of these large droplets is low, even a few large droplets are of considerable importance as they can result in incomplete combustion and air pollution [159].

A slight increase in the number frequency of droplets smaller than $40\mu\text{m}$ is observed with increase of axial location from the near field location of $z/d = 37.5$ to the far field location of $z/d = 87.5$. The number frequency of larger droplets also slightly decreases with increase of axial location. This can be due to disintegration and evaporation of the larger droplets as they move downstream. The slope of the initial reduction in droplet number frequency with increase of droplet size also becomes higher with increase of axial location. The comparison between the number frequency plots at different GLRs mainly shows reduction of the number of large droplets for both the multi-hole and the porous air injector.

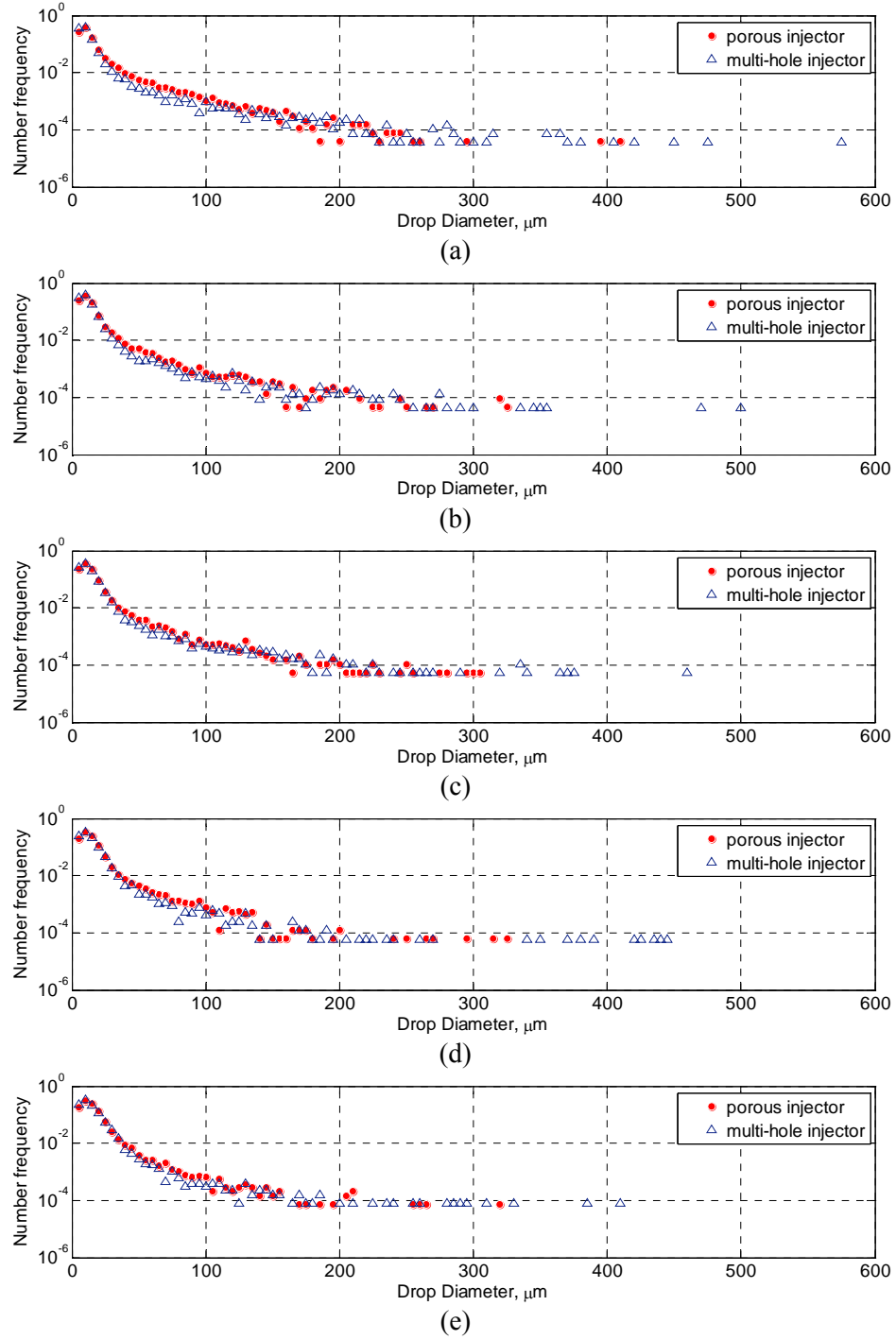


Figure 8-5. Number frequency of droplets at $\text{GLR}=0.0148$ for (a) $z/d = 37.5$, (b) 50, (c) 62.5, (d) 75, and (e) 87.5 locations along the spray centerline.

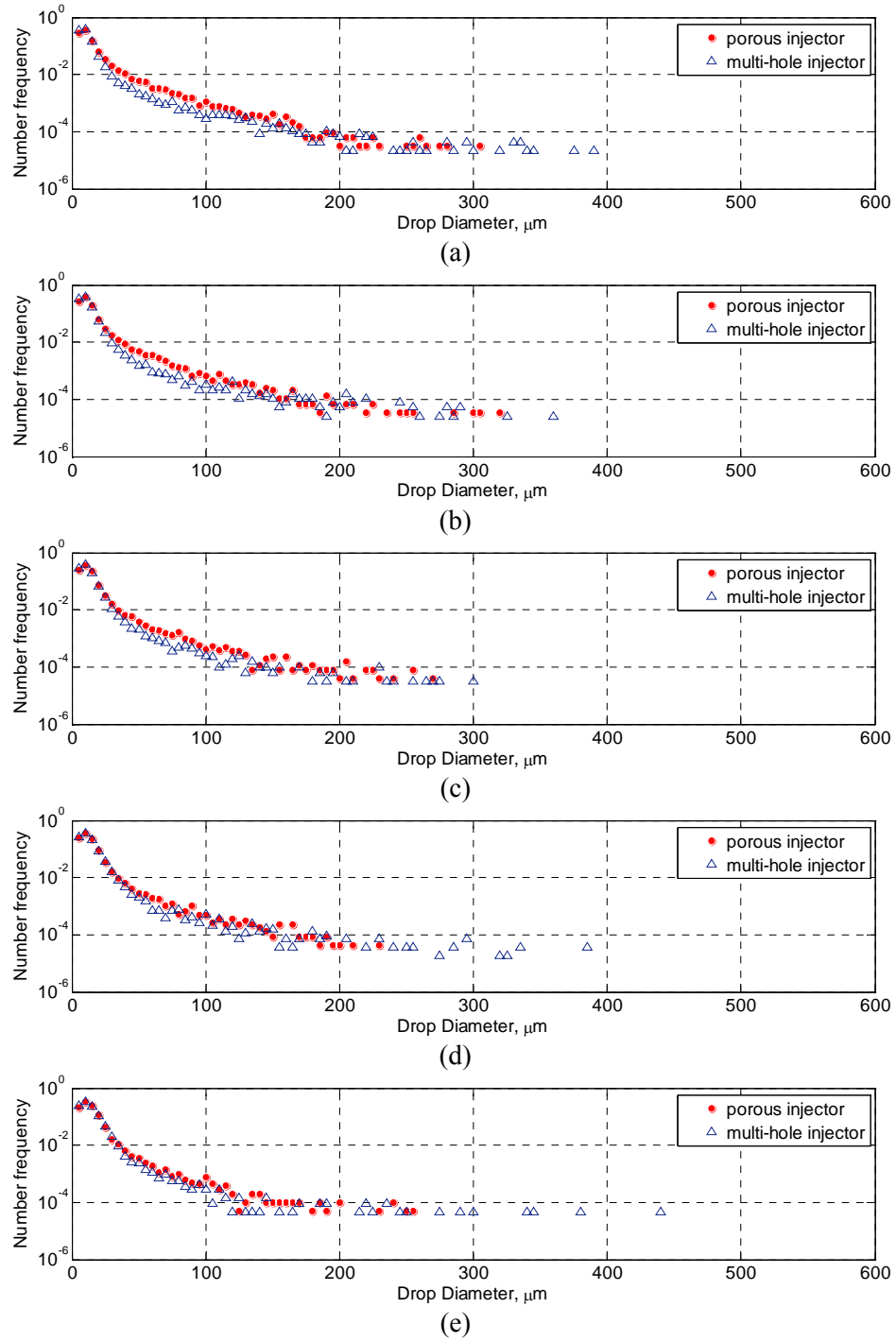


Figure 8-6. Number frequency of droplets at $\text{GLR}=0.0181$ for (a) $z/d = 37.5$, (b) 50, (c) 62.5, (d) 75, and (e) 87.5 locations along the spray centerline.

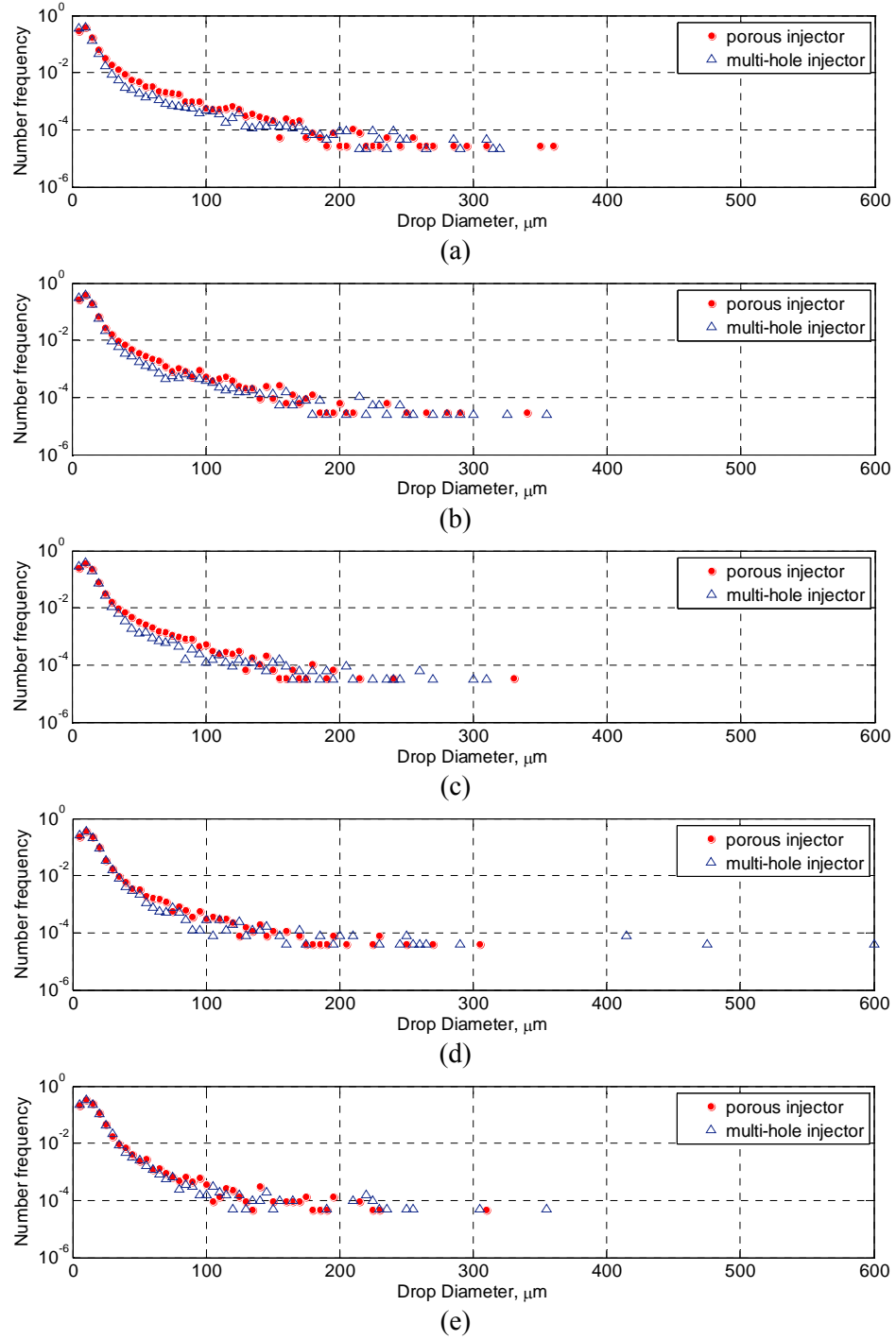


Figure 8-7. Number frequency of droplets at $\text{GLR}=0.0208$ for (a) $z/d = 37.5$, (b) 50, (c) 62.5, (d) 75, and (e) 87.5 locations along the spray centerline.

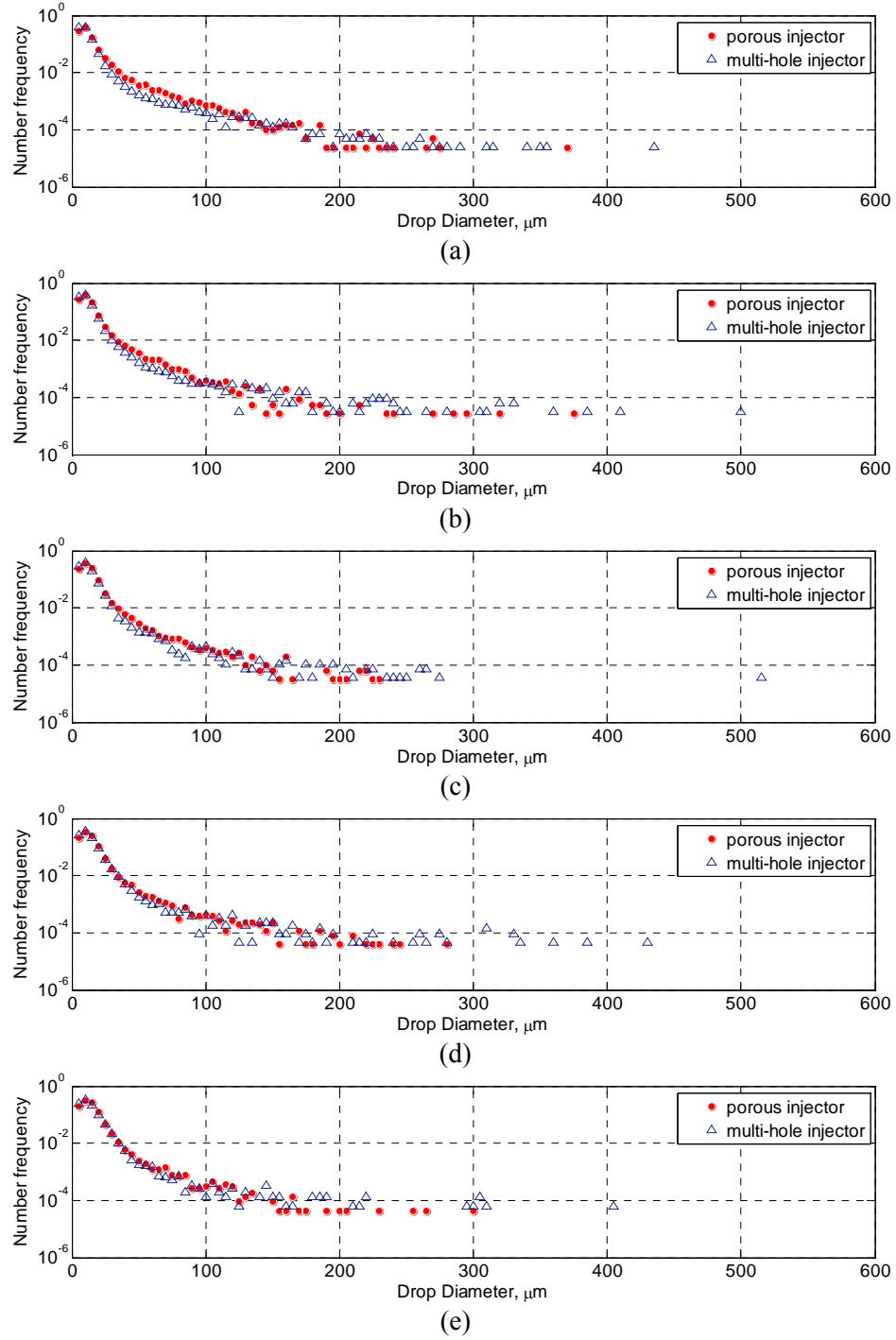


Figure 8-8. Number frequency of droplets at $\text{GLR}=0.0237$ for (a) $z/d = 37.5$, (b) 50, (c) 62.5, (d) 75, and (e) 87.5 locations along the spray centerline.

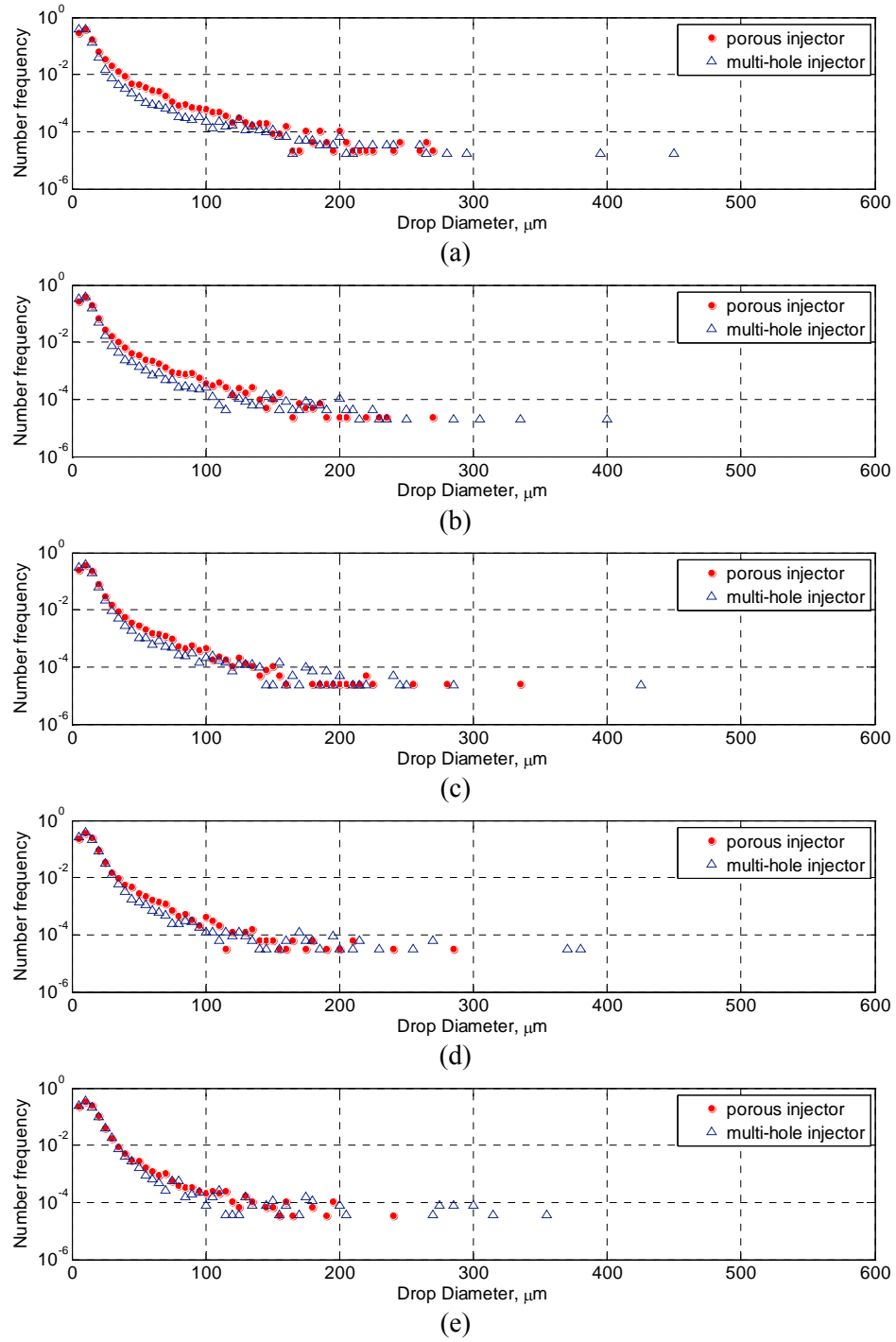


Figure 8-9. Number frequency of droplets at $\text{GLR}=0.0267$ for (a) $z/d = 37.5$, (b) 50, (c) 62.5, (d) 75, and (e) 87.5 locations along the spray centerline.

8.4.2. Droplet SMD

The SMD of all the droplets versus axial distance for GLRs of 0.0148, 0.0181, 0.0208, 0.0237, and 0.0267 are shown in Figure 8-10(a), (b), (c), (d), and (e), respectively, for the multi-hole and the porous air injectors. Slight reduction of the SMD with increase of axial distance is observed in Figure 8-11(a) - (e) for the porous air injector. The SMD of droplets is also observed to reduce at all of the axial locations with increase of GLR.

The generated spray field by the multi-hole air injector for GLR= 0.0148 shows an initially high SMD at $z/d = 37.5$ which decreases with increase of axial distance. A slight jump in SMD is also observed at $z/d = 75$ of this plot. The SMD plots of Figure 8-10(b) and (c) also demonstrate similar trend of SMD reduction with increase of axial distance except that the SMD jump at $z/d = 75$ is considerably magnified. A higher initial SMD at $z/d = 37.5$ is observed in Figure 8-10(d) which reduces at further downstream locations. The lowest SMD at $z/d = 37.5$ is observed in Figure 8-10(e) which contributes to the highest GLR. In this figure the SMD also decreases with increase of axial distance.

A smooth reduction of the SMD has been observed for the spray field generated by the atomizer applying the porous air injector. The porous air injector also generates a lower droplet SMD at all the investigated axial distances and GLRs. In general for the spray field generated by the multi-hole air injector, SMD reduction has been observed with increase of axial distance. However, several non-uniformities in terms of sudden increase or reduction of SMD have been observed along the axial distance. These flexions in the SMD trend of the multi-hole air injector can be due to a few large droplets which bias the results toward larger SMD.

Droplet SMD calculated for droplets in the range of 0 to 200 μm are shown in Figure 8-11. In the SMD calculation droplets larger than 200 μm have not been considered. The results for GLR = 0.0148, 0.0181, 0.0208, 0.0237, and 0.0267 are shown in Figure 8-11(a), (b), (c), (d), and (e), respectively, as SMD versus axial distance. It is observed that droplet SMD reduces slightly with increase of the axial distance in the spray field generated by the atomizer incorporating the porous air injector. Increase of GLR also results in slight reduction of SMD at the investigated axial locations.

Droplet SMD in the spray field generated by the multi-hole air injector demonstrates a slight reduction in droplet SMD with increase of axial distance. This trend is observed for all the GLRs except at $GLR=0.0237$ in which a significant increase in SMD is observed at $z/d = 50$. This local maximum can be contributed to the existence of a few large droplets in the recorded data of this location.

The comparison between the spray field corresponding to the porous and the multi-hole air injectors shows close SMD at majority of the investigated axial locations and GLRs. This shows that the spray fields are equivalent in terms of SMD if only droplets smaller than $200\mu\text{m}$ have been considered.

Droplet SMD for the spray field generated using the two air injectors has been calculated for the droplets smaller than $100\mu\text{m}$ and is demonstrated Figure 8-12. In the SMD calculations droplets larger than $100\mu\text{m}$ have not been considered. The results are shown in Figure 8-12(a) - (e) for $GLR = 0.0148, 0.0181, 0.0208, 0.0237, \text{ and } 0.0267$, respectively. Both types of air injectors demonstrate slight reduction in SMD with increase of axial distance. The results show that in general droplet SMD is lower for the multi-hole air injector in comparison to the porous air injector for droplets smaller than $100\mu\text{m}$. It is also observed that the difference between droplet SMD of both types of air injectors decreases as the GLR increases.

Droplet SMD for the spray field generated using the two air injectors calculated for the droplets smaller than $50\mu\text{m}$ is shown in Figure 8-13. In these calculations droplets larger than $50\mu\text{m}$ have not been considered. The results are shown in Figure 8-13 (a) - (e) for $GLR = 0.0148, 0.0181, 0.0208, 0.0237, \text{ and } 0.0267$, respectively. Droplet SMD is observed to be relatively constant with increase in axial distance for both types of air injectors. It is also observed that droplet SMD is lower for the porous air injector and the difference is reduced with increase of GLR.

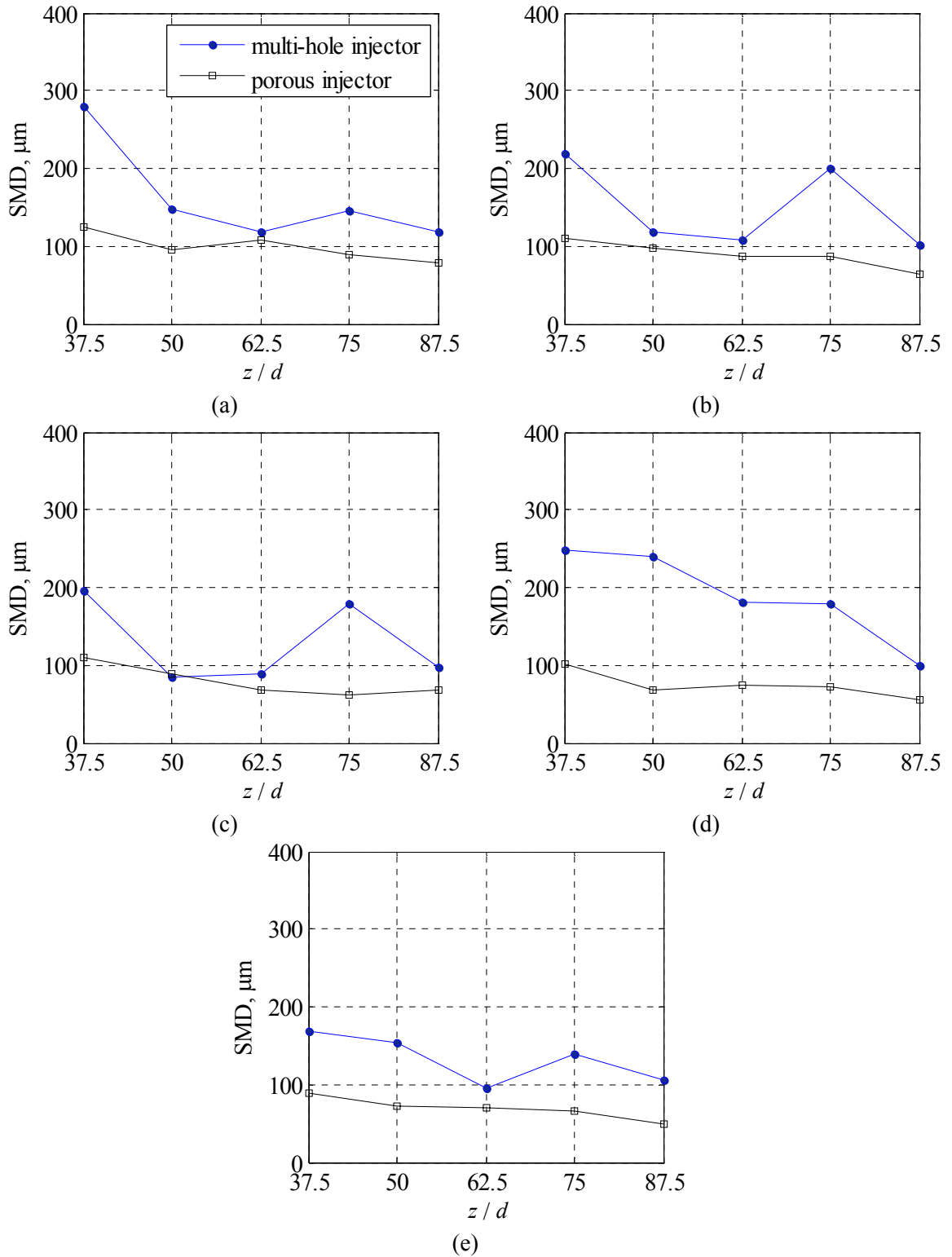


Figure 8-10. SMD of droplets generated versus axial distance generated at (a) $GLR = 0.0148$, (b) 0.0181 , (c) 0.0208 , (d) 0.0237 , (e) 0.0267 . All the droplets have been considered in the SMD calculations.

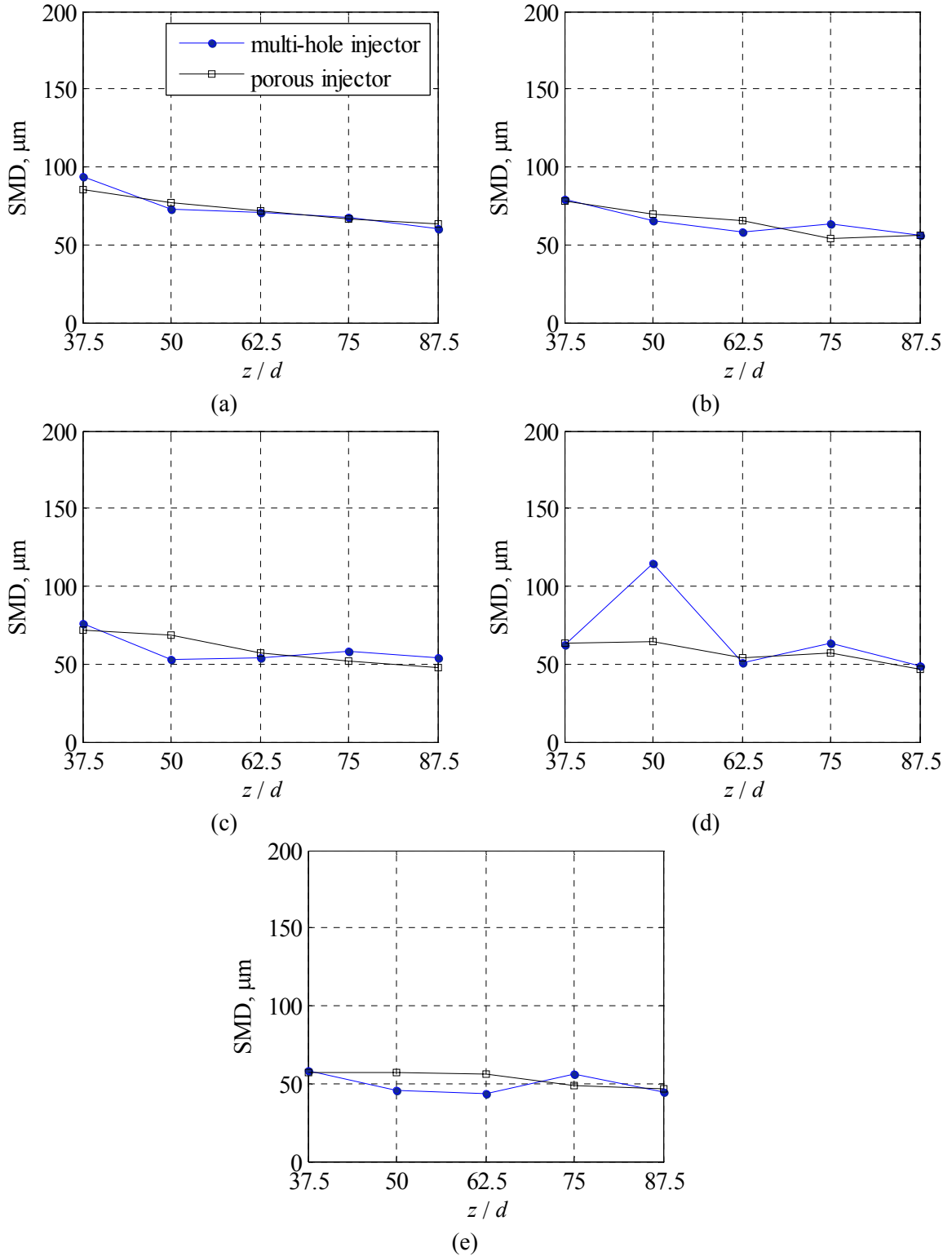


Figure 8-11. SMD of droplets generated versus axial distance generated at (a) 0.0148 (b) 0.0181 (c) 0.0208 (d) 0.0237 (e) 0.0267. Droplets larger than $200\mu\text{m}$ have not been considered in the SMD calculation.

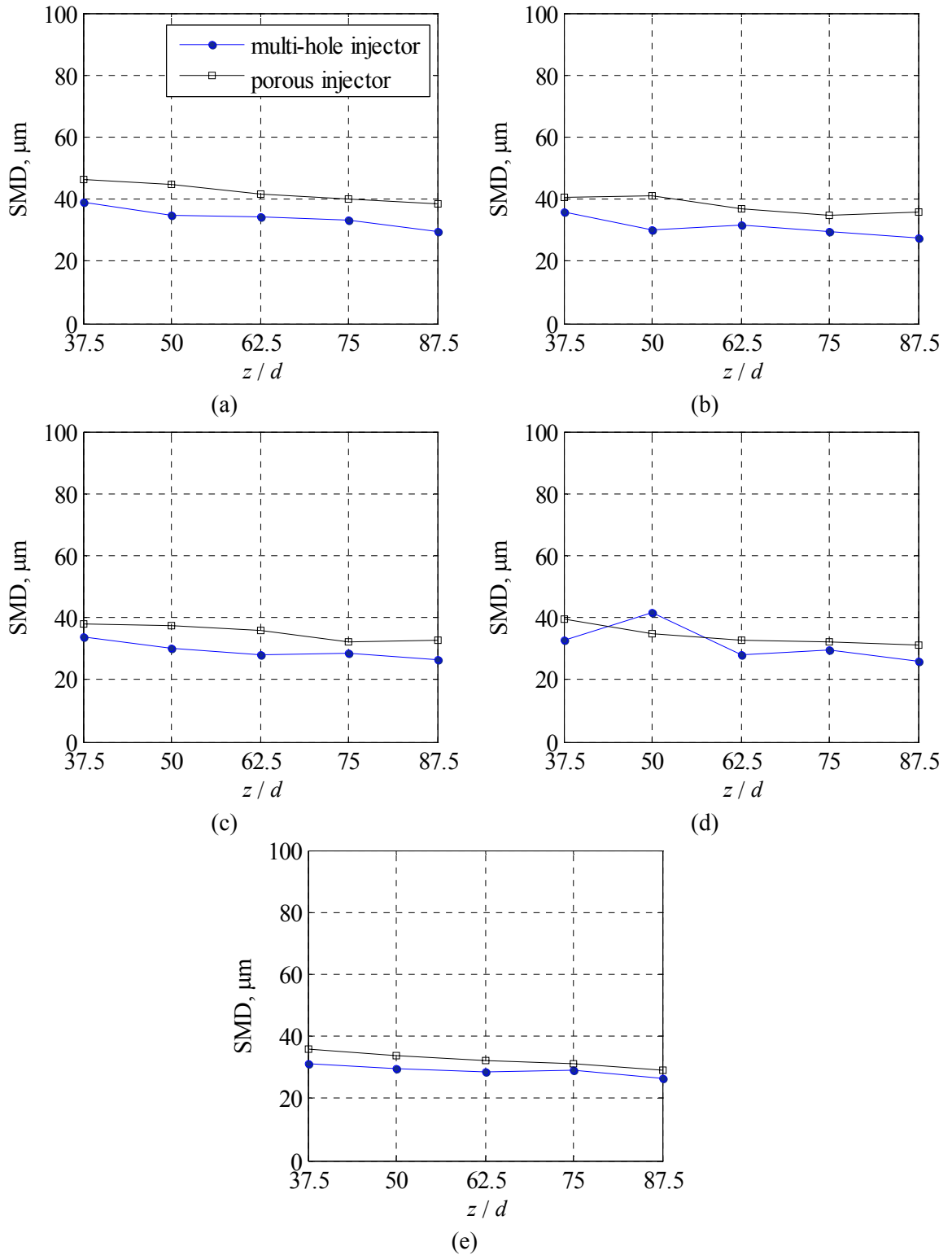


Figure 8-12. SMD of droplets generated versus axial distance generated at (a) 0.0148 (b) 0.0181 (c) 0.0208 (d) 0.0237 (e) 0.0267. Droplets larger than $100\mu\text{m}$ have not been considered in the SMD calculation.

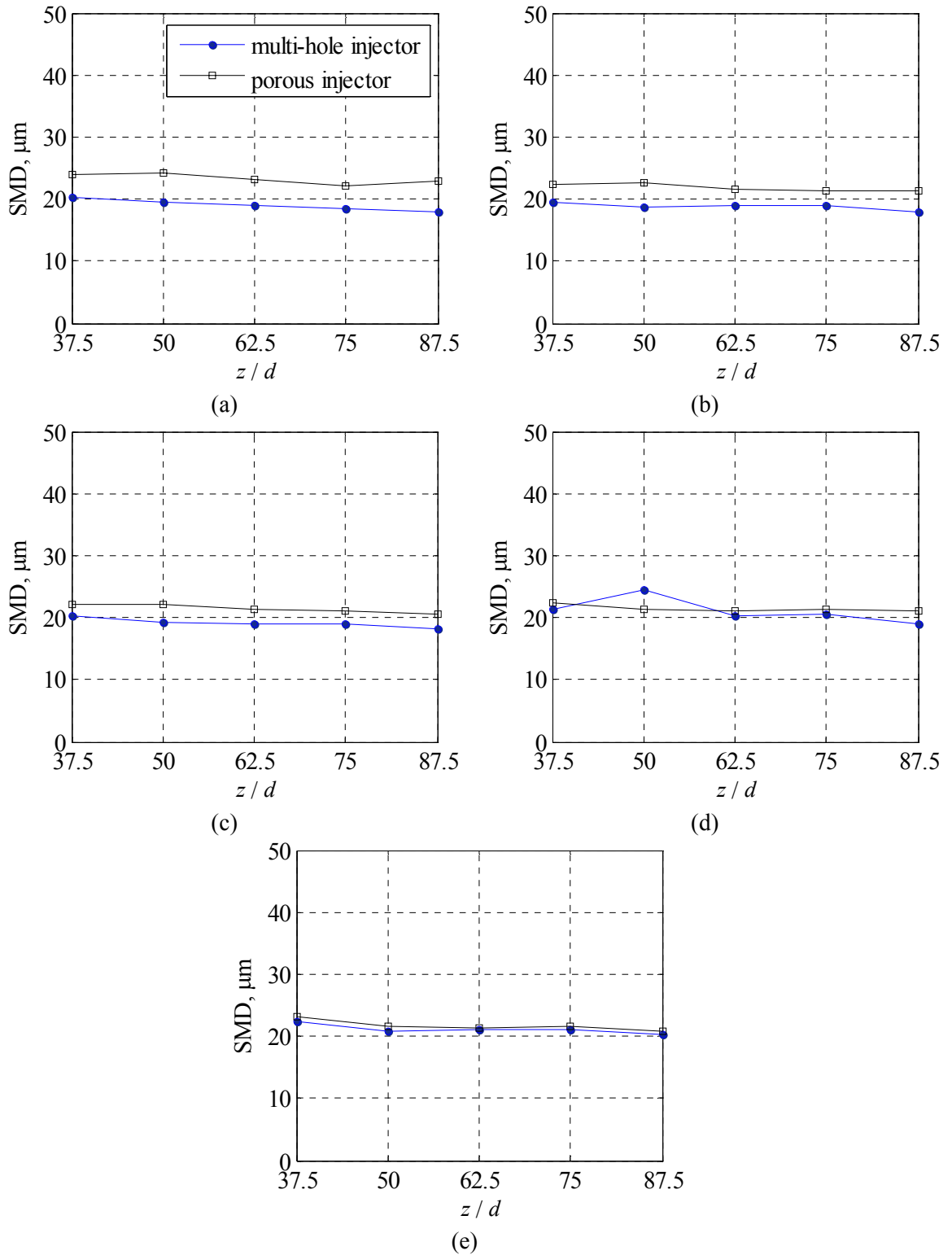


Figure 8-13. SMD of droplets generated versus axial distance generated at (a) 0.0148 (b) 0.0181 (c) 0.0208 (d) 0.0237 (e) 0.0267. Droplets larger than $50\mu\text{m}$ have not been considered in the SMD calculation.

8.4.3. Ligaments and Large Droplets

In this section the number of ligaments and large droplets in the generated spray fields are investigated. The shadowgraphy images have been processed separately to detect droplets and ligaments with an area equivalent diameter larger than $200\mu\text{m}$ in the recorded sets of 5000 images. In contrary to the previous processes, the droplets which are touching the image boarder have also been accounted. The plots are presented as number of droplets versus axial distance for $\text{GLR} = 0.0148, 0.0181, 0.0208, 0.0237,$ and 0.0267 in Figure 8-14(a), (b), (c), (d), and (e), respectively.

It is observed in Figure 8-14 that the number of droplets larger than $200\mu\text{m}$ is significantly higher for the multi-hole air injector in comparison to the porous air injector. The number of droplets larger than $200\mu\text{m}$ decreases with increase of axial distance for both the porous and the multi-hole air injectors. It is also observed that with increase of GLR the number of large droplets decreases. The reduction of the number of large droplets with increase of GLR is higher for the multi-hole air injector.

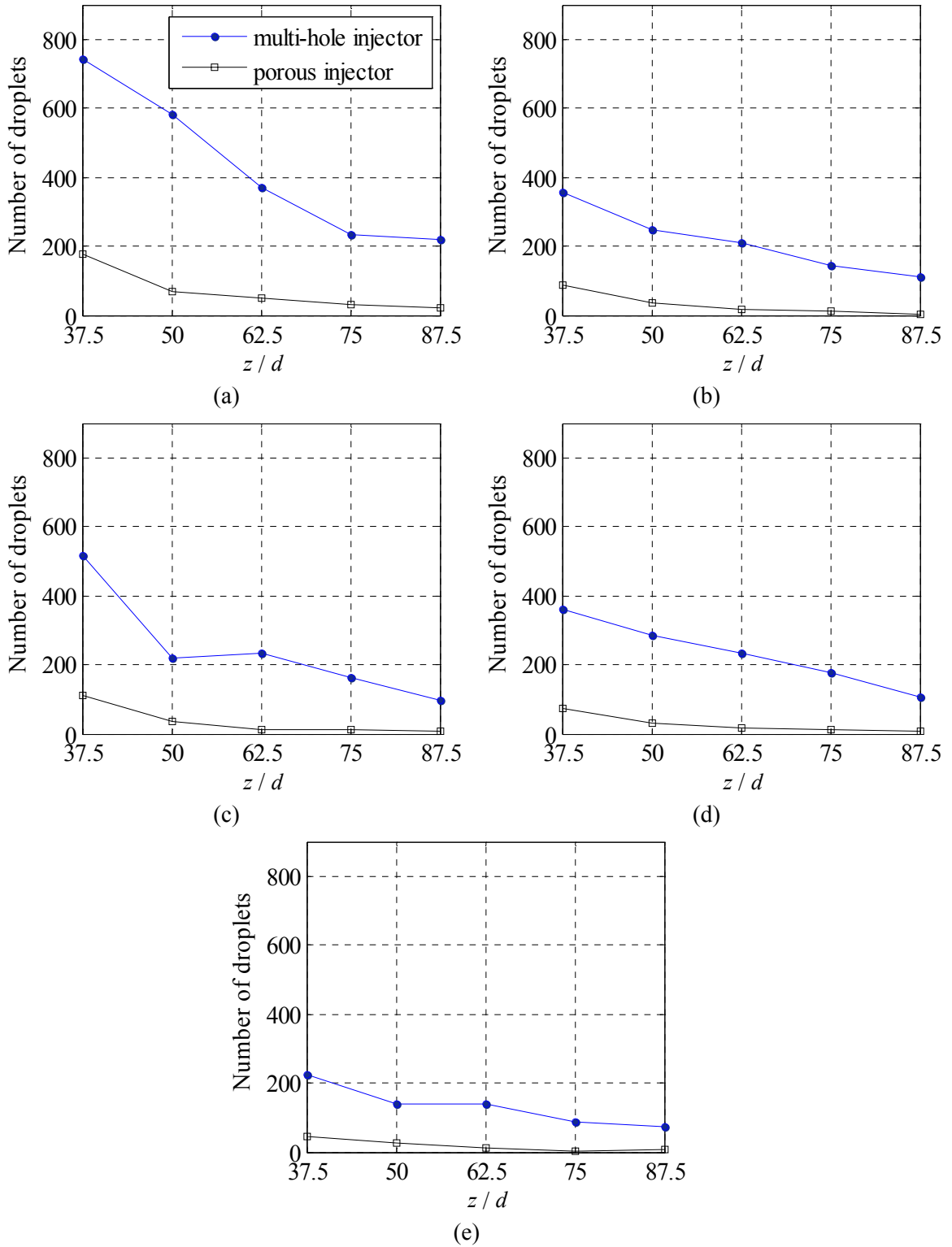


Figure 8-14. Number of droplets larger than 200 μm generated at (a) GLR = 0.0148, (b) 0.0181, (c) 0.0208, (d) 0.0237, (e) 0.0267.

8.5. Conclusion

The atomization mechanism and the generated spray field by the two effervescent atomizers incorporating the porous and the multi-hole air injectors were compared qualitatively and quantitatively.

The porous air injector generates a high number density population of small bubbles in the mixing chamber. This homogeneous mixture of gas and liquid feeds the discharge orifice with relatively constant instantaneous GLR. In the observed atomization mechanism, the liquid jet discharging from the orifice extends till $3d$ distance downward where it disintegrates into ligaments and droplets. The multi-hole air injector generates bubbles of approximately 5 mm in diameter. The generated bubbles are initially a few millimeters apart from each other and highly deformed. This mixture results in a fluctuating instantaneous GLR in the discharge orifice. Consequently, the exit orifice would be occupied by alternative liquid and gas slugs. Several atomization mechanisms have been observed which is due to fluctuations in the instantaneous GLR through the discharge orifice. This unsteady flow of gas and liquid through the discharge orifice results in pulsation and instability in the discharged spray.

The droplet size measurement demonstrated that in general droplet SMD is lower for the porous air injector in comparison to the multi-hole air injector. The droplet SMD in the spray field of the porous air injector has been observed to uniformly decrease with increase of axial distance and GLR. In general reduction of droplet SMD with increase of axial distance and GLR has also been observed for the multi-hole air injector case. However, high fluctuation in data has also been observed at a few axial locations and GLRs.

Investigation of the droplet size distribution demonstrated that the porous air injector results in formation of a narrower droplet size distribution in comparison to the multi-hole air injector. The multi-hole air injector generates higher number of droplets larger than $300\mu\text{m}$. These large droplets are generated as a result of the incomplete atomization process due to the pulsations and bursts in discharged two-phase flow.

9. Conclusion

9.1. Summary of Results

The first objective of this thesis was to contribute to the development of laser-based measurement techniques for the investigation of sprays and the atomization process. This goal has been addressed in chapters 4, 5, and 6. The second objective of this thesis was on the development of effervescent atomizers and has been addressed through chapters 7 and 8. A brief review on the results is provided here.

A review of the literature has been conducted on several shape parameters applied in various applications to identify object shape in image data. The gathered information consists of a mathematical definition, calculation procedure, application, and major characteristics of the shape parameters. A shadowgraph droplet analyzer has been applied to provide visual images of droplets of different shapes existing in a spray field. The droplets have been classified into three distinct categories of (i) spherical, (ii) deformed spheres, and (iii) ligaments based on their shape. A concavity parameter, *con*, has been suggested to distinguish the third group based on their shape concavity. The selected shape parameters have been multiplied by the *con* parameter. Among the parameters, *Parameter 8* is the most appropriate one for distinguishing spherical and deformed droplets. With the use of *Parameter 8* multiplied by the *con* factor, $con \times Parameter\ 8$, the captured spherical droplets from the experimental data images were located between values of -2 to 2. As the $con \times Parameter\ 8$ value increases toward positive or negative infinity deviation of droplet shape occurs toward the deformed sphere and the ligament groups, respectively.

A simulation has been conducted to investigate the effect of digital image discretization in quantifying droplet shape. The simulation demonstrated that the shape

parameters are influenced by image discretization with different degrees. Generally, discretization effect decreased as the ratio of image size to pixel size increases. Shape parameters which contain the geometric feature of perimeter in their mathematic definition did not approach to their theoretical values and the discretization error remained constant as the images size increased up to 160 pixels area equivalent diameter. The parameters also demonstrated different sensitivity to shape deviation. Some shape parameters introduce relatively low error due to image discretization effect but simultaneously low resolution to distinguish between different shapes. This highlights that both the sensitivity to image discretization and shape deviation should be considered to determine the most efficient shape parameter. A “clearance factor” has been suggested to rank the parameters based on lower sensitivity to image discretization and higher sensitivity to shape deviation. Results revealed that *Parameter 8* had the lowest clearance factor for a considered diameter and provides the highest resolution in distinguishing shape deviation in the presence of image discretization effect.

The effect of main characteristics of spray droplets which play the role of seeding particles in StereoPIV measurement on the accuracy of the spray droplet velocity measurement has been investigated. In the near-field dense spray region of $z/d < 70$, StereoPIV system under-measures the droplet velocity in comparison to Shadow-PTV measurement. The StereoPIV measurement at the near-field region of the spray is limited by (1) wider measurement depth-of-field and (2) higher droplet velocity gradient in the radial direction. The StereoPIV under-measurement reduces with increase of axial distance and disappears at around $z/d = 70$. With increase of axial distance, the spray becomes dilute and droplet number density decreases. In the far-field dilute region of the spray, the StereoPIV over-measures droplet velocity in comparison to Shadow-PTV measurement of 2.5 - 57.5 μm droplet size class. Comparison to the size-classified measurement also reveals that it is generally biased toward the 12.5 - 22.5 and 22.5 - 32.5 μm droplet size classes depending on the axial location. This bias is due to the droplet/pixel size ratio and also the combined effect of droplet number frequency and droplet cross-sectional area. The StereoPIV measurement would be biased toward the droplet mean diameter based on $N_f \times A$ at the far-field dilute region of the spray.

The investigations on bubble formation in liquid cross-flow showed different mechanisms and features for the generated bubbles using the wall orifice and nozzle injection configurations. In general, the average size of the bubbles generated by the wall orifice configuration is larger than the nozzle injector configuration. However, the wall orifice configuration generated bubbles with narrower size distribution. Air injection from a wall orifice configuration resulted in formation of a single group of bubbles termed preliminary bubbles. The investigation of the nozzle injection configurations demonstrated two distinct groups of bubbles: preliminary and secondary bubbles. The preliminary bubbles were smaller with a narrow size distribution and were relatively spherical. The group of secondary bubbles consisted of larger bubbles which had both spherical and non-spherical shapes. The non-spherical bubbles were caused as a result of bubble coalescence. The displacement of the air injector into the liquid cross flow also increases the number of the secondary bubbles.

The atomization mechanism and the generated spray field by the effervescent atomizer incorporating a porous air injector and a multi-hole air injector were compared qualitatively and quantitatively. The porous air injector generates a high number density population of small bubbles in the mixing chamber. The multi-hole air injector generates bubbles of approximately 5 mm in diameter which were initially a few millimeters apart from each other. The droplet size measurement demonstrated that in general droplet SMD is lower for the porous air injector in comparison to the multi-hole air injector. The porous air injector results in formation of a narrower droplet size distribution in comparison to the multi-hole air injector. The multi-hole air injector generates higher number of droplets larger than 300 μm . These large droplets are generated as a result of the incomplete atomization process due to the pulsations and bursts in discharged two-phase flow.

9.2. Future work

Some recommendations for future research in laser-based techniques for spray diagnostics and effervescent atomization.

- The developed procedure for measuring the shape of droplets is suggested to be implemented into an image-based droplet sizing software. This measurement technique can be applied to spray fields and provide a 2D map of droplet shape in a spray field.
- It is suggested to apply more advanced boundary detection algorithms to reduce the discretization error. The boundary detection methods should be capable of smoothing the boundary based on the gray-scale values of the pixels at the boundary region.
- In order to apply the StereoPIV technique to droplet velocity measurement in a spray field, it is suggested to apply imaging lenses with thin depth-of-field in order to control the measurement volume.
- Bubble formation during gas injection from a porous section into liquid cross-flow is suggested to be investigated. In this situation, the recognition of the conditions which can prevent the coalescence of bubbles is of considerable importance. The effect of certain conditions at the downstream such as blockage or change in the channel cross-section on bubble coalescent can also be investigated.
- In order to further investigate the mechanism of effervescent atomization, it is suggested to develop a facility which is accessible for conducting laser-based measurement of the internal flow. Measurement of the velocity and the liquid and the gas-phase in the discharge orifice along with their instantaneous GLR is of considerable importance.
- The correlation between the size and arrival the rate of the bubbles at the discharge orifice and the unsteadiness of effervescent atomization is also recommended as future works.

10. References

1. Cole Parmer (2007) Precision water flow meter and water flow controller operating manual.
2. Santangelo PJ, Sojka PE (1995) A holographic investigation of the near nozzle structure of an effervescent atomizer-produced spray, *Atomization and Sprays*, 5:137-155.
3. Lin SP, Reitz RD (1998) Drop and spray formation from a liquid jet, *Annual Rev Fluid Mech*, 30:85-105.
4. Ghaemi S, Nobes DS, Rahimi S (2008) Investigation of the spatial distribution of droplet SMD in the spray field of an effervescent atomizer, 21st Annual ILASS-Americas Conference, Orlando, FL, USA.
5. Ghaemi S, Nobes DS, Rahimi S (2008) Investigation of gas-liquid ratio effect on the near nozzle spatial structure of effervescent atomizer-produced spray, Canadian Society of Mechanical Engineering Forum, Ottawa, Canada.
6. Ghaemi S, Nobes DS, Rahimi S (2008) Measurement of droplet centricity and velocity in the spray field of an effervescent atomizer, 14th Int Symp on Application of Laser Techniques to Fluid Mech, Lisbon, Portugal.
7. Ghaemi S, Nobes DS, Rahimi S (2008) Effect of gas-liquid ratio on droplets centricity and velocity of an effervescent atomizer, American Society of Mechanical Engineering Fluid Engineering Conference, Jacksonville, FL, USA.
8. Ghaemi S, Nobes DS, Rahimi S (2008) Assessment of parameters for distinguishing droplet shape in a spray field using image-based techniques, *Atomization and Sprays*, under review.

9. Ghaemi S, Nobes DS, Rahimi S (2008) Evaluation of StereoPIV droplet velocity measurement in a spray field produced by an effervescent atomizer, *Spray and Combustion Dynamics*, under review.
10. Lund MT, Sojka PE, Lefebvre AH, Gosselin PG (1993) Effervescent atomization at low mass flow rates, *Atomization and Sprays*, 3:77-89.
11. Luong JK, Sojka PE (1999) Unsteadiness in effervescent sprays, *Atomization and Sprays*, 9:87-109.
12. Lefebvre AH (1988) *Atomization and sprays (combustion: an international series)*, CRC, FL, USA.
13. Mott Corporation (2009) Mott Porous Metal Data Sheet. Available via DIALOG.http://www.mottcorp.com/resource/pdf/RS_Perm_mg05.pdf. Accessed 11 Jan 2008.
14. Simmons HC, Gaag JH (1971) U.S. patent 3609043.
15. Simmons HC (1977a) The correlation of drop size distribution in fuel nozzle sprays part I: the drop-size/volume-fraction distribution, *Trans ASME J Engineering for Power*, 99:309-314.
16. Simmons HC (1977b) The correlation of drop size distribution in fuel nozzle sprays part II: the drop-size/number distribution, *Trans ASME J Engineering for Power*, 99:315-319.
17. Simmons HC (1980) The prediction of Sauter mean diameter for gas turbine fuel nozzles of different types, *Trans ASME J Engineering for Power*, 102:646-452.
18. Simmons HC, Harding CF (1981) Some effects of using water as a test fluid in fuel nozzle spray analysis, *Trans ASME J Engineering for Power*, 103:118-123.
19. Lecuona A, Sosa PA, Rodriguez PA, Zequeira RA (2000) Volumetric characterization of dispersed two phase flows by digital image analysis, *Meas Sci Technol*, 11:1151-1161.
20. Kim JY, Lee SY (2001) Dependence of spraying performance on the internal flow pattern in effervescent atomizers, *Atomization and Sprays*, 11:735-756.
21. Kashdan JT, Shrimpton, JS, Whybrew A (2007) A digital image analysis technique for quantitative characterization of high speed sprays, *Optics and Lasers in Engineering*, 45:106-115.

22. LaVision GmbH (2007) Sizing-Maser Shadow. Göttingen, Germany.
23. Adrian RJ (1991) Particle-imaging techniques for experimental fluid mechanics. *Ann Rev Fluid Mech*, 23:261-304.
24. Raffel M, Willert CE, Kompenhans J (1998) Particle image velocimetry: A practical guide, Springer Verlag, Berlin Heidelberg.
25. Adrian RJ (2005) Twenty years of Particle Image Velocimetry. *Experiments in Fluids*, 39:159-169.
26. Siegman AE (1990) New developments in laser resonators, *Proc. SPIE*, 1224:2-14.
27. Bröder D, Sommerfeld M (2007) Planar shadow image velocimetry for the analysis of the hydrodynamics in bubbly flows, *Meas Sci Technol*, 18:2513-2528.
28. Chigier NA, (1983) Drop size and velocity instrumentation, *Prog Energy Comb Sci*, 9:155-177.
29. Jones AR, (1977) A review of drop size measurement - The Application of Techniques to Dense Fuel Sprays, *Prog Energy Comb Sci*, 3:225-234.
30. Edwards CF, Marx KD (1992) Analysis of the ideal Phase-Doppler system: limitations imposed by single-particle constraint, *Atomization and Sprays*, 2:319-66.
31. Black DL, McQuay M, Bonin MP (1996) Laser-based techniques for particle-size measurement: a review of sizing methods and their industrial applications, *Prog Energy Comb Sci*, 22:267-306.
32. Alexander DR, Wiles KJ, Shaub SA, Seeman MP (1985) Effects of non-spherical particles on a Phase-Doppler spray analyzer, *Proc SPIE Particle Sizing and Spray Analysis*, 573:67-72.
33. Chigier NA and Chiu HH (1995) Mechanics and combustion of droplets and sprays, New York, Begell House.
34. Loth E (2008) Quasi-steady shape and drag of deformable bubbles and drops, *Int. Journal of Multiphase Flow*, 34:523-546.
35. Rallison JM (1984) The deformation of small viscous drops and bubbles in shear flows, *Ann Rev Fluid Mech*, 16:45-66.

36. Stiesch G (2003) Modeling engine spray and combustion processes, Germany, Springer.
37. Gelfand BE (1996) droplet breakup phenomena in flows with velocity lag, Proc Energy Comb Sci, 22:201-265.
38. Shraiber AA, Podvysotsky AM, Dubrovsky VV (1996) Deformation and breakup of drops by aerodynamic forces, Atomization and Sprays, 6:667-692.
39. Faeth GM, Hsiang LP, Wu PK (1995) Structure and breakup properties of sprays, Int. J. Multiphase Flow, 21:99-127.
40. Plich, M and Erdman, CA (1987) Use of breakup time data and velocity history data to predict the maximum size of stable fragments for acceleration-induced breakup of a liquid drop, Int. J. Multiphase Flow, 13:741-757.
41. Bachalo WD (2000) Spray diagnostics for the twenty-first century, Atomization and Sprays, 10:439-474.
42. Malot H, Blaisot JB (2000) Droplet size distribution and sphericity measurement of low density sprays through image analysis, Part. Part. Syst. Charact., 17:146-158.
43. Zeller W (1985) Direct measurement of aerosol shape factors, Aerosol Science and Technology, 4:45-63.
44. Eriksson M, Alderbornm G, Nystrom C, Podczek F, Newton JM (1997) Comparison between and evaluation of some methods for the assessment of the sphericity of pellets, Int. J. of Pharmaceutics, 148:149-154.
45. Podczek F, Rahman SR, Newton JM (1999) Evaluation of a standardized procedure to assess the shape of pellets using image analysis, International J. of Pharmaceutics, 192:123-138.
46. Bouwman AM, Bosma JM, Vonk P (2004) Which shape factor best describes a granules? Powder Technology, 146:66-72.
47. Carosone F, Cenedese A, Querzoli G (1995) Recognition of partially overlapped particle images using the kohonen neural network, Experiments in Fluids, 19:225-232.

48. Iwano S, Nalamura T, Kamioka Y, Ishigaki T (2005) Computer-aided diagnosis: a shape classification of pulmonary nodules imaged by high resolution CT, *Computerized Medical Imaging and Graphics*, 29:565-570.
49. Pouletaut P, Claude I, Winzenrieth R, Ho Ba Tho MC, Sebag G (2005) Automated analysis of MR image of hip: geometrical evaluation of the Legg-Calve-Perthes disease, *Medical Engineering and Physics*, 27:415-424.
50. Ito M, Chono T, Sekiguchi M, Shina T, Mori H, Tohno E (2005) Quantitative evaluation of diagnostic information around the contours in ultrasound images, *J Med Ultrasonics*, 32:135-144.
51. Mayor L, Pissarra J, Sereno AM (2008) Microstructural changes during osmotic Dehydration of parenchymatic pumpkin tissue, *Journal of Food Engineering*, 85:326-339.
52. Dickson MA, Bausch WC, Howarth MS (1994) Classification of a broadleaf weed a geeey weed and corn using image processing techniques, *Proceedings of SPIE*, 2345:297-305.
53. Sun DW, Brosnan T (2003) Pizza quality evaluation using computer vision part 1 pizza base and sauce spread, *Journal of food Engineering*, 57:81-89.
54. Lee DJ, Xu X, Lane RM, Zhan P (2004) Shape analysis for an automated oyster grading system, *Proceedings of SPIE*, 5606:27-36.
55. Montavon G, Coddet C (1996) Quantification of particle morphologies in view of quality control of the thermal spray process, *Material Characterization*, 36:257-269.
56. Patchigolla K, Wilkinson D (2008) Characterization of organic and inorganic chemicals formed by batch-cooling crystallization, *Shape and Size*, 47:804-812.
57. Patchigolla K, Wilkinson D, Li M (2006) Measuring size distribution of organic crystals of different shapes using different technologies, *Part Part Syst Charact*, 23:138-144.
58. Mayor L, Silva MA, Sereno AM (2005) Microstructural changes during drying of apple slices, *Drying Technology*, 23:2261-2276.
59. Podczeczek F, Newton JMA (1994) Shape factor to characterize the quality of spheroids, *J Pharm Pharmacol*, 46:82-85.

60. Almedia-Prieto S, Blanco-Mendez J, and Otero-Espinar FJ (2004) Image analysis of the shape of granulated powder grains, *J of Pharmaceutical Sciences*, 93:621-634.
61. Kim KS, Kim SS (1994) Drop sizing and depth-of-field correction in TV imaging, *Atomization and Sprays*, 4:65-78.
62. Sudheer KP, Panda RK (2000) Digital image processing for determining drop sizes from irrigation spray nozzles, *Agricultural Water Management*, 45:159-67.
63. Kashdan JT, Shrimpton JS, Whybrew A (2007) A digital image analysis technique for quantitative characterisation of high speed sprays, *Optics and Lasers in Engineering*, 45:106-115.
64. Kashdan JT, Shrimpton JS, Whybrew A (2004) Two phase flow characterization by automated digital image analysis part 2: application of PDIA for sizing sprays, *Part Part Syst Charact*, 21:15-23.
65. Almedia-Prieto S, Blanco-Mendez J, Otero-Espinar FJ (2006) Microscopic image analysis techniques for the morphological characterization of pharmaceutical particles: influence of process variables, *Journal of Pharmaceutical Science*, 95:348-357.
66. Podczek F, Newton JM (1995) The evaluation of a three dimensional shape factor for the quantitative assessment of the sphericity and surface roughness of pellets, *Int J Pharm*, 124:253-259.
67. Massa TM, Yang ML, Ho JYC, Brash JL, Santerre JP (2005) Fibrinogen surface distribution correlates to platelet adhesion pattern on fluorinated surface-modified polyetherurethane, *Biomaterials*, 26:7367-7376.
68. Leader JK, Rogers RM, Fuhrman CR, Scirba FC, Zheng B, Thompson PF, Weissfeld JL, Golla SK, Gur D (2004) Size and morphology of the trachea before and after lung volume reduction surgery, *American Journal of Roentgenology*, 183:316-321.
69. Saigo K, Hashimoto M, Kumagai S, Tanaka C, Imoto S (2005) Usefulness of particle image analyzer for evaluation of fragmented red cells, *Transfusion and Apheresis Science*, 33:71-73.

70. Hernandez-Aguilar JR, Coleman RG, Gomez CO, Finch, JO (2004) A comparison between capillary and imaging techniques for sizing bubbles in floating systems, *Minerals Engineering*, 17:53-61.
71. Malysa K, Ng S, Cymbalisty L, Czarnecki J, Masliyah J (1999) A method of visualization and characterization of aggregate flow inside a separation vessel, part 1 size, shape and rise velocity of the aggregates, *Int J Miner Process*, 55:171-188.
72. Maghrebi W, Baccour L, Khabou MA, Alimi AM (2007) An indexing and retrieval system of historic art images based on fuzzy shape similarity, *Lecture Notes in Computer Science*, 4827:623-533.
73. Hwang HG, Kim SW, Xu CP, Choi JW, Yun JW (2004) Morphological and rheological properties of the three different species of basidiomycetes phellinus in submerged cultures, *Journal of Applied Microbiology*, 96:1296-1305.
74. Wynn TJ, Stewart SA (2005) Comparative testing of ellipse fitting algorithm: implications for analysis of strain and curvature, *Journal of Structural Geology*, 27, 1973-1985.
75. Mohamed AA, Ashman RB, Kirleis AW (1993) Pericarp Thickness and Other Kernel Physical Characteristics Relate to Microwave Popping Quality of Popcorn, *Journal of food science*, 58:342-346.
76. Lewicki PP, Pawlak G (2003) Effect of drying on microstructure of plant issue, *Drying Technology*, 21:657-683.
77. Wanchoo RK, Sharma SK, Gupta R (2003) Shape of a Newtonian liquid drop moving through an immiscible quiescent non-Newtonian liquid, *Chemical Engineering and Processing*, 42:387-393.
78. Schneiderhohn P (1954) Eine vergleichende studie uber methoden zur quantitativen bestimmung von abrundung und Form an sandkornern, *heidelberger beitrage zur mineralogie und petrographie*, 4:172-91.
79. Chigier N (1990) Optical imaging of sprays, *Prog Energy Comust Sci*, 17:211-262.
80. Gonzalez RC, Woods RE, Eddins, SL (2004) *Digital image processing using Matlab*, New Jersey, Pearson Education Inc.

81. *MatLab help* (2007) The MathWorks Inc.
82. Haralick RM, Shapiro LG (1992) *Computer and robot vision*, Reading Mass, Addison-Wesley Publishing Company Inc.
83. Pentland A (1927) A method of measuring the angularity of sands, *Proceedings and Transactions of the Royal Society of Canada*, 21.
84. Parker JR (1994) *Practical Computer Vision Using C*, New York, John Wiley and Sons Inc.
85. Riddle DF (1984) *Calculus and Analytical Geometry 4th Ed*, Belmont, CA, Wadsworth Publishing Company.
86. Cox EP (1927) A Method of Assigning Numerical and Percentage Values to the Degree of Roundness of Sand Grains, *Journal of Paleontology*, 1:179-83.
87. Lee SY, Kim YD (2004) Sizing of Spray Particles Using Image Processing Techniques, *KSME International Journal*, 18:879-894.
88. Koh KU, Kim JY, Lee SY (2001) Determination of In-focus Criteria and Depth of Field in Image Processing of Spray Particles. *Atomization and Sprays*, 11:317-333.
89. Lebrun D, Touil CE, Ozkul C (1996) Methods for the Deconvolution of Defocused-images Pairs Recorded Separately on Two CCD Cameras: Application to Particle Sizing. *Applied Optics*, 35:6375-6381.
90. Hileman GA, Upadrashta SM, Neau SH, Drug Solubility Effects on Predicting Optimum Conditions for Extrusion and Spheronization of Pellets. *Pharm. Dev. Technol.* 1997, 2:43-52.
91. Hellen L, Yliruusi J, Process Variables of Instant Granulator and Spheroniser III. Shape and Shape Distribution of Pellets, *Int J of Pharm*, 96:217-223.
92. Wan LSC, Heng PWS, Liew CV (1993) Spheronization Conditions on Spheroid Shape and Size, *Int J Pharm*, 96:59-65.
93. Baert L, Fanara D, Remon JP, Massart D (1992) Correlation of Extrusion Forces, Raw Materials and Sphere Characteristics, *J Pharm Pharmacol*, 44:676-681.

94. Vervaet C, Remon JP (1996) Influence of impeller design, method of screen perforation and perforation geometry on the quality made by extrusion-spheronisation, *Int. J. Pharm*, 133:29-37.
95. Vervaet C, Baert L, Risha PA, Jean-Paul R, The influence of extrusion screen on pellet quality using an instrumented basket extruder, *Int J Pharm*, 1994, 107:29-39.
96. Pavlova AA, Otani K, Amitay M, Active Control of Sprays Using a Single Synthetic Jet Actuator, *Int J of Heat and Fluid Flow*, 2008, 29:131-148.
97. Parker JR (1994) *Practical Computer Vision Using C*. John Wiley and Sons, New York: Inc.
98. Berndt B (1985) *Ramanujan's Notebooks Part III*, Springer-Verlag, New York.
99. Turns SR (200) *An Introduction to Combustion*, McGraw-Hill, New York.
100. Suh HK, Park SW (2007) A Study of the Flow and Atomization Characteristics of Impinged Diesel Spray on a Chamber Wall, *Atomization and Sprays*, 17:569-599.
101. Cao ZM, Nishino K, Mizuno S, Torii K (2000) PIV measurement of internal structure of diesel fuel spray, *Experiments in Fluids*, 33:221-219.
102. Wicker RB, Loya HI, Aaton HP (1999) SIDI Fuel Spray Structure Investigation Using Flow Visualization and Digital Particle Image Velocimetry, *SAE Tech Paper*, 1999-01-3535.
103. Micheli P (2003) Understanding How a Spray Gun Atomizes Paint, *Metal Finishing*, 101:59-64.
104. Taylor WA, Womac AR, Miller, PCH, Taylor PB (2004) An Attempt to Relate Drop Size to Drift Risk, *Proc of the Int Conf on Pesticide Application for Drift Management*, Hawaii, 210-223.
105. Palero V, Ikeda Y (2001) Characterization of the Three-Dimensional Flame-Holding Mechanism in an Industrial Oil Burner with Stereoscopic Particle Image Velocimetry, *J of Turbulence*, 2.
106. Wu Z, Zhu Z, Huang Z (2006) An Experimental Study on the Spray Structure of Oxygenated Fuel Using Laser-Based Visualization and Particle Image Velocimetry, *Fuel*, 85:1458-1464.

107. Wang Y, Li Y, Weng S (2006) Experimental Investigation on Inner Two Phase Flow in Counter Flow Spray Saturator for HAT Cycle, *Applied Thermal Engineering*, 26:2417-2424.
108. Kosiwczuk W, Cessou A, Trinite M, Lecordier B (2005) Simultaneous Velocity Field Measurement in Two-Phase Flows for Turbulent Mixing of Sprays by Means of Two-Phase PIV, *Experiments in Fluids*, 39:895-908.
109. Yamakawa M, Isshiki S, Lee J, Nishida K (2001) 3-D PIV Analysis of Structural Behavior of D.I. Gasoline Spray, In SAE technical Paper Series: International Fall Fuels and Lubricants Meeting and Exposition.
110. Gerontakos P, Lee T (2008) Particle Image Velocimetry Investigation of Flow over Unsteady Airfoil with Trailing-Edge Strip, *Experiments in Fluids*, 44:539-556.
111. Hambleton WY, Hutchins N, Marusic I (2006) Simultaneous Orthogonal-Plane Particle Image Velocimetry Measurement in a Turbulent Boundary Layer, *Journal of Fluid Mechanics*, 560:53-64.
112. Ikeda Y, Yamada N, Kawahara N (1998) PIV Application for Spray Characteristic Measurement, 9th Symp. On Applic. of Laser Techniques to Fluid Mech, Lisbon.
113. Palero V, Sato K, Ikeda Y, Nakajima T (2000) Stereoscopic Particle Image Velocimetry Evaluation in a Spray, 8th ICLASS.
114. Ikeda Y, Yamada N, Nakajima T (2000) Multi-Intensity-Layer Particle-Image Velocimetry for Spray Measurement, *Meas Sci Technol*, 11:617-626.
115. Palero VR, Ikeda Y (2002) Droplet-Size-Classified Stereoscopic PIV for Spray Characteristics, *Meas Sci Technol*, 13:1050-1057.
116. Simmons HC, Investigating the Commercial Instrument Market. In: Tishkoff JM, Ingebo RD, Kennedy JB, Liquid particle size measurement techniques, ASTM STP 848, 1984, 5-21.
117. Sutherland KM, Derek DT, Gordon LS (1998) Independent control of blood gas PO₂ and PCO₂ in bubble oxygenator, *Clin Phys Physiol Meas*, 9:97.
118. Ishil M, Hibiki T (2006) Thermo-fluid dynamics of two-phase flow, Springer, New York.

119. Nahra HK, Kamotani Y (2000) Bubble formation from wall orifice in liquid cross-flow under low gravity, *Chemical Engineering Science* 55:4653.
120. Iguchi M, Chihara T, Takanashi N, Ogawa Y, Tokumitsu N, Morita Z (1995) X-ray fluoroscopic observation of bubble characteristics in a molten iron bar, *ISIJ International*, 35:1354.
121. Bai H, Thomas BG (2001) Bubble formation during horizontal gas injection into downward-flowing liquid, 32B:1143.
122. Loubiere K, Castaignede V, Hebrard G, Roustan M (2004) Bubble formation at flexible orifice with liquid cross-flow, *Chemical Engineering and Processing* 43, 717.
123. Ganan-Calvo AM, Gordillo JM (2001) Perfectly monodisperse microbubbling by capillary flow focusing, *Phys Rev Lett*, 87, 027301.
124. Gordillo JM, Ganan-Calvo AM, Perez-Saborid M (2001) Monodisperse microbubbling: Absolute instabilities in coflowing gas-liquid jets, *Phys Fluids*, 13:3839.
125. Gordillo JM, Cheng Z, Ganan-Calvo AM, Weitz DA (2004) A new device for the generation of microbubbles, *Phys. Fluids*, 15:2828.
126. Kulkarni AA, Joshi JB (2005) Bubble formation and bubble rise velocity on gas-liquid systems, a review, *Ind. Eng. Chem. Res.* 44:5873.
127. Tan RBH, Chen WB, Tan KH (2000) A non-spherical model for bubble formation with liquid cross-flow, *Chemical Engineering Science*, 55:6259.
128. Maier CG (1927) Producing small bubbles of gas in liquids by submerged orifices, *US Bureau of Mines Bulletin*, 260:62-121.
129. Sullivan SL, Hardy BR, Holland CD (1964) Formation of air bubbles at orifices submerged beneath liquids, *A.I.Ch.E. Journal*, 5:848.
130. Tsuge H, Hibino S (1983) Bubble formation from an orifice submerged in liquids, *Chem. Eng. Commum.*, 22:63.
131. Forrester SE, Rielly CD (1998) Bubble formation from cylindrical, flat and concave sections exposed to a strong liquid cross-flow, *Chemical Engineering Science*, 53:1517.

132. Zhang W, Tan RBH (2003) A model for bubble formation and weeping at a submerged orifice with liquid cross-flow, *Chemical Engineering Science*, 58:287.
133. Tsuge H (1986) Hydrodynamics of bubble formation from submerged orifices, *Encyclopedia of Fluid Mechanics 3*, edited by N.P. Chermisinoff, Gulf, Houston.
134. Kawase Y, Ulbrecht JJ (1981) Formation of drops and bubbles in flowing liquids, *Ind Eng Chem Process Des Dev*, 20:636.
135. Marshall SH, Chudacek MW, Bagster DF (1993) A model for bubble formation from an orifice with liquid cross-flow, *Chemical Engineering Science*, 48:2049.
136. Kim I, Kamotani Y, Ostrach S (1994) Modeling bubble and drop formation in flowing liquids in microgravity, *AIChE journal*, 40:19.
137. Lefebvre AH (1988) A Novel Method of Atomization with Potential Gas Turbine Applications, *Def Sci J*, 38:353-362.
138. Lefebvre AH, Wang XF, Martin CA (1988) Spray Characteristics of Aerated-Liquid Pressure Atomizers, *J Propulsion*, 4.
139. Wang XF, Chin JS (1989) Lefebvre AH, Influence of Gas-Injector Geometry on Atomization Performance of Aerated-Liquid Nozzles, *Int J of Turbo and Jet Engines*, 6:271-279.
140. Roesler TC, Lefebvre AH (1989) Studies on Aerated-Liquid Atomization, *Int J of Turbo and Jet Engines*, 6:221-230.
141. Sovania SD, Sojka PE, Lefebvre AH (2001) Effervescent Atomization, *Progress in Energy and Combustion Science*, 27:483-521.
142. Mostafa A, Fouad M, Enayet M, Osman S (2004) Measurements of Spray Characteristics Produced by Effervescent Atomizers, 40th AIAA/ASME/SAE/ASEE Joint Propulsion Conference and Exhibit, Florida.
143. Mullinger PJ, Chigier NA (1974) The Design and Performance of Internal Mixing Multijet Twin Fluid Atomizers, *J Inst Fuel*, 47:251-261.
144. Kim JY, Lee SY (2001) Dependence of Spraying Performance on the Internal Flow Pattern in Effervescent Atomizers, *Atomization and Sprays*, 11:735-756.

145. Lorcher M, Schmist F, Mewes D (2005) Effervescent atomization of liquids, *Atomization and Sprays*, 15:145-168.
146. Buckner HE, Sojka PE (1991) Effervescent atomization of high viscosity fluids. part 1: Newtonian liquids, *Atomization and Sprays*, 1:239-252.
147. Wade RA, Weerts JM, Sojka PE, Gore JP, Eckerle WA (1999) Effervescent atomization at injection pressures in the MPa range, *Atomization and Sprays*, 9:651-667.
148. Sovani SD, Crofts JD, Sojka PE, Gore, JP, Eckerle JP (2005) Structure and steady-state spray performance of an effervescent diesel injector, *Fuel*, 1503-1514.
149. Sovani SD, Chou E, Sojka PE, Gore JP, Eckerle WA, Crofts JD (2001) High pressure effervescent atomization: effect of ambient pressure on spray cone angle, *Fuel*, 427-735.
150. Panchagnula MV, Sojka PE (1999) Spatial droplet velocity and size profiles in effervescent atomizer-produced sprays, *Fuel*, 729-741.
151. Sutherland JJ, Sojka PE, Plesniak MW (1997) Ligament controlled effervescent atomization, *Atomization and Sprays*, 7:383-406.
152. Whitlow JD, Lefebvre AH (1993) Effervescent atomizer operation and spray characteristics, *Spray and Atomization*, 3:137-155.
153. Catlin CA, Swithenbank J (2001) Physical processes influencing effervescent atomizer performance in the slug and annular flow regimes, *Atomization and Sprays*, 575-595.
154. Jedelsky J, Miroslav J (2008) Unsteadiness in effervescent spray: a new evaluation method and the influence of operational condition, *Atomization and Sprays*, 18:49-83.
155. Chen SK, Lefebvre AH, Rollbuhler J (1993) Influence of ambient air pressure on effervescent atomization, *Journal of Propulsion and Power*, 9.
156. Rosin P, Rammler E (1993) The laws governing the fineness of powdered coal, *J Inst Fuel*, 7:29-36.
157. Turns SR (2000) *An introduction to combustion; concepts and applications*, McGrawHill, New York.

158. Nielsen AF, Bertelsen P, Kristensen HG, Kristensen J, Hovgaard L (2006) Investigation and comparison of performance of effervescent and standard pneumatic atomizer intended for soluble aqueous coating, *Pharmaceutical Development and Research*, 11:243-253.
159. Petersen FJ, Worts O, Schaefer T, Sojka PE (2004) Design and atomization properties for an inside-out type effervescent atomizer, 30:319-326.
160. Ghaemi S, Rahimi P, Nobes DS (2008) Evaluation of digital image discretization error in droplet shape measurement using simulation, *Particle and Particle Systems Characterization*, under review.
161. Ghaemi S, Rahimi P, Nobes DS (2008) The effect of gas-injector location on bubble formation in liquid cross flow, *Physics of Fluids*, under review.

11. Appendix A: CVI Code

Appendix A1 shows the CVI panel developed to communicate with the two flow meters and also two pressure transducers. The desired flow rates should be entered in the allocated areas. The panel also monitors the flow rates, temperatures, and line-pressures measured using the flow meters. Instantaneous plots of water flow rate, air flow rate, and pressure versus time can also shown in the panel. The GLR ratio which is the main non-dimensional parameter used for characterizing the operation of effervescent atomizers is calculated and shown on the panel. Appendix A2 shows the developed code in the CVI software.

Appendix A1: The CVI panel:

Effluvent Spray
File Advanced Settings Help

START Num 0

5.00 Time (sec) 0

2.50 Time (min) 0.0

5.00 Hz 0.0

QUIT

Water

AIR

DAQ

Log to File

Display Graph

Com Port Connection

Air Water

GLR %

0.00

Atomizer

Air SVFR (LPM) 0.0

Water VFR (MLPM) 0

Ave. Press. #1 psi 0

Ave. Press. #2 psi 0

Press. #1

0.0 Press #1 (psi) 0.0 Press #2 (psi)

0 Ave. Press #1 (psi) 0 Ave. Press #2 (psi)

0.00 Volt. 0.00 Volt.

Press. #2

0.0 Press #1 (psi) 0.0 Press #2 (psi)

0 Ave. Press #1 (psi) 0 Ave. Press #2 (psi)

0.00 Volt. 0.00 Volt.

Air Flow Meter

FlowRate (SLPM) 0.00

Set FlowRate

Temp C 0.00

Vol LPM 0.00

Vol SLPM 0.00

PSIA 0.00

Water Flow Meter

FlowRate (MLPM) 0.00

Set FlowRate

Temp C 0.00

Vol MLPM 0.00

PSIA 0.00

Pressure #1 (psig)

Pressure #2 (psig)

Air Mass Flow Rate (SLPM)

Water Volume Flow Rate (MLPM)

Appendix A2: The CVI code:

```
//#include <dataacq.h>
// ESpray
//
// Main program file for the
// Effervescent Flow Nozzle Project
//
// Who: DSN and Sina Ghaemi
//
// Date:          Version: Comment
// 25 May 2007   V_1
// Written to run one Cole-Parmer Air and Water Flow meters + DAQ

#include "cbw.h"
#include <gpib.h>
#include <formatio.h>
#include <rs232.h>
#include <utility.h>
#include <ansi_c.h>
#include <analysis.h>
#include <cvirte.h>
#include <userint.h>
#include <ctype.h>
#include <ESpray_Declare.h>
#include <ESpray.h>

/*****
// main          : MCP main function
*****/
int main (int argc, char *argv[])
{
    if (InitCVIRTE (0, argv, 0) == 0)
        return -1; /* out of memory */
    if ((panelHandle = LoadPanel (0, "ESpray.uir", PANEL)) < 0)
        return -1;
    // Set the panel variables
    g_Handle = LoadPanel (0, "ESpray.uir", G_SETUP );
    com_Handle = LoadPanel (0, "ESpray.uir", COM );
    a_Handle = LoadPanel (0, "ESpray.uir", ABOUT );
    s_Handle = LoadPanel (0, "ESpray.uir", SAVE_Con);

    DisplayPanel (panelHandle);
    DSN_Init();
    DSN_Init2();
    SetSleepPolicy (VAL_SLEEP_MORE);
    SetPanelAttribute (panelHandle, ATTR_WINDOW_ZOOM, VAL_MAXIMIZE);
    RunUserInterface ();
    DiscardPanel (panelHandle);
    CloseCVIRTE ();
    return 0;
}

/*****
// ExitCallback      : Exit menu
*****/
void CVICALLBACK ExitCallback (int menuBar, int menuItem, void *callbackData, int panel)
{
    DisplayPanel (s_Handle);
}

/*****
// QuitCallback      : Main panel quit
*****/
int CVICALLBACK QuitCallback (int panel, int control, int event,
    void *callbackData, int eventData1, int eventData2)
{
    switch (event)
    {
        case EVENT_COMMIT:
            DisplayPanel (s_Handle);
            break;
        case EVENT_RIGHT_CLICK:
            break;
    }
}
```

```

    return 0;
}
//*****
// DSN_MainPanelQuit: Main panel quit function
//*****
void DSN_MainPanelQuit(void)
{int i;
  QuitUserInterface (0);

return;
}
//*****
// Save_MCP_Config: Save the current configuration on exit
//*****
int CVICALLBACK Save_MCP_Config (int panel, int control, int event,
    void *callbackData, int eventData1, int eventData2)
{
  switch (event)
  {
    case EVENT_COMMIT:
      switch (control)
      {
        case SAVE_Con_SAVE_YES:
          DSN_Save_Config(0);
          HidePanel (s_Handle);
          DSN_MainPanelQuit();
          break;

        case SAVE_Con_SAVE_NO:
          HidePanel (s_Handle);
          DSN_MainPanelQuit();
          break;

        case SAVE_Con_SAVE_CANCEL:
          HidePanel (s_Handle);
          break;

      }
      break;
    case EVENT_RIGHT_CLICK:
      break;
  }
  return 0;
}
//*****
// SHOW AND CLOSE CALLBACKS FOR OTHER PANELS
//*****

//*****
// GRAPH SETUP
//*****
int CVICALLBACK SHOW_Graphs (int panel, int control, int event,
    void *callbackData, int eventData1, int eventData2)
{
  switch (event)
  {
    case EVENT_COMMIT:
      break;

    case EVENT_RIGHT_CLICK:
      DisplayPanel (g_Handle);
      break;
  }
  return 0;
}

int CVICALLBACK CLOSE_Graphs (int panel, int control, int event,
    void *callbackData, int eventData1, int eventData2)
{
  switch (event)
  {
    case EVENT_COMMIT:
      HidePanel (g_Handle);
      break;

    case EVENT_RIGHT_CLICK:
      break;
  }
  return 0;
}
//*****
// ABOUT
//*****

```

```

void CVICALLBACK SHOW_About (int menuBar, int menuItem, void *callbackData,
                             int panel)
{
    DisplayPanel (a_Handle);
}

int CVICALLBACK CLOSE_About (int panel, int control, int event,
                             void *callbackData, int eventData1, int eventData2)
{
    switch (event)
    {
        case EVENT_COMMIT:
            HidePanel (a_Handle);
            break;
        case EVENT_RIGHT_CLICK:

            break;
    }
    return 0;
}
//*****
// COMMUNICATIONS SETUP
//*****
void CVICALLBACK SHOW_Com (int menuBar, int menuItem, void *callbackData,
                           int panel)
{
    DisplayPanel (com_Handle);
}

int CVICALLBACK CLOSE_Com (int panel, int control, int event,
                            void *callbackData, int eventData1, int eventData2)
{
    switch (event)
    {
        case EVENT_COMMIT:
            HidePanel (com_Handle);
            break;
        case EVENT_RIGHT_CLICK:

            break;
    }
    return 0;
}

//*****
// DSN_SHIFT          : Will step data along an array
//                   : For all data that can be plotted
//*****
void DSN_SHIFT(void)
{
    Shift (step, NUM, 1, T_array);
    Copy1D (T_array, NUM, step );
    Shift (PRESS_1, NUM, 1, T_array);
    Copy1D (T_array, NUM, PRESS_1 );
    Shift (PRESS_1_ave, NUM, 1, T_array);
    Copy1D (T_array, NUM, PRESS_1_ave );
    Shift (PRESS_2, NUM, 1, T_array);
    Copy1D (T_array, NUM, PRESS_2 );
    Shift (PRESS_2_ave, NUM, 1, T_array);
    Copy1D (T_array, NUM, PRESS_2_ave );
    Shift (AIR_MFR, NUM, 1, T_array);
    Copy1D (T_array, NUM, AIR_MFR );
    Shift (AIR_MFR_ave, NUM, 1, T_array);
    Copy1D (T_array, NUM, AIR_MFR_ave );
    Shift (AIR_VFR, NUM, 1, T_array);
    Copy1D (T_array, NUM, AIR_VFR );
    Shift (AIR_VFR_ave, NUM, 1, T_array);
    Copy1D (T_array, NUM, AIR_VFR_ave );
    Shift (AIR_PSIA, NUM, 1, T_array);
    Copy1D (T_array, NUM, AIR_PSIA );
    Shift (AIR_degC, NUM, 1, T_array);
    Copy1D (T_array, NUM, AIR_degC );
    Shift (WATER_VFR, NUM, 1, T_array);
    Copy1D (T_array, NUM, WATER_VFR );
    Shift (WATER_VFR_ave, NUM, 1, T_array);
    Copy1D (T_array, NUM, WATER_VFR_ave );
    Shift (WATER_PSIA, NUM, 1, T_array);
    Copy1D (T_array, NUM, WATER_PSIA );
    Shift (WATER_degC, NUM, 1, T_array);
    Copy1D (T_array, NUM, WATER_degC );
    Shift (GLR, NUM, 1, T_array);
}

```

```

        CopyID (T_array, NUM ,GLR );

return;
}
/*****
/* DAQThreadFunction (): A thread to run DAQ in .
*****/
int CVICALLBACK DAQThreadFunction (void *functionData)
{
    double T1,T2,Hz;
    short read_cnt;
    char read_COM_Temp[100];
    int bytes_read;
    char seps[]=" ";
    double temp;

    // DAQ Variables
    int Mini1008 = 0; // Board Number as configure in InstaCal
    int PMD_1208FS = 2; // Board Number as configure in InstaCal
    int UDStat = 0;
    int Chan;
    int Gain = BIP10VOLTS ;
    WORD DataValue = 0;
    float EngUnits;
    double TEMP[10];
    int i, j, k = 0;
    int count = 0;

/* Start a loop that will process events for this thread */
while (DAQquitflag == 1 & Is_SYSTEM)
{
    ++SAMPLES;
        T1 = Timer (); // Start TIME
        ProcessSystemEvents ();
        //-----
        step[0] = Timer (); // Get Time

        if(Is_PRESS) // Displays and saves the pressure transducers data
        {
            SetCtrlVal (panelHandle,PANEL_LED_Press, 1);
            // CH 0 PRESS_1
            UDStat = cbAIn (Mini1008, 0, Gain, &DataValue);
            UDStat = cbToEngUnits (Mini1008, Gain, DataValue, &EngUnits);
            VOLT_PRESS_1[0] = EngUnits;
            PRESS_1[0]= 24.9924610*VOLT_PRESS_1[0]-25.1244288;

            Subset1D (PRESS_1, NUM, 0, 10, TEMP);
            Mean(TEMP,10,&PRESS_1_ave[0]);

            // CH 1 PRESS_2
            UDStat = cbAIn (Mini1008, 1, Gain, &DataValue);
            UDStat = cbToEngUnits (Mini1008, Gain, DataValue, &EngUnits);
            VOLT_PRESS_2[0] = EngUnits;
            PRESS_2[0]= 24.8525823*VOLT_PRESS_2[0]-24.8929739;

            Subset1D (PRESS_2, NUM, 0, 10, TEMP);
            Mean(TEMP,10,&PRESS_2_ave[0]);

        }

        if(Is_AIR_FM) // Communicate with the air flow meter
        {
            FlushInQ (SP_comport);
            FlushOutQ(SP_comport);
            ComWrt (SP_comport, "*@=A\r", 6); // Set the flow meter to poll mode
            SetCtrlVal (panelHandle,PANEL_LED_Air, 1);
            ComWrt (SP_comport, "A\r", 2); // Poll the meter for data
            Delay(0.04); // Allow it time to return the data
            read_cnt = GetInQLen (SP_comport); // See how big the input Q has grown to

            if(read_cnt >41)
            {
                read_COM_Temp[0]='\0';
                bytes_read = ComRdTerm (SP_comport, read_COM_Temp,
                SetCtrlVal (panelHandle, PANEL_Air_Flow_out,
read_cnt, 12);
read_COM_Temp);

```



```

        temp = atof(strtok(read_COM_Temp,seps));
// Read the A

        temp = atof(strtok(NULL,seps));
        AIR_PSIA[0] = temp;

//2
        temp = atof(strtok(NULL,seps));
        AIR_degC[0] = temp;

//3
        temp = atof(strtok(NULL,seps));
        AIR_VFR[0] = temp;

        Subset1D (AIR_VFR, NUM, 0, 10, TEMP);
        Mean(TEMP,10,&AIR_VFR_ave[0]);

//5
        temp = atof(strtok(NULL,seps));
        AIR_MFR[0] = temp;

        Subset1D (AIR_MFR, NUM, 0, 10, TEMP);
        Mean(TEMP,10,&AIR_MFR_ave[0]);

        FlushInQ (SP_comport)
    }
}

if(Is_WATER_FM) // Communicate with the water flow meter
{
    FlushInQ (SP2_comport);
    FlushOutQ(SP2_comport);
    ComWrt (SP2_comport, "*@=A\r", 6); // Set the flow meter to poll mode

SetCtrlVal (panelHandle,PANEL_LED_Water, 1);

    ComWrt (SP2_comport, "A\r", 2); // Poll the meter for data
    Delay(0.04); // Allow it time to return the data
    read_cnt = GetInQLen (SP2_comport); // See how big the input Q has grown to

    if(read_cnt >41)
    {
        read_COM_Temp[0]='\0';
        bytes_read = ComRdTerm (SP2_comport, read_COM_Temp, read_cnt, 12);
        SetCtrlVal (panelHandle, PANEL_Water_Flow_out, read_COM_Temp);

        temp = atof(strtok(read_COM_Temp,seps)); // Read the A

        temp = atof(strtok(NULL,seps));
        WATER_PSIA[0] = temp;

//2
        temp = atof(strtok(NULL,seps));
        WATER_degC[0] = temp;

//3
        temp = atof(strtok(NULL,seps));
        WATER_VFR[0] = temp;

        Subset1D (WATER_VFR, NUM, 0, 10, TEMP);
        Mean(TEMP,10,&WATER_VFR_ave[0]);

        FlushInQ (SP2_comport);
    }
}

if(Is_AIR_FM & Is_WATER_FM)
{
    GLR[0]=100 * 1.168/0.997*AIR_VFR[0]/WATER_VFR[0]; //Gas Liquid Ratio
}
}
//-----
DSN_UpdateScreen(); // Update Values on the Main Panel
ProcessSystemEvents ();
//-----
if(Is_Log)

```

```

        DSN_LogFile(); // Log to File

        ProcessSystemEvents ();

        if(Is_Graph)
            DSN_Graph(); // Do Graphing
        ProcessSystemEvents ();
        //-----
        DSN_SHIFT(); // SHIFT all arrays
        ProcessSystemEvents ();
        //-----
        T2 = Timer (); // Stop TIME
        Hz = (T2-T1);
        SetCtrlVal (panelHandle, PANEL_Sampling_Rate,1/Hz);
        //-----
    }
    return 0;
}
//*****
// LOG_ON_OFF : Check what functions to run
//*****
int CVICALLBACK LOG_ON_OFF (int panel, int control, int event,
    void *callbackData, int eventData1, int eventData2)
{
    switch (event)
    {
        case EVENT_COMMIT:

            GetCtrlVal(panelHandle, PANEL_LOG_AIR , &Is_AIR );
            GetCtrlVal(panelHandle, PANEL_LOG_DAQ , &Is_DAQ );
            GetCtrlVal(panelHandle, PANEL_LOG_Graph, &Is_Graph);
            GetCtrlVal(panelHandle, PANEL_LOG_LOGtoFile,&Is_Log );
            break;

        case EVENT_RIGHT_CLICK:

            break;

    }
    return 0;
}
//*****
// START_STOP : Start/Stop control of Timer Loop
// : Use a separate thread
//*****
int CVICALLBACK START_STOP (int panel, int control, int event,
    void *callbackData, int eventData1, int eventData2)
{
    int test, test2;
    int i,j;
    int bytes_read;

    switch (event)
    {
        case EVENT_COMMIT:

            DSN_Save_Vars();

            GetCtrlVal(panelHandle, PANEL_START_STOP, &Is_SYSTEM);
            if (Is_SYSTEM)
            {
                SetCtrlVal (panelHandle,PANEL_LED_System, 1);
            }
            else
            {
                SetCtrlVal (panelHandle,PANEL_LED_System, 0);
            }

            //-----
            // SETUP DAQ
            //-----

            /* Start a new thread function in the Default Thread Pool */
            //DAQcmtStatus= CmtScheduleThreadPoolFunctionAdv (DEFAULT_THREAD_POOL_HANDLE,
            DAQThreadFunction, NULL, THREAD_PRIORITY_ABOVE_NORMAL, NULL, EVENT_TP_THREAD_FUNCTION_END, NULL, NULL,
            &DAQthreadID);

            /* Start a new thread function in the Default Thread Pool */
            DAQcmtStatus = CmtScheduleThreadPoolFunction (DEFAULT_THREAD_POOL_HANDLE,
            DAQThreadFunction,
            NULL,
            &DAQthreadID);

            DAQquitflag = 1;

```

```

                break;
            case EVENT_RIGHT_CLICK:
                break;
        }
    return 0;
}

//*****
// DSN_UpdateScreen      : Update all parameters on the
//                          : main panel
//*****
void DSN_UpdateScreen(void)
{
    double total;
    double Pwater,Poil;

    SetCtrlVal (panelHandle, PANEL_SAMPLES,      SAMPLES);
    SetCtrlVal (panelHandle, PANEL_TIME,          step[0]);
    SetCtrlVal (panelHandle, PANEL_TIME_min,      step[0]/60);

    // DAQ -----

    if(Is_PRESS)
    {
        SetCtrlVal (panelHandle, PANEL_PRESS_1,          PRESS_1[0]);
        SetCtrlVal (panelHandle, PANEL_PRESS_1_ave,       PRESS_1_ave[0]);
        SetCtrlVal (panelHandle, PANEL_PRESS_1_avg_2,     PRESS_1_ave[0]);

        SetCtrlVal (panelHandle, PANEL_PRESS_1_Volt,      VOLT_PRESS_1[0]);

        SetCtrlVal (panelHandle, PANEL_PRESS_2,          PRESS_2[0]);
        SetCtrlVal (panelHandle, PANEL_PRESS_2_ave,       PRESS_2_ave[0]);
        SetCtrlVal (panelHandle, PANEL_PRESS_2_ave_2,     PRESS_2_ave[0]);
        SetCtrlVal (panelHandle, PANEL_PRESS_2_Volt,      VOLT_PRESS_2[0]);

        /*
        SetCtrlVal (panelHandle, PANEL_AIR_MFR,          AIR_MFR[0]);
        SetCtrlVal (panelHandle, PANEL_AIR_MFR_ave,       AIR_MFR_ave[0]);
        SetCtrlVal (panelHandle, PANEL_AIR_VFR,          AIR_VFR[0]);
        SetCtrlVal (panelHandle, PANEL_AIR_VFR_ave,       AIR_VFR_ave[0]);
        SetCtrlVal (panelHandle, PANEL_AIR_PSIA,         AIR_PSIA[0]);
        SetCtrlVal (panelHandle, PANEL_AIR_degC,         AIR_degC[0]);
        */
        /*
        // GOOD PLACE TO DO A CALCULATION
        if( WATER_FR_lpm[0]>2 || OIL_FR_lpm[0]>2)
        {
            total = WATER_FR_lpm[0] + OIL_FR_lpm[0];
            Pwater = 100*(WATER_FR_lpm[0]/total);
            Poil = 100*(OIL_FR_lpm[0]/total);

            SetCtrlVal (panelHandle, PANEL_WATER_percent, Pwater);
            SetCtrlVal (panelHandle, PANEL_OIL_percent,   Poil);
        }
        */
    }
    if(Is_AIR_FM)
    {
        SetCtrlVal (panelHandle, PANEL_AIR_PSIA, AIR_PSIA[0]);
        SetCtrlVal (panelHandle, PANEL_AIR_degC, AIR_degC[0]);
        SetCtrlVal (panelHandle, PANEL_AIR_VFR, AIR_VFR[0]);
        SetCtrlVal (panelHandle, PANEL_AIR_VFR_ave, AIR_VFR_ave[0]);
        SetCtrlVal (panelHandle, PANEL_AIR_MFR, AIR_MFR[0]);
        SetCtrlVal (panelHandle, PANEL_AIR_MFR_ave, AIR_MFR_ave[0]);
        SetCtrlVal (panelHandle, PANEL_AIR_FR_lpm_2, AIR_MFR_ave[0]);
    }

    if(Is_WATER_FM)
    {
        SetCtrlVal (panelHandle, PANEL_WATER_PSIA, WATER_PSIA[0]);
        SetCtrlVal (panelHandle, PANEL_WATER_degC, WATER_degC[0]);
        SetCtrlVal (panelHandle, PANEL_WATER_VFR, WATER_VFR[0]);
        SetCtrlVal (panelHandle, PANEL_WATER_VFR_ave, WATER_VFR_ave[0]);
        SetCtrlVal (panelHandle, PANEL_WATER_FR_mrpm_2, WATER_VFR_ave[0]);
    }

    if(Is_WATER_FM & Is_AIR)

```

```

    {
        SetCtrlVal (panelHandle, PANEL_GLR, GLR[0]);
        SetCtrlVal (panelHandle, PANEL_GLR_Rate, GLR[0]);
    }

return;
}
//*****
// OnOff_Graphs          : For turning graphs ON and OFF
//*****
int CVICALLBACK OnOff_Graphs (int panel, int control, int event,
    void *callbackData, int eventData1, int eventData2)
{
    int test;
    switch (event)
    {
        case EVENT_COMMIT:
            switch(control)
            {
                case G_SETUP_OnOff_G_1:
                    GetCtrlVal (g_Handle, G_SETUP_OnOff_G_1, &test);
                    if(test)
                    {
                        SetCtrlAttribute (panelHandle, PANEL_G_1, ATTR_DIMMED, 0);
                        OnOff_G1 = 1;
                    }
                    else
                    {
                        SetCtrlAttribute (panelHandle, PANEL_G_1, ATTR_DIMMED, 1);
                        OnOff_G1 = 0;
                    }
                    break;
                case G_SETUP_OnOff_G_2:
                    GetCtrlVal (g_Handle, G_SETUP_OnOff_G_2, &test);
                    if(test)
                    {
                        SetCtrlAttribute (panelHandle, PANEL_G_2, ATTR_DIMMED, 0);
                        OnOff_G2 = 1;
                    }
                    else
                    {
                        SetCtrlAttribute (panelHandle, PANEL_G_2, ATTR_DIMMED, 1);
                        OnOff_G2 = 0;
                    }
                    break;
                case G_SETUP_OnOff_G_3:
                    GetCtrlVal (g_Handle, G_SETUP_OnOff_G_3, &test);
                    if(test)
                    {
                        SetCtrlAttribute (panelHandle, PANEL_G_3, ATTR_DIMMED, 0);
                        OnOff_G3 = 1;
                    }
                    else
                    {
                        SetCtrlAttribute (panelHandle, PANEL_G_3, ATTR_DIMMED, 1);
                        OnOff_G3 = 0;
                    }
                    break;
                case G_SETUP_OnOff_G_4:
                    GetCtrlVal (g_Handle, G_SETUP_OnOff_G_4, &test);
                    if(test)
                    {
                        SetCtrlAttribute (panelHandle, PANEL_G_4, ATTR_DIMMED, 0);
                        OnOff_G4 = 1;
                    }
                    else
                    {
                        SetCtrlAttribute (panelHandle, PANEL_G_4, ATTR_DIMMED, 1);
                        OnOff_G4 = 0;
                    }
                    break;
            }
            break;
        case EVENT_RIGHT_CLICK:
            break;
    }
    return 0;
}
//*****
// DSN_Graph          : Do the graphing
//*****

```

```

void DSN_Graph(void)
{
// GPARH #1
if(OnOff_G1)
{
DSN_Graph_Select(plotVar_G_1, PANEL_G_1);
if(plotVar_G_1>=0)
{
SetAxisScalingMode (panelHandle, PANEL_G_1, VAL_XAXIS, VAL_MANUAL,
step[0]-X_Range_G_1, step[0]);

if(Y_Mode_G_1)
SetAxisScalingMode (panelHandle, PANEL_G_1, VAL_LEFT_YAXIS, VAL_AUTOSCALE,0 ,0 );
else
SetAxisScalingMode (panelHandle, PANEL_G_1, VAL_LEFT_YAXIS,
VAL_MANUAL, Y_Min_G_1, Y_Max_G_1);
}
}
// GPARH #2
if(OnOff_G2)
{
DSN_Graph_Select(plotVar_G_2, PANEL_G_2);
if(plotVar_G_2>=0)
{
SetAxisScalingMode (panelHandle, PANEL_G_2, VAL_XAXIS, VAL_MANUAL,
step[0]-X_Range_G_2, step[0]);

if(Y_Mode_G_2)
SetAxisScalingMode (panelHandle, PANEL_G_2, VAL_LEFT_YAXIS, VAL_AUTOSCALE,0 ,0 );
else
SetAxisScalingMode (panelHandle, PANEL_G_2, VAL_LEFT_YAXIS,
VAL_MANUAL, Y_Min_G_2, Y_Max_G_2);
}
}
// GPARH #3
if(OnOff_G3)
{
DSN_Graph_Select(plotVar_G_3, PANEL_G_3);
if(plotVar_G_3>=0)
{
SetAxisScalingMode (panelHandle, PANEL_G_3, VAL_XAXIS, VAL_MANUAL,
step[0]-X_Range_G_3, step[0]);

if(Y_Mode_G_3)
SetAxisScalingMode (panelHandle, PANEL_G_3, VAL_LEFT_YAXIS, VAL_AUTOSCALE,0 ,0 );
else
SetAxisScalingMode (panelHandle, PANEL_G_3, VAL_LEFT_YAXIS,
VAL_MANUAL, Y_Min_G_3, Y_Max_G_3);
}
}
// GPARH #4
if(OnOff_G4)
{
DSN_Graph_Select(plotVar_G_4, PANEL_G_4);

if(plotVar_G_4>=0)
{
SetAxisScalingMode (panelHandle, PANEL_G_4, VAL_XAXIS, VAL_MANUAL,
step[0]-X_Range_G_4, step[0]);

if(Y_Mode_G_4)
SetAxisScalingMode (panelHandle, PANEL_G_4, VAL_LEFT_YAXIS, VAL_AUTOSCALE,0 ,0 );
else
SetAxisScalingMode (panelHandle, PANEL_G_4, VAL_LEFT_YAXIS,
VAL_MANUAL, Y_Min_G_4, Y_Max_G_4);
}
}
return;
}
//*****
// DSN_Graph_Select : Select Graph to be plotted
//*****
void DSN_Graph_Select(int plotVar, int Panel_Graph)
{
switch(plotVar)
{
case -1:
DeleteGraphPlot (panelHandle, Panel_Graph, -1,VAL_IMMEDIATE_DRAW);
break;
case 1:
DeleteGraphPlot (panelHandle, Panel_Graph, -1,VAL_IMMEDIATE_DRAW);
PlotXY (panelHandle, Panel_Graph, step, PRESS_1, NUM, VAL_DOUBLE,
VAL_DOUBLE, VAL_FAT_LINE, VAL_EMPTY_SQUARE, VAL_SOLID, 1,
VAL_RED);
PlotXY (panelHandle, Panel_Graph, step, PRESS_1_ave, NUM, VAL_DOUBLE,
VAL_DOUBLE, VAL_FAT_LINE, VAL_EMPTY_SQUARE, VAL_SOLID, 1,
VAL_BLUE);
}
}

```

```

        break;
    case 2:
        DeleteGraphPlot (panelHandle, Panel_Graph, -1, VAL_IMMEDIATE_DRAW);
        PlotXY (panelHandle, Panel_Graph, step, PRESS_2, NUM, VAL_DOUBLE,
                VAL_DOUBLE, VAL_FAT_LINE, VAL_EMPTY_SQUARE, VAL_SOLID, 1,
                VAL_RED);
        PlotXY (panelHandle, Panel_Graph, step, PRESS_2_ave, NUM, VAL_DOUBLE,
                VAL_DOUBLE, VAL_FAT_LINE, VAL_EMPTY_SQUARE, VAL_SOLID, 1,
                VAL_BLUE);
        break;
    case 3:
        DeleteGraphPlot (panelHandle, Panel_Graph, -1, VAL_IMMEDIATE_DRAW);
        PlotXY (panelHandle, Panel_Graph, step, AIR_MFR, NUM, VAL_DOUBLE,
                VAL_DOUBLE, VAL_FAT_LINE, VAL_EMPTY_SQUARE, VAL_SOLID, 1,
                VAL_RED);
        PlotXY (panelHandle, Panel_Graph, step, AIR_MFR_ave, NUM, VAL_DOUBLE,
                VAL_DOUBLE, VAL_FAT_LINE, VAL_EMPTY_SQUARE, VAL_SOLID, 1,
                VAL_BLUE);
        break;
    case 4:
        DeleteGraphPlot (panelHandle, Panel_Graph, -1, VAL_IMMEDIATE_DRAW);
        PlotXY (panelHandle, Panel_Graph, step, AIR_VFR, NUM, VAL_DOUBLE,
                VAL_DOUBLE, VAL_FAT_LINE, VAL_EMPTY_SQUARE, VAL_SOLID, 1,
                VAL_RED);
        PlotXY (panelHandle, Panel_Graph, step, AIR_VFR_ave, NUM, VAL_DOUBLE,
                VAL_DOUBLE, VAL_FAT_LINE, VAL_EMPTY_SQUARE, VAL_SOLID, 1,
                VAL_BLUE);
        break;
    case 5:
        DeleteGraphPlot (panelHandle, Panel_Graph, -1, VAL_IMMEDIATE_DRAW);
        PlotXY (panelHandle, Panel_Graph, step, AIR_PSIA, NUM, VAL_DOUBLE,
                VAL_DOUBLE, VAL_FAT_LINE, VAL_EMPTY_SQUARE, VAL_SOLID, 1,
                VAL_RED);
        break;
    case 6:
        DeleteGraphPlot (panelHandle, Panel_Graph, -1, VAL_IMMEDIATE_DRAW);
        PlotXY (panelHandle, Panel_Graph, step, AIR_degC, NUM, VAL_DOUBLE,
                VAL_DOUBLE, VAL_FAT_LINE, VAL_EMPTY_SQUARE, VAL_SOLID, 1,
                VAL_RED);
        break;
    case 7:
        DeleteGraphPlot (panelHandle, Panel_Graph, -1, VAL_IMMEDIATE_DRAW);
        PlotXY (panelHandle, Panel_Graph, step, WATER_VFR, NUM, VAL_DOUBLE,
                VAL_DOUBLE, VAL_FAT_LINE, VAL_EMPTY_SQUARE, VAL_SOLID, 1,
                VAL_RED);
        PlotXY (panelHandle, Panel_Graph, step, WATER_VFR_ave, NUM, VAL_DOUBLE,
                VAL_DOUBLE, VAL_FAT_LINE, VAL_EMPTY_SQUARE, VAL_SOLID, 1,
                VAL_BLUE);
        break;
    case 8:
        DeleteGraphPlot (panelHandle, Panel_Graph, -1, VAL_IMMEDIATE_DRAW);
        PlotXY (panelHandle, Panel_Graph, step, WATER_PSIA, NUM, VAL_DOUBLE,
                VAL_DOUBLE, VAL_FAT_LINE, VAL_EMPTY_SQUARE, VAL_SOLID, 1,
                VAL_RED);
        break;
    case 9:
        DeleteGraphPlot (panelHandle, Panel_Graph, -1, VAL_IMMEDIATE_DRAW);
        PlotXY (panelHandle, Panel_Graph, step, WATER_degC, NUM, VAL_DOUBLE,
                VAL_DOUBLE, VAL_FAT_LINE, VAL_EMPTY_SQUARE, VAL_SOLID, 1,
                VAL_RED);
        break;
    case 10:
        DeleteGraphPlot (panelHandle, Panel_Graph, -1, VAL_IMMEDIATE_DRAW);
        PlotXY (panelHandle, Panel_Graph, step, GLR, NUM, VAL_DOUBLE,
                VAL_DOUBLE, VAL_FAT_LINE, VAL_EMPTY_SQUARE, VAL_SOLID, 1,
                VAL_RED);
        break;
    }
}
return;
}
//*****
// GRAPHS : Call to setup graphs
//*****
int CVICALLBACK DSN_SETUP_G (int panel, int control, int event,
                             void *callbackData, int eventData1, int eventData2)
{
    switch (event)
    {

```

```

        case EVENT_COMMIT:
            DSN_GraphSetup();
            break;
        case EVENT_RIGHT_CLICK:

            break;
    }
    return 0;
}
//*****
// DSN_GraphName      : Setup graphs
//*****
void DSN_GraphName(int Val, int GRAPH, int L1, int T1, int L2, int T2,
                  int L3, int T3, int L4, int T4)
{
    switch(Val)
    {
        case -1:
            SetCtrlAttribute (panelHandle, GRAPH, ATTR_ACTIVE_YAXIS, VAL_LEFT_YAXIS);
            SetCtrlAttribute (panelHandle, GRAPH, ATTR_YNAME, "Not Plotting");
            SetCtrlAttribute (panelHandle, GRAPH, ATTR_ACTIVE_YAXIS, VAL_RIGHT_YAXIS);
            SetCtrlAttribute (panelHandle, GRAPH, ATTR_YNAME, "");
            SetCtrlAttribute (g_Handle, L1, ATTR_FRAME_COLOR, VAL_LT_GRAY);
                SetCtrlVal (g_Handle, T1, " ");
            SetCtrlAttribute (g_Handle, L2, ATTR_FRAME_COLOR, VAL_LT_GRAY);
                SetCtrlVal (g_Handle, T2, " ");
            SetCtrlAttribute (g_Handle, L3, ATTR_FRAME_COLOR, VAL_LT_GRAY);
                SetCtrlVal (g_Handle, T3, "");
            SetCtrlAttribute (g_Handle, L4, ATTR_FRAME_COLOR, VAL_LT_GRAY);
                SetCtrlVal (g_Handle, T4, "");

            break;

        case 1:
            SetCtrlAttribute (panelHandle, GRAPH, ATTR_ACTIVE_YAXIS, VAL_LEFT_YAXIS);
            SetCtrlAttribute (panelHandle, GRAPH, ATTR_YNAME, "Pressure #1 (psig)");
            SetCtrlAttribute (g_Handle, L1, ATTR_FRAME_COLOR, VAL_LT_GRAY);
                SetCtrlVal (g_Handle, T1, "Instantaneous");
            SetCtrlAttribute (g_Handle, L2, ATTR_FRAME_COLOR, VAL_LT_GRAY);
                SetCtrlVal (g_Handle, T2, " ");
            SetCtrlAttribute (g_Handle, L3, ATTR_FRAME_COLOR, VAL_LT_GRAY);
                SetCtrlVal (g_Handle, T3, "");
            SetCtrlAttribute (g_Handle, L4, ATTR_FRAME_COLOR, VAL_LT_GRAY);
                SetCtrlVal (g_Handle, T4, "");

            break;

        case 2:
            SetCtrlAttribute (panelHandle, GRAPH, ATTR_ACTIVE_YAXIS, VAL_LEFT_YAXIS);
            SetCtrlAttribute (panelHandle, GRAPH, ATTR_YNAME, "Pressure #2 (psig)");
            SetCtrlAttribute (g_Handle, L1, ATTR_FRAME_COLOR, VAL_LT_GRAY);
                SetCtrlVal (g_Handle, T1, "Instantaneous");
            SetCtrlAttribute (g_Handle, L2, ATTR_FRAME_COLOR, VAL_LT_GRAY);
                SetCtrlVal (g_Handle, T2, " ");
            SetCtrlAttribute (g_Handle, L3, ATTR_FRAME_COLOR, VAL_LT_GRAY);
                SetCtrlVal (g_Handle, T3, "");
            SetCtrlAttribute (g_Handle, L4, ATTR_FRAME_COLOR, VAL_LT_GRAY);
                SetCtrlVal (g_Handle, T4, "");

            break;

        case 3:
            SetCtrlAttribute (panelHandle, GRAPH, ATTR_ACTIVE_YAXIS, VAL_LEFT_YAXIS);
            SetCtrlAttribute (panelHandle, GRAPH, ATTR_YNAME, "Air Mass Flow Rate
(SLPM)");

            SetCtrlAttribute (g_Handle, L1, ATTR_FRAME_COLOR, VAL_RED);
                SetCtrlVal (g_Handle, T1, "Instantaneous");
            SetCtrlAttribute (g_Handle, L2, ATTR_FRAME_COLOR, VAL_BLUE);
                SetCtrlVal (g_Handle, T2, "Average of 10 points");
            SetCtrlAttribute (g_Handle, L3, ATTR_FRAME_COLOR, VAL_LT_GRAY);
                SetCtrlVal (g_Handle, T3, "");
            SetCtrlAttribute (g_Handle, L4, ATTR_FRAME_COLOR, VAL_LT_GRAY);
                SetCtrlVal (g_Handle, T4, "");

            break;

        case 4:
            SetCtrlAttribute (panelHandle, GRAPH, ATTR_ACTIVE_YAXIS, VAL_LEFT_YAXIS);
            SetCtrlAttribute (panelHandle, GRAPH, ATTR_YNAME, "Air Volume Flow Rate
(LPM)");

            SetCtrlAttribute (g_Handle, L1, ATTR_FRAME_COLOR, VAL_RED);
                SetCtrlVal (g_Handle, T1, "Instantaneous");
            SetCtrlAttribute (g_Handle, L2, ATTR_FRAME_COLOR, VAL_BLUE);
                SetCtrlVal (g_Handle, T2, "Average of 10 points");
            SetCtrlAttribute (g_Handle, L3, ATTR_FRAME_COLOR, VAL_LT_GRAY);
                SetCtrlVal (g_Handle, T3, "");
            SetCtrlAttribute (g_Handle, L4, ATTR_FRAME_COLOR, VAL_LT_GRAY);
                SetCtrlVal (g_Handle, T4, "");
    }
}

```

```

        break;
    case 5:
        SetCtrlAttribute (panelHandle, GRAPH, ATTR_ACTIVE_YAXIS, VAL_LEFT_YAXIS);
        SetCtrlAttribute (panelHandle, GRAPH, ATTR_YNAME, "Air Pressure (PSIA)");
        break;
    case 6:
        SetCtrlAttribute (panelHandle, GRAPH, ATTR_ACTIVE_YAXIS, VAL_LEFT_YAXIS);
        SetCtrlAttribute (panelHandle, GRAPH, ATTR_YNAME, "Air Temperature (degC)");
        break;
    case 7:
        SetCtrlAttribute (panelHandle, GRAPH, ATTR_ACTIVE_YAXIS, VAL_LEFT_YAXIS);
        SetCtrlAttribute (panelHandle, GRAPH, ATTR_YNAME, "Water Vloume Flow Rate
(MLPM)");
        SetCtrlAttribute (g_Handle, L1, ATTR_FRAME_COLOR, VAL_RED);
        SetCtrlVal (g_Handle, T1, "Instantaneous");
        SetCtrlAttribute (g_Handle, L2, ATTR_FRAME_COLOR, VAL_BLUE);
        SetCtrlVal (g_Handle, T2, "Average of 10 points");
        SetCtrlAttribute (g_Handle, L3, ATTR_FRAME_COLOR, VAL_LT_GRAY);
        SetCtrlVal (g_Handle, T3, "");
        SetCtrlAttribute (g_Handle, L4, ATTR_FRAME_COLOR, VAL_LT_GRAY);
        SetCtrlVal (g_Handle, T4, "");
        break;
    case 8:
        SetCtrlAttribute (panelHandle, GRAPH, ATTR_ACTIVE_YAXIS, VAL_LEFT_YAXIS);
        SetCtrlAttribute (panelHandle, GRAPH, ATTR_YNAME, "Water Pressure (PSIA)");
        break;
    case 9:
        SetCtrlAttribute (panelHandle, GRAPH, ATTR_ACTIVE_YAXIS, VAL_LEFT_YAXIS);
        SetCtrlAttribute (panelHandle, GRAPH, ATTR_YNAME, "Water Temperature
(degC)");
        break;
    case 10:
        SetCtrlAttribute (panelHandle, GRAPH, ATTR_ACTIVE_YAXIS, VAL_LEFT_YAXIS);
        SetCtrlAttribute (panelHandle, GRAPH, ATTR_YNAME, "GLR");
        break;
    }
}

return;
}
//*****
// DSN_GraphSetup : Setup graphs
//*****
void DSN_GraphSetup(void)
{
    // Update the variables from the panels
    DSN_Save_Vars();
    //Read Graph #1
    if(Y_Mode_G_1)
    {
        SetCtrlAttribute (g_Handle, G_SETUP_Y_Mode_G_1, ATTR_LABEL_TEXT, "Auto");
        SetCtrlAttribute (g_Handle, G_SETUP_Y_Min_G_1, ATTR_DIMMED, 1);
        SetCtrlAttribute (g_Handle, G_SETUP_Y_Max_G_1, ATTR_DIMMED, 1);
    }
    else
    {
        SetCtrlAttribute (g_Handle, G_SETUP_Y_Mode_G_1, ATTR_LABEL_TEXT, "Fixed");
        SetCtrlAttribute (g_Handle, G_SETUP_Y_Min_G_1, ATTR_DIMMED, 0);
        SetCtrlAttribute (g_Handle, G_SETUP_Y_Max_G_1, ATTR_DIMMED, 0);
    }
    DSN_GraphName(plotVar_G_1, PANEL_G_1,G_SETUP_G1_L_1,G_SETUP_G1_T_1,
G_SETUP_G1_L_2,G_SETUP_G1_T_2,
G_SETUP_G1_L_3,G_SETUP_G1_T_3,
G_SETUP_G1_L_4,G_SETUP_G1_T_4);
    //Read Graph #2
    if(Y_Mode_G_2)
    {
        SetCtrlAttribute (g_Handle, G_SETUP_Y_Mode_G_2, ATTR_LABEL_TEXT, "Auto");
        SetCtrlAttribute (g_Handle, G_SETUP_Y_Min_G_2, ATTR_DIMMED, 1);
        SetCtrlAttribute (g_Handle, G_SETUP_Y_Max_G_2, ATTR_DIMMED, 1);
    }
    else
    {
        SetCtrlAttribute (g_Handle, G_SETUP_Y_Mode_G_2, ATTR_LABEL_TEXT, "Fixed");
        SetCtrlAttribute (g_Handle, G_SETUP_Y_Min_G_2, ATTR_DIMMED, 0);
        SetCtrlAttribute (g_Handle, G_SETUP_Y_Max_G_2, ATTR_DIMMED, 0);
    }
    DSN_GraphName(plotVar_G_2, PANEL_G_2,G_SETUP_G2_L_1,G_SETUP_G2_T_1,
G_SETUP_G2_L_2,G_SETUP_G2_T_2,

```



```

G_SETUP_G2_L_3,G_SETUP_G2_T_3,
G_SETUP_G2_L_4,G_SETUP_G2_T_4);
//Read Graph #3
if(Y_Mode_G_3)
{
SetCtrlAttribute (g_Handle, G_SETUP_Y_Mode_G_3, ATTR_LABEL_TEXT, "Auto");
SetCtrlAttribute (g_Handle, G_SETUP_Y_Min_G_3, ATTR_DIMMED, 1);
SetCtrlAttribute (g_Handle, G_SETUP_Y_Max_G_3, ATTR_DIMMED, 1);
}
else
{
SetCtrlAttribute (g_Handle, G_SETUP_Y_Mode_G_3, ATTR_LABEL_TEXT, "Fixed");
SetCtrlAttribute (g_Handle, G_SETUP_Y_Min_G_3, ATTR_DIMMED, 0);
SetCtrlAttribute (g_Handle, G_SETUP_Y_Max_G_3, ATTR_DIMMED, 0);
}
DSN_GraphName(plotVar_G_3, PANEL_G_3,G_SETUP_G3_L_1,G_SETUP_G3_T_1,
G_SETUP_G3_L_2,G_SETUP_G3_T_2,
G_SETUP_G3_L_3,G_SETUP_G3_T_3,
G_SETUP_G3_L_4,G_SETUP_G3_T_4);
//Read Graph #4
if(Y_Mode_G_4)
{
SetCtrlAttribute (g_Handle, G_SETUP_Y_Mode_G_4, ATTR_LABEL_TEXT, "Auto");
SetCtrlAttribute (g_Handle, G_SETUP_Y_Min_G_4, ATTR_DIMMED, 1);
SetCtrlAttribute (g_Handle, G_SETUP_Y_Max_G_4, ATTR_DIMMED, 1);
}
else
{
SetCtrlAttribute (g_Handle, G_SETUP_Y_Mode_G_4, ATTR_LABEL_TEXT, "Fixed");
SetCtrlAttribute (g_Handle, G_SETUP_Y_Min_G_4, ATTR_DIMMED, 0);
SetCtrlAttribute (g_Handle, G_SETUP_Y_Max_G_4, ATTR_DIMMED, 0);
}
DSN_GraphName(plotVar_G_4, PANEL_G_4,G_SETUP_G4_L_1,G_SETUP_G4_T_1,
G_SETUP_G4_L_2,G_SETUP_G4_T_2,
G_SETUP_G4_L_3,G_SETUP_G4_T_3,
G_SETUP_G4_L_4,G_SETUP_G4_T_4);
return;
}
//*****
// COM #1 - Air Flow Meter
//*****
// SP_OPEN : Open the com port
//*****
int CVICALLBACK SP_OPEN (int panel, int control, int event,
void *callbackData, int eventData1, int eventData2)
{
switch (event)
{
case EVENT_COMMIT:
DSN_SP_OPEN();
break;
case EVENT_RIGHT_CLICK:
break;
}
return 0;
}
//*****
// DSN_SP_OPEN : Open the com port to the
//*****
void DSN_SP_OPEN(void)
{
int test;
SetCtrlVal (com_Handle, COM_SP_STRING_1, '\0');
SetCtrlVal (com_Handle, COM_SP_STRING_2, '\0');
SetCtrlVal (com_Handle, COM_SP_STRING_3, '\0');
SetCtrlVal (com_Handle, COM_SP_STRING_4, '\0');
rmd2[0]='\0';
DSN_GetSPConfig();

SP_port_open = 0; /* initialize flag to 0 - unopened */
DisableBreakOnLibraryErrors ();
RS232Error = OpenComConfig (SP_comport, "", SP_baudrate, SP_parity,
SP_databits, SP_stopbits, SP_inputq, SP_outputq);
SetCtrlVal (com_Handle, COM_NUM, RS232Error);

```

```

EnableBreakOnLibraryErrors ();

if (RS232Error)
{
    DisplayRS232Error ();
}
else
{
    SP_port_open = 1;
    SetCtrlVal (com_Handle, COM_NUM, SP_port_open);
    GetCtrlVal (com_Handle, COM_SP_XMODE, &SP_xmode);
    SetXMode (SP_comport, SP_xmode);
    GetCtrlVal (com_Handle, COM_SP_CTS, &SP_ctsmode);
    SetCTSMode (SP_comport, SP_ctsmode);
    GetCtrlVal (com_Handle, COM_SP_TIMEOUT, &SP_timeout);
    SetComTime (SP_comport, SP_timeout);
}

//SetCtrlVal (com_Handle, COM_SP_STRING_2, rmd2);

if (SP_port_open)
{
    SetCtrlAttribute (com_Handle, COM_SP_LED, ATTR_DIMMED, 0);
    SetCtrlAttribute (panelHandle, PANEL_SP_LED, ATTR_DIMMED, 0);

    test=1;
    if(test)
    {
        SetCtrlVal (com_Handle, COM_SP_LED, 1);
        SetCtrlVal (panelHandle, PANEL_SP_LED, 1);
    }
    else
    {
        SetCtrlVal (com_Handle, COM_SP_LED, 0);
        SetCtrlVal (panelHandle, PANEL_SP_LED, 0);
    }
}

return;
}
//*****
// DSN_GetSPConfig : Load vars with SP config from screen
//*****
void DSN_GetSPConfig (void)
{
    DSN_Save_Vars();

    #ifdef _NI_unix_
        SP_devicename[0]=0;
    #else
        GetLabelFromIndex (com_Handle, COM_SP_COM, SP_portindex,
            SP_devicename);
    #endif
}
//*****
//
//          COM #2 - Water Flow Meter
//*****
// SP2_OPEN : Open the com port
//*****
int CVICALLBACK SP2_OPEN (int panel, int control, int event,
    void *callbackData, int eventData1, int eventData2)
{
    switch (event)
    {
        case EVENT_COMMIT:
            DSN_SP2_OPEN();
            break;
        case EVENT_RIGHT_CLICK:
            break;
    }
    return 0;
}
//*****
// DSN_SP2_OPEN : Open the com port to the
//*****
void DSN_SP2_OPEN(void)
{
    int test;
    SetCtrlVal (com_Handle, COM_SP_STRING_1, '\0');
    SetCtrlVal (com_Handle, COM_SP_STRING_2, '\0');
    SetCtrlVal (com_Handle, COM_SP_STRING_3, '\0');
}

```

```

SetCtrlVal (com_Handle, COM_SP_STRING_4, '\0');
rmd2[0]='\0';
DSN_GetSP2Config();

SP2_port_open = 0; /* initialize flag to 0 - unopened */
DisableBreakOnLibraryErrors ();
RS232Error = OpenComConfig (SP2_comport, "", SP2_baudrate, SP2_parity,
                             SP2_databits, SP2_stopbits, SP2_inputq, SP2_outputq);
SetCtrlVal      (com_Handle, COM_NUM,      RS232Error);
EnableBreakOnLibraryErrors ();

if (RS232Error)
{
    DisplayRS232Error ();
}
else
{
    SP2_port_open = 1;
    SetCtrlVal (com_Handle, COM_NUM,      SP2_port_open);
    GetCtrlVal (com_Handle, COM_SP_XMODE_2, &SP2_xmode);
    SetXMode (SP2_comport, SP2_xmode);
    GetCtrlVal (com_Handle, COM_SP_CTS_2, &SP2_ctsmode);
    SetCTSMode (SP2_comport, SP2_ctsmode);
    GetCtrlVal (com_Handle, COM_SP_TIMEOUT_2, &SP2_timeout);
    SetComTime (SP2_comport, SP2_timeout);
}

//SetCtrlVal (com_Handle, COM_SP2_STRING_2, rmd2);

if (SP2_port_open)
{
    SetCtrlAttribute (com_Handle, COM_SP_LED_2, ATTR_DIMMED, 0);
    SetCtrlAttribute (panelHandle, PANEL_SP_LED_2, ATTR_DIMMED, 0);

    test=1;
    if(test)
    {
        SetCtrlVal (com_Handle, COM_SP_LED_2, 1);
        SetCtrlVal (panelHandle, PANEL_SP_LED_2, 1);
    }
    else
    {
        SetCtrlVal (com_Handle, COM_SP_LED_2, 0);
        SetCtrlVal (panelHandle, PANEL_SP_LED_2, 0);
    }
}

return;
}
//*****
// DSN_GetSP2Config : Load vars with SP config from screen
//*****
void DSN_GetSP2Config (void)
{
    DSN_Save_Vars();

    #ifdef _NI_unix_
        SP2_devicename[0]=0;
    #else
        GetLabelFromIndex (com_Handle, COM_SP_COM_2, SP2_portindex,
                            SP2_devicename);
    #endif
}
//*****
// DisplayRS232Error : Display error information to the user.
//*****
void DisplayRS232Error (void)
{
    char ErrorMessage[200];
    switch (RS232Error)
    {
        default :
            if (RS232Error < 0)
            {
                Fmt (ErrorMessage, "%s<RS232 error number %i", RS232Error);
                MessagePopup ("RS232 Message", ErrorMessage);
            }
            break;
        case 0 :
            MessagePopup ("RS232 Message", "No errors.");
    }
}

```

```

        break;
    case -2 :
        Fmt (ErrorMessage, "%s", "Connection failed. \n"
            "Check port settings.");
        MessagePopup ("RS232 Message", ErrorMessage);
        break;
    case -3 :
        Fmt (ErrorMessage, "%s", "No port is open.\n"
            "Check port settings.");
        MessagePopup ("RS232 Message", ErrorMessage);
        break;
    case -99 :
        Fmt (ErrorMessage, "%s", "Timeout error.\n"
            "Check port settings.");
        MessagePopup ("RS232 Message", ErrorMessage);
        break;
    }
}
//*****
// Load_Config      : Load variables from config file
//                   : Update screen from variables
//*****
void CVICALLBACK Load_Config (int menuBar, int menuItem, void *callbackData,
    int panel)
{
    DSN_Load_Config();
    DSN_Load_Vars();
}
//*****
// Save_Config      : Save screen to variables
//                   : Save variables to config file
//*****
void CVICALLBACK Save_Config (int menuBar, int menuItem, void *callbackData,
    int panel)
{
    DSN_Save_Vars();
    DSN_Save_Config(0);
}
//*****
// Save_Config_As   : Save screen to variables
//                   : Save variables to config file
//                   : Allow the config file to be selected
//*****
void CVICALLBACK Save_Config_As (int menuBar, int menuItem, void *callbackData,
    int panel)
{
    DSN_Save_Vars();
    DSN_Save_Config(1);
}
//*****
// DSN_Save_Vars    : Save screen to variables
//*****
void DSN_Save_Vars(void)
{
    int i;
    double J_temp, ALPHA_temp;

// MAIN PANEL
    GetCtrlVal(panelHandle, PANEL_LOG_AIR , &Is_AIR);
    GetCtrlVal(panelHandle, PANEL_LOG_DAQ , &Is_DAQ);
    GetCtrlVal(panelHandle, PANEL_LOG_Graph, &Is_Graph);
    GetCtrlVal(panelHandle, PANEL_LOG_LOGtoFile, &Is_Log);

// GRAPH PANEL
//Read Graph #1
    GetCtrlVal( g_Handle, G_SETUP_Var_G_1 , &plotVar_G_1);
    GetCtrlVal( g_Handle, G_SETUP_X_Range_G_1, &X_Range_G_1);
    GetCtrlVal( g_Handle, G_SETUP_Y_Mode_G_1 , &Y_Mode_G_1 );
    GetCtrlVal( g_Handle, G_SETUP_Y_Min_G_1 , &Y_Min_G_1 );
    GetCtrlVal( g_Handle, G_SETUP_Y_Max_G_1 , &Y_Max_G_1 );
    if (Y_Min_G_1 >= Y_Max_G_1)
        Y_Min_G_1 = Y_Max_G_1-0.5;
    SetCtrlVal( g_Handle, G_SETUP_Y_Min_G_1, Y_Min_G_1);

//Read Graph #2
    GetCtrlVal( g_Handle, G_SETUP_Var_G_2 , &plotVar_G_2);
    GetCtrlVal( g_Handle, G_SETUP_X_Range_G_2, &X_Range_G_2);
    GetCtrlVal( g_Handle, G_SETUP_Y_Mode_G_2 , &Y_Mode_G_2 );
    GetCtrlVal( g_Handle, G_SETUP_Y_Min_G_2 , &Y_Min_G_2 );
    GetCtrlVal( g_Handle, G_SETUP_Y_Max_G_2 , &Y_Max_G_2 );
    if (Y_Min_G_2 >= Y_Max_G_2)
        Y_Min_G_2 = Y_Max_G_2-0.5;
    SetCtrlVal( g_Handle, G_SETUP_Y_Min_G_2, Y_Min_G_2);

```

```

//Read Graph #3
GetCtrlVal( g_Handle, G_SETUP_Var_G_3 , &plotVar_G_3);
GetCtrlVal( g_Handle, G_SETUP_X_Range_G_3 , &X_Range_G_3);
GetCtrlVal( g_Handle, G_SETUP_Y_Mode_G_3 , &Y_Mode_G_3 );
GetCtrlVal( g_Handle, G_SETUP_Y_Min_G_3 , &Y_Min_G_3 );
GetCtrlVal( g_Handle, G_SETUP_Y_Max_G_3 , &Y_Max_G_3 );
if (Y_Min_G_3 >= Y_Max_G_3)
    Y_Min_G_3 = Y_Max_G_3-0.5;
SetCtrlVal( g_Handle, G_SETUP_Y_Min_G_3, Y_Min_G_3);
//Read Graph #4
GetCtrlVal( g_Handle, G_SETUP_Var_G_4 , &plotVar_G_4);
GetCtrlVal( g_Handle, G_SETUP_X_Range_G_4 , &X_Range_G_4);
GetCtrlVal( g_Handle, G_SETUP_Y_Mode_G_4 , &Y_Mode_G_4 );
GetCtrlVal( g_Handle, G_SETUP_Y_Min_G_4 , &Y_Min_G_4 );
GetCtrlVal( g_Handle, G_SETUP_Y_Max_G_4 , &Y_Max_G_4 );
if (Y_Min_G_4 >= Y_Max_G_4)
    Y_Min_G_4 = Y_Max_G_4-0.5;
SetCtrlVal( g_Handle, G_SETUP_Y_Min_G_4, Y_Min_G_4);

// COM PANEL
GetCtrlVal( com_Handle, COM_SP_COM, &SP_comport);
GetCtrlVal( com_Handle, COM_SP_BR, &SP_baudrate);
GetCtrlVal( com_Handle, COM_SP_P, &SP_parity);
GetCtrlVal( com_Handle, COM_SP_DB, &SP_databits);
GetCtrlVal( com_Handle, COM_SP_SB, &SP_stopbits);
GetCtrlVal( com_Handle, COM_SP_INPUTQ, &SP_inputq);
GetCtrlVal( com_Handle, COM_SP_OUTPUTQ, &SP_outputq);
GetCtrlIndex(com_Handle, COM_SP_COM, &SP_portindex);

GetCtrlVal( com_Handle, COM_SP_COM_2, &SP2_comport);
GetCtrlVal( com_Handle, COM_SP_BR_2, &SP2_baudrate);
GetCtrlVal( com_Handle, COM_SP_P_2, &SP2_parity);
GetCtrlVal( com_Handle, COM_SP_DB_2, &SP2_databits);
GetCtrlVal( com_Handle, COM_SP_SB_2, &SP2_stopbits);
GetCtrlVal( com_Handle, COM_SP_INPUTQ_2, &SP2_inputq);
GetCtrlVal( com_Handle, COM_SP_OUTPUTQ_2, &SP2_outputq);
GetCtrlIndex(com_Handle, COM_SP_COM_2, &SP2_portindex);

return;
}
//*****
// DSN_Load_Vars : Load variables to the screen
//*****
void DSN_Load_Vars(void)
{
// MAIN PANEL

// GRAPH PANEL
//Read Graph #1
SetCtrlVal( g_Handle, G_SETUP_Var_G_1, plotVar_G_1);
SetCtrlVal( g_Handle, G_SETUP_X_Range_G_1, X_Range_G_1);
SetCtrlVal( g_Handle, G_SETUP_Y_Mode_G_1, Y_Mode_G_1);
SetCtrlVal( g_Handle, G_SETUP_Y_Min_G_1, Y_Min_G_1);
SetCtrlVal( g_Handle, G_SETUP_Y_Max_G_1, Y_Max_G_1);
//Read Graph #2
SetCtrlVal( g_Handle, G_SETUP_Var_G_2, plotVar_G_2);
SetCtrlVal( g_Handle, G_SETUP_X_Range_G_2, X_Range_G_2);
SetCtrlVal( g_Handle, G_SETUP_Y_Mode_G_2, Y_Mode_G_2);
SetCtrlVal( g_Handle, G_SETUP_Y_Min_G_2, Y_Min_G_2);
SetCtrlVal( g_Handle, G_SETUP_Y_Max_G_2, Y_Max_G_2);
//Read Graph #3
SetCtrlVal( g_Handle, G_SETUP_Var_G_3, plotVar_G_3);
SetCtrlVal( g_Handle, G_SETUP_X_Range_G_3, X_Range_G_3);
SetCtrlVal( g_Handle, G_SETUP_Y_Mode_G_3, Y_Mode_G_3);
SetCtrlVal( g_Handle, G_SETUP_Y_Min_G_3, Y_Min_G_3);
SetCtrlVal( g_Handle, G_SETUP_Y_Max_G_3, Y_Max_G_3);
//Read Graph #4
SetCtrlVal( g_Handle, G_SETUP_Var_G_4, plotVar_G_4);
SetCtrlVal( g_Handle, G_SETUP_X_Range_G_4, X_Range_G_4);
SetCtrlVal( g_Handle, G_SETUP_Y_Mode_G_4, Y_Mode_G_4);
SetCtrlVal( g_Handle, G_SETUP_Y_Min_G_4, Y_Min_G_4);
SetCtrlVal( g_Handle, G_SETUP_Y_Max_G_4, Y_Max_G_4);

// COM PANEL
SetCtrlVal( com_Handle, COM_SP_COM, SP_comport);
SetCtrlVal( com_Handle, COM_SP_BR, SP_baudrate);
SetCtrlVal( com_Handle, COM_SP_P, SP_parity);
SetCtrlVal( com_Handle, COM_SP_DB, SP_databits);
SetCtrlVal( com_Handle, COM_SP_SB, SP_stopbits);
SetCtrlVal( com_Handle, COM_SP_INPUTQ, SP_inputq);
SetCtrlVal( com_Handle, COM_SP_OUTPUTQ, SP_outputq);

```

```

        //SetCtrlIndex(com_Handle, COM_SP_COM,          SP_portindex);

SetCtrlVal( com_Handle, COM_SP_COM_2,          SP2_comport);
SetCtrlVal( com_Handle, COM_SP_BR_2,          SP2_baudrate);
SetCtrlVal( com_Handle, COM_SP_P_2,          SP2_parity);
SetCtrlVal( com_Handle, COM_SP_DB_2,          SP2_databits);
SetCtrlVal( com_Handle, COM_SP_SB_2,          SP2_stopbits);
SetCtrlVal( com_Handle, COM_SP_INPUTQ_2,      SP2_inputq);
SetCtrlVal( com_Handle, COM_SP_OUTPUTQ_2,     SP2_outputq);

return;
}
//*****
// DSN_Init2          : Init some variable and do some setup
//*****
void DSN_Init2()
{ // Set the colours up

return;
}
//*****
//*****
// DSN_Parse_SP      : Used to parse the syringe pump return string
//*****

void DSN_Parse_SP(char IN_str[], char prom[], int *vol_sp)
{
    int i=0;
    int j=0;
    int k=0;
    char str[30];
    double temp;

i = strstr( IN_str, "<>E");          // Find the position of the Prompt
//SetCtrlVal(lic_Handle,LICOM_Count, i);

j = strstr( IN_str, "0123456789"); // Find the position of the first number
k = strstr( IN_str, "l");          // Find the position of the end of the volume units
if (i>1 && (k-j)<30)
{
    CopyString (str, 0, IN_str, j, k-j);
    (*vol_sp) = atoi(str);
    // Get the Prompt
    CopyString (prom, 0, IN_str, i-1, 2);
}
}
//*****
// Flesh_LED: Flash the LED on the miniLAB 1008
//*****
int CVICALLBACK Flesh_LED (int panel, int control, int event,
void *callbackData, int eventData1, int eventData2)
{
    /* Variable Declarations */
    int BoardNum = 0;
    int UDStat = 0;
    switch (event)
    {
        case EVENT_COMMIT:
            switch(control)
            {
                case COM_Minil008:
                    UDStat = cbFlashLED(0);
                    //SetCtrlVal (panelHandle, PANEL_LED_Err, UDStat);
                    break;
                case COM_PMD_1208FS:
                    UDStat = cbFlashLED(2);
                    //SetCtrlVal (panelHandle, PANEL_LED_Err, UDStat);
                    break;
            }
        case EVENT_RIGHT_CLICK:
            break;
    }
    return 0;
}

//*****
// PRESS_ON_OFF: Turns on/off Pressure Transducer's data on the screen
//*****

int CVICALLBACK PRESS_ON_OFF (int panel, int control, int event,
void *callbackData, int eventData1, int eventData2)

```

```

{

int bytes_read;
int Mini1008 = 0; // Board Number as configure in InstaCal
int UDStat = 0;
int Chan;
int Gain = BIP10VOLTS ;
WORD DataValue = 0;
float EngUnits;
double TEMP[10];

switch (event)
{
    case EVENT_COMMIT:

        GetCtrlVal(panelHandle, PANEL_PRESS_TRANS, &Is_PRESS);

        if(~Is_PRESS)
        {
            SetCtrlVal (panelHandle,PANEL_LED_Press, 0);
        }
        break;

}
return 0;
}
//*****
// AIR_FM_ON_OFF: Turns on/off the air flow meter
//*****

int CVICALLBACK AIR_FM_ON_OFF (int panel, int control, int event,
    void *callbackData, int eventData1, int eventData2)
{
    double AIR_FLOW=0;
    int flow,length;
    short read_cnt;
    char read_COM_Temp[150];
    int bytes_read;
    char seps[]=" ";
    double temp;
    double TEMP[10];

    switch (event)
    {
        case EVENT_COMMIT:

            GetCtrlVal(panelHandle, PANEL_AIR_FM, &Is_AIR_FM);

            if(~Is_AIR_FM)
            {
                SetCtrlVal (panelHandle,PANEL_LED_Air, 0);
                FlushInQ (SP_comport);
                FlushOutQ(SP_comport);
                // Turn the flow rate to zero
                AIR_FLOW = 0;
                flow = abs(AIR_FLOW);
                Fmt(send_data, "%s<A%i\r",flow);
                length = StringLength (send_data);
                FlushInQ (SP_comport);
                FlushOutQ(SP_comport);
                ComWrt (SP_comport, send_data, length);
            }
            break;

    }
    return 0;
}
//*****
// WATER_FM_ON_OFF: Turns on/off the water flow meter
//*****

int CVICALLBACK WATER_FM_ON_OFF (int panel, int control, int event,
    void *callbackData, int eventData1, int eventData2)
{
    double Water_FLOW=0;
    int flow,length;

    switch (event)
    {
        case EVENT_COMMIT:

            GetCtrlVal(panelHandle, PANEL_WATER_FM, &Is_WATER_FM);

            if(~Is_WATER_FM)
            {

```

```

        SetCtrlVal (panelHandle,PANEL_LED_Water, 0);
        FlushInQ (SP2_comport);
        FlushOutQ(SP2_comport);
        // Turn the flow rate to zero
        Water_FLOW = 0;
        flow = abs(Water_FLOW);
        Fmt(send_data, "%s<A%i\r",flow);
        length = StringLength (send_data);
        FlushInQ (SP2_comport);
        FlushOutQ(SP2_comport);
        ComWrt (SP2_comport, send_data, length)
    }

    break;
}

return 0;
}
//*****
// Send_Air_SetPoint: Send set point to the air flow meter
//*****

int CVICALLBACK Send_Air_SetPoint (int panel, int control, int event,
    void *callbackData, int eventData1, int eventData2)
{
    double AIR_FLOW=0;
    int flow,length;

    switch (event)
    {
        case EVENT_COMMIT:

            GetCtrlVal (panelHandle, PANEL_set_Air_set_point, &AIR_FLOW);
            // Do calc
            AIR_FLOW = (AIR_FLOW * 64000) / 5 ;
            flow = abs(AIR_FLOW);
            Fmt(send_data, "%s<A%i\r",flow);
            //Fmt(send_data, "%s<A0\r");
            length = StringLength (send_data);
            FlushInQ (SP_comport);
            FlushOutQ(SP_comport);
            ComWrt (SP_comport, send_data, length); // Poll the meter for data
            //ComWrt (SP_comport, "A0\r", ); // Poll the meter for data

            break;
    }
    return 0;
}
//*****
// Send_Water_SetPoint: Send set point to the water flow meter
//*****

int CVICALLBACK Send_Water_SetPoint (int panel, int control, int event,
    void *callbackData, int eventData1, int eventData2)
{
    double Water_FLOW=0;
    int flow,length;

    switch (event)
    {
        case EVENT_COMMIT:

            GetCtrlVal (panelHandle, PANEL_set_Water_set_point, &Water_FLOW);
            // Do calc
            Water_FLOW = (Water_FLOW * 64000) / 500 ;
            flow = abs(Water_FLOW);
            Fmt(send_data, "%s<A%i\r",flow);
            //Fmt(send_data, "%s<A0\r");
            length = StringLength (send_data);
            FlushInQ (SP2_comport);
            FlushOutQ(SP2_comport);
            ComWrt (SP2_comport, send_data, length); // Poll the meter for data
            //ComWrt (SP2_comport, "A0\r", 3); // Poll the meter for data

            break;
    }
    return 0;
}
}
}

```

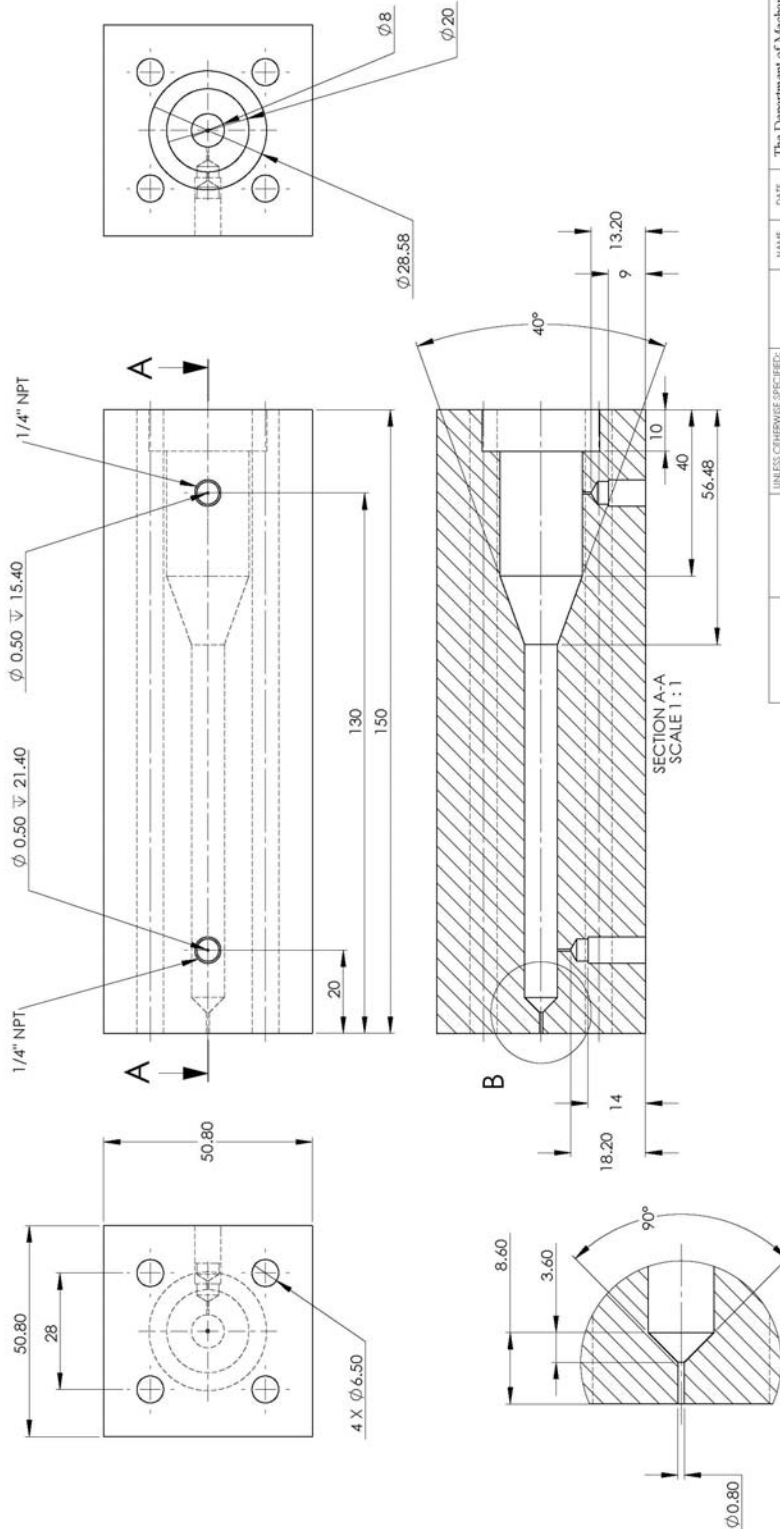

Appendix B: Drawings

In this appendix the drawings of the atomizers and the other parts are presented. The drawings have been developed in SolidWorks software.

Appendix B-1 contains drawings of the main body of the atomizer mark I and also the air injector used in this atomizer. Appendix B-2 provides drawings of the body of the atomizer mark II and also the porous and the multi-hole air injectors. Appendix B-2 shows the drawing of the air and liquid supply part. The air and liquid supply part provides the connection between the air/water tubes and the atomizer body. This part has been used with both the first and the atomizer mark IIs.

Appendix B1: Atomizer Mark I

Atomizer Body:

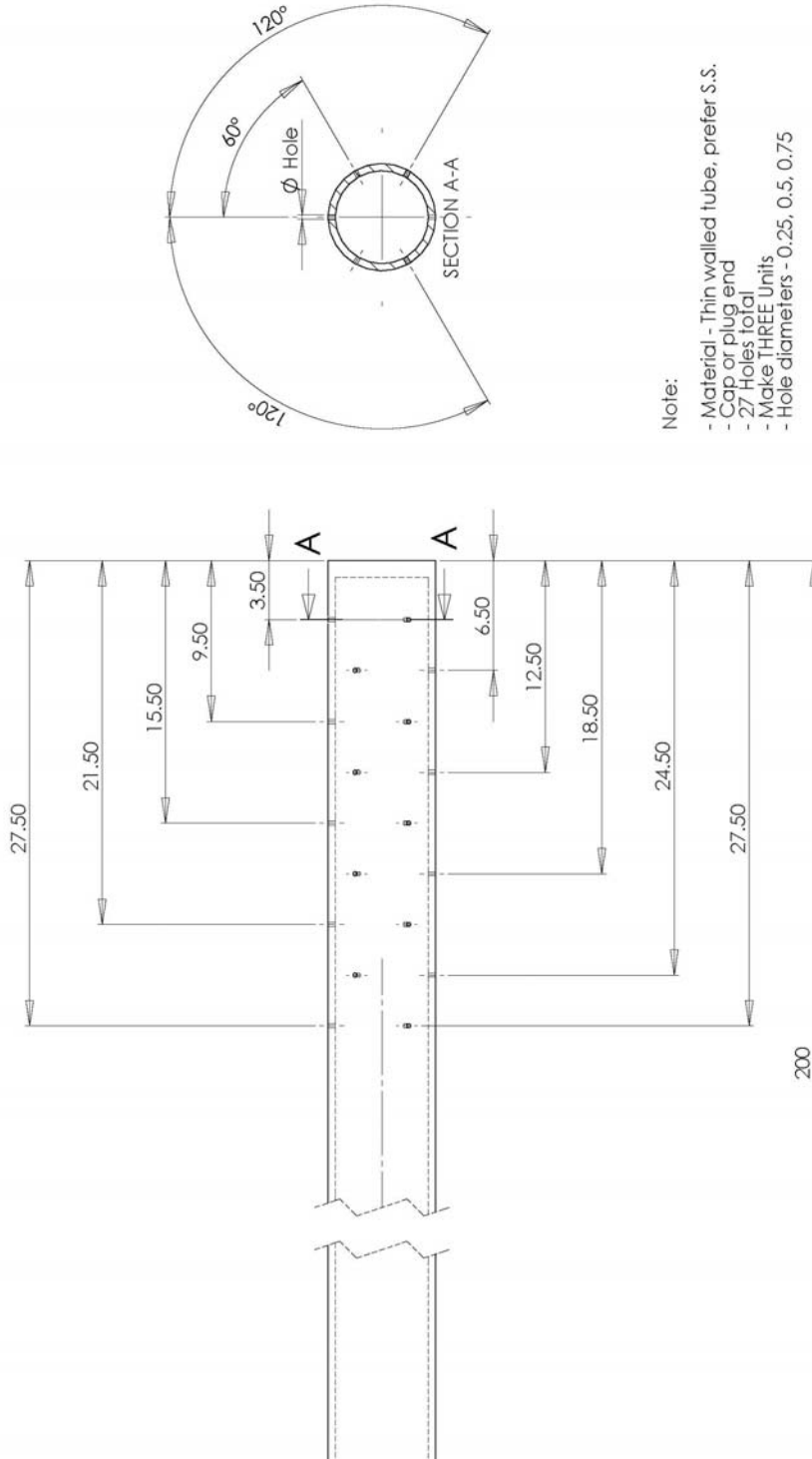


UNLESS OTHERWISE SPECIFIED:		DRAWN		DATE	
TOLERANCES:	ARE IN MILLIMETERS	DSN			
ANGULAR DIMENSIONS:	BEND TO	CHECKED			
TWO PLACE DECIMAL		ENG. APPR.			
THREE PLACE DECIMAL		MFG. APPR.			
TOLERANCING:		D.A.			
INTERPRET GEOMETRIC TOLERANCING:		COMMENTS:			
MATERIAL:		DATE:			
FINISH:		APPICATION:			
NEST ASST:		USED ON:			
		DO NOT SCALE DRAWING			

PROPERTY AND CONFIDENTIALITY OF THE UNIVERSITY OF MICHIGAN IS HEREBY DECLARED. ANY REPRODUCTION OR DISTRIBUTION OF THIS DRAWING WITHOUT THE WRITTEN PERMISSION OF THE UNIVERSITY OF MICHIGAN IS PROHIBITED.

The Department of Mechanical Engineering		UNIVERSITY OF MICHIGAN	
TITLE:			
Body for visu			
SIZE	DWG. NO.		
B			
SCALE: 1:2		WEIGHT:	

Multi-Hole Air Injector

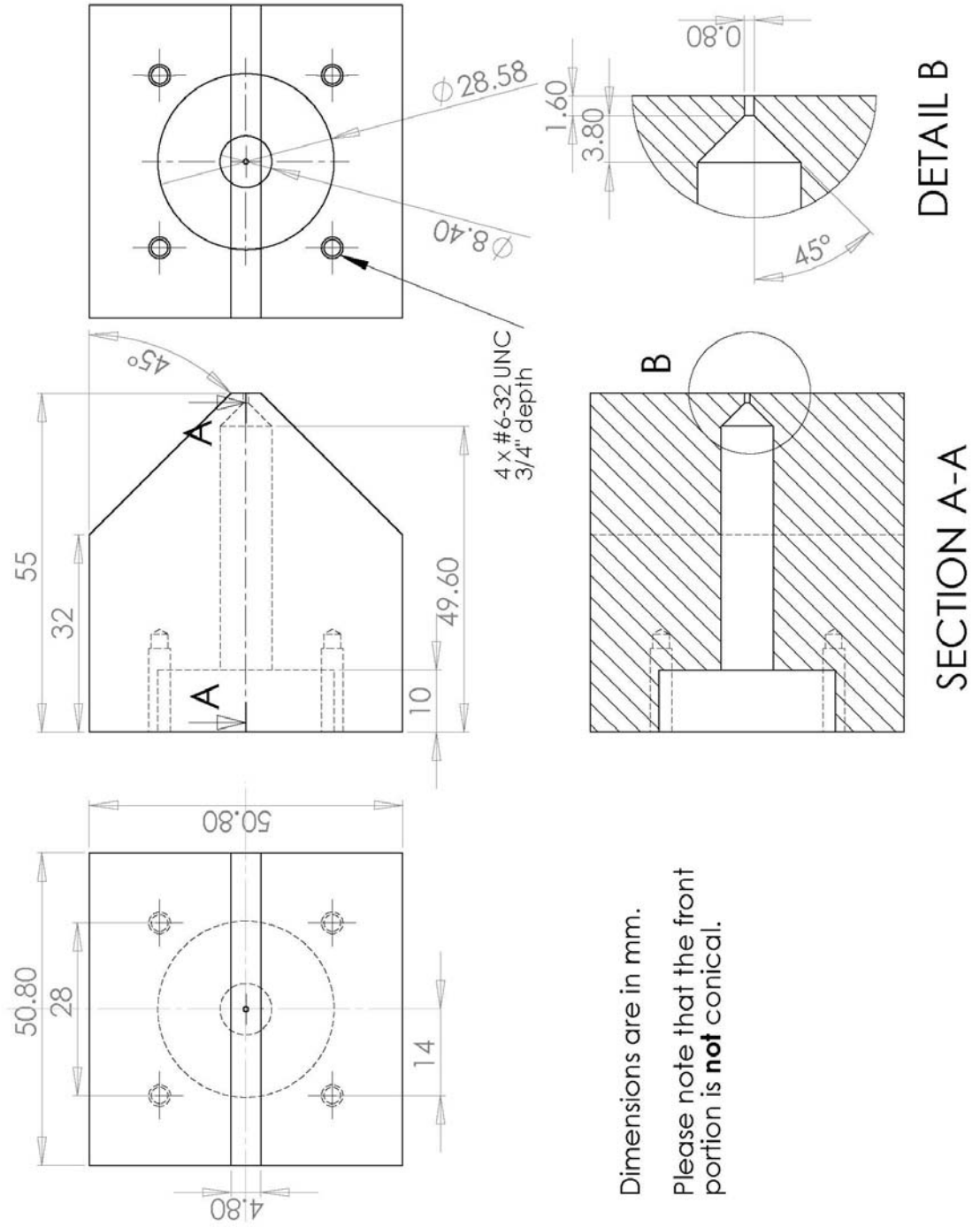


- Note:**
- Material - Thin walled tube, prefer S.S.
 - Cap or plug end
 - 27 Holes total
 - Make THREE Units
 - Hole diameters - 0.25, 0.5, 0.75

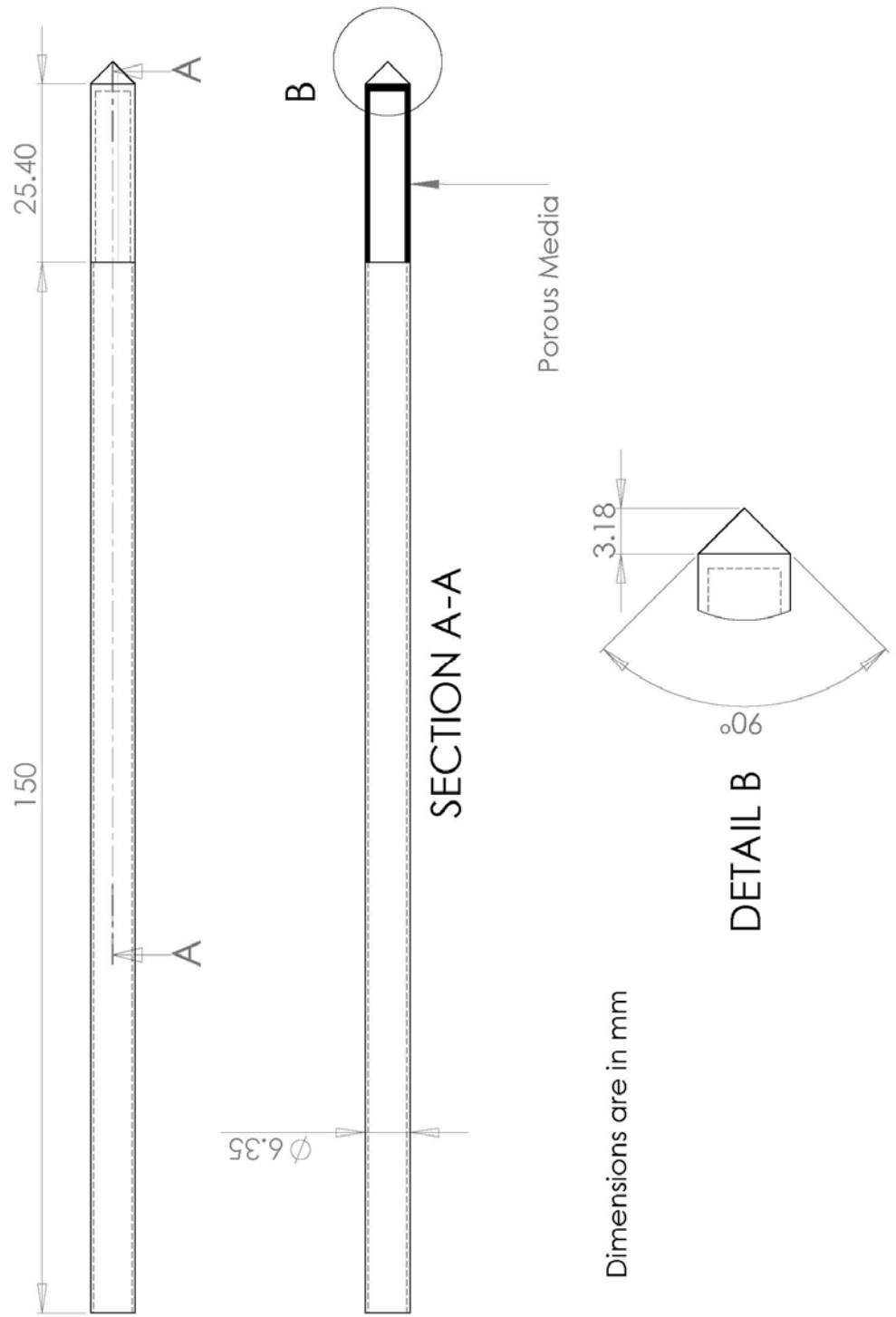
UNLESS OTHERWISE SPECIFIED:		NAME	DATE	The Department of Mechanical Engineering UNIVERSITY OF ALBERTA	
DIMENSIONS ARE IN INCHES	DRAWN	ESN		TITLE: RKN Spray Nozzle Air Injector	
TOLERANCES:	CHECKED				
ANGULAR: MACH ± .005	END APPR.				
TWO PLACE DECIMAL	INFO APPR.				
THREE PLACE DECIMAL	G.A.				
INTERFERE GEOMETRIC TOLERANCING FIB.	COMMENTS:				
MATERIAL:	FINISH:				
88	88				
PROPERTY AND CONFIDENTIAL THIS DRAWING IS THE SOLE PROPERTY OF RKN SPRAY NOZZLE CO. ANY REPRODUCTION OR USE WITHOUT THE WRITTEN PERMISSION OF RKN SPRAY NOZZLE CO. IS PROHIBITED.	APPROVAL:				
NEET ASST	USED ON				
SCALE: 4:1	WEIGHT:				
SIZE	DWG. NO.	RKN-006		REV	SHEET 1 OF 1

Appendix B2: Atomizer Mark II

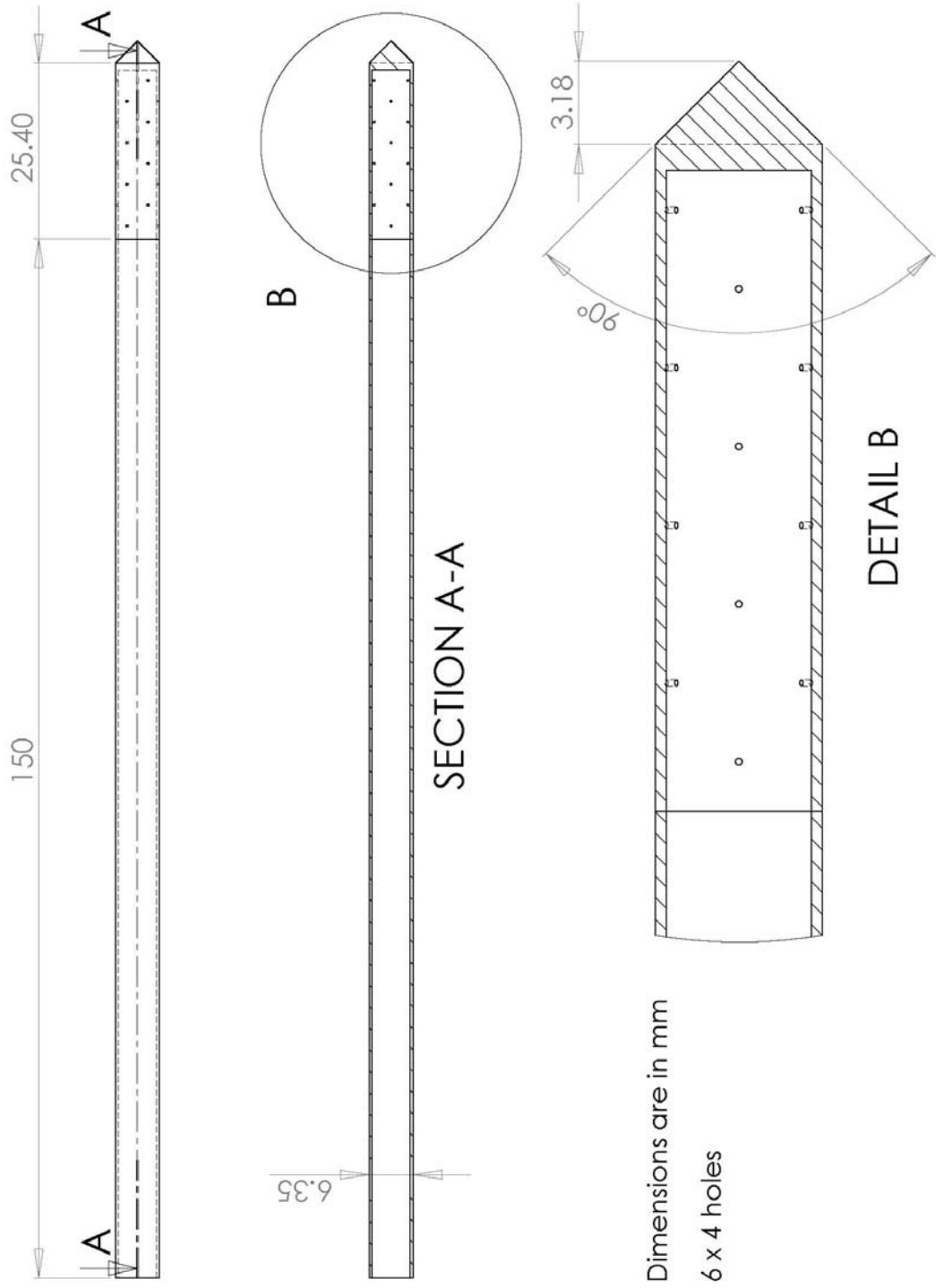
Atomizer Body:



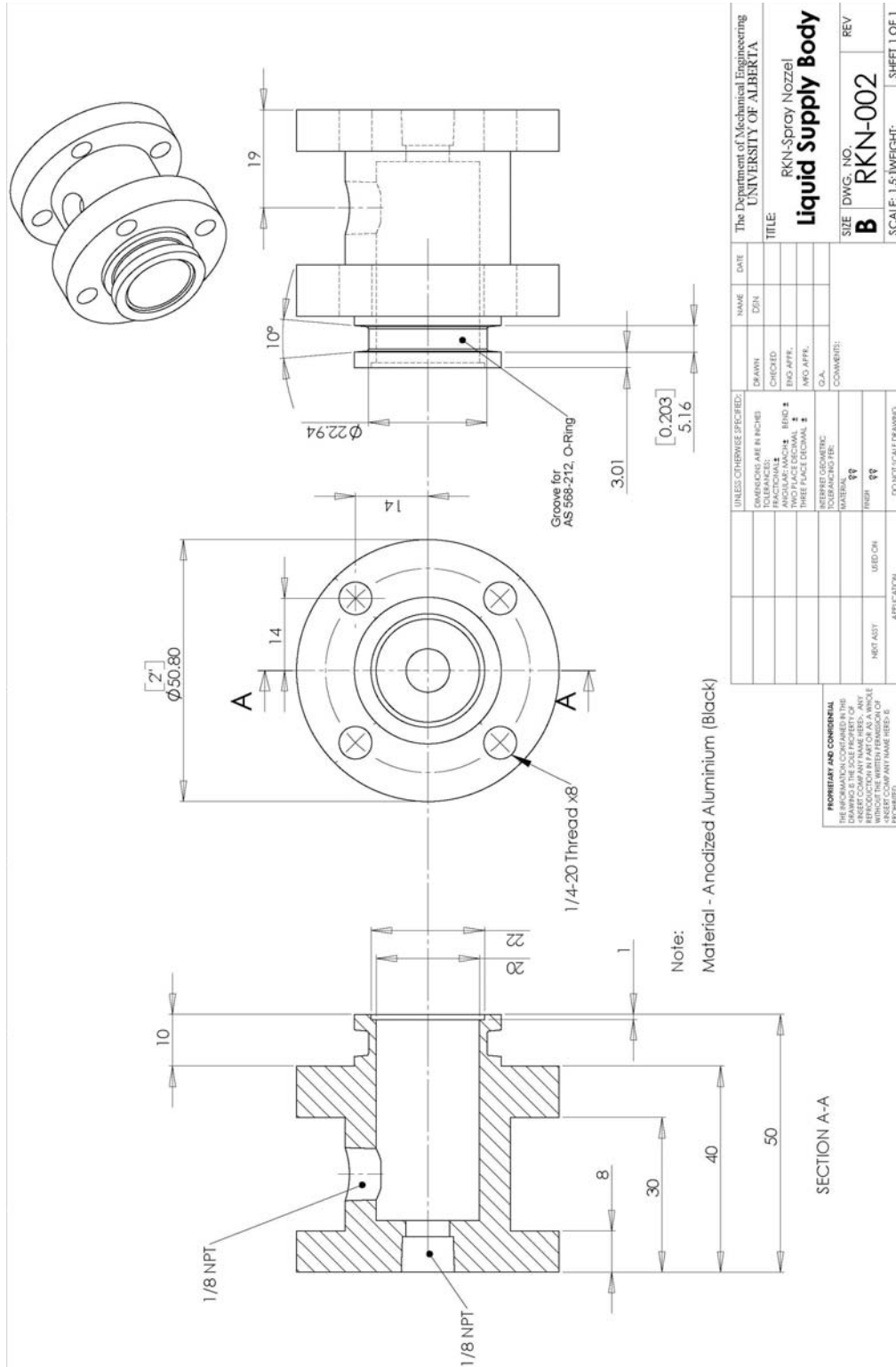
Porous Air Injector



Multi-Hole Air Injector



Appendix B3: Air and Liquid Supply



UNLESS OTHERWISE SPECIFIED:	NAME	DATE	THE DEPARTMENT OF MECHANICAL ENGINEERING UNIVERSITY OF ALBERTA
DIMENSIONS ARE IN INCHES	DSN		
FRACTIONAL	CHKD		
DECIMAL	ENG APPR.		
THREE PLACE DECIMAL	MFG APPR.		
TOLERANCES UNLESS OTHERWISE SPECIFIED:	COMMENTS:		
FRACTIONAL			
DECIMAL			
TEMP			
LEAD IN			
NET ASY	APPLICATION		
	DO NOT SCALE DRAWING		

PROPRIETARY AND CONFIDENTIAL
 THE INFORMATION CONTAINED IN THIS DRAWING IS THE PROPERTY OF THE UNIVERSITY OF ALBERTA. IT IS TO BE USED ONLY FOR THE PROJECT AND FOR WHICH IT WAS PREPARED. ANY REUSE OR DISSEMINATION OF THIS INFORMATION WITHOUT THE WRITTEN PERMISSION OF THE UNIVERSITY OF ALBERTA IS PROHIBITED.

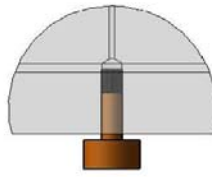
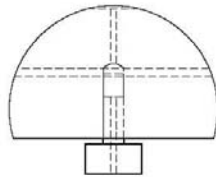
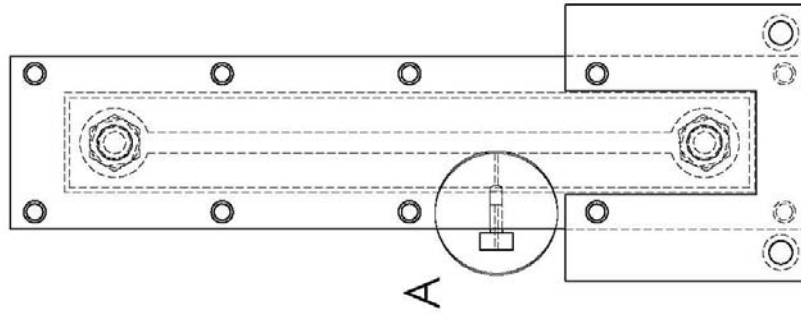
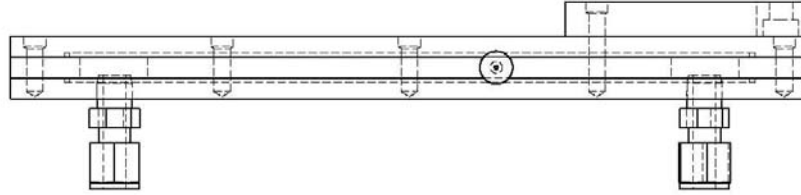
REV
B RKN-002

SCALE: 1:1 (WEIGHT)

SHEET 1 OF 1

Appendix B3: Bubble Generator Setup

The Assembly:

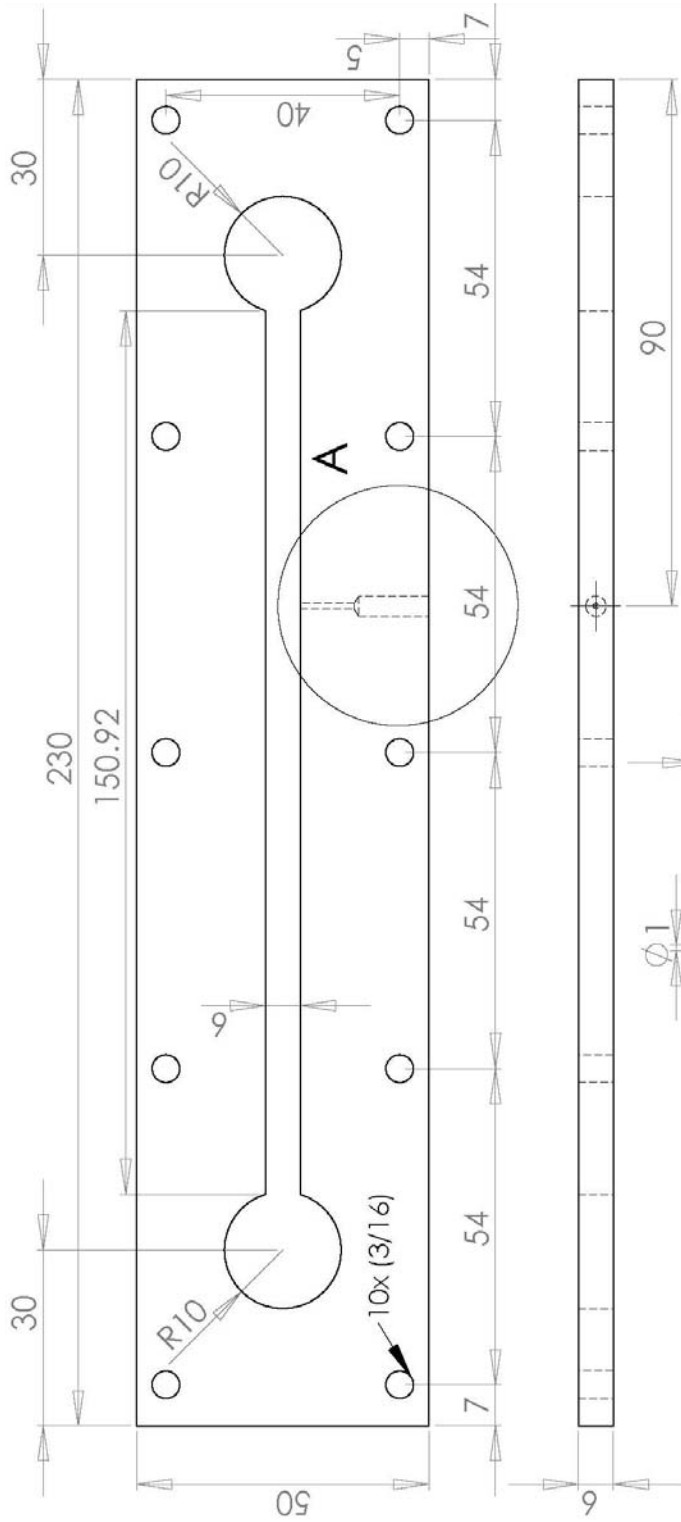


DETAIL A
SCALE 1:1

UNLESS OTHERWISE SPECIFIED:		DRAWN	NAME	DATE
DIMENSIONS ARE IN INCHES		CHECKED		
TOLERANCES:		ENG APPR.		
FRACTIONAL ±		MFG APPR.		
ANGULAR: MACH ± BEND ±		Q.A.		
TWO PLACE DECIMAL ±		COMMENTS:		
THREE PLACE DECIMAL ±				
INTERPRET GEOMETRIC TOLERANCING PER:				
MATERIAL				
FINISH				
NEXT ASSY		USED ON		
APPLICATION				
DO NOT SCALE DRAWING				

<p>PROPRIETARY AND CONFIDENTIAL THE INFORMATION CONTAINED IN THIS DRAWING IS THE SOLE PROPERTY OF <INSERT COMPANY NAME HERE>. ANY REPRODUCTION IN PART OR AS A WHOLE WITHOUT THE WRITTEN PERMISSION OF <INSERT COMPANY NAME HERE> IS PROHIBITED.</p>	
SIZE	DWG. NO.
A	Assem1
REV	
SCALE: 1:5	WEIGHT:
	SHEET 1 OF 1

Middle Plane:



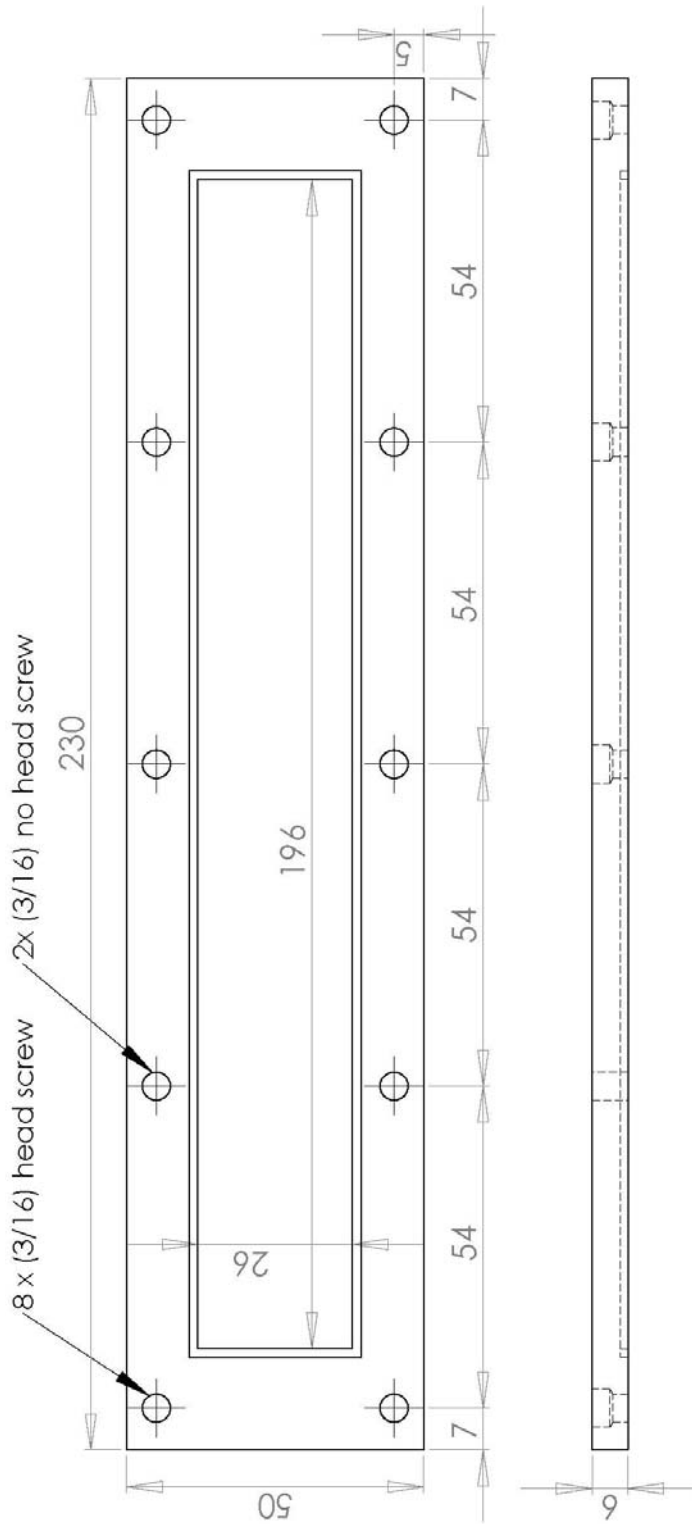
DETAIL A
SCALE 1:1

UNLESS OTHERWISE SPECIFIED:		NAME	DATE
DIMENSIONS ARE IN INCHES	DRAWN		
TOLERANCES:	CHECKED		
FRACTIONAL:	ENG APPR.		
ANGULAR: MACH ± BEND ±	MFG APPR.		
TWO PLACE DECIMAL ±	G.A.		
THREE PLACE DECIMAL ±	COMMENTS:		
INTERPRET GEOMETRIC TOLERANCING PER	MATERIAL		
FINISH	USED ON		
APPLICATION	DO NOT SCALE DRAWING		
NEXT ASSY			

TITLE:	
SIZE	DWG. NO.
A	main
REV	
SCALE: 1:2	WEIGHT:
	SHEET 1 OF 1

PROPRIETARY AND CONFIDENTIAL
THE INFORMATION CONTAINED IN THIS DRAWING IS THE SOLE PROPERTY OF [INSERT COMPANY NAME HERE]. ANY REPRODUCTION IN PART OR AS A WHOLE WITHOUT THE WRITTEN PERMISSION OF [INSERT COMPANY NAME HERE] IS PROHIBITED.

Front Window:



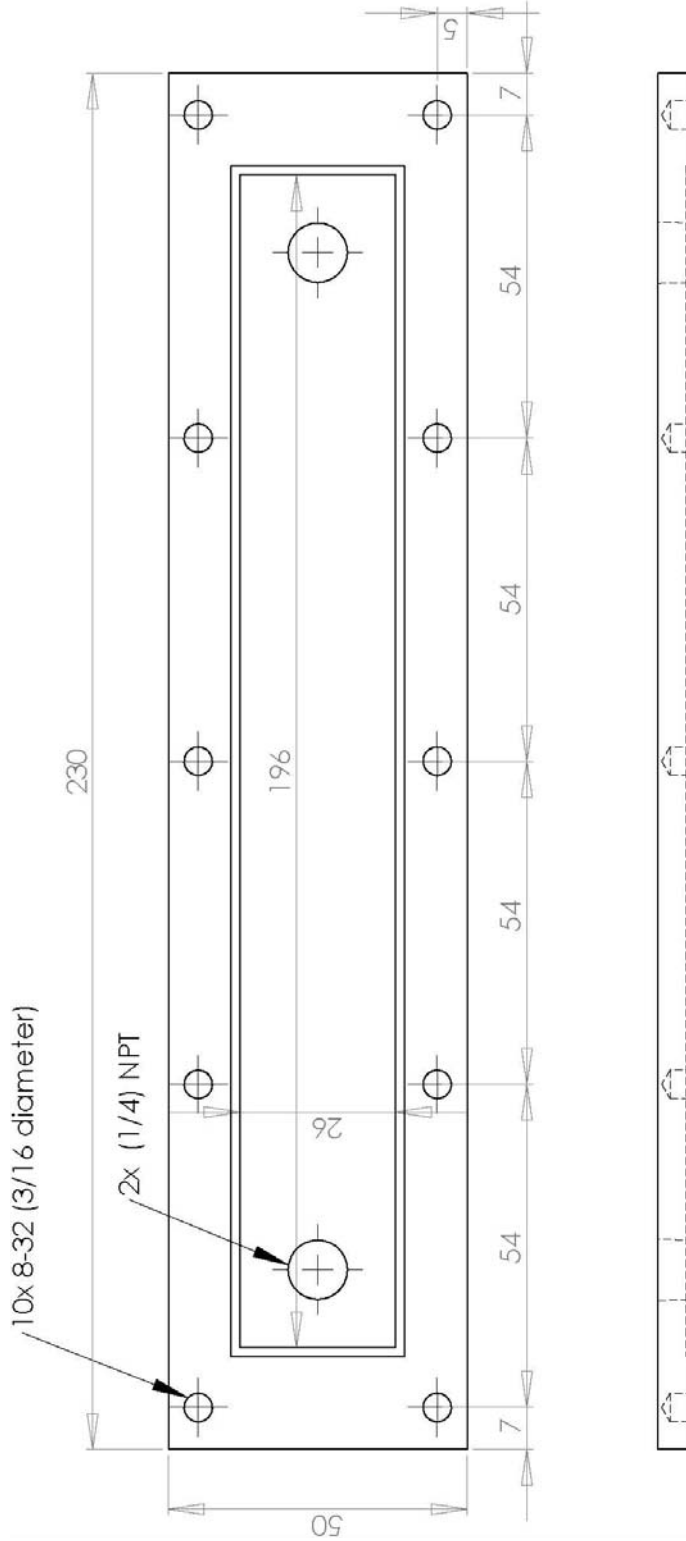
UNLESS OTHERWISE SPECIFIED:		NAME	DATE
DRAWN			
CHECKED			
ENG APPR.			
MFG APPR.			
Q.A.			
COMMENTS:			
DIMENSIONS ARE IN INCHES			
TOLERANCES:			
FRACTIONAL ±	BEND ±		
ANGULAR: MACH ±	TWO PLACE DECIMAL ±		
THREE PLACE DECIMAL ±			
INTERPRET GEOMETRIC TOLERANCING PER			
MATERIAL			
FINISH			
NEXT ASSY	USED ON		
APPLICATION			

TITLE:

PROPRIETARY AND CONFIDENTIAL
 THE INFORMATION CONTAINED IN THIS DRAWING IS THE SOLE PROPERTY OF [INSERT COMPANY NAME HERE]. ANY REPRODUCTION IN PART OR AS A WHOLE WITHOUT THE WRITTEN PERMISSION OF [INSERT COMPANY NAME HERE] IS PROHIBITED.

SIZE DWG. NO. REV
A window 1
 SCALE: 1:2 WEIGHT: SHEET 1 OF 1

Back Window:



UNLESS OTHERWISE SPECIFIED:		NAME	DATE
DIMENSIONS ARE IN INCHES	DRAWN		
TOLERANCES:	CHECKED		
FRACTIONAL ±	ENG APPR.		
ANGULAR: MACH ± BEND ±	MFG APPR.		
TWO PLACE DECIMAL ±	Q.A.		
THREE PLACE DECIMAL ±	COMMENTS:		
INTERPRET GEOMETRIC TOLERANCING PER:			
MATERIAL			
FINISH			
USED ON			
NEXT ASSY			
APPLICATION			

TITLE:

PROPRIETARY AND CONFIDENTIAL
 THE INFORMATION CONTAINED IN THIS DRAWING IS THE SOLE PROPERTY OF <INSERT COMPANY NAME HERE>. ANY REPRODUCTION IN PART OR AS A WHOLE WITHOUT THE WRITTEN PERMISSION OF <INSERT COMPANY NAME HERE> IS PROHIBITED.

SIZE DWG. NO. REV
A window 2
 SCALE: 1:2 WEIGHT: SHEET 1 OF 1

Appendix C: Processes using Davis Software

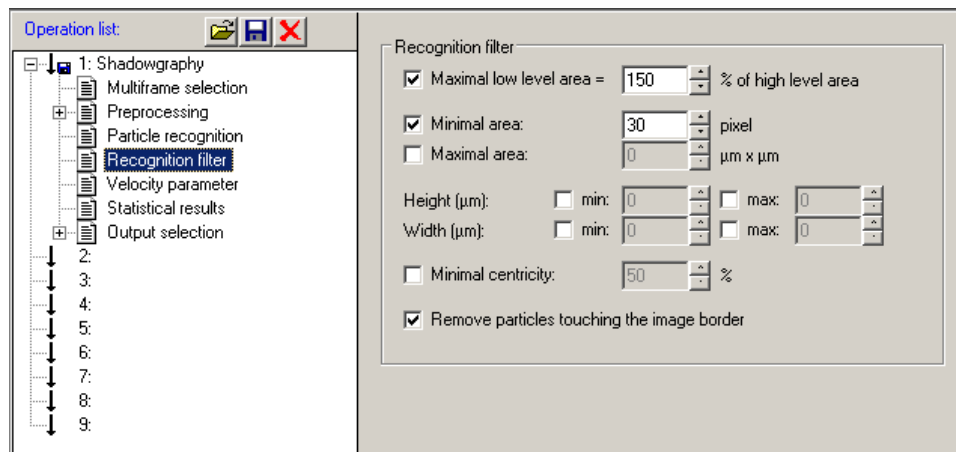
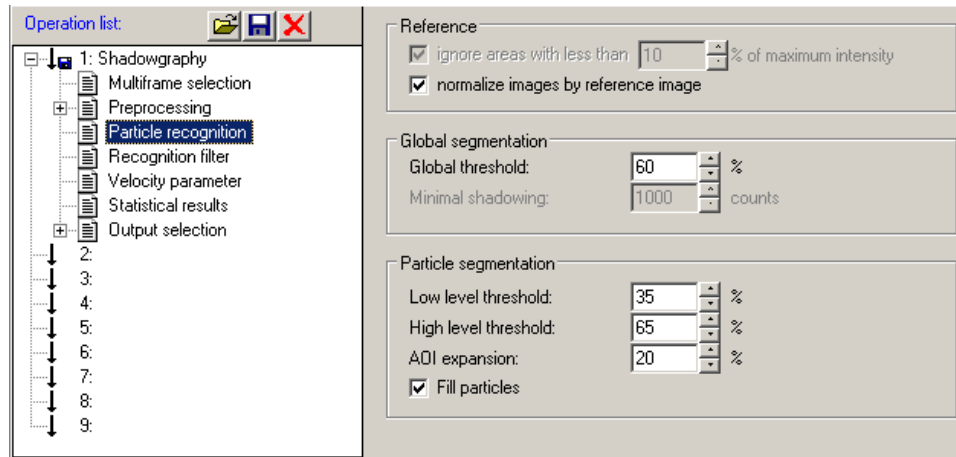
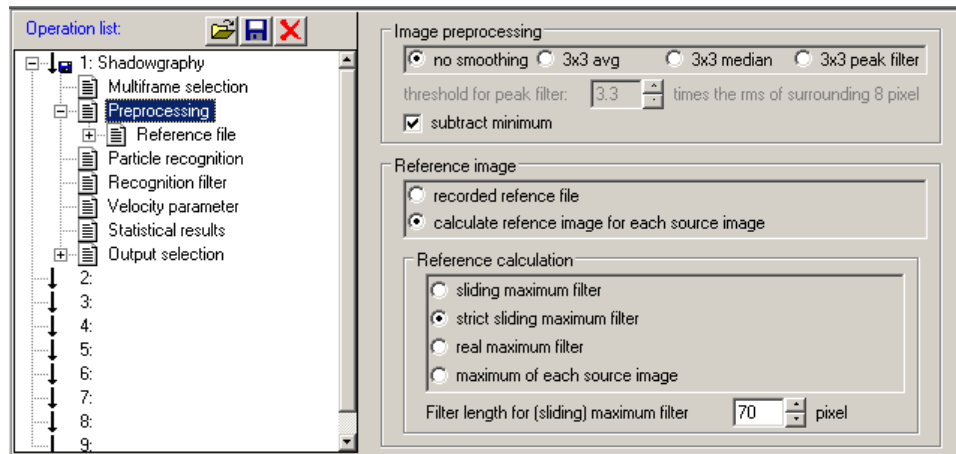
Appendix C1 provides the parameters used in the shadow-PTV process of the spray droplets. This process measures the area equivalent diameter and the velocity of the recorded droplets.




Appendix C2 presents the parameters used in the StereoPIV process. This StereoPIV process has been applied to measure the velocity of the droplets in the spray field.

Appendix C3 shows the parameters used in the PTV process of the shadow-PIV/PTV experiment. This process calculates area equivalent diameter, shape, location and velocity of the bubbles.

Appendix C4 shows the parameters used in the PIV process of the shadow-PIV/PTV experiment. This process calculates the velocity of the liquid field in the bubble generation experiment.

Appendix C1: Shadow-PTV Process



Operation list:   

- 1: Shadowgraphy
 - Multiframe selection
 - Preprocessing
 - Particle recognition
 - Recognition filter
 - Velocity parameter**
 - Statistical results
 - Output selection
- 2:
- 3:
- 4:
- 5:
- 6:
- 7:
- 8:
- 9:

Interrogation window

Initial window size: X: 30 × Y: 70 μm

Final window size: X: 20.8333 × Y: 48.6111 μm

Passes: 3

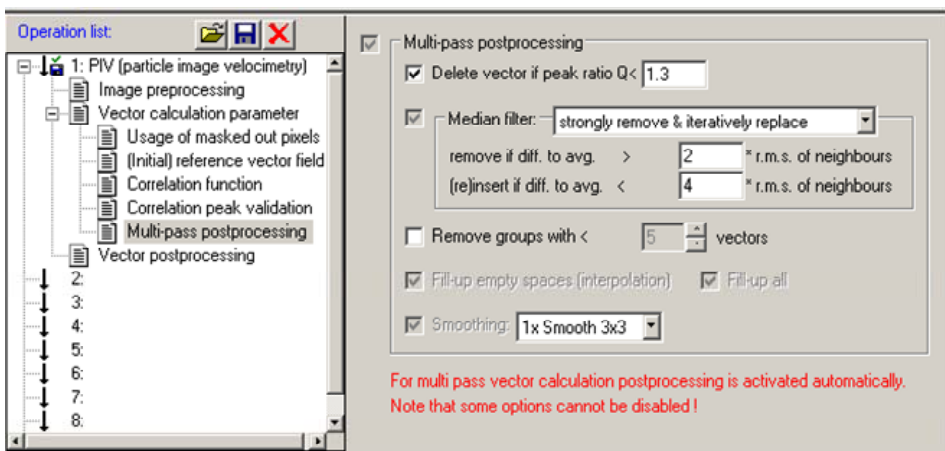
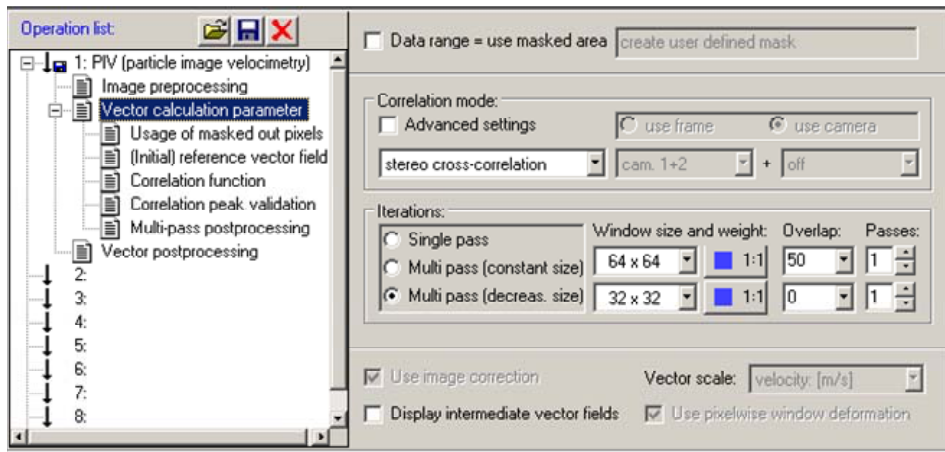
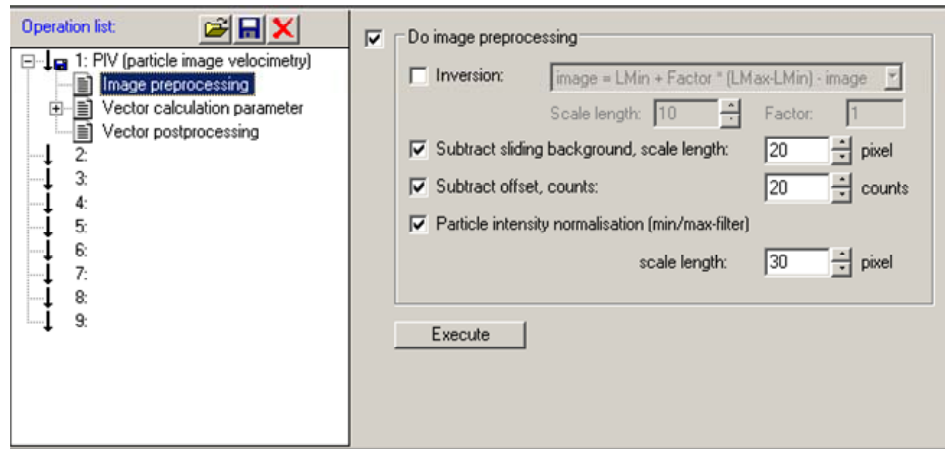
Decrease size: 1.2 time(s) in each pass

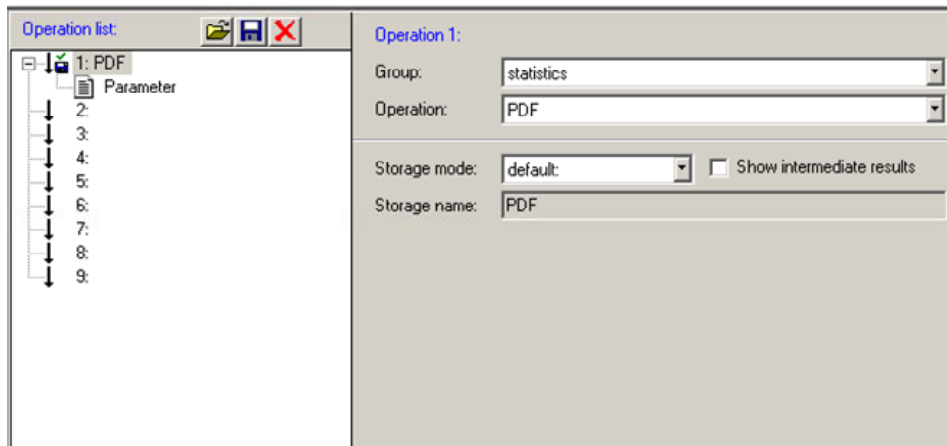
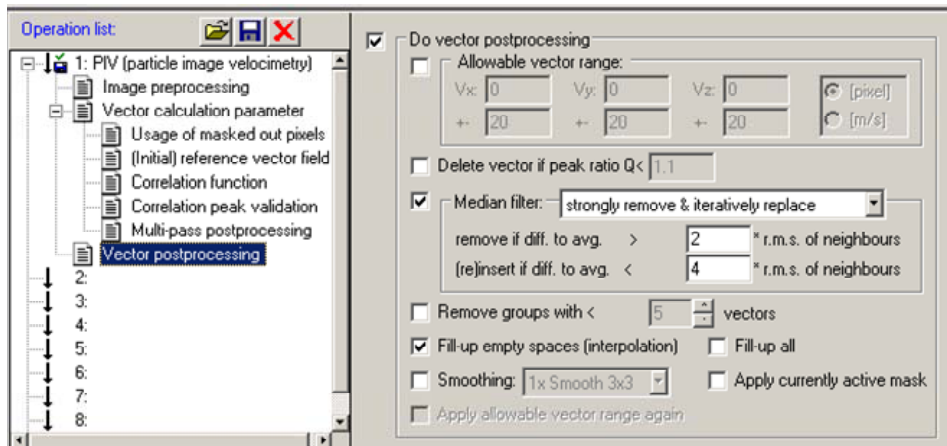
Options

Diameter deviation: +/- 15 %

Initial shift: X: 0 Y: 15 μm

Appendix C2: StereoPIV Process





Appendix C3: The PTV Process of the Shadow-PIV/PTV Experiment

Operation list:

- 1: inside rectangle = const
- 2: inside rectangle = const
- 3: inside rectangle = const
- 4:
- 5: Shadowgraphy
 - Multiframe selection
 - Preprocessing
 - Reference file
 - Particle recognition
 - Recognition filter
 - Velocity parameter
 - Statistical results
 - Output selection
- 6:
- 7:
- 8:
- 9:

Image preprocessing

no smoothing
 3x3 avg
 3x3 median
 3x3 peak filter

threshold for peak filter: 3.3 times the rms of surrounding 8 pixel

subtract minimum

Reference image

recorded reference file
 calculate reference image for each source image

Reference calculation

sliding maximum filter
 strict sliding maximum filter
 real maximum filter
 maximum of each source image

Filter length for (sliding) maximum filter: 40 pixel

Operation list:

- 1: inside rectangle = const
- 2: inside rectangle = const
- 3: inside rectangle = const
- 4:
- 5: Shadowgraphy
 - Multiframe selection
 - Preprocessing
 - Particle recognition
 - Recognition filter
 - Velocity parameter
 - Statistical results
 - Output selection
- 6:
- 7:
- 8:
- 9:

Reference

ignore areas with less than 10 % of maximum intensity
 normalize images by reference image

Global segmentation

Global threshold: 80 %

Minimal shadowing: 100 counts

Particle segmentation

Low level threshold: 48 %
 High level threshold: 52 %
 ADI expansion: 2 %
 Fill particles

Operation list:

- 1: inside rectangle = const
- 2: inside rectangle = const
- 3: inside rectangle = const
- 4:
- 5: Shadowgraphy
 - Multiframe selection
 - Preprocessing
 - Particle recognition
 - Recognition filter
 - Velocity parameter
 - Statistical results
 - Output selection
- 6:
- 7:
- 8:
- 9:

Recognition filter

Maximal low level area = 103 % of high level area
 Minimal area: 1000 pixel
 Maximal area: 0 $\mu\text{m} \times \mu\text{m}$

Height (μm): min: 0 max: 0
 Width (μm): min: 0 max: 0

Minimal centricity: 50 %
 Remove particles touching the image border

Operation list: [Save] [Print] [Close]

- 1: inside rectangle = const
- 2: inside rectangle = const
- 3: inside rectangle = const
- 4:
- 5: Shadowgraphy
 - Multiframe selection
 - Preprocessing
 - Particle recognition
 - Recognition filter
 - Velocity parameter
 - Statistical results
 - Output selection
- 6:
- 7:
- 8:
- 9:

Interrogation window

Initial window size: X: 10 Y: 10 μm

Final window size: X: 4.44444 Y: 4.44444 μm

Passes: 3

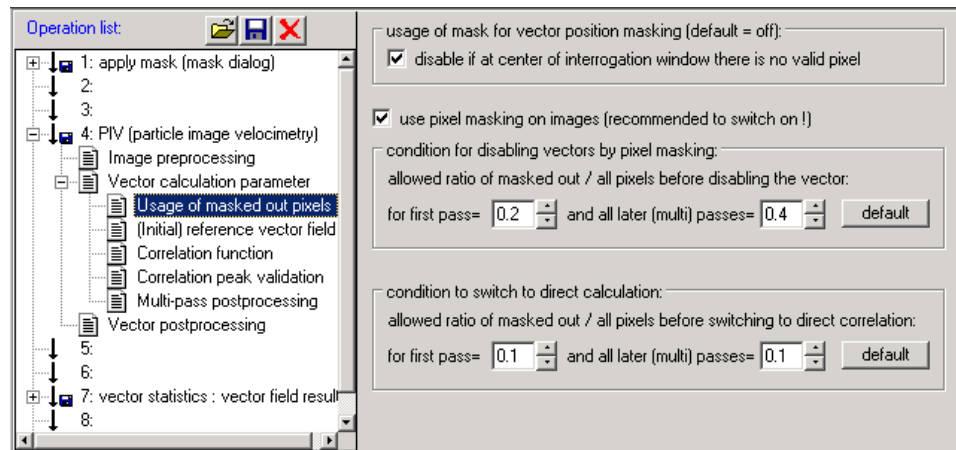
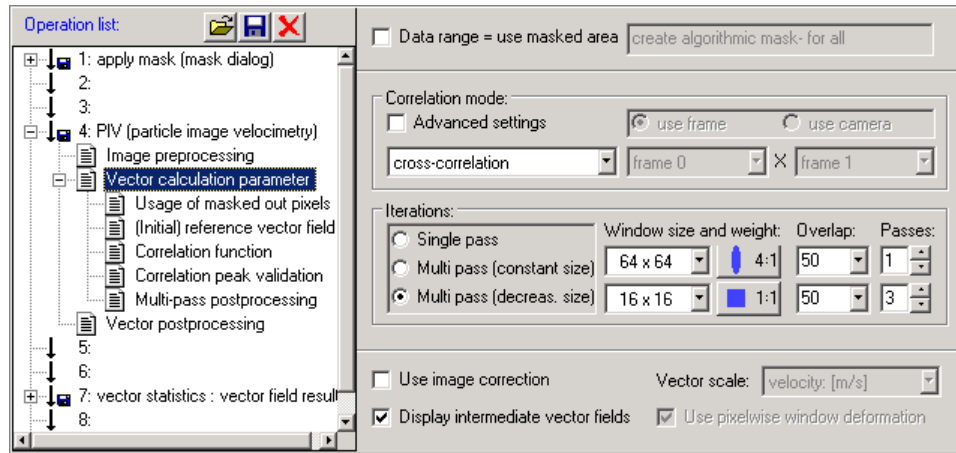
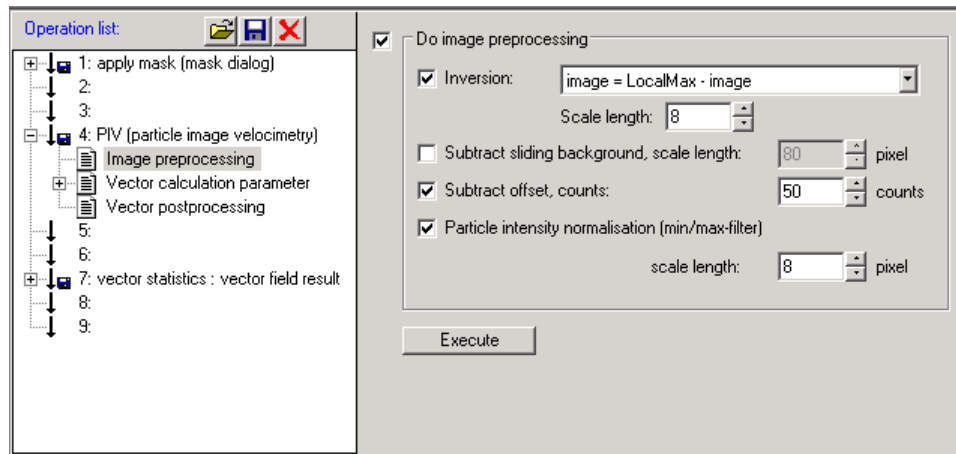
Decrease size: 1.5 time(s) in each pass




Options

Diameter deviation: +/- 20 %

Initial shift: X: 0 Y: 1 μm

Appendix C4: The PIV process of the Shadow-PIV/PTV Experiment




Operation list:   

- 1: apply mask (mask dialog)
- 2:
- 3:
- 4: PIV (particle image velocimetry)
 - Image preprocessing
 - Vector calculation parameter
 - Usage of masked out pixels
 - (Initial) reference vector field
 - Correlation function
 - Correlation peak validation
 - Multi-pass postprocessing
 - Vector postprocessing
- 5:
- 6:
- 7: vector statistics : vector field result
- 8:

Initial interrogation window shift (first pass only):

Constant dx: 0 dy: 0 dz: 0 pixel

Use reference vector field C:\TEMP\vectorfunction_1wirbel.VEC 

Restrictions implied by (adaptive multipass / initial) reference vector fields:

Relative vector range restriction = reference + all (window size/2)




AND

Absolute vector range restriction = reference + 8 pixel

Vector position:

Symmetrical: in the middle between interrogation windows/images

At position of first interrogation window / image (use for time-series data)

Operation list:   

- 1: apply mask (mask dialog)
- 2:
- 3:
- 4: PIV (particle image velocimetry)
 - Image preprocessing
 - Vector calculation parameter
 - Usage of masked out pixels
 - (Initial) reference vector field
 - Correlation function
 - Correlation peak validation
 - Multi-pass postprocessing
 - Vector postprocessing
- 5:
- 6:
- 7: vector statistics : vector field result
- 8:

Multi-pass postprocessing

Delete vector if peak ratio Q < 1.3

Median filter: strongly remove & iteratively replace

remove if diff. to avg. > 5 * r.m.s. of neighbours




(re)insert if diff. to avg. < 3 * r.m.s. of neighbours

Remove groups with < 5 vectors

Fill-up empty spaces (interpolation) Fill-up all

Smoothing: 1x Smooth 3x3

For multi pass vector calculation postprocessing is activated automatically.
Note that some options cannot be disabled!

Operation list:   

- 1: apply mask (mask dialog)
- 2:
- 3:
- 4: PIV (particle image velocimetry)
 - Image preprocessing
 - Vector calculation parameter
 - Usage of masked out pixels
 - (Initial) reference vector field
 - Correlation function
 - Correlation peak validation
 - Multi-pass postprocessing
 - Vector postprocessing
- 5:
- 6:
- 7: vector statistics : vector field result
- 8:

Do vector postprocessing

Allowable vector range:

Vx: 0 Vy: 0 Vz: 0 [pixel]

+ 20 + 20 + 20 [m/s]

Delete vector if peak ratio Q < 1.3

Median filter: strongly remove & iteratively replace

remove if diff. to avg. > 4 * r.m.s. of neighbours

(re)insert if diff. to avg. < 3 * r.m.s. of neighbours

Remove groups with < 10 vectors

Fill-up empty spaces (interpolation) Fill-up all

Smoothing: 2x Smooth 3x3 Apply currently active mask

Apply allowable vector range again

Appendix D: Simulation Codes

Appendix D provides the codes developed in MATLAB regarding the bubble shape measurement (chapter 4) and evaluation of discretization error (chapter 5). A brief description of each part of this appendix is provided here.

Appendix D1 presents the main code which incorporates a number of for different steps.

Appendix D2 presents the function developed to read the images, conduct the preprocessing step, and detect the droplets.

Appendix D3 calculates a number of basic geometric features of the detected shapes. These geometric features are later used to calculate the shape parameters.

Appendixes D4, D5, D6, D7, D8, D9, D10, and D14 present the functions developed to calculate shape parameters 1, 2, 3, 4, 5, 6, 7, 8, 9, 10, and 14, respectively.

Appendix D15 provides the code developed to generate the circular and the elliptical discs used in the evaluation of discretization error.

Appendix D1: The Main Script

```
clear all
close all
clc

%%% labels of the first row of the results' matrix
result=[0 0 0 0 1 21 22 23 3 4 6 7 8 9 10 141 142];

%%%%%%%%%%%%%%%%%%%%%%%%%%%%%%%%%%%%%%%%%%%%%%%%%%%%%%%%%%%%%%%%%%%%%%%% file name and path generator %%%%%%%%%

for r=3:0.5:130;
    for x_move=0:0.1:0.5
        for y_move=0:0.1:0.5
%for r=3:0.5:3;
%    for x_move=0:0.1:00
%        for y_move=0:0.1:0.5

                filename=['D:\Research\Projects\DropIet Shape
Measurement\Codes\images\Circles (Original
images)\',num2str(2*r),'\Fig_',num2str(2*r),'pix_',num2str(x_move),'x_',num2str(y_move),'
y','.bmp'];
                num=round((r-3)*36*2+(x_move)*6*10+(y_move+0.1)*10);
                file(num).name=filename;
            end
        end
    end
end

for image_num=1:num

%%%%%%%%%%%%%%%%%%%%%%%%%%%%%%%%%%%%%%%%%%%%%%%%%%%%%%%%%%%%%%%%%%%%%%%% Read image %%%%%%%%%

%figure
%set(gcf,'Position',[100 650 550 440])
image_matrix = imread(file(image_num).name);
imshow(image_matrix);

%%%%%%%%%%%%%%%%%%%%%%%%%%%%%%%%%%%%%%%%%%%%%%%%%%%%%%%%%%%%%%%%%%%%%%%% Pre-Processing %%%%%%%%%

%%% reversing the intensity values for an 8 bit image
%%% threshold is 0.7 of the maximum value
%%% remove all object containing fewer than 5 pixels
%%% fill any holes, so that regionprops can be used to estimate the area enclosed by
each of the boundaries

image_binary=PreProc( image_matrix );

%%%%%%%%%%%%%%%%%%%%%%%%%%%%%%%%%%%%%%%%%%%%%%%%%%%%%%%%%%%%%%%%%%%%%%%% Boundary Detection and calculating the main parameters %%%%%%%%%

% Display the label matrix and draw each boundary
% obtain (X,Y) boundary coordinates corresponding to label '1'
% compute a simple estimate of the object's perimeter
% obtain the area calculation corresponding to the label '1'

Result=BasicPara( image_binary );

Area=Result.area;
Perimeter=Result.perimeter;
Perimeter_4connectivity=Result.perimeter2;
MajorAxisLength_SecMom=Result.MajorAxisLength_SecMom;
```



```
Para_14 =  
Parameter_14(MajorAxisLength_SecMom,MinorAxisLength_SecMom,MajorAxisLength_LMS,MinorAxisL  
ength_LMS,Area);
```

```
%%%%%%%%%%%%%%%%%%%%%%%%%%%%%%%%%%%%%%%%%%%%%%%%%%%%%%%%%%%%%%%%%%%%%%%%  
%%%%%%%%%%%%%%%%%%%%%%%%%%%%%%%%%%%%%%%%%%%%%%%%%%%%%%%%%%%%%%%%%%%%%%%% Display the results %%%%%%%%%%%%%%%%%%%%%%%%%%%%%%%%%%%%%%%%%%%%%%%%%%%%%%%%%%%%%%%%%%%%%%%%%  
%%%%%%%%%%%%%%%%%%%%%%%%%%%%%%%%%%%%%%%%%%%%%%%%%%%%%%%%%%%%%%%%%%%%%%%%
```

```
%DisplayRes(Para_1,Para_2,Para_3,Para_4,Para_6,Para_7,Para_8,Para_9,Para_10,Para_14);
```

```
result=[result; (2*r)-1 SMD Perimeter Perimeter_4connectivity Para_1 Para_2 Para_3  
Para_4 Para_6 Para_7 Para_8 Para_9 Para_10 Para_14 ];
```

```
end
```

```
Save_result(result)
```


Appendix D2: The Preprocessing Function

```
function PreProc = PreProc( image )

global plot_para
%%%%%%%%%%%%%%%%%%%%%%%%%%%%%%%%%%%%%%%%%%%%%%%%%%%%%%%%%%%%%%%%%%%%%%%% Threshold the image %%%%%%%%%%
if plot_para==1
    figure
    set(gcf,'Position',[100 650-450 550 440])
    % image = rgb2gray(image);
end

image=2^8-image;          %%% reversing the intensity values for an 8 bit image
bw = im2bw(image,0.65);  %%% threshold is 0.7 of the maximum value

if plot_para==1
    imshow(bw);
end

%%%%%%%%%%%%%%%%%%%%%%%%%%%%%%%%%%%%%%%%%%%%%%%%%%%%%%%%%%%%%%%%%%%%%%%% Remove the small particle %%%%%%%%%%
% remove all object containing fewer than 5 pixels
bw = bwareaopen(bw,5);

%%%%%%%%%%%%%%%%%%%%%%%%%%%%%%%%%%%%%%%%%%%%%%%%%%%%%%%%%%%%%%%%%%%%%%%% Fill the particle %%%%%%%%%%
% fill any holes, so that regionprops can be used to estimate
% the area enclosed by each of the boundaries
bw = imfill(bw,'holes');

if plot_para==1
    imshow(bw);
end

PreProc=bw;
```

Appendix D3: Basic Geometric Features

```
function BasicPara= BasicPara( bw )

global plot_para

%%% check for the connectivity number in calculating perimeter

[B,L] = bwboundaries(bw,8,'noholes'); %%%%% MATLAB fuction is used to get the
boundary
[B2,L2] = bwboundaries(bw,4,'noholes'); %%%%% MATLAB fuction is used to get the
boundary based on 4 connectivity

% Display the label matrix and draw each boundary

if plot_para==1
    imshow(label2rgb(L, @jet, [.5 .5 .5]))
    hold on
end

for k = 1:length(B)
    boundary = B{k};
    if plot_para==1
        plot(boundary(:,2), boundary(:,1), 'w', 'LineWidth', 2);
    end
end

stats =
regionprops(L, 'PixelList', 'Area', 'Centroid', 'ConvexHull', 'MajorAxisLength', 'MinorAxisLeng
th', 'Orientation', 'ConvexArea', 'BoundingBox');

%%%%%%%%%%%%% Compute basic parameters, Area, Perimeter %%%%%%%%%%%%%%

% obtain (X,Y) boundary coordinates corresponding to label '1'
boundary = B{1};
% compute a simple estimate of the object's perimeter
delta_sq = diff(boundary).^2;
perimeter = sum(sqrt(sum(delta_sq,2)));

% obtain (X,Y) boundary coordinates corresponding to label '1'
boundary2 = B2{1};

% compute a simple estimate of the object's perimeter
delta_sq2 = diff(boundary2).^2;
perimeter2 = sum(sqrt(sum(delta_sq2,2)));

% obtain the area calculation corresponding to label 'k'
area = stats(1).Area;

% Major and Minor axis and orientation of fitted ellipse base on MATLAB procedure of
having the same second moment as the image

MajorAxisLength_SecMom = stats(1).MajorAxisLength;
MinorAxisLength_SecMom = stats(1).MinorAxisLength;
Orientaion_M1 = stats(k).Orientation;

% compute longest axis
Longest_axis = 0 ; %%% first assumption
for i=1:length(boundary(:,1))
    for j=1:length(boundary(:,1))
```

```

        distance=( (boundary(i,1)-boundary(j,1)).^2 + (boundary(i,2)-boundary(j,2)).^2 )
^ 0.5 ;
        if distance > Longest_axis
            Longest_axis= distance;
        end
    end
end

% obtain the convex region boundary corresponding to label 'k'
ConvexRegion_boundary = stats(1).ConvexHull;

if plot_para==1
    plot(ConvexRegion_boundary(:,1), ConvexRegion_boundary(:,2), 'r', 'LineWidth', 2);
end

% obtain the convex region perimeter corresponding to label 'k'

delta_sq_Convex = diff(ConvexRegion_boundary).^2;
CHP = sum(sqrt(sum(delta_sq_Convex,2)));

CHA=stats(1).ConvexArea;

% center of mass of the image
centroid = stats(1).Centroid;

% calculating the radii from the centroid to boundary
for i=1:length(boundary)
    radius(i,1) = ( (boundary(i,2)-centroid(1)).^2 + (boundary(i,1)-centroid(2)).^2 ) ^
0.5 ;
end

% mean radius length
mean_radius= mean(radius);

% Fit ellipse base on least mean square, ellipsefit function
fit_ellipse_res=fit_ellipse(boundary(:,1), boundary(:,2));

MajorAxisLength_LMS=fit_ellipse_res(8);
MinorAxisLength_LMS=fit_ellipse_res(9);

% BoundingBox (the smallest enclosing rectange) length and width
Rectangle = stats(1).BoundingBox;

width_Rect=min(Rectangle(3:4));
length_Rect=max(Rectangle(3:4));

% list of the pixels inside the region
Pixel_List=stats(1).PixelList;

% SMD
SMD= ( 4 * area / pi )^0.5;

%%%%%%%%%%%%%%%%%%%%%%%%%%%%%%%%%%%%%%%%%%%%%%%%%%%%%%%%%%%%%%%%%%%%%%%%%% Export Results %%%%%%%%%%%%%%%%%%%%%%%%%%%%%%%%%%%%%%%%%%%%%%%%%%%%%%%%%%%%%%%%%%%%%%%%%%%

BasicPara.area=area;
BasicPara.perimeter=perimeter;
BasicPara.perimeter2=perimeter2;
BasicPara.MajorAxisLength_SecMom=MajorAxisLength_SecMom;
BasicPara.MinorAxisLength_SecMom=MinorAxisLength_SecMom;
BasicPara.Longest_axis=Longest_axis;

```

```
BasicPara.CHA=CHA;  
BasicPara.CHP=CHP;  
BasicPara.centroid=centroid;  
BasicPara.Boundary=boundary;  
BasicPara.radius=radius;  
BasicPara.mean_radius=mean_radius;  
BasicPara.MajorAxisLength_LMS=MajorAxisLength_LMS;  
BasicPara.MinorAxisLength_LMS=MinorAxisLength_LMS;  
BasicPara.Width_Rect=width_Rect;  
BasicPara.Length_Rect=length_Rect;  
BasicPara.Pixel_List=Pixel_List;  
BasicPara.SMD=SMD;
```

Appendix D4: Parameter 1

```
function Parameter_1 = Parameter_1( area, perimeter )
%%%%%% Method 1, based on distances %%%%%%%%%%%%%%%%%%%%%%%%%%%%%%%
Parameter_1 = (4*pi*area)/(perimeter^2);
```

Appendix D5: Parameter 2

```
function Parameter_2 = Parameter_2( MajorAxisLength_SecMom, MinorAxisLength_SecMom,
MajorAxisLength_LMS ,MinorAxisLength_LMS, width_Rect, length_Rect)
%%%%%% Method 1, Fitted ellipse having the same second moment as the object
%%%%%%%%%%%%%%%%%%%%%%%%%%%%%%%%%%%%%%%%%%%%%%%%%%%%%%%%%%%%%%%%%%%%%%%%
method1 = MinorAxisLength_SecMom / MajorAxisLength_SecMom;

%%%%%% Method 2, Fitted ellipse by the least mean square method
%%%%%%%%%%%%%%%%%%%%%%%%%%%%%%%%%%%%%%%%%%%%%%%%%%%%%%%%%%%%%%%%%%%%%%%%
method2 = MinorAxisLength_LMS / MajorAxisLength_LMS;

%%%%%% Method 3, BoundingBox, matlab code to fit the smallest enclosing recatngle
%%%%%%%%%%%%%%%%%%%%%%%%%%%%%%%%%%%%%%%%%%%%%%%%%%%%%%%%%%%%%%%%%%%%%%%%

%%%%%% This method is only appropriate when the major axis is horizontal or vertical
%%%%%%%%%%%%%%%%%%%%%%%%%%%%%%%%%%%%%%%%%%%%%%%%%%%%%%%%%%%%%%%%%%%%%%%%
method3=width_Rect/length_Rect;

Parameter_2=[method1 method2 method3];
```

Appendix D6: Parameter 3

```
function Parameter_3 = Parameter_3( area, longest_axis )
Parameter_3 = (4*area) / (pi* (longest_axis)^2 );
```

Appendix D7: Parameter 4

```
function Parameter_4 = Parameter_4(mean_radius, Width_Rect, Length_Rect, Perimeter);
f = 1.008 - 0.231 * ( 1 - Width_Rect / Length_Rect);
Parameter_4 = (2*pi*mean_radius)/(Perimeter*f) - ( 1 - (Width_Rect / Length_Rect)^2
)^0.5;
```

Appendix D8: Parameter 5

```
function Parameter_5 = Parameter_5( area, CHA )  
Parameter_5 = (CHA - area )/CHA;
```

Appendix D9: Parameter 6

```
function Parameter_6 = Parameter_6( Perimeter, CHP )  
Parameter_6 = (CHP)/Perimeter;
```

Appendix D10: Parameter 7

```
function Parameter_7 = Parameter_7( Area, CHA)  
Parameter_7 = (CHA)/Area;
```

Appendix D11: Parameter 8

```
function Parameter_8 = Parameter_8( x_centroid, y_centroid, x_boundary, y_boundary,  
radius, mean_radius)  
for i=1:length(radius)  
    A(i)=(abs(radius(i)-mean_radius)*100)/mean_radius;  
end  
  
Parameter_8 = mean(A);
```

Appendix D12: Parameter 9

```
function Parameter_9 = Parameter_9( perimeter, mean_radius)  
Parameter_9= abs(2*pi*mean_radius-perimeter)/(2*pi*mean_radius)*100;
```

Appendix D13: Parameter 10

```
function Parameter_10 = Parameter_10( x_centroid, y_centroid, area, Pixel_list_x,
Pixel_list_y)

Parameter_10 = area^2 / (2*pi*(sum ( (Pixel_list_x - x_centroid).^2 + (Pixel_list_y -
y_centroid).^2 )) );
```

Appendix D14: Parameter 14

```
function Parameter_14 = Parameter_14(MajorAxisLength_SecMom
,MinorAxisLength_SecMom,MajorAxisLength_LMS ,MinorAxisLength_LMS,Area )

%%%%% Method 1, The ellipse is fitted by the second moment method

Para_14_1 = (pi * MajorAxisLength_SecMom * MinorAxisLength_SecMom / 4) / Area;

%%%%% Method 2, The ellipse is fitted by the least mean square method

Para_14_2 = (pi * MajorAxisLength_LMS* MinorAxisLength_LMS / 4) / Area;

%%%%% export the results

Parameter_14=[Para_14_1 Para_14_2];
```

Appendix D15: Circular and Elliptical Discs

```
close all
clear all
clc

r_C2_m=[5:1:125]';
r2_over_r1=[1 0.8 0.6 0.4 0.2]';
for i=1:5
    r_C1_m(:,i)=r_C2_m/r2_over_r1(i);
end
r_C1_m=round(r_C1_m);

%%%%%%%%%%%%%%%%%%%%%%%%%%%%%%%%%%%%%%%%%%%%%%%%%%%%%%%%%%%%%%%%%%%%%%%%

for i=1:length(r2_over_r1)
    for j=1:length(r_C1_m(:,1))

        r_C1=r_C1_m(j,i);
        r_C2=r_C2_m(j);

        %    for r_C2=5:5:r_C1
        %        for move=r_C1-r_C2+1:1:2*r_C2-1

        newfolder=['\\NOBES-OFFICE\GHAEMI\Centricity\coalescing and elongated droplets
images\images\Coalescing\' ,num2str(r_C2)];
        mkdir(newfolder)

        newfolder=['\\NOBES-OFFICE\GHAEMI\Centricity\coalescing and elongated droplets
images\images\Elongated\' ,num2str(r_C2)];
```

```

mkdir(newfolder)

for move_parameter = 0.1:0.1:0.9

    move = round( move_parameter * (r_C1+r_C2) );

    % figure
    im_plane=ones(2*r_C1+6,4*r_C1+6);
    im_plane=im_plane*256;
    colormap(gray(256));
    xC1=r_C1+2;
    yC1=r_C1+2;

    im_plane_2=DrawCircle(DrawCircle(im_plane,r_C1,xC1,yC1),r_C2,xC1,yC1+move);
    filename=['\\NOBES-OFFICE\GHAEMI\Centricity\coalescing and elongated droplets
images\images\Coalescing\' ,num2str(r_C2), '\Fig_Coal_r1_',num2str(r_C1), '_r2_',num2str(r_C
2), '_move',num2str(move), 'r2Or1_',num2str(round(r_C2/r_C1)), '.bmp'];
    imwrite(im_plane_2,filename,'bmp')

    for m=1:1:r_C1+3
        if im_plane_2(m,yC1)==0
            x_apex1=m;
            break
        end
    end

    for n=1:1:r_C1+3

        if im_plane_2(n,yC1+move)==0
            x_apex2=n;
            break
        end
    end

    % figure
    % LineFill(im_plane_2,x_apex1,yC1,x_apex2,yC1+move,xC1);

    % figure
    im_plane_3=LineFill(im_plane_2,xC1-r_C1,yC1,xC1-r_C2,yC1+move,xC1);

    filename=['\\NOBES-OFFICE\GHAEMI\Centricity\coalescing and elongated droplets
images\images\Elongated\' ,num2str(r_C2), '\Fig_Elon_r1_',num2str(r_C1), '_r2_',num2str(r_C2
), '_move',num2str(move), 'r2Or1_',num2str(round(r_C2/r_C1)), '.bmp'];
    imwrite(im_plane_3,filename,'bmp')

    end
end
end

```


Appendix E: Contributions:

Publications:

Ghaemi S, Rahimi P, Nobes DS (2008) Assessment of parameters for distinguishing droplet shape in a spray field using image-based techniques, *Atomization and Sprays*, under review.

Ghaemi S, Rahimi P, Nobes DS (2008) Evaluation of digital image discretization error in droplet shape measurement using simulation, *Particle and Particle Systems Characterization*, under review.

Ghaemi S, Rahimi P, Nobes DS (2008) Evaluation of StereoPIV measurement of droplet velocity in an effervescent spray, *Spray and Combustion Dynamics*, under review.

Ghaemi S, Rahimi P, Nobes DS (2008) The effect of gas-injector location on bubble formation in liquid cross flow, *Physics of Fluids*, under review.

Refereed Conference Proceedings:

Ghaemi S, Rahimi P, Nobes DS (2008) Investigation of the spatial distribution of droplet SMD in the spray field of an effervescent atomizer, 21st Annual ILASS-Americas Conference. Orlando, FL, USA.

Ghaemi S, Rahimi P, Nobes DS (2008) Investigation of gas-liquid ratio effect on the near nozzle spatial structure of effervescent atomizer-produced spray, Canadian Society of Mechanical Engineering Forum, Ottawa, Canada.

Ghaemi S, Rahimi P, Nobes DS (2008) Measurement of droplet centricity and velocity in the spray field of an effervescent atomizer, 14th Int Symp on Application of Laser Techniques to Fluid Mechanics, Lisbon, Portugal.

Ghaemi S, Rahimi P, Nobes DS (2008) Effect of gas-liquid ratio on droplets centricity and velocity of an effervescent atomizer, ASME Fluid Engineering Conference, Jacksonville, FL, USA.

Presentations:

Ghaemi S, Rahimi P, Nobes DS (2008) Evolution of bubbles through gas injection from a micro-tube into liquid cross-flow, American Physical Society 61st Annual Division of Fluid Dynamics Meeting, San Antonio, Texas, USA.